

# University of St Andrews



Full metadata for this thesis is available in  
St Andrews Research Repository  
at:

<http://research-repository.st-andrews.ac.uk/>

This thesis is protected by original copyright

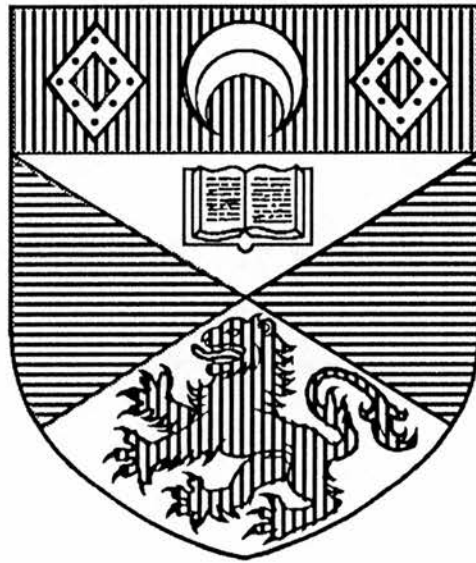
**OPTICAL PROPERTIES OF NOVEL GaAs-BASED SEMICONDUCTORS**

**BY**

**IAN THOMAS FERGUSON**

**B.Sc., Heriot Watt University, 1984**

**M.Sc., University of St. Andrews, 1985**



**A thesis submitted for the degree of**

**Doctor of Philosophy**

**to the**

**University of St Andrews**



**May 1989**

Th A 996

### Declaration

I Ian Ferguson, hereby certify that this thesis has been composed by myself, that it is a record of my own work, and that it has not been accepted in partial or complete fulfilment of any other degree or professional qualification.

16<sup>th</sup> June 1989

I was admitted to the Faculty of Science of the University of St. Andrews under Ordinance General No 12 on October 1985 and as a candidate for the degree of Ph. D. on May 1986.

16<sup>th</sup> June 1989

I hereby certify that the candidate has fulfilled the conditions of the Resolution and Regulations appropriate to the Degree of Ph. D.

16<sup>th</sup> June 1989

### Copyright

In submitting this thesis to the University of St. Andrews I understand that I am giving permission for it to be made available for use in accordance with the regulations of the University Library for the time being in force, subject to any copyright vested in the work not being affected thereby. I also understand that the title and abstract will be published, and that a copy of the work may be made and supplied to any bona fide library or research worker.

For mum and dad

## Acknowledgements

I would like to express my gratitude to my supervisor, Dr Clivia Sotomayor Torres, for her patient help, constant encouragement and smoothing off my rough edges. I appreciated the opportunity my industrial supervisor, Dr Tom Kerr, provided to learn MBE at GEC and the many fruitful discussions we had.

I would like to thank: B Mitchell and all the technical staff at St. Andrews for their assistance and anyone who lent equipment particularly, Derek and Les, Prof. J W Allen for the temperature controller and Dr G Walker (UMIST) for the cryostat. Dr David Finlayson for his cryogenics expertise and proof reading the final drafts of this work. David Crust for help with computing. Dr David Tunstall for dealing with the paperwork and Prof. W Sibbett for extending the use of the facilities of the department. Tom Wright at Glasgow University who ensured that I obtained the necessary back-up during my short stay there. Tin Cheng for providing a place to stay on many occasions and useful discussions throughout this work. Prof. I Spain for sharing his knowledge of DAC techniques.

I spent an informative and profitable time at GEC within the MBE group with Tom Kerr, Paul Rees, Robin Smith and Colin Wood and I am indebted to Paul Kirby for providing the use of his PL system. I would also like to thank, Dr Tim Beales and Prof. C Goodman for the use of facilities at SERC High Pressure Facility, and particularly Tim for continuing with the work we started together.

Samples for this work were donated by P A Claxton, J S Roberts at the SERC Central Facility for III-V semiconductors, T Kerr at GEC Hirst Research Centre, Wembley, G Scott at British Telecom Research Laboratories and T Cheng, C Stanley at Glasgow University.

During the course of this work I was supported by a SERC-CASE studentship from GEC Hirst Research Centre and in the latter part by; City of Dundee Educational Trust , Fife

Educational Trust , Sir Richard Stapley Educational Trust , Nancy Balfour Charitable Trust and the Master's Welfare Fund.

The last few years have been perhaps the most informative of my life. I have made many friends at St. Andrews and have always been aware of their encouragement and prayers. My last thoughts must be with my family for their support throughout my academic career and particularly my wife for her patience and understanding. I can assure her that there will be life after this thesis.

Experiments are the only means of knowledge at our disposal. The rest is poetry,  
imagination.

Max Planck

## Abstract

This thesis has considered the optical properties of III-V semiconductors and quantum well structures. Detailed optical assessment of the near band-edge luminescence from high quality  $\text{Al}_{0.48}\text{In}_{0.52}\text{As}$  including the use of photoluminescence excitation and the application of hydrostatic pressure is reported. The emission is dominated by a broad luminescence band too large to be accounted for by a simple model of alloy scattering of an excitonic transition. Experimental results show that the low temperature emission is due to 'deep' ( $\text{D}^0, \text{A}^0$ ) transitions. At higher temperature another transition was observed and assigned to ( $\text{e}, \text{A}^0$ ). A linear pressure coefficient of  $10.1 \text{ meV/kbar}^{-1}$  was obtained for  $\text{Al}_{0.48}\text{In}_{0.52}\text{As}$  and a deformation potential of  $6.59 \pm 0.25 \text{ eV}$  was calculated.

The observation of structure in the free exciton emission from InP was tentatively assigned to polaritons. Scattering of the polariton from neutral donors was proposed as an explanation of the excitation power density dependence of the emission structure.

Exciton emission from quantum well heterostructures was also studied. In  $\text{Ga}_{0.47}\text{In}_{0.53}\text{As-InP}$  the exciton was found to be bound to potential fluctuations in the well. The very narrow linewidths observed in the  $\text{GaAs-Al}_x\text{Ga}_{1-x}\text{As}$  wells were comparable with the best values reported elsewhere. A detailed study of the growth and luminescence from thin  $\text{GaAs-Al}_x\text{Ga}_{1-x}\text{As}$  wells on substrates misorientated towards the [110] direction was undertaken. The linewidths of the wells showed a 0.2 monolayer fluctuation regardless of substrate orientation since the exciton sensed a pseudo-rough inverted interface. Growth interruption did not result in a decrease of the linewidth and the observation of interface islands reported by other groups. Instead linewidths increased which was attributed to incomplete island formation at the inverted interface. The luminescence from the wells did not show a functional dependence on substrate

# CONTENTS

	<u>Page</u>	
<b>I</b>	<b>Introduction</b>	1
1.1	Historical Background and Introduction	2
1.2	General features from PL of direct-gap III-V semiconductors	4
1.2.1	Semiconductor Parameters	11
1.3	Spatial Quantisation in Heterostructures	12
1.4	Envelope Function Approximation in Heterostructures	14
1.4.1	Optical Transitions in Heterostructures	16
1.4.2	Parity and Polarization Selection rules	17
1.4.3	Excitonic Emission in Heterostructures	18
<b>II</b>	<b>Experimental Method</b>	20
2.1	MBE Growth of GaAs and $\text{Al}_x\text{Ga}_{1-x}\text{As}$	21
2.1.1	Principle of MBE	21
2.1.2	Growth Mechanism of III-V compounds	21
2.1.3	Doping and Alloy Growth	23
2.1.4	Growth on Misorientated Substrates	24
2.1.5	The VG V80H MBE Growth System	25
2.1.6	Sample Preparation and Growth Method	27
2.2	Photoluminescence Apparatus	28
2.2.1	Spectrometer	30
2.2.2	Detectors	31
2.2.3	Normalized System Response	33
2.2.4	Cryostats	35
2.3	High Pressure Optical Cell	40
2.3.1	Diamond Anvil Cell	41
2.3.2	Ruby line Calibration	43
2.3.3	Low Temperature Pressure Media	44
2.4	Samples used in this work	45
<b>III</b>	<b>Luminescence from Bulk III-V Semiconductors</b>	46
3.1	GaAs	47
3.2	InP	50

3.2.1	Polariton Emission in InP	54
3.2.2	Mg doping of MBE InP	60
3.2.3	The 1.36 eV emission in InP	63
3.3	$\text{Al}_x\text{Ga}_{1-x}\text{As}$	63
3.4	$\text{Ga}_{0.47}\text{In}_{0.53}\text{As}$	67
3.5	Summary	71
<b>IV</b>	<b>Luminescence Properties of <math>\text{Al}_{0.48}\text{In}_{0.52}\text{As}</math></b>	<b>73</b>
4.1	Introduction	74
4.2	Growth of $\text{Al}_{0.48}\text{In}_{0.52}\text{As}$	74
4.2.1	Previous Luminescence Results	77
4.3	Low Temperature Photoluminescence of $\text{Al}_{0.48}\text{In}_{0.52}\text{As}$	79
4.3.1	Linewidth Considerations	80
4.3.1.1	Alloy Broadening in $\text{Al}_{0.48}\text{In}_{0.52}\text{As}$	81
4.3.1.2	The effect of clustering in $\text{Al}_{0.48}\text{In}_{0.52}\text{As}$	84
4.3.1.3	Bimodal ordering in Semiconductor Alloys	86
4.3.2	Lineshape considerations	87
4.4	Temperature Dependence of the emission	90
4.5	Dependence on Excitation Power Density	94
4.6	Selective Photoluminescence Excitation	95
4.7	Summary	99
<b>V</b>	<b>Luminescence from Quantum Well Structures</b>	
5.1	Introduction	102
5.2	Review of previous work	103
5.2.1	Impurity and Exciton Binding Energy	104
5.2.2	Interfacial Disorder and Growth Interruption	107
5.2.3	Band Offset	109
5.3	Lineshape and Linewidth Considerations	110
5.4	$\text{GaAs-Al}_x\text{Ga}_{1-x}\text{As}$	115
5.4.1	Intrinsic and Extrinsic Emission	115
5.4.1.1	Temperature dependence	118
5.4.1.2	Excitation Power Density Dependence	119
5.4.1.3	Doping Study	120
5.4.2	Carrier Capture	121
5.4.3	Growth on Misorientated Substrates	124
5.4.3.1	Barrier of composition $x=0.3$	127

	5.4.3.2	Barrier of composition $x=0.4$	129
	5.4.3.3	Barrier of composition $x=0.2$	130
5.5	$\text{Ga}_{0.47}\text{In}_{0.53}\text{As-InP}$		130
	5.5.1	Review	131
	5.5.2	Temperature dependence	132
	5.5.3	Some Comments	135
5.6	Pseudomorphic HEMTs		135
5.7	Summary		137
<b>VI</b>	<b>PL of <math>\text{Al}_{0.48}\text{In}_{0.52}\text{As}</math> under hydrostatic pressure</b>		<b>140</b>
	6.1	Introduction	141
	6.2	Calculation of Deformation Potential	142
	6.2.1	Review	144
	6.3	$\text{Al}_{0.48}\text{In}_{0.52}\text{As}$ under Hydrostatic Pressure	148
	6.3.1	Experimental Considerations	149
	6.3.2	Luminescence $\text{Al}_{0.48}\text{In}_{0.52}\text{As}$ under Hydrostatic Pressure	150
	6.3.3	Deformation Potential of $\text{Al}_{0.48}\text{In}_{0.52}\text{As}$	152
	6.3.4	Effective Mass dependence on Pressure in $\text{Al}_{0.48}\text{In}_{0.52}\text{As}$	155
	6.4	Summary	156
<b>VII</b>	<b>Conclusions</b>		<b>158</b>
	7.1	Conclusions and suggested further work	159
	<b>References</b>		<b>163</b>
	<b>Appendices</b>		
	A:	Compensation ratio from optical spectra	
	B:	Pressurization of a diamond anvil cell	
	C:	Programs used in this work	

# I INTRODUCTION

	<u>Page</u>
1.1 Historical Background and Introduction	2
1.2 General features from PL of direct-gap III-V semiconductors	4
1.2.1 Semiconductor Parameters	11
1.3 Spatial Quantisation in Heterostructures	12
1.4 Envelope Function Approximation in Heterostructures	14
1.4.1 Optical Transitions in Heterostructures	16
1.4.2 Parity and Polarization Selection rules	17
1.4.3 Excitonic Emission in Heterostructures	18

## 1.1 Historical Background and Introduction

Semiconductor physics came of age in 1947 with the revolutionary invention of the transistor by Bardeen, Brattain and Shockley (1948). Until this decade, silicon formed the back bone of the semiconductor industry for device fabrication and large scale integration. The advent of III-V compounds, particularly GaAs, spurred on by new and improved growth techniques, are now making a large and important technological contribution. GaAs offers increased carrier concentrations, nearly parabolic band structure and a direct energy gap leading to high quantum efficiencies necessary for optical devices such as lasers. The relative ease of forming III-V ternary and quaternary alloys from the constituent binaries has meant a large range of different materials are now available. The refinement of growth techniques has allowed semiconductors to be defined on the monolayer atomic scale with the production of lattice matched superlattices from various III-V compounds and alloys. The quantum confinement of energy levels and carriers has resulted in the birth of a new branch of physics to study the two dimensional properties of these new structures.

The optical characterization of III-V epitaxial layers is particularly important as it allows observation of fundamental material properties and provides a critical assessment of material quality. Photoluminescence which implies excitation by a optical source, allows accurate band-edge determination and impurity identification at very low concentrations that cannot easily be probed by other methods. It is important for the growth and further purification of materials that substitutional donor and acceptor impurities can be identified. Further experimental refinements to PL; selective excitation techniques and the application of perturbations such as electric or magnetic fields, or the use of pressure or strain, enhances the data obtained. For the study of luminescence to be effective, a number of samples should be considered to eliminate any anomalous

## I Introduction

results from the data. Although the study of luminescence was initiated by the alchemistic work of Vincenzo Cascariolo, an inquisitive cobbler from Bologna, in 1603 (Queisser 1981); it was not until the advent of the laser in the 1960's, providing a narrow bandwidth source with high excitation power density, that photoluminescence became a widely used technique.

In this work, chapter 1 provides the basic understanding of the luminescence properties of direct gap III-V semiconductors and is extended to show how spatial quantisation in heterostructures results in increased electron/hole wavefunction overlap with enhanced excitonic emission. Chapter 2 details the MBE growth of the III-V samples studied here, the construction of a photoluminescence excitation and collection system, and the use of a diamond anvil cell, suitably modified, for optical spectroscopy at high pressures and low temperatures.

In chapter 3, luminescence from the more common III-V compounds and alloys, GaAs, InP,  $\text{Al}_x\text{Ga}_{1-x}\text{As}$  and  $\text{Ga}_{0.47}\text{In}_{0.53}\text{As}$  are given as background. This provides the correct framework before attempting the assessment of  $\text{Al}_{0.48}\text{In}_{0.52}\text{As}$  and quantum well heterostructures. Chapter 4, gives to the best of our knowledge, the first in depth analysis of the optical properties of  $\text{Al}_{0.48}\text{In}_{0.52}\text{As}$ , considering particularly the problem of emission assignment. This work was motivated because  $\text{Al}_{0.48}\text{In}_{0.52}\text{As}$  was becoming more technologically important in devices, such as HEMTs, and superlattice structures. In chapter 5, the assignment of the excitonic emission from GaAs- $\text{Al}_x\text{Ga}_{1-x}\text{As}$  wells is made and contrasted to that observed from  $\text{Ga}_{0.47}\text{In}_{0.53}\text{As}$ -InP wells and bulk binaries in chapter 3. This was extended by study of growth and the luminescence emission from thin wells, grown by MBE on misorientated substrates. The final chapter explores the application of hydrostatic pressure to  $\text{Al}_{0.48}\text{In}_{0.52}\text{As}$  considered in chapter 4, giving the deformation potential for  $\text{Al}_{0.48}\text{In}_{0.52}\text{As}$  and variation of effective mass with pressure.

## I Introduction

### 1.2 General Features of Photoluminescence from Direct Gap III-V Semiconductors

Photoluminescence has proved a valuable technique in the study of semiconductor electronic levels, for example, in impurity identification and band-edge determination in semiconductors. When a semiconductor crystal is excited by an optical pump such as a laser, electrons are excited to the conduction band leaving behind a hole in the valence band; subsequently the excited carriers relax towards the band-edge in a picosecond time scale. If the electron and the hole stay within the vicinity of each other coulombic attraction occurs to form a bound electron-hole pair, an exciton. In III-V semiconductors the electrons and holes form loosely bound Wannier excitons and are free to move throughout the whole crystal. The exciton has no associated charge transfer and forms the lowest excited state of the whole crystal. The Wannier exciton is hydrogenic in nature and its properties are well described by the effective mass approximation (Knox 1963). Therefore a modified Rydberg equation can be used to estimate the exciton binding energy.

If the semiconductor was perfectly crystalline and contained no impurities, only a transition associated with the annihilation of the free exciton (X) would be observed. This is not generally the case and the luminescence spectra from even the purest semiconductors are dominated by impurity related transitions. Four main types of recombination pathways can be observed: excitonic, free-to-bound, donor-acceptor-pair and phonon assisted transitions (see figure 1.1 and table 1.1). Emission from the conduction band to valence band (e,h) is normally only observed in degenerately doped semiconductors or alloys as a result of tail states (Schubert and Ploog 1985). Even though non-radiative transitions are not directly detected in the luminescence they are important because they compete with the radiative transitions, thus altering the emission intensity and time-dependence.

Electron-hole pair  
created by optical  
pumping

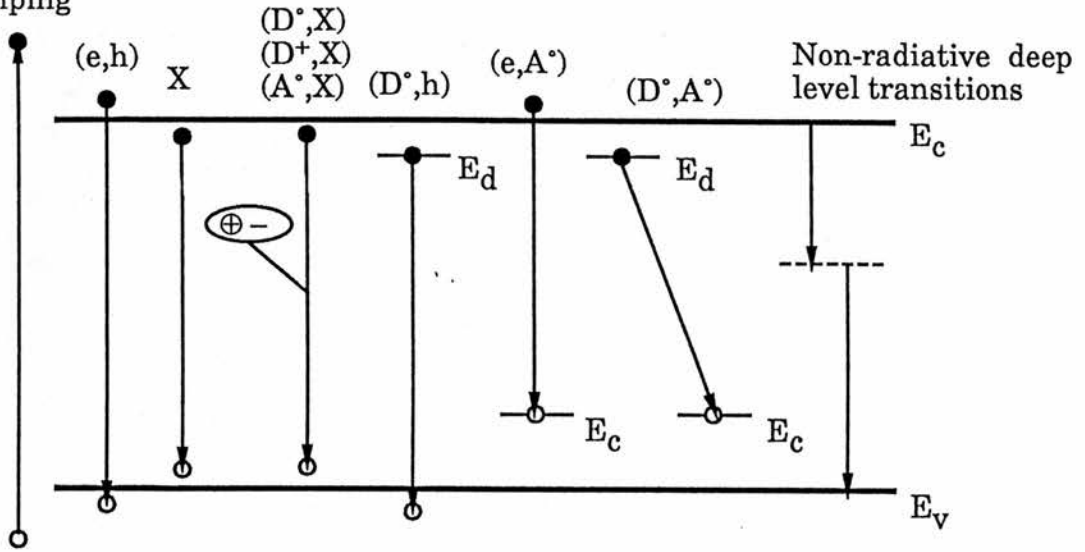


Figure 1.1 Idealized band-edge diagram showing possible optical transitions (Cavenett 1978)

---

(e,h)	Conduction band to valence band
X	Free exciton
(D°,X)	Neutral Donor bound exciton
(D+,X)	Exciton bound at an ionized donor, transition intensity increases with temperature due to thermal ionization of donors.
(A°,X) <sub>j</sub>	Shallow Acceptor bound exciton, on recombination the exciton may leave the acceptor in a excited state where its total angular momentum quantum number $j=0.5, 1.5, 2.5$
(D°,h)	Neutral Donor to free hole
(e,A°)	Free electron to neutral acceptor
(D°,A°)	Donor acceptor pair

---

Table 1.1 Symbols used for labeling optical transitions (Cavenett 1978)

## I Introduction

All the semiconductors studied in this work have the zincblende structure. It consists of two face-centred cubic (fcc) lattices, the point lattice group, displaced by one quarter of a body diagonal (figure 1.2). When considering a III-V compound such as GaAs; then Ga atoms will be placed on one fcc lattice and As atoms on the other fcc lattice. The diamond structure is similar but the atoms are of the same chemical type on each fcc lattice. Each atom has four equally distant atoms arranged in the form of a regular tetrahedron as a result of directional covalent bonding. The diamond structure possesses a centre of inversion symmetry at the midpoint of each line connecting nearest neighbour atoms. The zincblende structure does not have this inversion symmetry due to the differing atoms.

Before considering the optical emission observed from samples in this work, it will be useful to consider the luminescence from GaAs as an example of a direct-gap, III-V semiconductor (see figure 1.3). The lightly doped material, in this instance  $n \sim 10^{14} \text{ cm}^{-3}$ , provides a simplified spectrum, without impurity broadening, of the radiative recombination channels labeled in table 1.1. Samples are typically cooled to  $\sim 4 \text{ K}$  to reduce the effects of thermal broadening. In GaAs the band-gap energy ( $E_g = E_c - E_v$ ) is 1.5192 eV, the dielectric constant 12.8, electron and hole masses are  $0.065 m_0$  and  $0.450 m_0$ , respectively (see section 1.2.1). Using the effective mass approximation the binding energies for the shallow donor,  $E_d = 5.4 \text{ meV}$  and shallow acceptor,  $E_a = 37.2 \text{ meV}$  can be estimated. The features of the luminescence transitions are discussed below. The same transitions and features should also be present in III-V alloys, this will be dealt with elsewhere.

In GaAs the free exciton has a binding energy of 4.2 meV (Sell 1972) and is only observed in very pure material. Since free excitons are mobile they become trapped or localized at shallow impurities, thus different mechanisms contribute to the luminescence (see figure 1.3). The bound exciton shows a narrow,

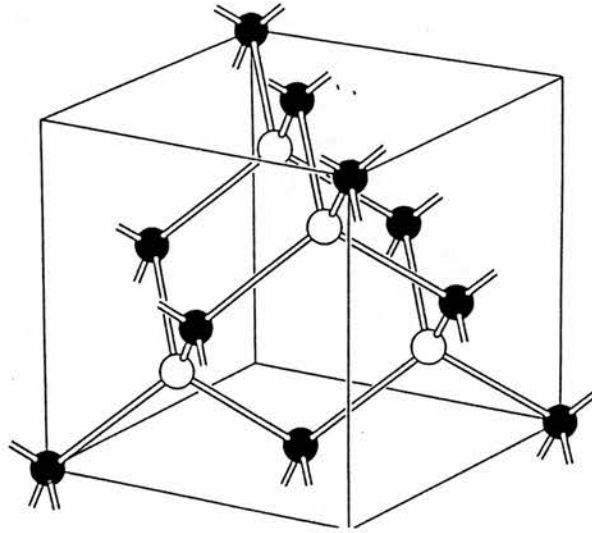


**Figure 1.2** In zinc blende structure the different atoms (e.g. Ga and As) are on a interpenetrating face-centred cubic lattice. Diamond is similar but both atoms are chemically the same. Note the tetrahedral arrangement of bonds (Elliot and Gibson 1982).

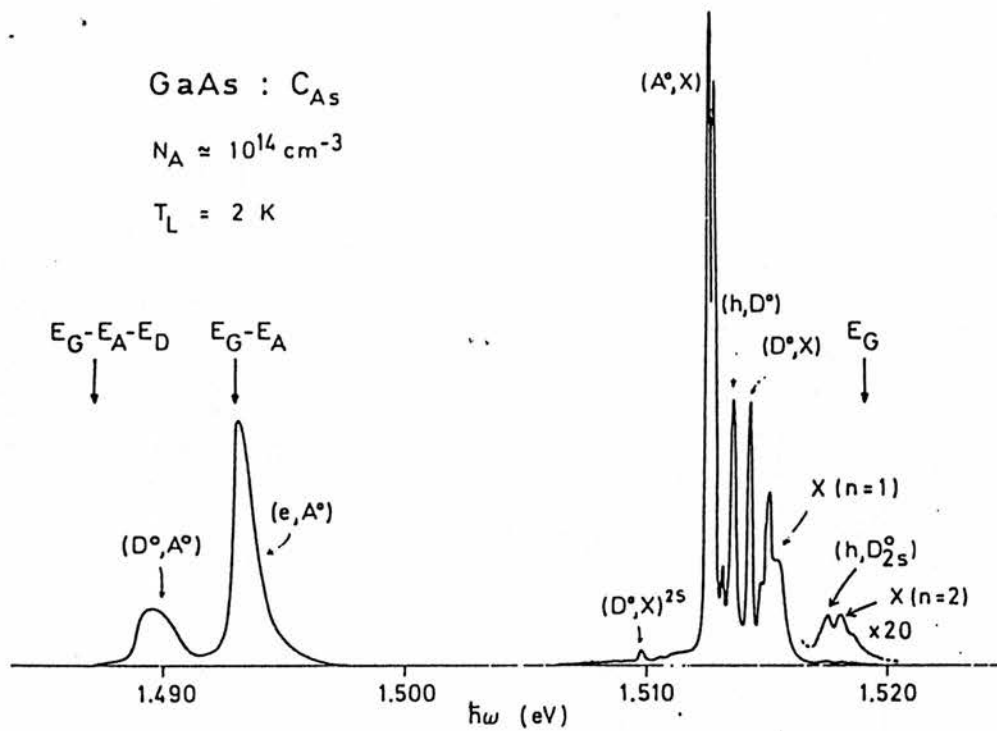


**Figure 1.3** Typical emission spectrum of lightly doped GaAs at low temperature under optical excitation  $\hbar\omega > E_g$  with excitation power 10 mW/cm<sup>2</sup> (Ulbrich 1978).

## I Introduction

Lorentzian shaped, symmetrical luminescence unbroadened by kinetic energy. There can also be emission from excitonic complexes and molecules, however, these are beyond the scope of the present work. Hopfield (1964) considered a function of the effective mass  $\sigma = m_e/m_h$  to indicate whether or not an exciton binds. He proved that the exciton always binds to shallow neutral impurity centres such as  $D^\circ$  or  $A^\circ$ . But the exciton only binds to ionized donors or acceptors when  $0.72 < \sigma < 1.4$ , i.e. the energy to localize a hole at a neutral donor does not exceed the corresponding gain in potential energy. He also noted that a semiconductor crystal cannot have excitons bound to both ionized donors and acceptors, this was later supported by Levy-Leblond (1969). The binding energy of the exciton to an impurity depends on the impurity binding energy. But excitons do not normally bind to impurities, complexes or interstitials whose own binding energies are large (Dean and Herbert 1969). Haynes (1960) established the empirical relationship that exciton binding energy was  $\sim 10\%$  of the impurity binding energy for shallow impurities in silicon, "Haynes' rule". This rule holds in III-V materials such as GaAs but because variations of  $E_d$  are small it will not be observed as a difference in exciton binding energy except in very high resolution spectroscopy. Excitons bound to shallow neutral acceptors can show up to three different principal recombination transitions. The structure is explained as a consequence of j-j coupling of holes forming a two hole state that then couples to the electron (Table 1.1).

On increasing the temperature of a sample, the emission dependence on temperature can give further evidence of what the transition can be. The intensity variation due to the dissociation process can, in the high temperature limit, be described by  $I(T) \sim \exp(E_a/kT)$ , where  $E_a$  is the activation energy associated with the dissociation process. In GaAs the temperature dependence of the  $(D^\circ, X)$  and  $(D^+, X)$  differ over the temperature range 2-16 K since the  $(D^\circ, X)$

## I Introduction

transition dissociates easily into  $D^{\circ}$  and an exciton quenching rapidly (Williams and Bebb 1967).

The intensity dependence of excitonic emission with increasing excitation power density appears confused in the literature possibly because the results are sample dependent. Interpretation of experimental data is difficult since many different transitions can compete and the effects of non-radiative channels are unknown. But no one has reported a excitonic emission which has a power dependence less than unity and if the emission were impurity related it would saturate when the density of incident photons exceeds the density of impurities. Since the formation of excitons is proportional to the product of the two photo-created populations in the bands the exciton emission intensity should increase quadratically with excitation density. Bimberg et al (1970) observed this in Sn-doped GaAs at low excitation intensities but as the excitation power density was increased an unity intensity dependence was obtained.

Non-excitonic transitions such as, free-to-bound or donor-acceptor-pair, occur at lower energies than the excitonic emission. A free-to-bound transition occurs when either; a loosely bound electron on a donor combines with a hole in the valence band, donor-to-free hole ( $D^{\circ},h$ ) or a loosely bound hole on an acceptor combines with a electron in the conduction band, free electron-to-acceptor ( $e,A^{\circ}$ ). The binding energy for shallow donors is similar for most impurities in GaAs, ranging from 5.789 meV to 5.915 meV (Madelung 1982). For hydrogenic impurities deviations from the binding energy estimated by the effective mass theory, which arise from differences in impurity and host core potentials, are accounted for by a central cell correction. The small energy difference between donors in narrow gap III-V compounds, makes it difficult to resolve emission involving different donor species using the ( $D^{\circ},h$ ) transition. But more refined techniques such as selective excitation and magneto-luminescence can be used (Venghaus et al 1984). A further complication arises in this spectral region

## I Introduction

because the ( $D^{\circ},h$ ) and the ( $D^+,X$ ) transitions occur at the same energy making unclear which transition is present. As a consequence of larger hole masses, shallow acceptor binding energies range from 27 meV to 40 meV for different impurities. So the ( $e,A^{\circ}$ ) transition can be used to identify and label acceptor impurities with reasonable accuracy,  $\pm 1$  meV. The free-to-bound transition may not necessarily be seen at low temperatures (4.2K), its observation depends on carrier concentration, non-radiative transition rate and compensation, see section 3.3.2. The peak energy of a free-to-bound transition such as the ( $e,A^{\circ}$ ) as the temperature is increased is given by

$$E_{FB}(e,A^{\circ}) = E_g - E_a + 0.5kT \quad (1.1)$$

where  $k$  is the Boltzmann constant. The kinetic energy of the electrons in the conduction band acts to increase the linewidth of the transition as the temperature is increased. Eagles (1960) showed that the recombination spectra for a conduction band to acceptor transition could be approximated by

$$I(\hbar\omega) \sim (\hbar\omega - E_g + E_a)^{0.5} \exp[ -(\hbar\omega - E_g + E_a)/kT ] \quad (1.2)$$

where  $I(\hbar\omega)$  is the recombination intensity. This equation is similar to that for band-to-band transitions (see equation 4.12). This expression has proved very successful in lineshape fitting to spectra to estimate impurity binding energies (Williams and Bebb 1967).

The donor-acceptor-pair transition, ( $D^{\circ},A^{\circ}$ ), occurs between a neutral donor and a neutral acceptor leaving the impurities partially ionized. The energy of the recombination depends on the real space separation of the donor and acceptor,  $r_{da}$  via the coulombic interaction:

$$E_{da}(r_{da}) = E_g - (E_a + E_d) + (e^2/4\pi\epsilon_0\epsilon_r r_{da}) \quad (1.3)$$

## I Introduction

The donors and acceptors are on specific lattice sites and the distance between them depends on crystallographic direction. Since  $r_{da}$  is discrete, fine structure can be observed in the luminescence but as the donor to acceptor separation increases a continuum of energy states form, showing broad-band luminescence. The radiative transition probability  $W(r_{da})$  is also found to change with distance and is given as

$$W(r_{da}) = W_0 \exp(-2r_{da}/a_0) \quad (1.4)$$

where  $a_0$  is the Bohr radius. Since the transition probability  $W_0$  is similar for all the donor-acceptor-pairs, then the close pairs recombine more rapidly than distant pairs (Thomas 1965). In III-V compounds the transition rate is such that only distant pair luminescence is observed and since the binding energies of donors and acceptors are small, emission of any fine structure would occur above the band-edge. A theoretical lineshape was derived by Lorenz et al (1968) for the saturated emission of distant donor-acceptor-pairs in n-type semiconductors,

$$I(\hbar\omega) = r_{ad}^4(\hbar\omega) \exp[-4/3\pi r_{ad}^3(\hbar\omega)n_d] \exp[-2r_{ad}(\hbar\omega)/a_0] \quad (1.5)$$

where  $n_d$  is the donor concentration and  $r_{ad}$  is the donor-acceptor-pair separation which is related to the emission energy as given previously in equation 1.4. In the relationship 1.5,  $r_{ad}^4$  accounts for the number of donor sites per unit energy range,  $\exp[-4/3\pi r_{ad}^3(\hbar\omega)n_d]$  is the nearest neighbour factor giving the probability that an acceptor does not have a donor closer than  $r_{ad}$  and  $\exp[-2r_{ad}(\hbar\omega)/a_0]$  relates to the electron-hole wave function overlap. It is assumed the overlap is predominantly determined by the effective Bohr radius of the donor electron.

The  $(D^{\circ}, A^{\circ})$  and  $(e, A^{\circ})$  transitions can be typically separated by approximately 6 meV in GaAs depending on the impurities present. The

## I Introduction

transitions can compete with each other in the same spectral region of the luminescence sometimes making their assignment difficult. By considering the temperature and power density dependence of the emission in the  $(D^{\circ},A^{\circ})/(e,A^{\circ})$  region the transitions can be labelled. Increasing sample temperature causes a shift of the  $(D^{\circ},A^{\circ})$  emission to higher energy. Thermally released inactive carriers from donor sites migrate to energetically more favourable positions before recombining thus reducing  $r_{da}$ . Increasing the temperature also increases the intensity of the free-to-bound transition  $(e,A^{\circ})$  over the donor acceptor pair  $(D^{\circ},A^{\circ})$  since the free carrier population is increased and the number of donors available is reduced by thermal ionization. By lineshape analysis of the free-to-bound and donor-acceptor-pair luminescence at different temperatures Kamiya and Wagner (1977) were able to calculate sample compensation in n-GaAs, appendix A. If the excitation power density is increased the  $(D^{\circ},A^{\circ})$  transition again moves to higher energies,  $\sim 0.4$  meV/decade. Increasing the excitation power density reduces the probability of recombination of larger  $r_{da}$ , effectively increasing the importance of shorter  $r_{da}$  transitions. The rate of shift depends on compensation ratio, tending to be greater for highly compensated samples. When the excitation density is increased the  $(e,A^{\circ})$  emission is found to dominate over the  $(D^{\circ},A^{\circ})$  emission since the free carrier population generation becomes larger than that of the limited number of donors. Since a limited number of impurities exist within a semiconductor as the excitation power density is increased the observed emission intensity should saturate as the photon flux approaches the donor/acceptor density.

Phonon related transitions occur because not all the energy is transferred to a photon but some goes to the crystal lattice (Shah 1978). This is particularly important in indirect gap materials where the phonon is required for momentum conservation. The number of phonon replicas increases with the

binding energy of an impurity. In direct gap, III-V compounds such as GaAs, acceptor transitions will generally show one phonon replica whereas those involving donors will not show any.

### 1.2.1 Semiconductor Parameters

The physical properties of semiconductor materials are summarized in many good reviews and books, for example Neuberger (1971) and Madelung (1982). These reviews reflect the variety of different possible ways to measure a particular physical parameter depending on the fundamental interactions involved. Each method gives its own slightly different value possibly reflecting material quality at the time but also because the interactions may be different. Many authors use a particular material parameter as a fitting factor to give the best results for their calculations (see Shum 1982). An attempt is made in table 1.2 to compare and cross reference parameters for the relevant semiconductors from various sources.

One problem associated with alloys is estimating their material properties at a particular composition (Adachi 1985). In many instances using a linear, Vegard's law extrapolation from the alloys' binary end-points is sufficient but some properties show a non-linear dependence possibly due to alloy disorder. When considering the electronic band structure of an alloy of the form  $A_xB_{1-x}C$ , the band-gap has a quadratic dependence on composition thus

$$E_0(x) = a + bx + cx^2 \quad (1.6)$$

where  $a$  and  $b$  are determined from the binaries and  $c$  is known as the bowing parameter which is four times the deviation of  $E_0$  at  $x=0.5$ . Van Vechten and Bergstresser (1970) used a two band dielectric model based on the Philips theory of electronegativity differences to give a good agreement with experiment using only one free parameter. Essentially the bowing parameter  $c$  was the sum of the

Table 1.2a Relevant semiconductor parameters

Material	Energy Gap (eV)		Temperature Coefficient (dE <sub>g</sub> /dT) (-10 <sup>-4</sup> eV/K)	Effective mass (m <sub>0</sub> ) <sup>a</sup>	μ <sub>n</sub> (cm <sup>2</sup> /Vsec)	n (cm <sup>-3</sup> )
	0-4K	~300K				
AlAs	2.238 <sup>1</sup>	2.13 <sup>1</sup>	4.0 <sup>1</sup>	0.500 <sup>1,2</sup>	180 <sup>1</sup>	180 <sup>1</sup> (300K)
	2.2291 <sup>2</sup>	2.141 <sup>2</sup>	3.6 <sup>4</sup>	0.260 <sup>2</sup>	294 <sup>2</sup>	294 <sup>2</sup> (300K)
	2.2281 <sup>2</sup>	2.168 <sup>4</sup>		0.208 <sup>5</sup>	0.487 <sup>5</sup>	
GaAs	1.522 <sup>1</sup>	1.428 <sup>1</sup>	3.95 <sup>1,4</sup>	0.067 <sup>1,3,4,6</sup>	0.45 <sup>1,2</sup>	250000 <sup>1,2</sup> (50K) ~10 <sup>13</sup>
	1.5177 <sup>2</sup>	1.4257 <sup>2</sup>	3.9 <sup>2</sup>	0.065 <sup>2</sup>	0.51 <sup>2</sup>	
	1.5192 <sup>2</sup>	1.424 <sup>4,6</sup>	4.52 <sup>3</sup>	0.062 <sup>5</sup>	0.403 <sup>5</sup>	
InAs	0.4105 <sup>1,2</sup>	0.356 <sup>1,2</sup>	3.5 <sup>1,2</sup>	0.023 <sup>11,2</sup>	0.41 <sup>1,2</sup>	2×10 <sup>15</sup>
	0.4180 <sup>2</sup>	0.359 <sup>1,2</sup>	3.35 <sup>2</sup>	0.027 <sup>1,2</sup>		
InP	1.4233	1.3511 <sup>1,2</sup>	4.5 <sup>1</sup>	0.077 <sup>1</sup>	0.80 <sup>1</sup>	44000 <sup>1,2</sup> 3×10 <sup>14</sup>
	1.4236		4.75 <sup>2</sup>	0.079 <sup>2</sup>	0.65 <sup>2</sup>	
Al <sub>x</sub> Ga <sub>1-x</sub> As 0 ≤ x ≤ 0.45	4.61.424+1.247x		43.95+1.15x	4.60.067+ 0.083x	40.62+0.14x 60.48+0.31x	
Al <sub>1-x</sub> In <sub>x</sub> As						
Ga <sub>0.47</sub> In <sub>0.53</sub> As	0.813 <sup>2</sup>	0.750 <sup>2</sup>		0.0503 <sup>2</sup>	0.465 <sup>2</sup>	277000 <sup>2</sup> 5.2×10 <sup>15</sup>

1 Neuberger (1971)

2 Madelung et al (1982)

3 Blakemore (1982)

4 Adachi (1985)

5 Shun et al (1988)

6 Casey and Panish (1978)

Table 1.2b Relevant semiconductor parameters

Material	Dielectric Constant		Refractive Index		Density (gm <sup>-3</sup> )	Lattice parameter (Å)	Thermal Expansion Coeff (10 <sup>-6</sup> /K)	Other
	$\epsilon_{\infty}$	$\epsilon_0$	$n_0$	$\lambda(\mu\text{m})$				
AlAs	8.5 <sup>1</sup>	10.9 <sup>1</sup>	0.3 <sup>1</sup>	0.5	3.598 <sup>1</sup>	5.6611 <sup>1,4</sup>	5.20 <sup>1,4</sup>	
	8.16 <sup>4</sup>	10.06 <sup>4</sup>	3.12 <sup>2</sup>	0.62	3.7 <sup>2</sup>	5.6600 <sup>2</sup>	5.00 <sup>2</sup>	
GaAs	10.9 <sup>1,2</sup>	13.18 <sup>1,4</sup>	4.025 <sup>1,2</sup>		5.3161 <sup>2</sup>	5.64191 <sup>1</sup>	6.0 <sup>1</sup>	6E <sub>g</sub> (T)=1.519-5.405×10 <sup>-4</sup> T <sup>2</sup> /(204+T)
	10.88 <sup>3</sup>	12.79 <sup>2</sup>	0.546		5.3174 <sup>3</sup>	5.65325 <sup>3,4</sup>	6.86 <sup>2</sup>	
	10.89 <sup>4</sup>	12.85 <sup>3</sup>			5.360 <sup>4</sup>		6.4 <sup>4</sup>	
InAs	11.8 <sup>1</sup>	14.55 <sup>2</sup>	4.558 <sup>1,2</sup>		5.667 <sup>1,2</sup>	6.0584 <sup>1,2</sup>	5.19 <sup>1</sup>	
	12.25 <sup>2</sup>	15.15 <sup>2</sup>	0.517				4.52 <sup>2</sup>	
InP	9.52 <sup>1</sup>	12.35 <sup>1</sup>	3.49 <sup>1</sup>	0.59	4.787 <sup>1</sup>	5.86875 <sup>1,2</sup>	4.5 <sup>1</sup>	
	9.61 <sup>2</sup>	12.61 <sup>2</sup>	3.41 <sup>2</sup>	0.62	4.81 <sup>2</sup>		4.75 <sup>2</sup>	
Al <sub>x</sub> Ga <sub>1-x</sub> As 0≤x≤0.45	210.9-2.3x				45.36-1.6x	45.6533+	46.4-1.2x	2c(Γ) <sup>b</sup> =0.37 E <sub>g</sub> <sup>Γ</sup> (0)=1.425 E <sub>g</sub> <sup>Γ</sup> (1)=1.298
	410.89-2.73x					0.0078x		2c(x)=0.245 E <sub>g</sub> <sup>x</sup> (0)=1.911 E <sub>g</sub> <sup>x</sup> (1)=2.161
	413.18-3.12x							2x <sub>c</sub> (Γ) <sup>c</sup> =0.405
Al <sub>1-x</sub> In <sub>x</sub> As								2c(Γ)=0.24 E <sub>g</sub> <sup>Γ</sup> (0)=0.36 E <sub>g</sub> <sup>Γ</sup> (1)=2.95
								2x <sub>c</sub> (Γ)=0.68 E <sub>g</sub> (x <sub>c</sub> )=2.05
Ga <sub>0.47</sub> In <sub>0.53</sub> As								2c(Γ)=0.61 E <sub>g</sub> <sup>Γ</sup> (0)=0.36 E <sub>g</sub> <sup>Γ</sup> (1)=1.43

a. m<sub>0</sub>=9.11×10<sup>-22</sup>g

b. c(Γ,X) bowing parameter, eV

c. crossover concentration

## I Introduction

intrinsic bowing parameter estimated from the virtual crystal approximation  $c_i$  and the extrinsic bowing parameter due to aperiodicity in the lattice  $c_e$ . The extrinsic term  $c_e$  was proportional to  $C_{AB}^2$ , the square of the electronegativity difference between A and B. However PL only provides a relative not an absolute measure of the band-gap energy which is most useful when comparing different alloy compositions. Normally an absolute value for the band gap energy requires careful analysis of the emission lineshape particularly in alloys as the near band-edge luminescence does not show the sharp excitonic transitions observed in binaries such as GaAs.

### 1.3 Spatial Quantisation in Heterostructures

Over the last decade, an area which has seen the greatest advances within semiconductor physics has been that of low dimensional structures. This covers the growth, characterization, fabrication and physics associated with thin, lattice matched, semiconductor layers and devices. The concept of semiconductor superlattices was initially proposed by Esaki and Tui (1970) as a periodic structure of alternating ultra thin layers, although, it took a number of years before growth techniques had developed sufficiently to produce suitable material. When the layer thickness was comparable to the DeBroglie wavelength of a carrier within the superlattice then quantum mechanical size effects, such as discrete energy levels within the band-structure occur (figure 1.4). This quantisation was observed as a pronounced structure in the optical absorption spectrum, in which the light and heavy were also seen to decouple (Dingle 1975, figure 1.5). From a simple theoretical fit, to a finite 1-dimensional quantum well, the band gap discontinuity was found to divide 0.85:0.15 to the conduction and valence bands, respectively. The question of band offset and how best to determine it is still a source of controversy (see section 5.2.3). In photoluminescence only excitonic recombination between the lowest energy  $n=1$

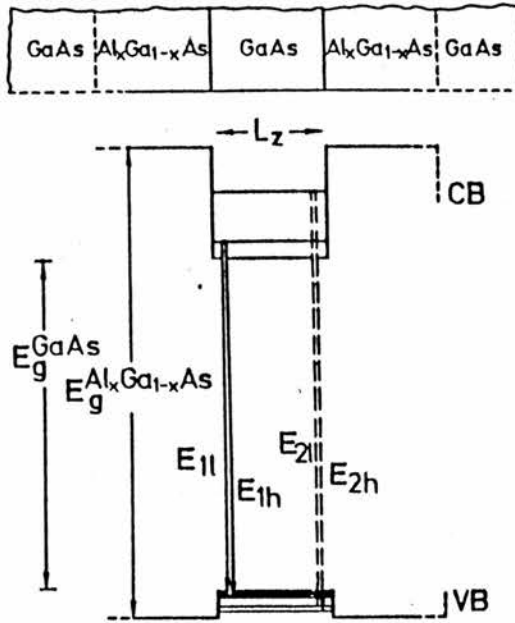


Figure 1.4 Schematic real-space energy band diagram of a  $Al_xGa_{1-x}As/GaAs$  quantum well heterostructure. The smaller gap GaAs forms a well of width  $L_z$  between  $Al_xGa_{1-x}As$  barriers for the electrons and holes near the band edges (Jung et al 1984).

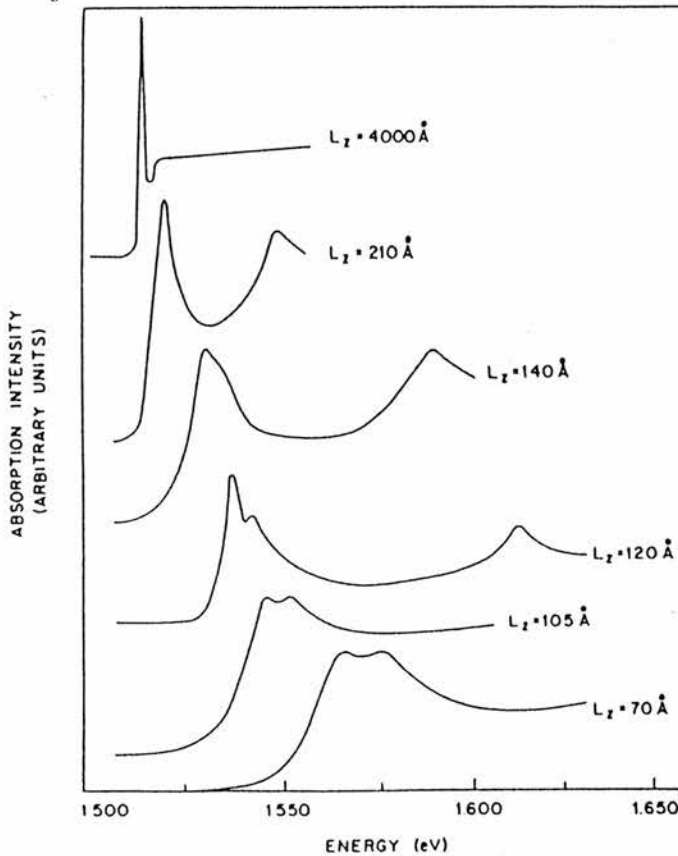


Figure 1.5 Shifting and additional splitting of the lowest quantum transitions of GaAs of thickness  $L_z \geq 70 \text{ \AA}$  (Dingle 1975).

## I Introduction

electron and a  $n=1$  heavy hole transition ( $E_{1h}$ ) is normally observed, with the emission shifted to higher energy depending on the well thickness (see below).

It was the development growth techniques such as molecular beam epitaxy and metal-organic CVD which meant the superlattice structures could be realized (section 2.1). Now, very thin epitaxial layers can be deposited, defined on the monolayer scale. The first heterojunctions were fabricated from GaAs- $Al_xGa_{1-x}As$  because of the relaxed requirements for lattice match between the epitaxial layers, but as growth techniques were refined other heterojunctions such as  $Ga_{0.47}In_{0.53}As-InP$  were produced in which there was more stringent requirements for lattice matching. In figure 1.6 a plot of the energy gaps for different materials and their respective lattice constants is given. It was soon noted experimentally that the heterojunction band alignment depended on the materials used. Consequently, in GaAs- $AlGaAs$  and  $Ga_{0.47}In_{0.53}As-InP$  wells electrons and holes are confined in the same layer (type I), whereas in  $InAs-GaSb$  wells the electron and hole are confined in alternative layers (type II). In this work we shall consider type I heterojunctions. These improved growth techniques have caused a revolution within device physics; quantum well laser where the emission energy is tuned by varying well thickness, a solid state analogy to the photomultiplier tube and high electron mobility transistors have been produced whose properties depend on engineered band structure.

The luminescence from a GaAs quantum well contrasts sharply with that obtained from similar purity GaAs (figure 1.3) in that the intrinsic free-exciton recombination dominates the spectrum at low temperatures where impurity related processes normally dominate. In an isolated quantum well the impurity related emission is strongly reduced, at least in part, due to a reduced probability of a carrier binding to an impurity before excitonic recombination occurs (Weisbuch et al 1981). Christen et al (1984) found using time resolved measurements shallow impurity related emission was bypassed and quenched

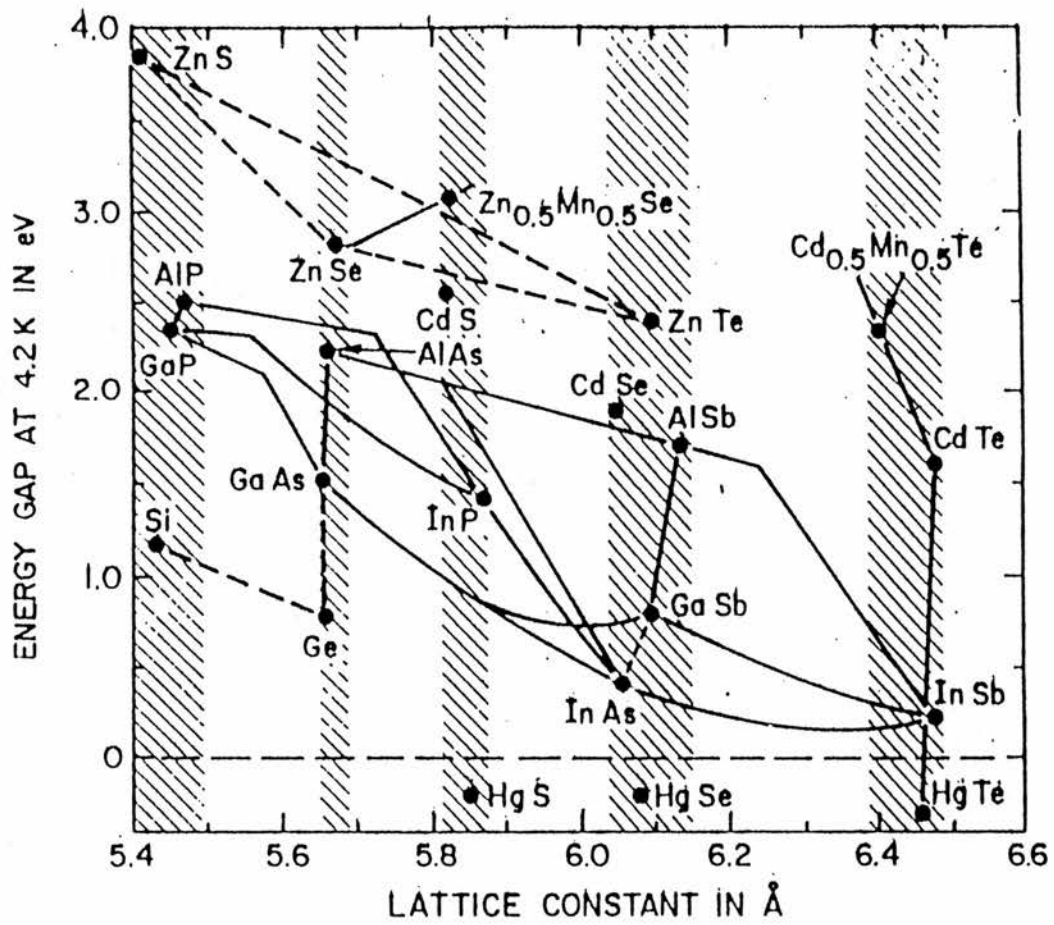


Figure 1.6 Energy gaps at 4.2 K against lattice constants (Esaki 1986).

## I Introduction

by the more rapid excitonic emission. The enhanced radiative efficiency in quantum wells has been attributed to the larger exciton binding energy, the increased electron-hole overlap and getting of non-radiative impurities at interfaces. Proof that the emission was due to free excitons was obtained from the quasi-coincidence of PL and PLE spectra but particularly from circularly polarization experiments (figure 1.10). An impurity trapped within a quantum well, its binding energy  $E_b$ , depends on the well thickness and distance from the well centre. In two limiting cases; for a strictly two-dimensional hydrogenic impurity then the binding energy will be  $4E_b$ , but an impurity at a heterojunction boundary has binding energy of  $E_b/4$  (Levine 1965). A discussion of luminescence from GaAs wells where PL is used as a probe of interface quality is given in chapter 5. The emphasis for a theoretical description of the properties of quantum well heterostructures has been made within the framework of the envelope function approximation, (see Bastard and Brum (1986) and references therein) so we will use this to describe optical transitions in heterostructures.

### 1.4 Envelope Function Approximation in Heterostructures

It is assumed that two different semiconductors, A and B, forming the heterojunction have the same crystallographic structure and are lattice matched. The band structures are similar, essentially non-aligned, with valence band energy peaking at the  $\Gamma$ -point. The relevant host band structure is described by the  $\mathbf{k}\cdot\mathbf{p}$  method (Kane 1957) with eight bands assumed to contribute to the wavefunction  $\Gamma_6, \Gamma_7$  and  $\Gamma_8$  (figure 1.7). At  $k=0$  decoupling occurs between the  $\Gamma_8$  and coupled  $\Gamma_6, \Gamma_7, \Gamma_8$ , light and heavy holes. The envelope function scheme defines a wavefunction of the form

$$\Psi(\vec{r}) = \sum_m f_m(\vec{r}) u_{m0}(\vec{r}) \quad (1.7)$$

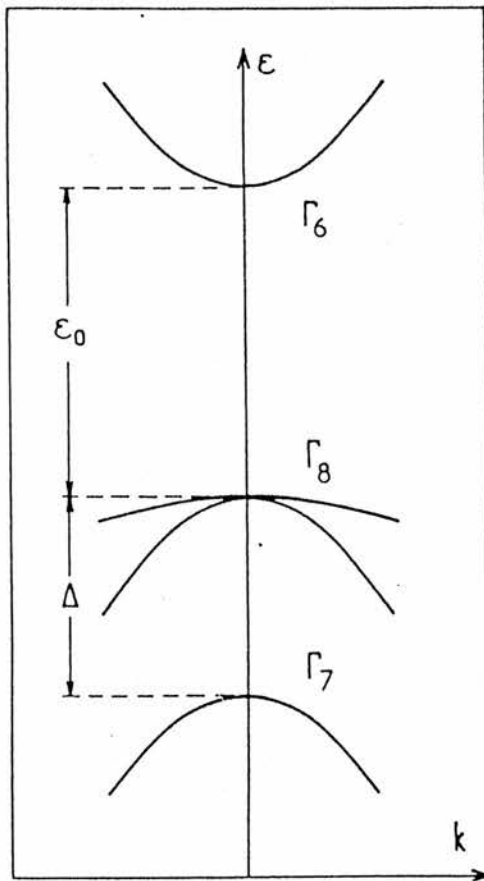


**Figure 1.7** Band structure of a direct gap III-V compound (e.g. GaAs) in the vicinity of the centre of the Brillouin zone (Bastard and Brum 1986).

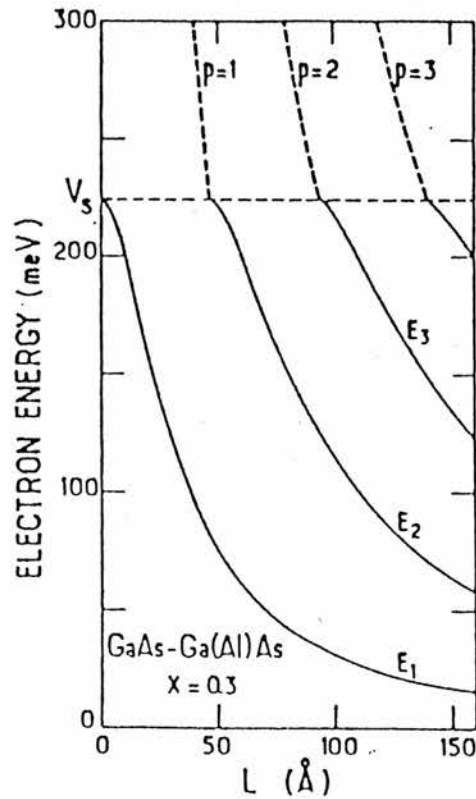


**Figure 1.8** Thickness dependence of the  $\Gamma_6$  related energy levels in  $\text{As}_{0.3}\text{Ga}_{0.7}\text{As}$  single quantum well. Solid lines are bound states and dashed lines are virtual bound states (Bastard 1987).

## I Introduction

where  $m$  runs over the  $\Gamma_6, \Gamma_7$  and  $\Gamma_8$  edges.  $\psi(\vec{r})$  is the product of slowly varying function, on the unit cell scale,  $f_m(\vec{r})$  with the bandedge periodic Bloch functions  $u_{m0}(\vec{r})$ . Since the periodic parts of the Bloch function differs very little from host material to the other it is assumed to be identical at the  $\Gamma$ -point in layers A and B. Within the  $\Gamma_6, \Gamma_7$  and  $\Gamma_8$  subspace the  $\mathbf{k}\cdot\mathbf{p}$  interaction is exactly taken into account and  $f_m$  are solutions of the effective mass type Hamiltonian of the form

$$\sum_m (E_{l0} + V_1(z) - E) \delta_{lm} - \left[ \frac{\hbar}{m_0} \vec{\nabla} \cdot \vec{p}_{lm} - \frac{\hbar^2}{2} \vec{\nabla} \frac{1}{\mu_{lm}} \vec{\nabla} \right] f_m(\vec{r}) = 0 \quad (1.8)$$

where  $p_{lm}$  is the interband  $p$  matrix elements between periodic parts of the Bloch function at the  $l^{\text{th}}$  and  $m^{\text{th}}$  edge and  $\mu_{lm}$  is the effective mass tensor. How the bands line-up and the valence band offset are crucial in evaluating 1.8. Current continuity requires the boundary conditions of  $f_m$  and  $\mu_{lm}^{-1} df_m/dz$  to be continuous everywhere. Thus the envelope function  $f_m$  can be written in the form

$$f_m(\vec{r}) = \chi_m(z) \exp(i\vec{k}_\perp \cdot \vec{r}_\perp) \quad (1.9)$$

where  $\vec{k}_\perp = (k_x, k_y)$  and  $\vec{r}_\perp(x, y)$  are the in-plane carrier wave and position vectors. Neglecting inversion symmetry splitting of the host materials, at  $\vec{k}_\perp = 0$ , the  $z$  projection of the total angular momentum  $J_z$  can classify the electronic states  $J_z = \pm\frac{3}{2}, \pm\frac{1}{2}$  for heavy and light holes respectively. An admixture of heavy and light holes occur for  $\vec{k}_\perp \neq 0$  but fortunately optical data is normally restricted to a well defined region of  $k$ -space around  $\vec{k}_\perp = 0$ . In figure 1.8 the dependence on layer thickness of the  $\Gamma_6$  related energy level  $E_n$  in a single well quantum was calculated using a band offset of 224 meV and neglecting the effects of remote bands in 1.8. The quantum well always contains at least one bound state and excited states,  $E_2$  and above, which transform into resonant states when their energy exceeds the confining barrier. Assuming the subbands  $E_n$  have a simple parabolic dispersion

## I Introduction

$$E_n(\mathbf{k}) = E_n(0) + \frac{\hbar^2}{2m^*} k^2 \quad (1.10)$$

then the density of states (DOS) per unit energy is given by

$$\rho(\epsilon) = \frac{m^*S}{\pi\hbar^2} \sum_n Y(E - E_n) \quad (1.11)$$

where the summation runs over the bound states,  $S$  is area and  $Y(E - E_n)$  is the step function. So the DOS for bound states  $E_n$  is step-like and constant above each  $E_n$ , as observed in the absorption or PLE spectra. This contrasts with the bulk result

$$\rho^{\text{bulk}}(E) = \frac{m^*}{\pi\hbar^2} \left( \frac{2m^*\epsilon}{\hbar^2} \right)^{0.5} \quad (1.12)$$

in which the DOS varies continuously with a  $E^{0.5}$  dependence. Despite the envelope function sometimes severe assumptions still produces predictions close to those found experimentally, so, it is within this framework that we will consider optical transitions in quantum wells.

### 1.4.1 Optical Transitions in Heterostructures

Interband optical phenomenon can be described within the terms of the dielectric function in which the absorption coefficient is proportional to the imaginary part of  $\epsilon(\omega) = \epsilon_1(\omega) + i\epsilon_2(\omega)$  (Weisbuch 1987). So, optical transitions are induced by an e.m. wave between electronic states  $|i\rangle$  and  $|f\rangle$  at a rate calculated using Fermi's golden rule, thus

$$\alpha(\omega) \sim \epsilon_2(\omega) \sim |\langle f | \vec{\epsilon} \cdot \vec{p} | i \rangle|^2 \rho(\omega) \quad (1.13)$$

where  $\epsilon$  and  $p$  are the light polarization vector and momentum operator, respectively and  $\rho(\omega)$  is the density of states at energy,  $E_n$  (equation 1.11). Within the envelope approximation the wavefunctions  $|i\rangle$  and  $|f\rangle$  are given by equations 1.7 and 1.9 as

## I Introduction

$$\psi^{i,f}(\vec{r}) = \chi^{e,h} \exp^{i\vec{k}_{\perp} \cdot \vec{r}_{\perp}} u_{c,v}(\vec{k}(\vec{r})) \quad (1.14)$$

In calculating the matrix element in equation 1.13 it can be factorized into a sum at the lattice points  $R_i$  of the envelope wavefunction and an integral over the unit cell of the Bloch functions thus

$$|\langle f | \vec{\epsilon} \cdot \vec{p} | i \rangle| = \sum_{R_i} \chi^e(\vec{R}_i) \chi^h(\vec{R}_i) \exp^{i(\vec{k}_{e\perp} - \vec{k}_{h\perp}) \cdot \vec{R}_i} \int_{\Omega} u_{c,\vec{k}_{e\perp}} \vec{\epsilon} \cdot \vec{p} u_{v,\vec{k}_{h\perp}} d^3r \quad (1.15)$$

The integral is the usual bulk matrix element  $P$  which contains the selection rules due to light polarization and band symmetry. So, normalising we can write

$$|\langle f | \vec{\epsilon} \cdot \vec{p} | i \rangle| = L_z^{-0.5} \langle \chi^e | \chi^h \rangle P \delta_{\vec{k}_{e\perp}, \vec{k}_{h\perp}} \quad (1.16)$$

Since  $\vec{k}_{e\perp} = \vec{k}_{h\perp}$  then transitions are vertical. The DOS is constant in heterostructures (equation 1.11), thus equation 1.13 becomes

$$\alpha(\omega) \cdot L(z) \sim \text{const} |\langle f | \vec{\epsilon} \cdot \vec{p} | i \rangle|^2 P^2 \sim \text{const} P^2 \quad (1.17)$$

and since  $P^2$  is almost constant for all semiconductors ( $p^2/2m_0 \sim 23$  eV) then absorption probability is independent of well thickness,  $6 \times 10^{-3}$  per transition per quantum well.

### 1.4.2 Polarity and Polarization Selection Rules

The overlap integral  $\langle \chi^e | \chi^h \rangle$  (in equation 1.16) contains important selection rules. In type I quantum wells the conduction and valence band wavefunctions are localized in the same quantum layer. In an infinite well  $\chi^e$  and  $\chi^h$  are orthogonal so the integral is zero unless the wavefunctions have the same quantum number, thus  $\Delta n = 0$  (known as Dingle's rule, figure 1.5). With finite depth wells, the conduction and valence wavefunctions are no longer identical because evanescent wings occur into the adjacent barriers. The

## I Introduction

localized single-particle wavefunctions still retain their parity and  $\Delta n \neq 0$  transitions with either even or odd parity become weakly allowed. A detailed study of the optical selection rules in superlattices within the envelope function approximation (type I and II) has been completed by Voisin et al (1984).

The correspondence principle shows that quantum mechanical electric dipoles radiate like their classical counterparts. So, it is easy to obtain selection rules in the optical matrix element  $P$  (equation 1.15) deduced from their atomic counterparts (table 1.3). We can see from table 1.3 that for an e.m. wave propagating in the layer plane with  $\epsilon_z$  polarisation  $HH_n-E_m$  transitions are forbidden and transitions associated with light holes are 3 x weaker than those with heavy holes. In figure 1.9 the optical selection rules for absorption and luminescence between Bloch states are shown.

### 1.4.3 Excitonic Emission in Heterostructures

In section 1.4.1 electron-hole correlation was ignored but coulombic interaction in the final state leads to an excitonic state. The exciton can be described by a two particle envelope wavefunction with either 0 or 1 occupancy, so

$$\alpha(\omega) \sim |\langle 0 | \epsilon.p | \psi_{exc} \rangle|^2 \sim |\langle u_{c,ke} | \epsilon.p | u_{v,kh} \rangle|^2 |\phi^n|^2 \delta_{0,k} \quad (1.18)$$

where  $|\phi^n|$  is a measure of the electron-hole wavefunction overlap which decreases rapidly with  $n$ . This is observed experimentally, particularly in PLE spectra, where excitonic emission is not normally observed above a  $\Delta n=0$  transition. In type I quantum wells  $|\phi^n|$  is correlative larger than in the bulk and the exciton binding energy increases as well width decreases. The exciton appears as a sharp peak in the emission spectrum due to  $k$  conservation,  $\delta_{0,k}$ , although this may be relaxed due to interface disorder. As we would expect the selection rules discussed in section 1.4.2 also hold for excitonic emission. This was clearly shown by Miller and Kleinman (1985) using an optical electron spin

Polarization	$\epsilon_x$	$\epsilon_y$	$\epsilon_z$	
Propagation // z	$\frac{P}{\sqrt{2}}$	$\frac{iP}{\sqrt{2}}$		$HH_n \rightarrow E_m$
Propagation // x		$\frac{iP}{\sqrt{2}}$	forbidden	
Propagation // y	$\frac{P}{\sqrt{2}}$		forbidden	$ \frac{3}{2}, \frac{3}{2}\rangle = \frac{ (X+iY)+\rangle}{\sqrt{2}}$
Propagation // z	$\frac{iP}{\sqrt{6}}$	$-\frac{P}{\sqrt{6}}$		$LH_n \rightarrow E_m$
Propagation // x		$-\frac{P}{\sqrt{6}}$	$\frac{-2iP}{\sqrt{6}}$	$ \frac{3}{2}, \frac{1}{2}\rangle =$
Propagation // y	$\frac{iP}{\sqrt{6}}$		$\frac{-2iP}{\sqrt{6}}$	$\frac{1}{\sqrt{6}}  (X+iY)+\rangle - \frac{\sqrt{2}}{\sqrt{3}}  Z+\rangle$
Propagation // z	$-\frac{iP}{\sqrt{3}}$	$-\frac{P}{\sqrt{3}}$		$(\Gamma_7)_n \rightarrow E_m$
Propagation // x		$-\frac{P}{\sqrt{3}}$	$\frac{iP}{\sqrt{3}}$	$ \frac{1}{2}, \frac{1}{2}\rangle =$
Propagation // y	$-\frac{iP}{\sqrt{3}}$		$\frac{iP}{\sqrt{3}}$	$\frac{1}{\sqrt{3}}  (X+iY)+\rangle + \frac{1}{\sqrt{3}}  Z+\rangle$

**Table 1.3** Polarization selection rule for interband transitions (Voisin 1986)

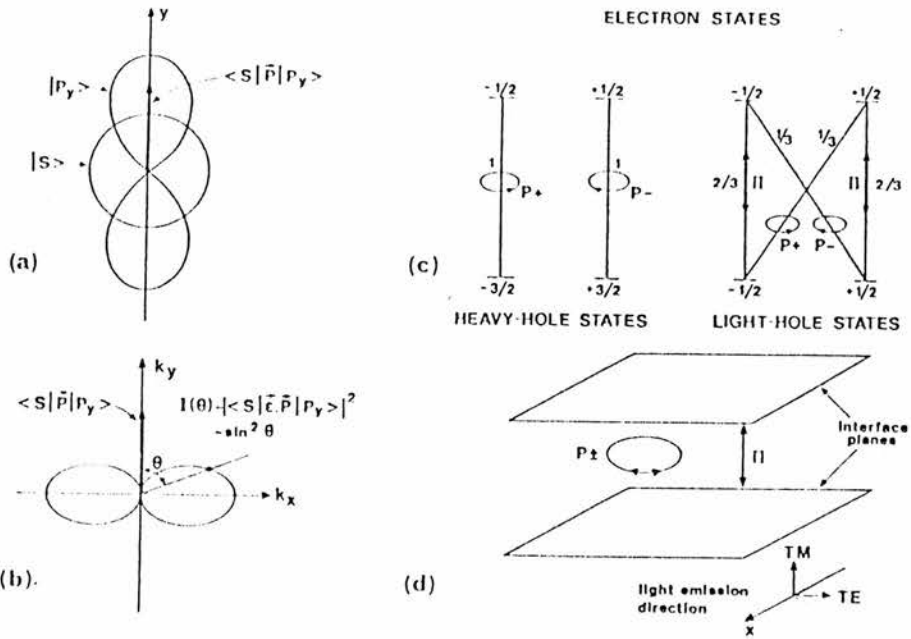


**Figure 1.9** Optical selection rules for absorption and luminescence between atomic-like (Bloch States) of valence and conduction band. a) Dipole matrix element between a s and p state. b) Emission diagram of that dipole according to the correspondence principle. c) Possible dipole moments between conduction and valence band states;  $p_+$ ( $-$ ) indicate rotating dipole moments which emit circularly polarized light ;  $\pi$  indicates a linearly polarized dipole. Relative dipole strengths are indicated. d) Geometry of the dipoles in the quantum well situation. One can see that heavy-holes only emit TE polarized light in the x-direction (Weisbuch 1987).

## I Introduction

orientation technique with circular polarization excitation and detection (figure 1.10). This provided a direct confirmation of the heavy and light hole assignment of the emission and showed the relative oscillator strengths of 3 and 1, respectively.

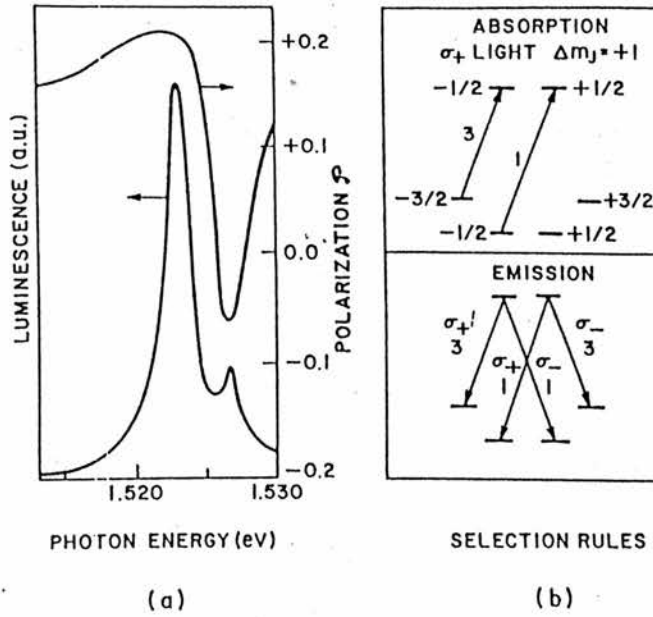


**Figure 1.10** a) Photoluminescence and its circular polarization at 50 K for excitation at 1.65 eV with circular polarized light. The sample has 25 GaAs wells with 188 Å and  $L_z=19$  Å,  $x=0.3$  alloy barriers. For this nonresonant excitation,  $m_j=-1/2$  electrons are preferentially created which leads to heavy and light hole exciton emission with positive and negative polarizations, respectively. b) Absorption and emission transitions for GaAs quantum wells with circular polarized light. The transitions involving heavy ( $m_j=\pm 3/2$ ) and light ( $m_j=\pm 1/2$ ) holes have relative strength of 3 and 1, respectively (Miller and Kleinman 1985).

## II EXPERIMENTAL METHOD

	<u>Page</u>
2.1 MBE Growth of GaAs and $\text{Al}_x\text{Ga}_{1-x}\text{As}$	21
2.1.1 Principle of MBE	21
2.1.2 Growth Mechanism of III-V compounds	21
2.1.3 Doping and Alloy Growth	23
2.1.4 Growth on Misorientated Substrates	24
2.1.5 The VG V80H MBE Growth System	25
2.1.6 Sample Preparation and Growth Method	27
2.2 Photoluminescence Apparatus	28
2.2.1 Spectrometer	30
2.2.2 Detectors	31
2.2.3 Normalized System Response	33
2.2.4 Cryostat	35
(i) Large Bore Optical Cryostat	35
(ii) Oxford Instrument cryostat and flow controller	37
(iii) Temperature control and calibration	39
2.3 High Pressure Optical Cell	40
2.3.1 Diamond Anvil Cell	41
2.3.2 Ruby line Calibration	43
2.3.3 Low Temperature Pressure Media	44
2.4 Samples used in this work	45

## II Experimental Method

### 2.1 MBE Growth of GaAs and $\text{Al}_x\text{Ga}_{1-x}\text{As}$

Many different techniques have been developed for the epitaxial growth of III-V compound semiconductors. These include liquid-phase epitaxy (LPE), vapour-phase epitaxy (VPE), metal-organic chemical vapour deposition (MOCVD) and molecular beam epitaxy (MBE). Of these the growth control in MOCVD and in particular MBE, has allowed the production of III-V compound structures with monolayer definition in composition and doping profile. As a consequence a new area of physics has developed, low dimensional structures, with many technologically important applications such as heterojunction lasers and high electron mobility transistors. During my research I spent some time at GEC Hirst Research Centre learning the principles of MBE and relating it to the photoluminescence observed from different samples. A brief description of MBE growth of GaAs based compounds applicable to my work follows.

#### 2.1.1 Principle of MBE

MBE, was developed from the pioneering work of Arthur (1968) and Cho (1970), and is essentially a refined form of vacuum evaporation. A neutral thermal energy atomic or molecular beam (Ga, Al, As, etc) impinges on a hot crystalline substrate contained in an ultra high vacuum (UHV) environment as shown schematically in figure 2.1. Growth occurs, with the required stoichiometry, as a single layer is deposited continuously with the substrate orientation. It is the low growth rate,  $\sim 1 \mu\text{m h}^{-1}$  combined with almost instantaneous interruption of growth using shutters over each molecular beam source that allows growth control down to monolayer thickness.

#### 2.1.2 Growth Mechanism of III-V compounds

The growth kinetics of GaAs is the same as most III-V compounds and can be explained in a relatively simple manner by considering surface effects. The

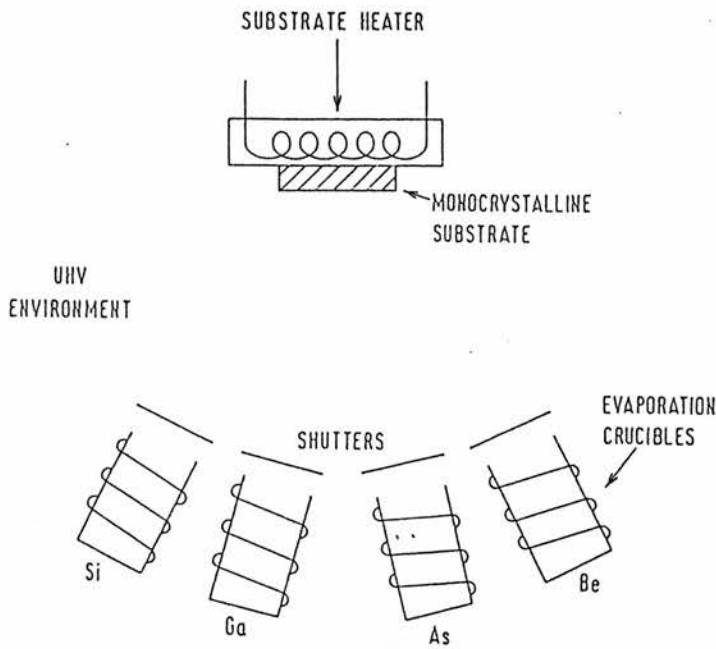


**Figure 2.1** Schematic of a MBE growth system.

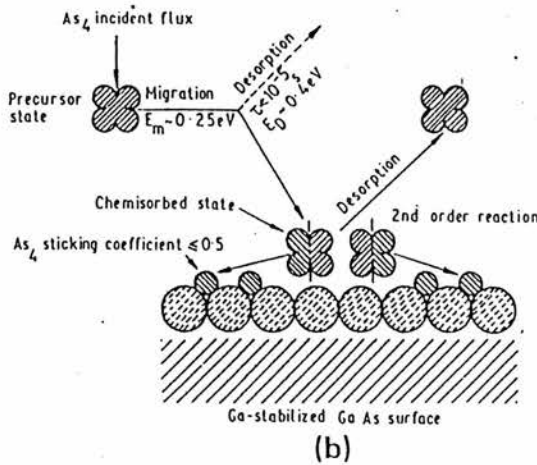
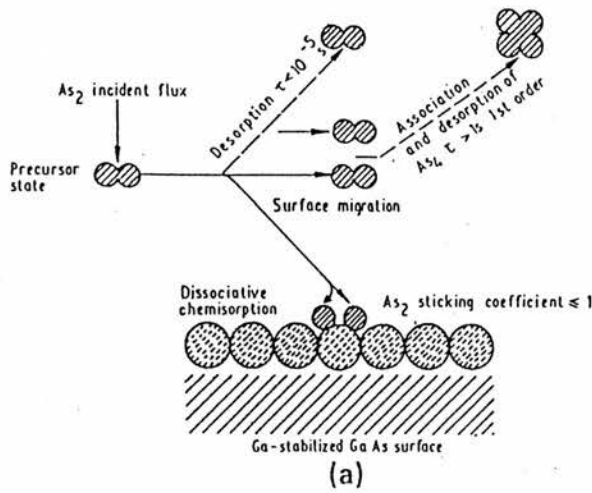


**Figure 2.2** a) Model for growth of GaAs from Ga and  $As_2$ , and b) Model for the growth of GaAs from Ga and  $As_4$ . (Neave et al 1983)

## II Experimental Method

group III elements (Ga, Al) normally evaporate in the form of monomers and their unity sticking coefficient determines growth rate at low substrate temperatures. Optimal growth conditions require excess group V species (i.e. when the flux  $J_{As} > J_{Ga}$ ) which are desorbed to achieve correct stoichiometry, the sticking coefficient is dependent on allotropic form. Most III-V compounds are unstable above the congruent evaporation temperature so excess group V species avoid non-stoichiometric growth. Although MBE growth can occur at temperatures well below the congruent sublimation temperature, device quality material has required the use of higher growth temperatures. Arsenic can be evaporated from GaAs as a dimer with sticking coefficient of  $\leq 1$  or from an elemental source in its tetrameric form with a sticking coefficient of  $\leq 0.5$ . An explanation is summarized in figure 2.2, (Neave et al 1983). By considering a gallium stabilized surface it is apparent that while the dimer may be incorporated directly, a process of dissociative chemisorption takes place. The tetramer requires pair dissociation of  $As_4$  molecules on adjacent Ga sites with the desorption of  $As_4$  limiting the sticking coefficient to 0.5. Source choice is relatively unimportant because other factors such as surface reconstruction have more effect on the material properties.

Surface reconstruction is the relaxation of the outermost atomic layers of the crystal during growth to reduce the free energy of the surface. Reconstruction is monitored using reflection high energy electron diffraction (RHEED), (see section 2.1.5). A particular surface structure can be maintained over a range of flux ratios and growth temperature. The growth of good quality GaAs on a [100] substrate is normally achieved under an As stabilized surface structure, (2x4) reconstruction, as explained above. However, the (3x1) reconstruction, which occurs at higher growth temperatures and is a preliminary to the (4x2) Ga stable surface, has shown greater luminescence efficiencies (Neave et al 1984).

## II Experimental Method

### 2.1.3 Doping and Alloy Growth

The number of useful dopants for III-V MBE is comparable to other growth techniques but they must incorporate via the growing surface. As a consequence, volatile impurities can re-evaporate before they incorporate and other impurities show size effects such as segregation (Wood 1985). The best behaved and most commonly used shallow acceptor and donor dopants in MBE growth of GaAs are beryllium and silicon respectively. The beryllium permits controllable doping levels between  $<10^{14}$  to  $\sim 10^{19}$   $\text{cm}^{-3}$  with 100% electrically active centres. The silicon behaviour is slightly more complicated, since it is a group IV element it is amphoteric and this is the case particularly at the highest doping levels and under certain growth conditions. But for most doping levels,  $<10^{18}$   $\text{cm}^{-3}$ , silicon is non-amphoteric favouring the Ga site. Nominally undoped GaAs is usually p-type,  $\sim 2\text{-}3 \times 10^{14}$   $\text{cm}^{-3}$ , due to residual gases, such as hydrocarbons from the arsenic charge, in the growth chamber. Recent refinements in MBE, particularly in the choice of As source, has produced n-type GaAs with backgrounds of  $<10^{13}$   $\text{cm}^{-3}$  (Elman et al 1987).

Since all the alloys considered in this work are ternaries of the form  $\text{III}_a\text{III}_b\text{V}_c$  we will restrict the discussion to these. Their growth can be considered as the simultaneous growth of the two binary members  $\text{III}_a\text{V}_c$ - $\text{III}_b\text{V}_c$ , limited by the thermal stability of the less stable member. The low substrate temperature and non-equilibrium nature of MBE allows growth within the miscibility gap but complications can arise with clustering, as will be discussed in section 4.2. Better quality ternaries with less associated deep levels are produced at higher growth temperatures. Congruent sublimation affects the composition of the alloy since one group III element sublimes more rapidly than the other. The growth mechanism for a  $\text{III}_a\text{III}_b\text{V}_c$  alloy is the same as for a GaAs like compound (section 2.1.2), hence the alloy composition is controlled by the group III flux ratio since both elements normally have a unity sticking

## II Experimental Method

coefficient. Thus the growth of alloys require close control of the absolute fluxes and group III ratio with time. Maintaining uniformity over a large substrate can prove difficult since lattice matching is required for optimum crystalline quality.

### 2.1.4 Growth on Misorientated Substrates

In section 5.4.3 the photoluminescence from quantum well grown onto misorientated substrates is explored. When a GaAs substrate [100] is cut misorientated towards the [011] direction it can be assumed the surface breaks up into monatomic steps forming vicinal planes. Since gallium lattice sites are available at vicinal planes, growth is preferentially nucleated from there, since a chemisorbed molecule can reduce its energy more than binding to a surface site. A study of gallium diffusion across misorientated substrates during growth by Neave et al (1985) has important consequences for interfacial quality.

Interface quality and planar growth are normally monitored using RHEED oscillations. They occur as a result of monolayer deposition and require two dimensional nucleation on the substrate surface to be observed. If the diffusion length,  $\lambda$ , of the growth controlling species exceeds the step length,  $l$ , growth occurs from vicinal planes and no RHEED oscillations are observed (figure 2.3). By varying the main growth parameters, substrate temperature and flux ratio Neave et al (1985) were able to estimate the gallium atom diffusion length,  $\lambda_{\text{Ga}}$ . Under normal growth conditions, substrate at 680 °C and a flux of  $2 \times 10^{14} \text{ cm}^{-2}\text{s}^{-1}$ ,  $\lambda_{\text{Ga}}$  was  $\sim 200 \text{ \AA}$ . By scaling to the ratio of cohesive energies of AlAs and GaAs,  $\lambda_{\text{Al}}$  was found to be 40 Å, and as a consequence Al will form the nucleation centre in the AlGaAs based alloys. Another, more important consequence is for interfacial quality, a GaAs epilayer will form terraces of width 200 Å while growing whereas the alloy would form a more random interface with 40 Å terraces.

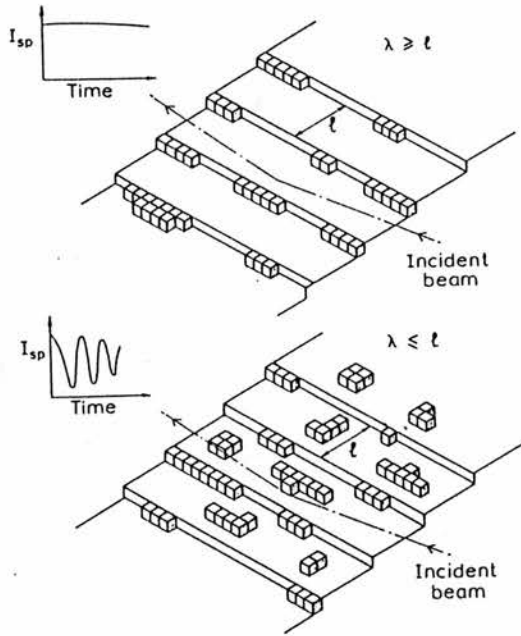


**Figure 2.3** Schematic illustration of the principle of the method, showing the change in RHEED information as the growth mode changes from 'step flow' to 2-D nucleation. Steps lie along [100]. (Neave et al 1985)

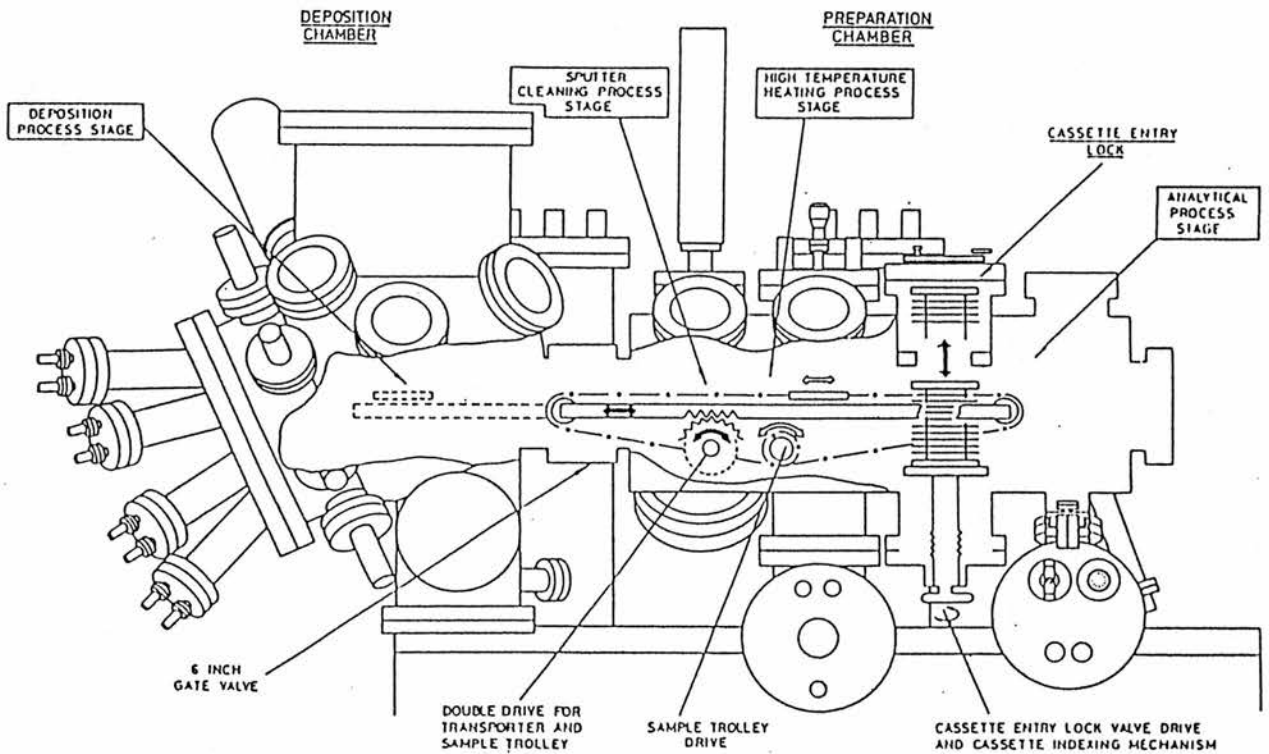


**Figure 2.4** Cross-section of the VG V80H MBE growth system illustrating the configuration of the major components. (courtesy of VG)

## II Experimental Method

### 2.1.5 The VG V80H MBE Growth System

The majority of the samples used in this work were grown using a VG V80H MBE system, figure 2.4. The sample, normally a cleaned substrate was mounted on a high purity molybdenum block, see section 2.1.6. The VG V80H consists of two UHV chambers, a deposition chamber and a sample preparation chamber. To protect the vacuum, mounted samples were introduced into the preparation chamber via a load lock system and then outgassed for an hour at 350 °C to remove water vapour and other absorbents. When a sample was required for growth it was transported into the deposition chamber using a 'cassetrac' sample transfer system. The deposition chamber was opened to the preparation chamber for the minimum of time required for the transfer to reduce any cross-contamination between the chambers. The chambers used separate ion and titanium sublimation pumps. The deposition chamber was additionally helium cryo-pumped and surrounded by liquid nitrogen cooled cryoshields to condense unwanted impurity gasses and excess reactant species.

The substrate heater assembly was positioned centrally in the deposition chamber with a number of effusion cells placed radially around it (as in figure 2.1). The distribution of sources was such as to give the best flux uniformity at the sample surface. Some sources Ga, Al were very directional depending on the melt surface area and volume of the charge, whilst others As, Si which sublime from the solid to a gas are less directional. Substrate rotation effectively averaged out the beam profiles from the effusion cells optimising uniformity of thickness, composition and doping during growth. A shutter was placed in front of each cell to allow for source choice and mono-layer deposition control. The effusion cells contain the elemental charges within pyrolytic boron nitride PBN crucibles surrounded by tantalum heating foils. The cells were water cooled and their temperature monitored by a thermocouple in contact with the PBN crucible. An ion gauge was mounted on the rear of the substrate heater and could be rotated

## II Experimental Method

into view when required to measure beam fluxes from the matrix element of effusion cells.

The UHV environment allows a wide range of in-situ diagnostic equipment such as a quadrupole gas analyzer for residual gas analysis. But the most useful analysis technique included in the deposition chamber was RHEED. It monitored the thermal cleaning of the substrate, and provided information about crystallographic orientation and surface reconstruction during growth. The RHEED system comprises of an high energy electron beam (5-20 keV) set, almost perpendicular to the molecular beams, at a glancing angle to the crystal surface (1-2°). The resulting diffracted beams are projected onto a phosphor coated screen imaging the growing surface. The diffraction features intensity can oscillate during growth reflecting the monolayer deposition of the epilayer and can be used to calibrate group III fluxes (Neave et al 1983). Other surface analysis techniques such as X-ray photo-electron spectroscopy XPS were available in the preparation chamber.

Before use, the VG V80H, like all MBE machines, required careful and methodical baking, pumping and outgassing of the UHV chambers and effusion cells over a period of days. Some more outgassing was required on a daily basis to remove any impurities deposited in the chamber overnight. When the effusion cells were refilled they required re-calibration as a function of temperature using various assessment techniques; scanning electron microscopy to estimate growth rate, photoluminescence for alloy composition or 'step and etch' Hall measurements and C-V profiles to determine doping densities. Normally ~10  $\mu\text{m}$  of films were grown during this calibration period to clean the sources before good quality epilayers were grown (with  $|N_A - N_D| < 5 \times 10^{14} \text{ cm}^{-3}$ ).

## II Experimental Method

### 2.1.6 Sample Preparation and Growth Method

The substrate quality and cleaning process must be stressed since the grown epilayer quality depends critically upon them. The following substrate cleaning procedure was used with the etch chosen depending on substrate type and personal experience. The substrate was ultrasonically cleaned in trichlorethane to degrease it and then washed in propanol to dissolve the trichlorethane. Since the propanol was water soluble the substrate was rinsed in high purity deionised water until its surface was hydrophilic in nature. The substrate (GaAs p-type Zn-doped) was etched using a  $\text{H}_2\text{SO}_4:\text{H}_2\text{O}_2:\text{H}_2\text{O}$  (7:1:1) mix under constant agitation for a minute. The etch had to be quenched rapidly to avoid the formation of etch pits or surface defects from localized boiling. After etching the substrate was thoroughly rinsed and then spun dry on a centrifuge before mounting. Two mounting techniques were used, either, soldering the sample with molten indium onto the substrate holder or clipping it directly onto the holder, known as 'indium-free' mounting. In either case to ensure growth reproducibility it was important to ensure good thermal contact between the substrate and substrate holder. To reduce any thermal stresses or temperature gradients the emissivity of the substrate and the substrate holder were matched whenever possible.

Since the gallium flux effectively determines growth rate its effusion cell temperature was set first and all other flux ratios were calibrated from it. Then the other effusion cell temperatures were set to give the required fluxes for alloy composition or doping (from electrical assessment) taking into account that when the shutter to the arsenic cell was opened the background pressure increased significantly,  $\sim 10^{-6}$  Torr. The effusion cell depletes during use, so cell temperatures were raised from run to run to give the required flux. Good quality GaAs required the arsenic source to show a beam equivalent ratio of 6:1 on the

## II Experimental Method

ion gauge with the arsenic pressure set to a minimum for best nucleation. The GaAs substrate temperature was raised under an arsenic flux to minimize any non-congruent evaporation at the surface. At 580 °C the oxide formed during the etch, desorbs, leaving the substrate clean and ready for growth. By using computer control of the appropriate shutters the required structure could be grown. All AlGaAs layers were capped with a  $\sim 14\text{\AA}$  deposit of GaAs to improve surface recombination.

Although MBE is an excellent growth technique it is like most growth methods not ideal. Problems can arise with deposition reproducibility because the emissivity of the substrate changes with use and it is difficult to measure actual substrate temperatures unless a pyrometer is used. The existence of oval defects on the sample surface, 1-10  $\mu\text{m}$  long with densities of  $10^2$ - $10^4\text{ cm}^{-2}$ , can seriously affect device processing. Unwanted impurity incorporation and point defects resulting from deviations in stoichiometry can act as non-radiative recombination centres and reduce luminescence efficiency.

### 2.2 Photoluminescence Apparatus

This project has involved setting up a high resolution, low temperature (1.8 K) and high pressure (150 kbar) photoluminescence system, the schematic diagram of which is shown in figure 2.5. Low temperature measurements required the sample to be placed in the cryostat and cooled. A laser was used to photocreate electron-hole pairs to obtain the luminescence spectrum. The emitted radiation was dispersed by a monochromator and detected using either photon counting or lock-in techniques. A large bore optical cryostat was specially designed specifically to accommodate a diamond anvil cell for high pressure measurements, section 2.2.4(i).

A Krypton or Argon laser was used either directly or as a pump for a dye laser to excite the sample to produce the photoluminescence spectra. The

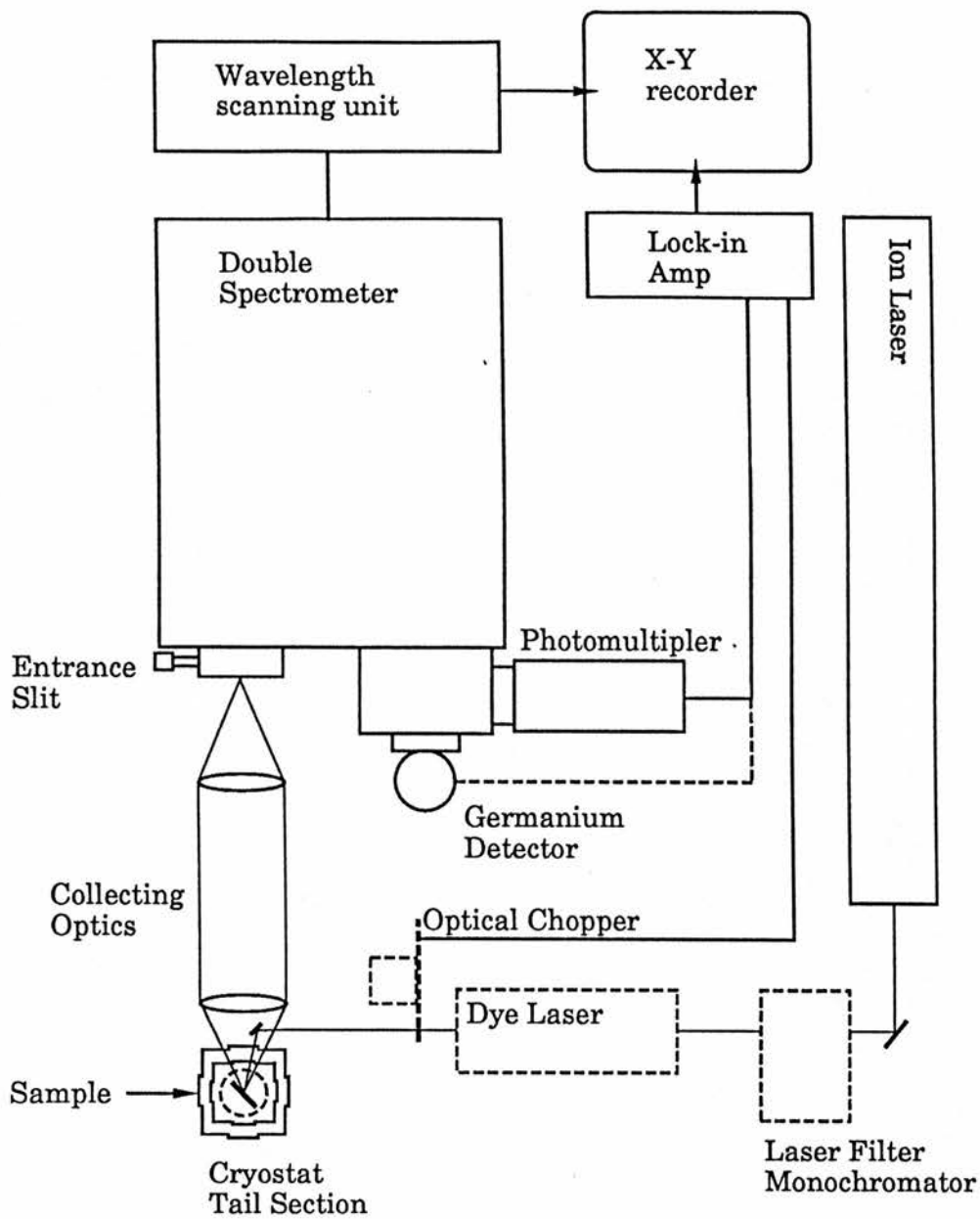


**Figure 2.5** Schematic of the photoluminescence apparatus.

## II Experimental Method

luminescence from a semiconductor should be essentially independent of the pump laser wavelength but it wants to be as close to the band-edge as possible in order to eliminate the contribution from hot carrier effects (Weisbuch 1978, Leite 1978). Varying the pump wavelength changes the penetration depth of the laser light into the semiconductor crystal. The effect of penetration depends on the semiconductor band-gap, absorption coefficient and refractive index and is generally more important in light scattering experiments (Aspnes and Stunda 1983).

The laser filter prism monochromator ensured only single line excitation of the sample and was important for removing the laser plasma background when using the photon counting system. The Krypton laser was a Coherent Supergraphite series CR 2000K type and the Argon laser was a Spectral Physics model 2030. The dye laser was also by Coherent, model 599-01 and could be used in conjunction with DCM (610-720 nm), Stryl 9 (800-890 nm) and other dyes depending on the laser optics. By correct choice of the lasing wavelength photoluminescence excitation experiments could be performed for some samples.

The collecting optics were arranged to have the sample in the cryostat placed at the focal length of one its lenses to produce a collimated beam. This was necessary when an analyzer was required in polarization experiments. Another lens focused the beam onto the monochromator slits, such that it just filled its first mirror,  $MC_1$ , to maximize the collected signal, figure 2.6. The monochromator's large F-number necessitated the use of a helium neon laser to define an optical axis relative to the monochromator slits. The centre of the first mirror, the sample in the cryostat, and the collecting optics were then aligned around this reference and the signal could then be maximized using the detection system.

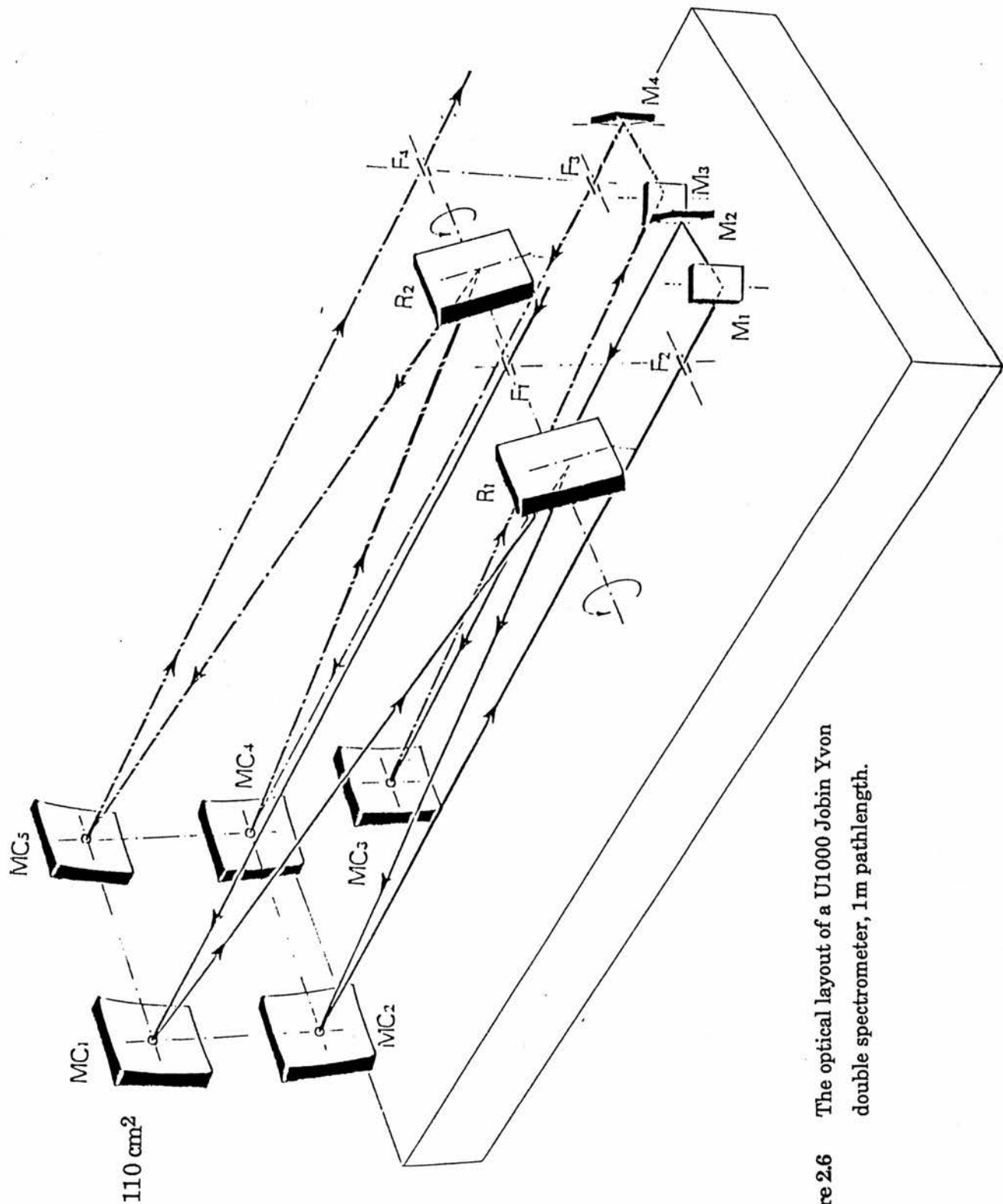


Figure 2.6 The optical layout of a U1000 Jobin Yvon double spectrometer, 1 m pathlength.

## II Experimental Method

### 2.2.1. Spectrometer

The spectrometer used was an ISA Jobin Yvon, Ramanor U1000 monochromator, with a 1 metre focal length and a mirror size of 110 mm<sup>2</sup> giving an aperture ratio of F/8. The Ramanor U1000 is a double Czerny-Turner type monochromator the gratings of which work with additive dispersion giving a stray light rejection of  $10^{-14}$  at 20 cm<sup>-1</sup> from the Rayleigh line. All monochromator functions such as scanning could be accessed using the spectral link control unit. A calibration of the monochromator was made periodically against the known emission from sodium and neon sources. The monochromator calibration could then be accurately related to a mechanical counter and spectra re-calibrated as was necessary. As the slit width was reduced below 100  $\mu\text{m}$ , the coupling between the essentially independent halves of the monochromator became more important. The coupling was very sensitive to temperature change,  $\pm 1-2^\circ\text{C}$ . However once this coupling was optimized it did not drift significantly during the day due to the relatively large thermal mass of the monochromator, 120 kg.

Two sets of grating were available covering two different spectral regions: in the visible (0.5-0.9  $\mu\text{m}$ ), holographic master gratings with 1800 grooves mm<sup>-1</sup>, blazed for use between 0.45 to 0.8  $\mu\text{m}$  were used, while in the near infra red (0.9-1.6  $\mu\text{m}$ ), ruled gratings with 600 grooves mm<sup>-1</sup>, blazed at 1.5  $\mu\text{m}$  were used.

The monochromator resolution was limited by its static bandwidth which is found by multiplying the reciprocal linear dispersion by the slit width used. Normally the monochromator is used in scanning mode, which means that the total bandwidth is the sum of the static and dynamic bandwidths. The dynamic bandwidth is defined as the scanning rate in  $\text{\AA s}^{-1}$  multiplied by the time constant of the associated detector. The static bandwidth for the visible and the near infra-red gratings used is given in figure 2.7a. While figure 2.8b shows the dynamic

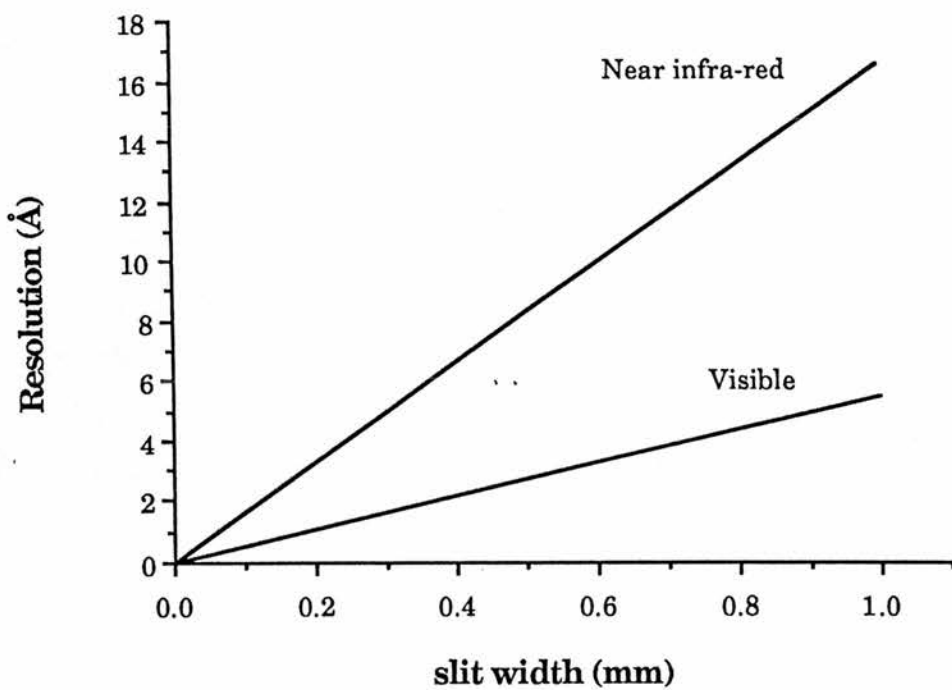


Figure 2.7a Static bandwidth for the visible and near-infra red gratings.

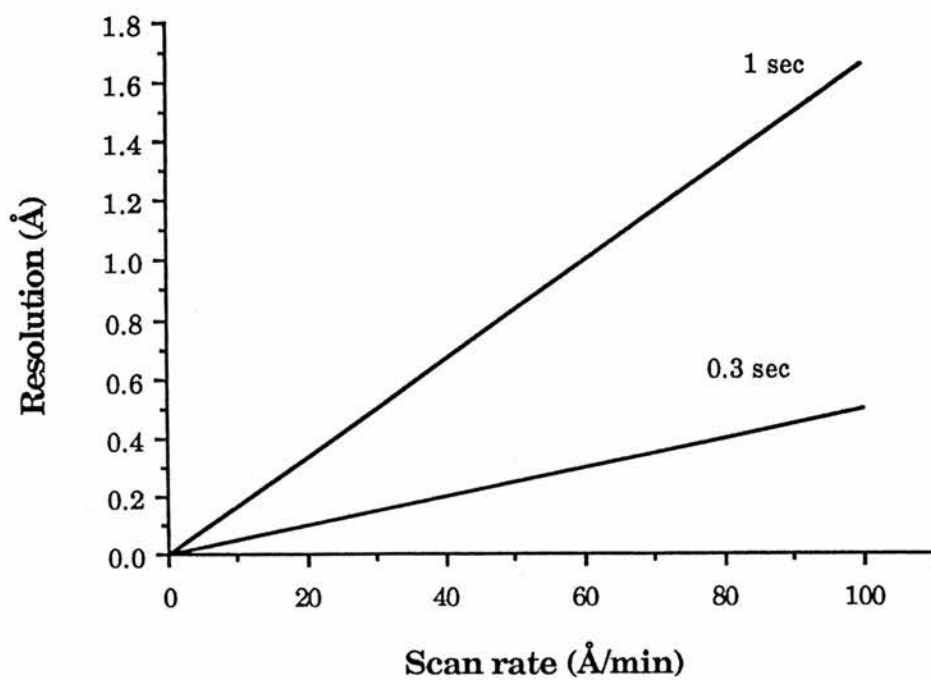


Figure 2.7b Dynamic bandwidth for different detector time constants.

## II Experimental Method

bandwidth for different detector time constants. There is always a trade off between resolution and the signal-to-noise ratio, depending on equipment stability, scanning speed and time available for a scan (Lumb 1978).

One problem arising with working in the near infra red was the effects of atmospheric absorption due to water vapour particularly in the region 1.34-1.42  $\mu\text{m}$ . An air tight tent was constructed around the apparatus including the cryostat and collecting optics. The tent and the monochromator, which had a 8 metre path length, figure 2.6, required purging. The purge was normally done using oxygen free nitrogen which was filtered through a silicon gel filter to remove any water vapour from it. The dried nitrogen was then passed through a 50  $\mu\text{m}$  dust filter to protect the optics. The purge was normally left on overnight and silicon gel crystals were placed in the tent and monochromator to help with drying process. A reduction in the background water absorption is clearly observed, figure 2.8 shows the dramatic improvement made by the purge on a broadband black body spectrum.

### 2.2.2 Detectors

Lock-in amplification provides a method for signal retrieval from noise. A weak signal contaminated by noise is modulated and is then fed into a synchronous switching detector with a reference signal from the modulator. The synchronous switching or phase sensitive detector gain bandwidth is such that it only amplifies around the particular modulation frequency. The output of the detector contains a smoothing low pass filter, whose RC time constant determines the effective bandwidth of the lock-in amplifier. This form of detection reduces only non-white noise sources such as 1/f or flicker noise to give a better signal to noise ratio when compared to dc methods.

For low light level detection and for signal to noise ratio an order of magnitude better than lock-in techniques (Lumb 1978), a photomultiplier in

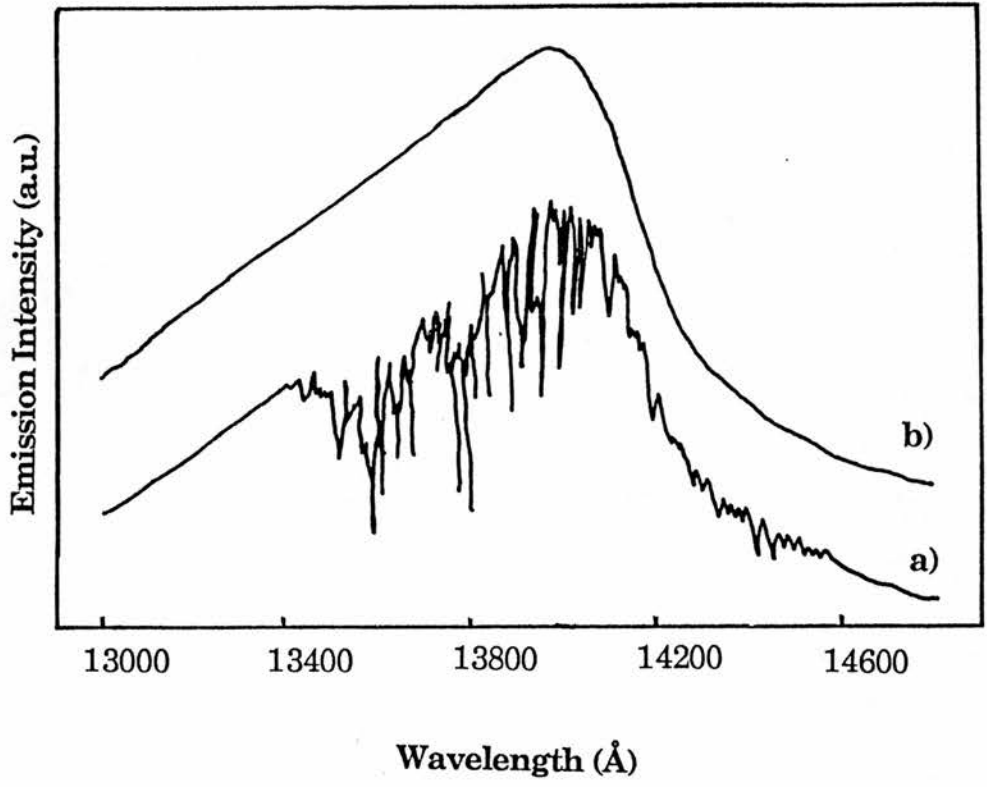


**Figure 2.8** The effects of atmospheric water absorption on a wide body emission source a) without nitrogen purge b) with nitrogen purge.

## II Experimental Method

conjunction with photon counting can be used. However due to a limited choice of photocathodes this technique can only be used in the visible region of the spectrum. Whenever a photon is incident on a photosensitive photocathode an electrical impulse is produced, this is amplified by a dynode chain before reaching the anode. A pulse height distribution occurs associated with noise from the dynode chain, but since the gain between the first dynode and photocathode is greatest, pulses due to photons dominate. These are then fed to a charge integrating amplifier and the pulses due to detected photons at the photocathode can be discriminated against. Photon counting is limited by thermal noise particularly from the first dynode and photocathode, resulting in a count even when the tube is darkened. This dark count is normally reduced by cooling the photomultiplier, in this instance to  $\sim 20^{\circ}\text{C}$ . Photon counting benefits from the advantages of digital measurement and processing, but requires a stable voltage supply since tube gain is exponential with voltage.

Hence two different detection systems and detectors were used to cover the near infra red and visible optical regions. For detection in the near infra red a Judson Infra Red Inc J16 D liquid nitrogen cooled germanium detector was connected to an EG&G model 5207 lock-in amplifier for signal retrieval. The laser light was chopped to provide a reference for the lock-in amplifier, figure 2.5. For the visible region a Hamamatsu photomultiplier tube, type R943-02, was used. It had a Cs-activated GaAs photocathode with an extended red response to 930 nm. The photomultiplier was placed in a Pacific Instrument model 3470/AD6 housing and cooled to  $\sim 20^{\circ}\text{C}$  to reduce thermal noise. The anode output was connected through the Pacific AD6 amplifier-discriminator to a Thorn EMI C10 photon counting system which provided analogue and digital outputs.

## II Experimental Method

### 2.2.3 Normalised System Response

When comparing the intensity of emission of two different spectra or considering the spectral lineshape, the spectral response of the detecting system must be known. The absolute response is not required as relative values can be used to correct the spectra. To obtain the spectral response of the photoluminescence apparatus, a black body source whose black body spectral response could be calculated was used. It consisted of piece of graphite placed inside a stabilized oven and heated to 900°C. The oven containing the source was placed in the usual position of the cryostat to find the response of the monochromator, detector and collecting optics.

Planck's radiation law defines the spectral radiance,  $L_\lambda$ , as the radiant flux emitted per unit area per unit wavelength per unit solid angle normal to the surface at given wavelength. The spectral radiant emittance is given by  $W_{b\lambda} = \pi L_\lambda / \epsilon$ , where  $\epsilon$  is the emissivity. The graphite can be considered to be an ideal black body source with the emissivity assumed to be unity and not to vary with wavelength. So Planck's radiation gives

$$W_{b\lambda} = 3.745 \times 10^4 \lambda^{-5} \left[ \frac{1.4338 \times 10^4}{\exp^{\lambda T} - 1} \right]^{-1} \quad (2.1)$$

where  $T$  is the absolute temperature in K,  $\lambda$  is in  $\mu\text{m}$  and  $W_{b\lambda}$  is in units of  $\text{W}/\text{cm}^2\mu\text{m}$ .

When a flux of photons is emitted from the black body source into an energy interval  $\delta E$  there are  $I_E \delta E$  photons corresponding to a power of  $h\nu I_E \delta E$ . The power in the range  $\delta\lambda$  from a black body source is  $L_\lambda \delta\lambda$ , where  $L_\lambda$  can be calculated as described above. Therefore we have

$$L_\lambda \delta\lambda = h\nu I_E \delta E \quad (2.2)$$

## II Experimental Method

so 
$$I_E = \frac{L_\lambda \delta\lambda}{h\nu \delta E} \quad (2.3)$$

and 
$$I_\lambda = \frac{\lambda^3 L_\lambda}{h^2 c^2} \quad (2.4)$$

When a black body spectrum is recorded with the experimental apparatus then  $i_\lambda = S_\lambda I_\lambda$  is detected, where  $S_\lambda$  is the overall system response for the monochromator and detector. The calibration factor for each wavelength is thus simply found.

$$S_\lambda \sim \frac{i_\lambda}{\lambda^3 W_{b\lambda}} \quad (2.5)$$

The above holds if we are using the photon counting system to detect photons from the black body source, but in the case of the Germanium detector, power (watts) is detected and the system response factor  $S_{\lambda Ge}$  is then given by:

$$S_{\lambda Ge} \sim \frac{i_\lambda}{\lambda W_b} \quad (2.6)$$

The system response and correction factor for the photomultiplier and for the germanium detector connected to the monochromator with their respective gratings are shown in figures 2.9 and 2.11. It became apparent that the grating efficiency associated with each detector grating had the greatest effect on the uncorrected spectral response.

Over the visible region the black body source energy varies rapidly and is quite sensitive to the oven temperature in this region. If a variation of oven temperature occurred of  $\pm 25^\circ\text{C}$ , accounted for by, for example, a bad thermocouple contact, figure 2.10. Then, the calculated system response for the photomultiplier calibration would be unreliable below 650 nm where a large error would occur, figure 2.9b. This possible uncertainty will not affect the majority of the spectra reported here since the luminescence obtained for most samples was in the region, 700 to 800 nm.

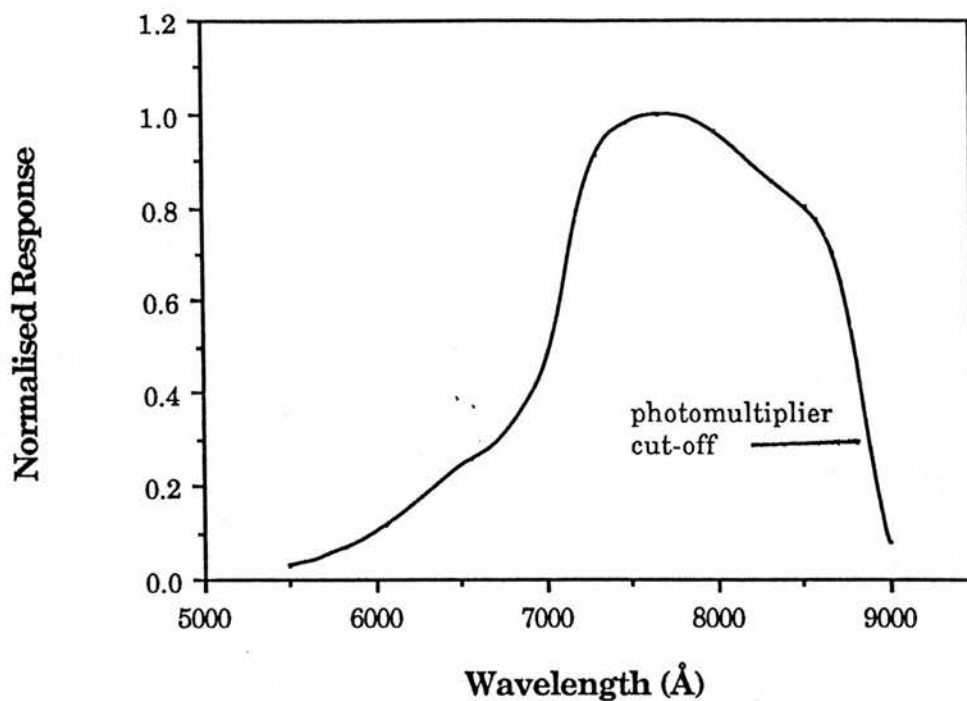


**Figure 2.9a** The normalized detected signal for the photon counter and visible gratings.

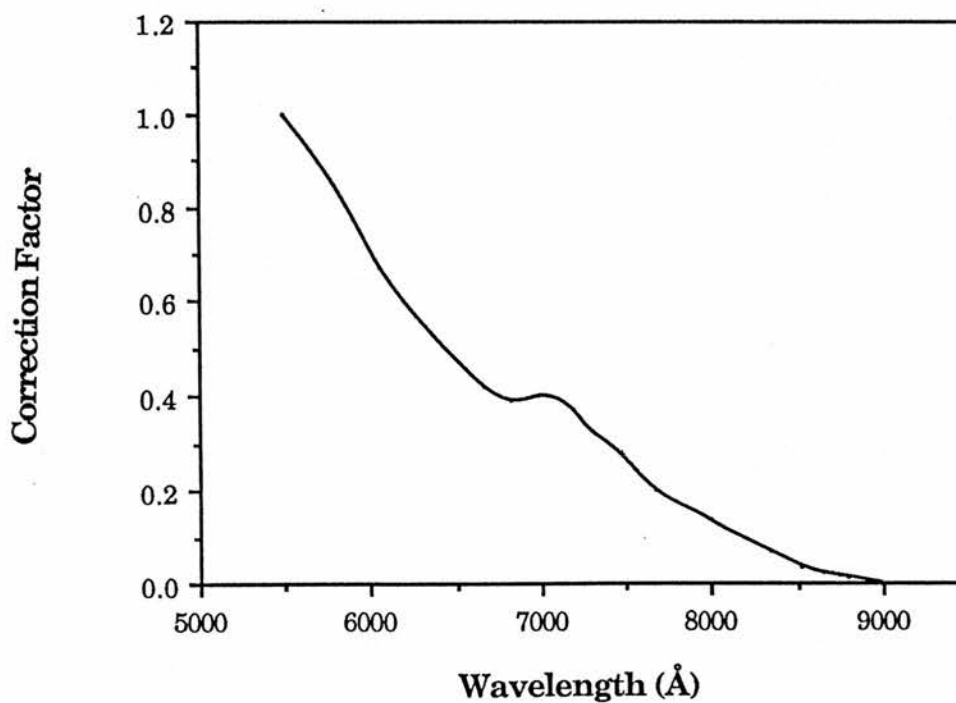


**Figure 2.9b** Corrected spectral response for recalibration of spectra taken using the photon counter and visible gratings.

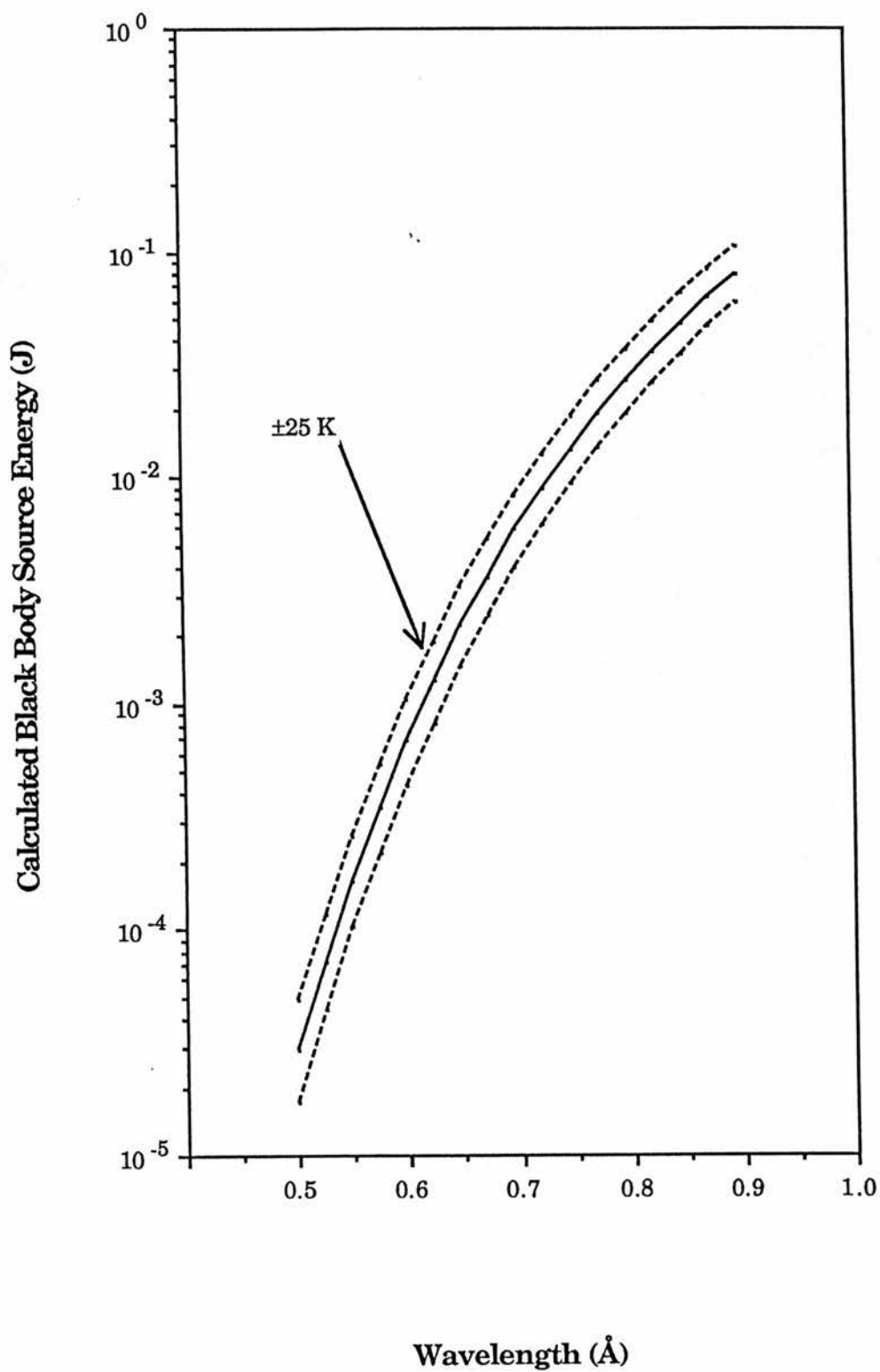


**Figure 2.10** The calculated black-body radiation energy into a particular wavelength for the source at 1173 K. The error-limits show the effect of a  $\pm 25$  K change in source temperature.

## II Experimental Method

The germanium detector can easily be used at two temperatures, room temperature and 77K where detector noise is much reduced. The main effect of cooling the detector on the spectral response is to apparently shift the long wavelength cut off to shorter wavelengths, figure 2.11a. This can be seen in the system responses, figures 2.11b and 2.11c, by a movement of the spectral position of the maximum peak response and with the observation of a sharp, detector related, cut-off at 1.4  $\mu\text{m}$ , figure 2.11c. The peak detector response (A/W) is also reduced on cooling by a factor of  $\sim 2.5$  making the detector less sensitive, figure 2.11a.

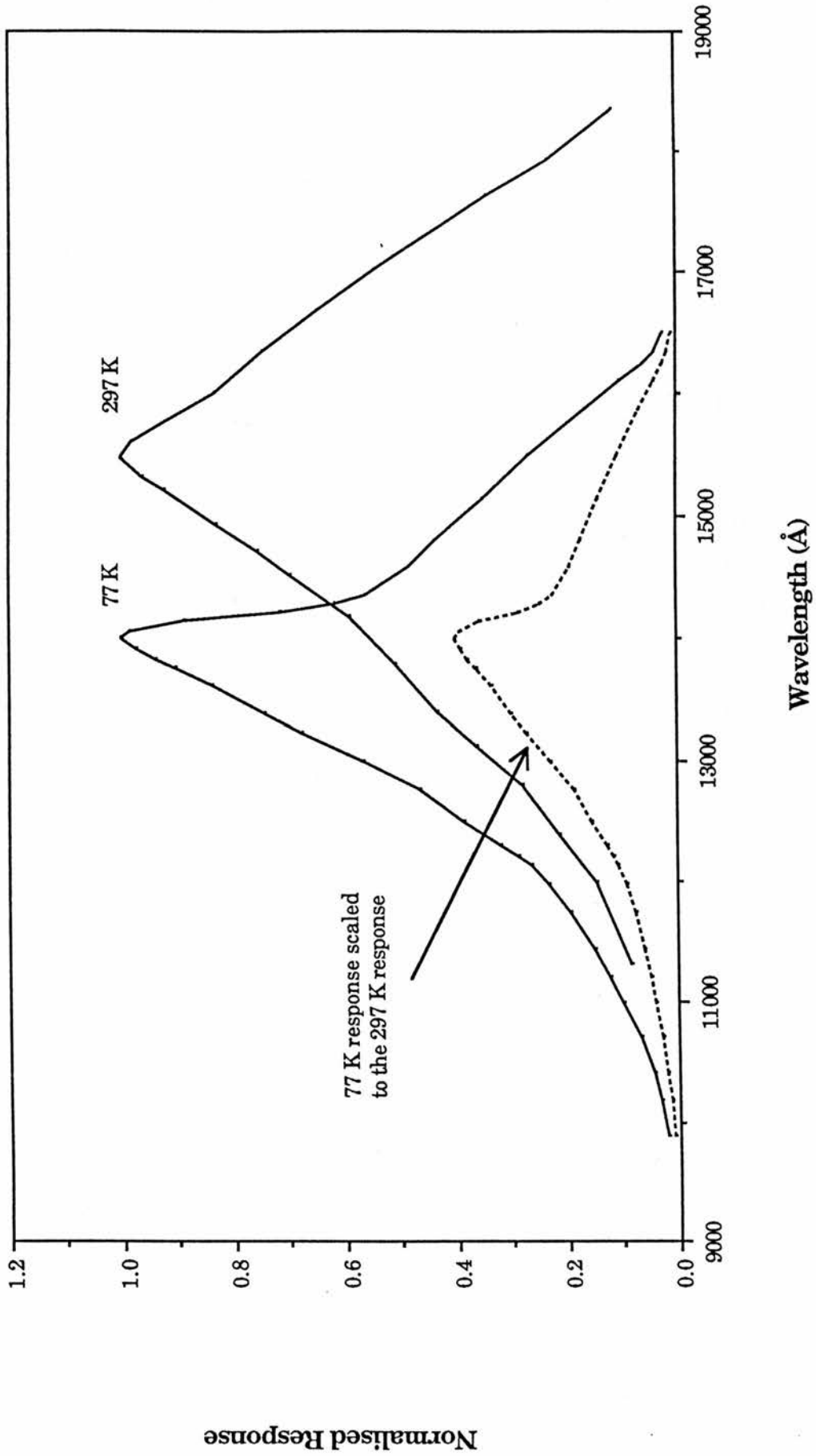
### 2.2.4 Cryostat

#### (i) Large Bore Optical Cryostat

The cryostat, figure 2.12, was custom-built at Quantum Production Ltd to specifications including: a temperature range of 1.5-300K, a 50° optical access to the sample, and most importantly a top loading aperture of 49 mm to take a diamond anvil cell, section 2.3.

The cryostat vacuum jacket surrounding the helium II space, the nitrogen and helium storage pots, was normally pumped to  $\sim 10^{-6}$  Torr using a diffusion pump backed by a single stage rotary pump. The vacuum jacket required continuous pumping since it contained super-insulation that required a long time to outgas properly. The base pressure normally dropped to  $\sim 10^{-7}$  Torr once there was liquid helium in the cryostat as a consequence of cryopumping. Since the cryostat has a large thermal mass it was important to ensure that the nitrogen pot and its radiation shields were pre-cooled before transferring helium into the helium pot. Consequently once the radiation shields were cooled to 77K it proved difficult to raise quickly the helium II sample chamber above this temperature.

**Figure 2.11a** The normalized detected signal for the germanium detector at, both 297 K and 77 K , with the infra-red gratings. The main effect of cooling the detector was to shift the long wavelength cut-off to higher energies and reduce reponsivity.



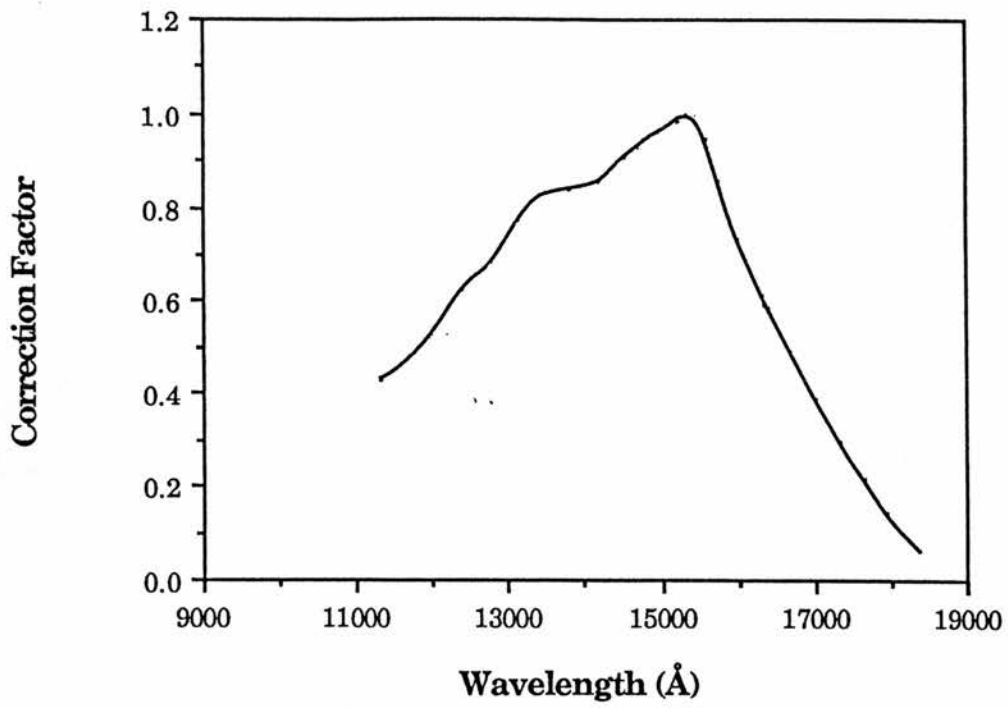


**Figure 2.11b** Corrected spectral response for recalibration of spectra taken using the germanium detector at 297 K and infra-red gratings.

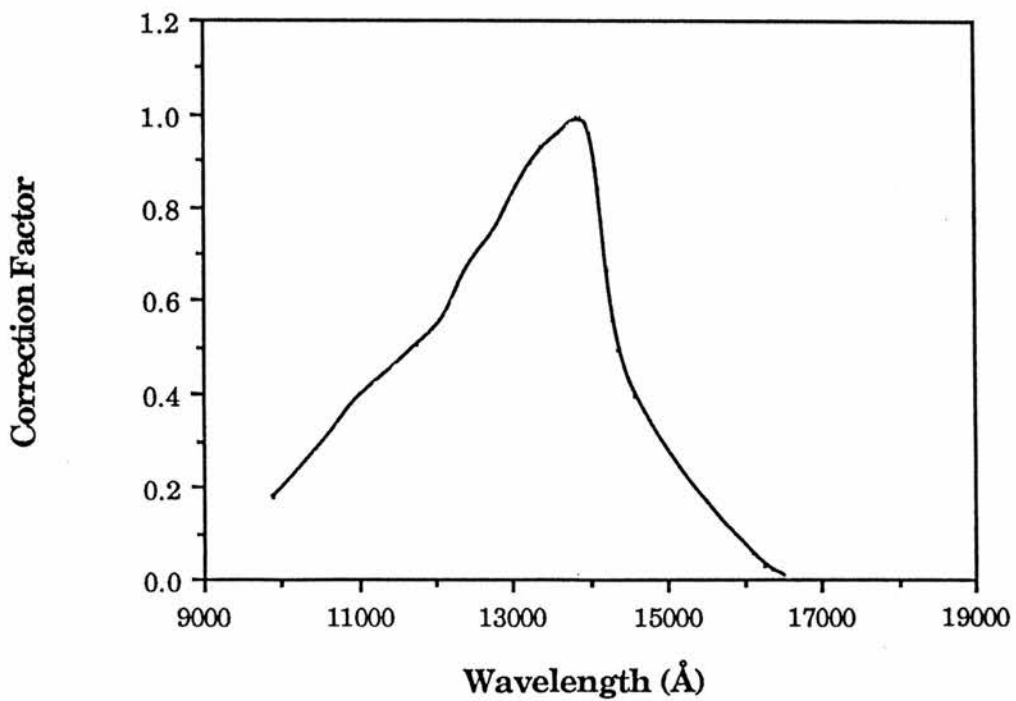


**Figure 2.11c** Corrected spectral response for recalibration of spectra taken using the germanium detector at 77 K and infra-red gratings.

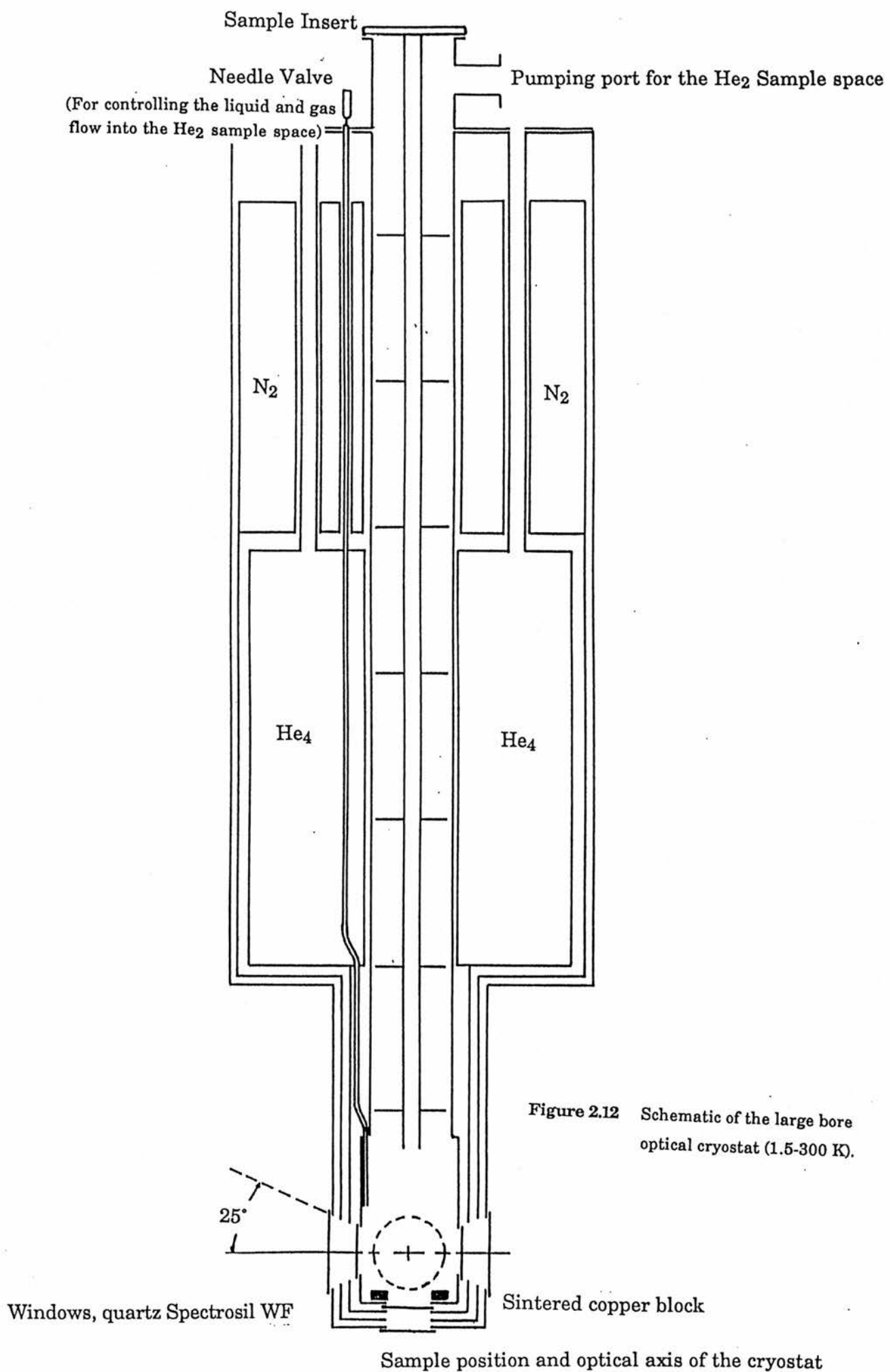


Figure 2.12 Schematic of the large bore optical cryostat (1.5-300 K).

## II Experimental Method

The helium II or variable temperature sample space contained a sintered copper block with a  $100\Omega$  heater wound around it. A Lake Shore DT500 DRC diode was embedded in the block and acted as a temperature sensor. The liquid or gas helium is delivered via a needle valve below the copper block into the helium II sample space which had a continuously replenishable capacity of 0.15 litres. Quartz spectrosil WF windows were used throughout as they gave a flatband spectral response from 0.2-2.0  $\mu\text{m}$ .

The large bore and wide optical access to the cryostat required very large cold windows, 32 mm diameter, on the sample space to obtain an almost unity F-number,  $\sim 1.07$ . The windows could not be mounted in the allowed space in the cryostat tail section using a standard technique. So Quantum Products supplied the cryostat with cold windows bonded directly onto the tailpiece using an integral, Mylar and glue join. Unfortunately during use the mounting work-hardened due to thermal cycling causing the windows to shatter on edge and a loss of vacuum to occur. The cryostat never operated to the required specifications despite attempts by the manufacturers to rectify the running problems. Eventually the cryostat windows failed catastrophically. The cryostat tail section was redesigned and rebuilt to take standard indium mounted Oxford Instrument spectrosil WF windows. Once the modifications had been completed the cryostat operated as required with a base temperature of  $\sim 1.7$  K and hold times up to 1.5 hrs depending on the jacket vacuum quality.

The cryostat mode of operation depends on the temperature region of interest. Below 4.2K, in bath mode, the cryostat operated by transferring helium from the storage pot in the cryostat to the helium II sample space through a needle valve. Once full, the sample space is sealed and pumped continuously by a rotary pump reducing the pressure and hence the temperature. At  $\sim 2.17$ K the helium under-goes a phase transition to become bubble free, superfluid helium, necessary for noise free spectra. The temperature of the sample is calibrated

## II Experimental Method

accurately from the helium vapour pressure (Brickwedde 1960) and can be controlled using the needle valve to leak normal helium through to the sample chamber. For temperatures between 4.2-77K the cryostat operates in a gas flow configuration. Helium gas is sucked through to the sample chamber and the temperature is controlled by balancing this flow with electrical power applied to the heater in the sintered copper block. A temperature controller, Thor Cryogenics Series 3000, was used to control the temperature to within  $\pm 0.5\text{K}$ .

An insert was designed for the cryostat to allow the sample position to be rotated through  $360^\circ$  and varied in the y-direction by 1 cm. The sample was mounted on the insert and then suspended in the sample chamber. In the gas flow configuration a temperature gradient between the sample and the sintered copper block occurred. A sensor was attached to the insert to determine when the sample had reached thermal equilibrium and obtain an accurate measurement of the actual sample temperature.

To operate the Quantum Production cryostat a gas handling system was constructed, figure 2.13. Its main purpose was to monitor and control the gas flow through the cryostat into the helium return line. By using the associated rotary pump, the helium II sample space and the helium storage pot could be roughed out for back filling with helium gas in preparation for a helium transfer. The pump, in conjunction with the needle valve, controlled the helium flow through the cryostat when operating in either gas flow or bath configuration.

### (ii) Oxford Instrument cryostat and flow controller

The Oxford Instrument CF1204 is a hybrid continuous flow and bath cryostat containing a helium reservoir with a needle valve which allows it operate below 2K. The sample is either cooled with a dynamic flow of coolant

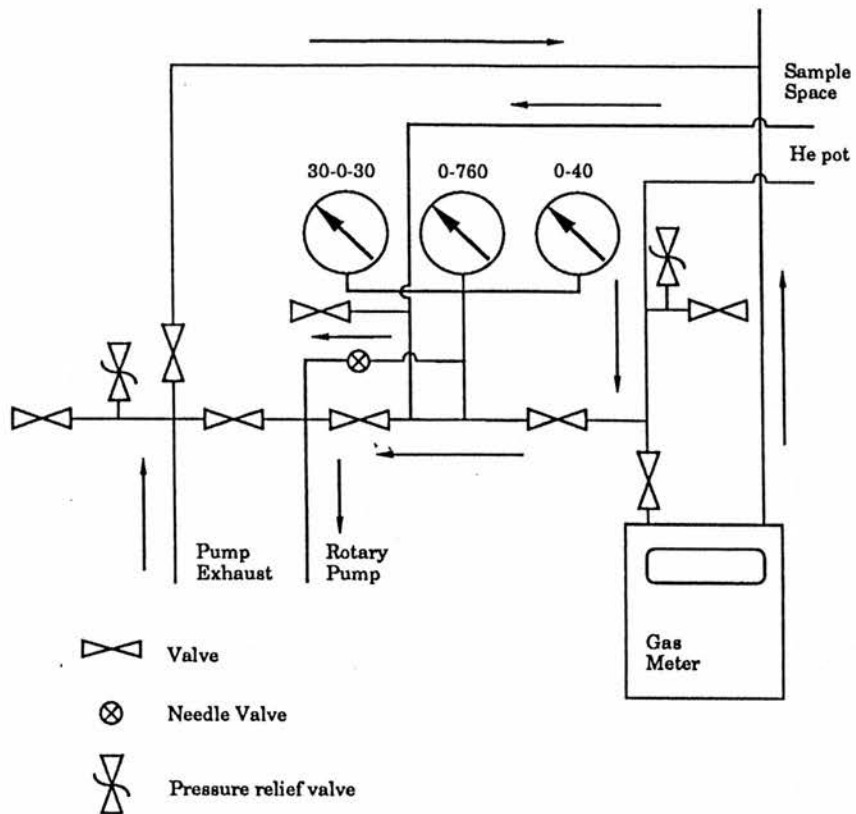


Figure 2.13 Gas handling system for the Quantum Products cryostat.

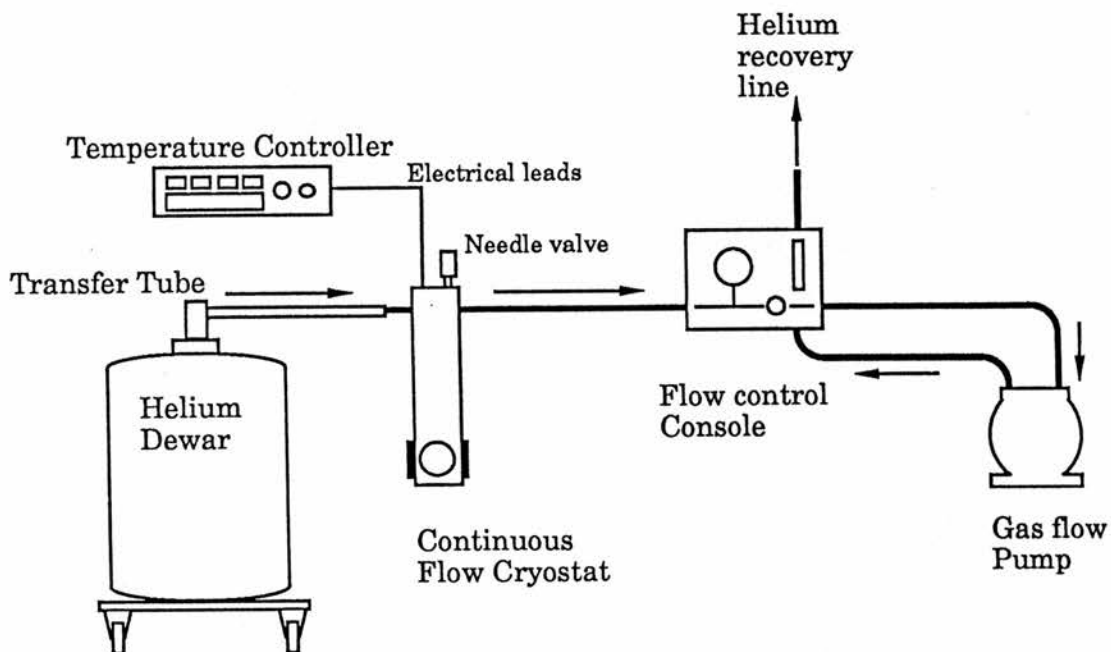


Figure 2.14 CF gas flow system for the Oxford Instrument CF1204 cryostat.

## II Experimental Method

passing over the sample and exhausting at the top of the sample space or in a pool of liquid helium. The CF gas flow system is shown in figure 2.14.

The continuous flow cryostat operates by controlling the transfer of helium to a vacuum insulated, radiation shielded, sample space in the cryostat. Sample temperature is again maintained by balancing the flow through the cryostat with power applied to an electrical heater attached to a heat exchanger. Coolant flow is produced by generating a pressure difference between the sample vessel and the helium return line with a gas flow pump. The flow and pressure in the helium return line are monitored and controlled by the flow control console. The cryostat operates in bath mode by transferring helium from a dewar into a reservoir in the cryostat. Once the reservoir was full coolant flow through the cryostat could be controlled by the needle valve. By collecting helium in the sample chamber, sealing with the needle valve and pumping as described in the previous section a base temperature of  $\sim 1.8\text{K}$  can be reached. The CF system was a replacement cryostat (on loan from UMIST) while the QP bath cryostat was undergoing modifications.

The cryostat sample chamber uses indium mounted spectro-sil quartz windows units which are 20 mm in diameter. The outer vacuum jacket window of 38 mm give the cryostat a F-number of 1.05. The sample space had a 120 cc volume which acted as a lower reservoir for single shot operation in bath mode. The sample space is fitted with a  $70\Omega$  wire wound heater, a CLTS sensor and a calibrated  $100\Omega$  Allen Bradley resistor. A  $100\Omega$  Allen Bradley resistor was also fitted to the sample insert to check for temperature offsets particularly at low temperatures.

A CLTS, resistance thermometer, was used as the feedback sensor when controlling the sample chamber temperature in the gas flow configuration. The CLTS is made from a grid of nickel and manganin connected in series which

## **II Experimental Method**

gives an almost linear response with temperature, figure 2.15. A calibrated Allen Bradley resistor gave a more accurate measurement of the actual sample temperature.

A flow control console was constructed for use with the CF1204 cryostat. It consists basically of a vacuum gauge, needle valve and flowmeter, figure 2.16. The gas from the cryostat enters the console passes through the needle valve into the gas flow pump and flows along the helium return line through a calibrated flow meter. This unit controls the flow of helium through the cryostat and records helium consumption. A negative pressure gauge is connected to the gas flow line after it enters the console from the cryostat. This monitors the line pressure and can be used to check for blockages in transfer tube or air leaks in the CF system. A diaphragm pump is used for the CF system as it is oil-free and provides an airtight helium return line.

### **(iii) Temperature control and calibration**

Temperature control and stability is an important consideration when using a cryostat particularly above liquid helium temperatures. This can only be achieved with a temperature control unit providing a feedback system. The required temperature was first approximately obtained by controlling the flow of cold gas through a needle valve in the cryostat. The temperature controller was preset to the required temperature and provided an error signal relating to the difference between the set point and the actual temperature. The error signal gave a proportional level for the electrical heat input to the cryostat tail to balance the cooling by the cold gas. The Thor Cryogenics Series 3000, model S-3010 temperature controller provided a three term control to damp any unstable feedback oscillations.

A temperature gradient existed in the Quantum Products cryostat between the tail section and sample insert. An accurate measure of the sample

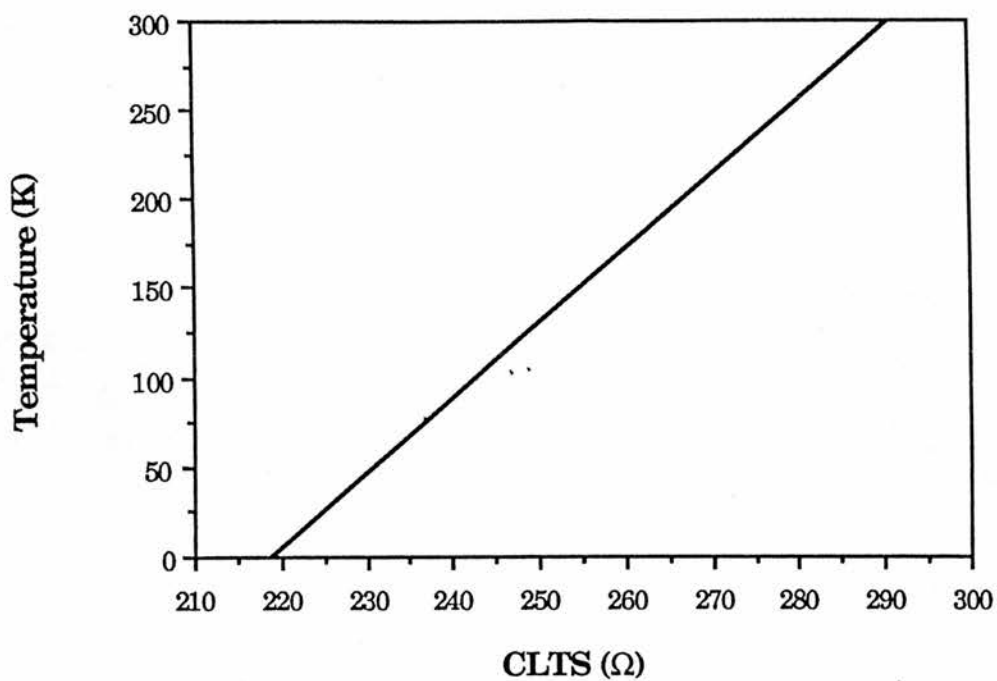


Figure 2.15 CLTS calibration.

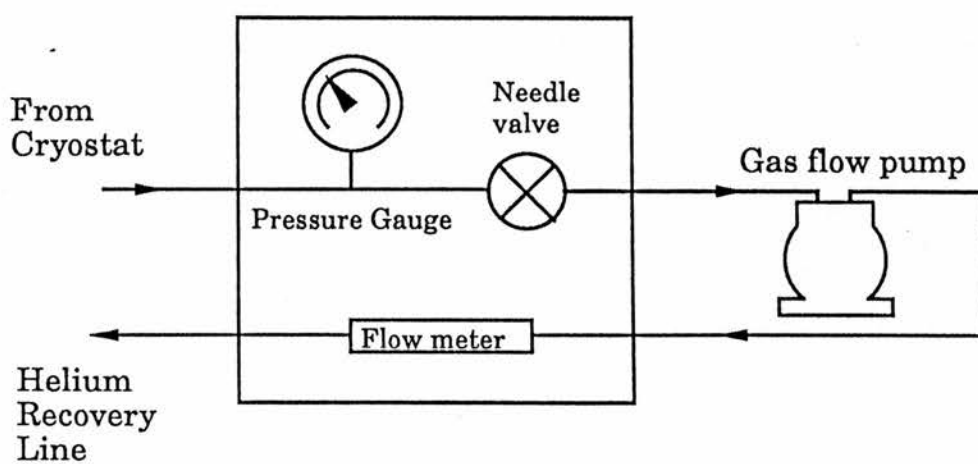


Figure 2.16 Flow control console for CF gas flow system.

## II Experimental Method

temperature was necessary and to achieve this the sample insert was fitted with an Allen Bradley carbon resistor calibrated against a silicon diode (Lake Shore D7-470-SD-11), figure 2.17. An estimate of the sample temperature could be made using the relationship  $\log_{10}R=a+b(\log_{10}R/T)^{0.5}$ , where the constants  $a, b$  are estimated from the resistor's nominal value, in this case  $125 \Omega$  (Rose-Innes 1964). For temperatures above 150K an Oxford Instrument RhFe resistor, PHZ0002 had been fitted to the insert. The calibration for RhFe resistor (Cryogenic Calibrations) was estimated to within  $\pm 0.25K$  and is shown in figure 2.18. Micro-ampere constant current sources, incorporating a highly stabilized instrumentation operational amplifier, were used for the input to the thermometer. The output voltages were read with Datron Precision voltmeters.

### 2.3 High Pressure Optical Cell

The use of high pressure, low temperature, optical spectroscopy has arisen mainly due to advances in cell design (Shaw and Nicol 1981, Silvera and Wijngarden 1985). The diamond anvil cell (DAC) has emerged as a useful tool for high pressure research mainly due to several important innovations; the introduction of a metal gasket for hydrostatic pressure generation and the use of the ruby fluorescence technique for pressure calibration. Although many different types of cells have evolved, NBS, Mao-Bell, Syassen-Holzappel, Merrill-Bassett to name a few (Jayaraman 1983), the basic principle of a diamond anvil cell is quite simple.

A schematic of a diamond anvil cell with its main components is shown in figure 2.19. The diamonds are brilliant cut gem stones with the points ground to form a flat cutlet or anvil 0.5-1 mm in diameter. The diamonds are normally mounted on a face plate of some hardened material and the anvils are aligned parallel to one optical fringe since diamond failure can occur due to misalignment stresses. A metallic gasket of beryllium-copper or inconel, 100-200

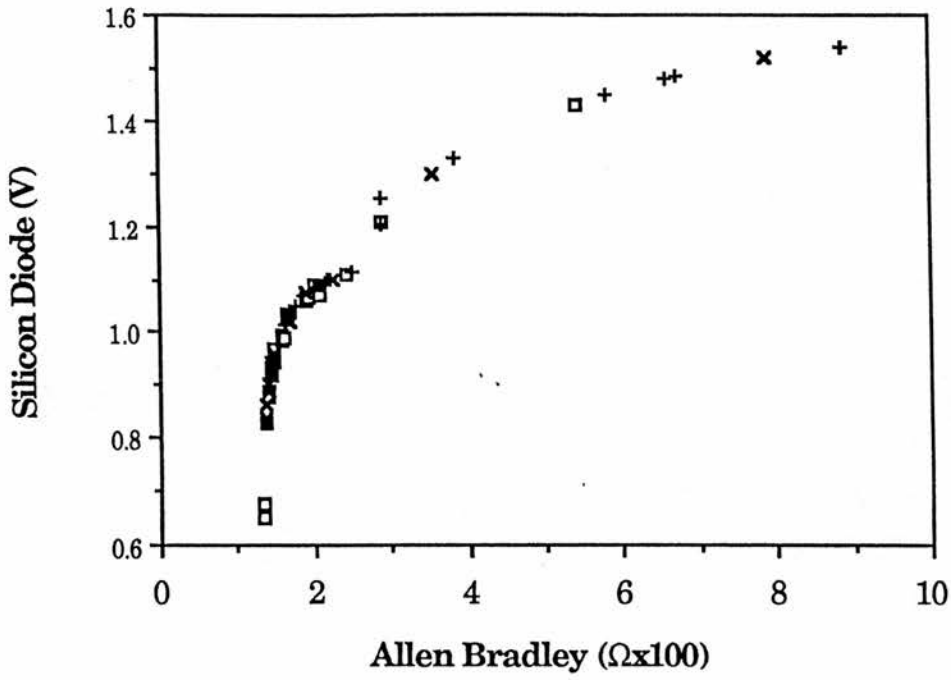


Figure 2.17 Allen Bradley resistor calibrated against a Lake Shore, D7-470-S10-11, silicon diode,  $I=10\mu\text{A}$ .

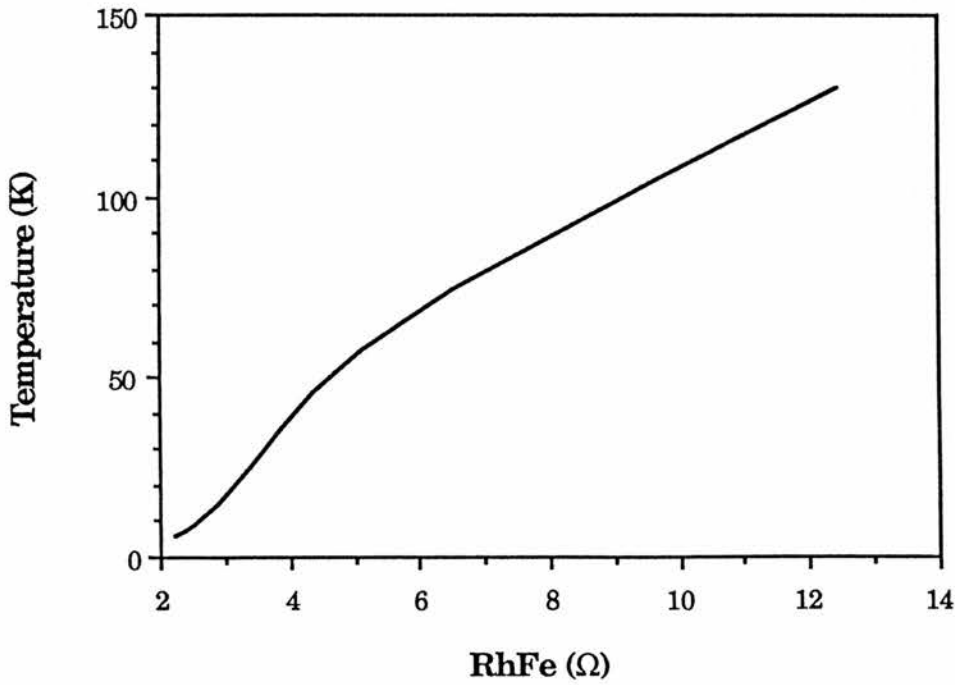


Figure 2.18 RhFe resistor calibration with  $I=10\mu\text{A}$ .

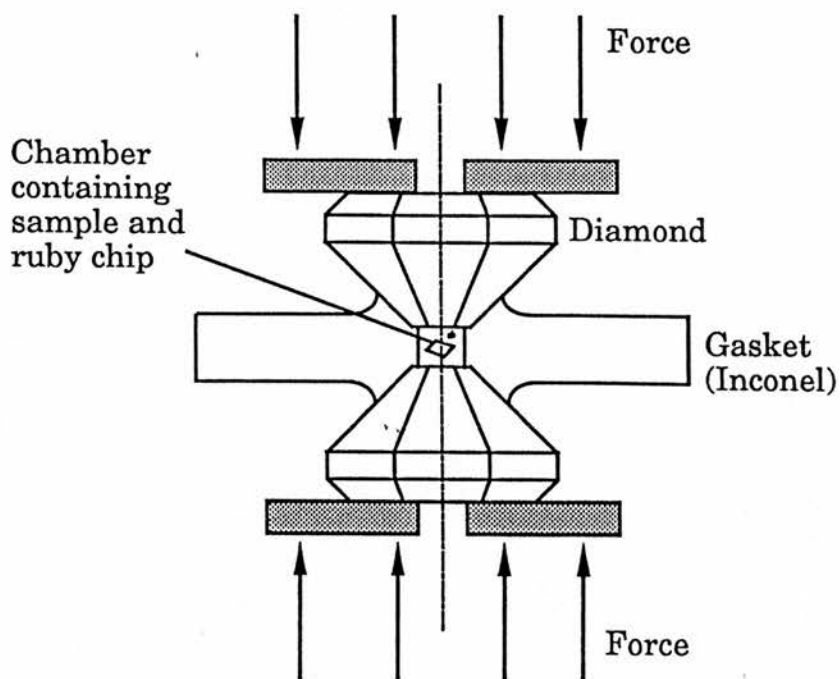


Figure 2.19 Basic principle of a diamond anvil cell.

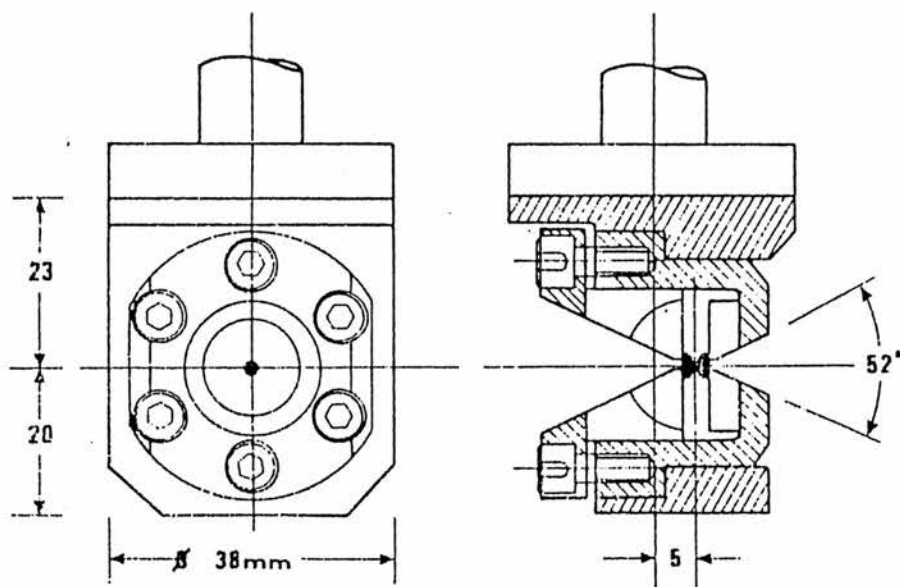


Figure 2.20 A Diacell D0-1 mounted on a cold station.

## II Experimental Method

$\mu\text{m}$  thick, has a 200-300  $\mu\text{m}$  hole drilled in it to form a sample chamber. A sample typically 50-100  $\mu\text{m}$  square and 20-40  $\mu\text{m}$  thick is placed inside the hole together with a ruby chip 10-20  $\mu\text{m}$  and the pressure transmitting medium. In the diamond anvil cell, sample volume is normally sacrificed for higher pressures. Pressure is then induced in the sample chamber by applying a force to the back surfaces of the diamonds, deforming the gasket. The different cell designs mentioned above normally concentrate on different methods of applying the force to the diamonds.

The choice of diamond type for a DAC is important. Depending on the particular application, type I are generally satisfactory, while type II are required for Raman scattering or infra red absorption experiments due to its lower fluorescence (Adams and Sharma 1977). A pair of matched anvils with 8-sided flats are required for most applications. Although 16-sided flats can withstand the highest stress gradients they may not produce a good seal onto the gasket. The most important development in diamond anvil cell usage, and the key to hydrostatic pressure generation, was the introduction of a metal gasket between the diamonds (Valkenburg 1965). The gasket is normally pre-indented before drilling to reduce material flow and to provide a work hardened area. Not only does the gasket form the sample chamber containing the pressure medium, but it also extrudes around the diamonds, forming a seal acting as a supporting ring for them. The use of ruby for pressure calibration and pressure transmitting media is discussed later.

### 2.3.1 Diamond Anvil Cell

The diamond anvil cell used in this work is a Diacell D0-1 clamp cell based on the Mao-Bell piston/cylinder cell (Jayaraman 1986) and was designed by Diacell Products, figure 2.20. Force is applied by symmetrically tightening left-hand, right-hand paired Allen screws. This transmits the force to a piston via

## II Experimental Method

the diamonds to the sample chamber. The diamonds used here were type II 0.32 carat, Drukker standard cut, with a 0.7 mm anvil. They are aligned for parallelism using three screw adjustment of a hemisphere contained within the piston. The cell was provided with a custom-designed mount for use with the Quantum Production cryostat described in section 2.2.4(i).

When preparing the DAC for use, a gasket of Inconel 600 was normally pre-indented from 200  $\mu\text{m}$  to 100  $\mu\text{m}$ , using the diamonds, before a hole of 250  $\mu\text{m}$  was drilled in the centre. Measurements were normally made on single crystal semiconductors thinned by hand to  $\sim 30$   $\mu\text{m}$  thick and then cleaved to a square  $\sim 100$   $\mu\text{m}$  using a technique suggested by Iain Spain (1987). The crystal was loaded into the cell and surrounded by a number of ruby chips 10-20  $\mu\text{m}$  in diameter. In use the cell was found to show slight differential contractions on temperature cycling causing the gasket to lose its seal at lower pressures ( $<10$  kbar). To avoid this the use of bevel washers within the cell and different gasket materials were considered. It was important to ensure that the diamond cell was aligned both before use and particularly after pressurization as distortion can occur in operation. Full instructions on cell usage can be found in appendix B.

The diamond anvil cell was supplied for use with the diamonds glued into position using a low temperature araldite. This form of mount proved unsuitable for cryogenic use as the glue cracked, probably as a result of thermal cycling, making the DAC unusable. Collets were designed to centre and hold the diamonds in place in the DAC. Since it was necessary to retain the gaskets in position, when pre-indenting and to minimize movement during cell pressurization, locating pins were also included, figure 2.21. The collets were screwed down onto the diamond face plate, this required softening for holes to be tapped. The face plate was then rehardened to 100 tonnes per square inch (EM42 treatment) before use. The diamond was forced onto the retaining plate by the

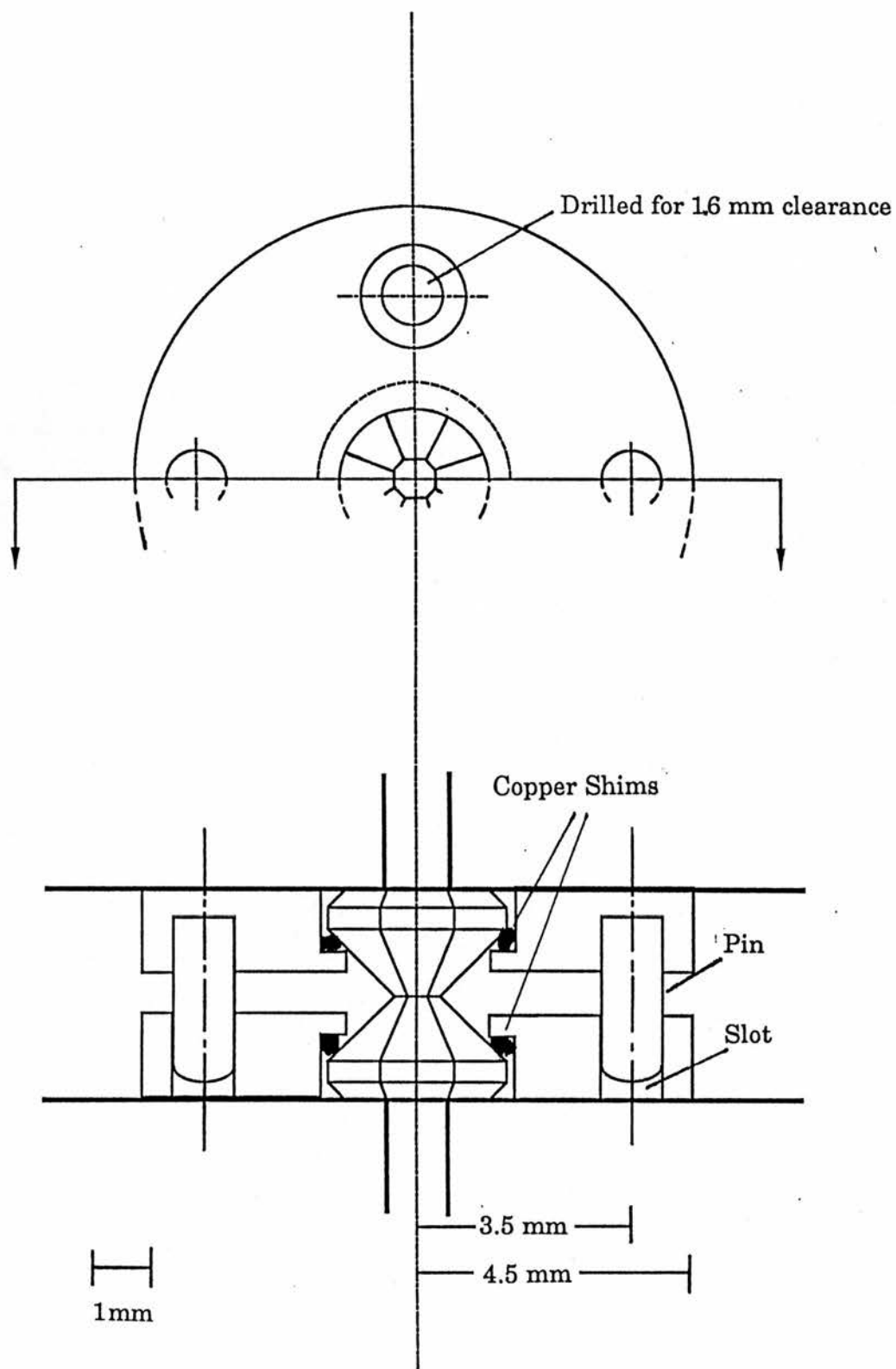


**Figure 2.21** Collet designed to centre and lock diamonds into place in the Diacell diamond anvil cell.

## II Experimental Method

collet deforming a copper shim, ensuring the diamond could not rotate. A pin and slot arrangement ensured the diamonds' rotational symmetry constant with respect to each other. The diamond anvil cell was then realigned for use as described in appendix B.

### 2.3.2 Ruby line Calibration

The ruby fluorescence method (Forman et al 1972) removed problems associated with pressure calibration in the diamond anvil cell and is now widely used. A laser is used to excite the ruby R lines ( $R_1$  at 6972 Å,  $R_2$  at 6942 Å) which show intense, narrow linewidth fluorescence. Below 200 kbar, the region of interest in this work, a linear shift of these lines occurs to longer wavelengths at the rate of  $0.365 \text{ Åkbar}^{-1}$  (Piermarini 1975). In the megabar pressure region the ruby line shift becomes sublinear, and a relationship,  $P(\text{mbar})=3.808(1+(\Delta\lambda/\lambda)^5-1)$ , was proposed by Mao (1978). The fluorescence also gives an indication of the hydrosticity of the pressure medium as the peaks broaden with non-hydrostatic stress.

Ruby fluorescence was obtained for pressures of 60 kbar from a 10  $\mu\text{m}$  diameter sample in the Diacold clamp cell. A methanol and ethanol mix was normally used as the hydrostatic transmitting medium, sect 2.3.3. As the cell was cooled, a shift with temperature of the  $R_1$  line of  $0.038 \text{ ÅK}^{-1}$  occurred and the  $R_2$  branch shifted and thermally quenched, figure 2.22a, this meant only the  $R_1$  line was useful for low temperature calibration. It has been suggested that the intensity ratio of the R lines can be used to give an indication of cell temperature (Weinstein et al 1987).

Noak and Holzapfel (1979) have shown that the gradient  $\Delta\lambda/\Delta P$  to remain the same regardless of the ruby temperature. So in this study, correction was made for the ruby line temperature shift by using a zero bar reference sample at the DAC temperature. In figure 2.22b a wavelength shift of the  $R_1$  branch of 18.5 Å

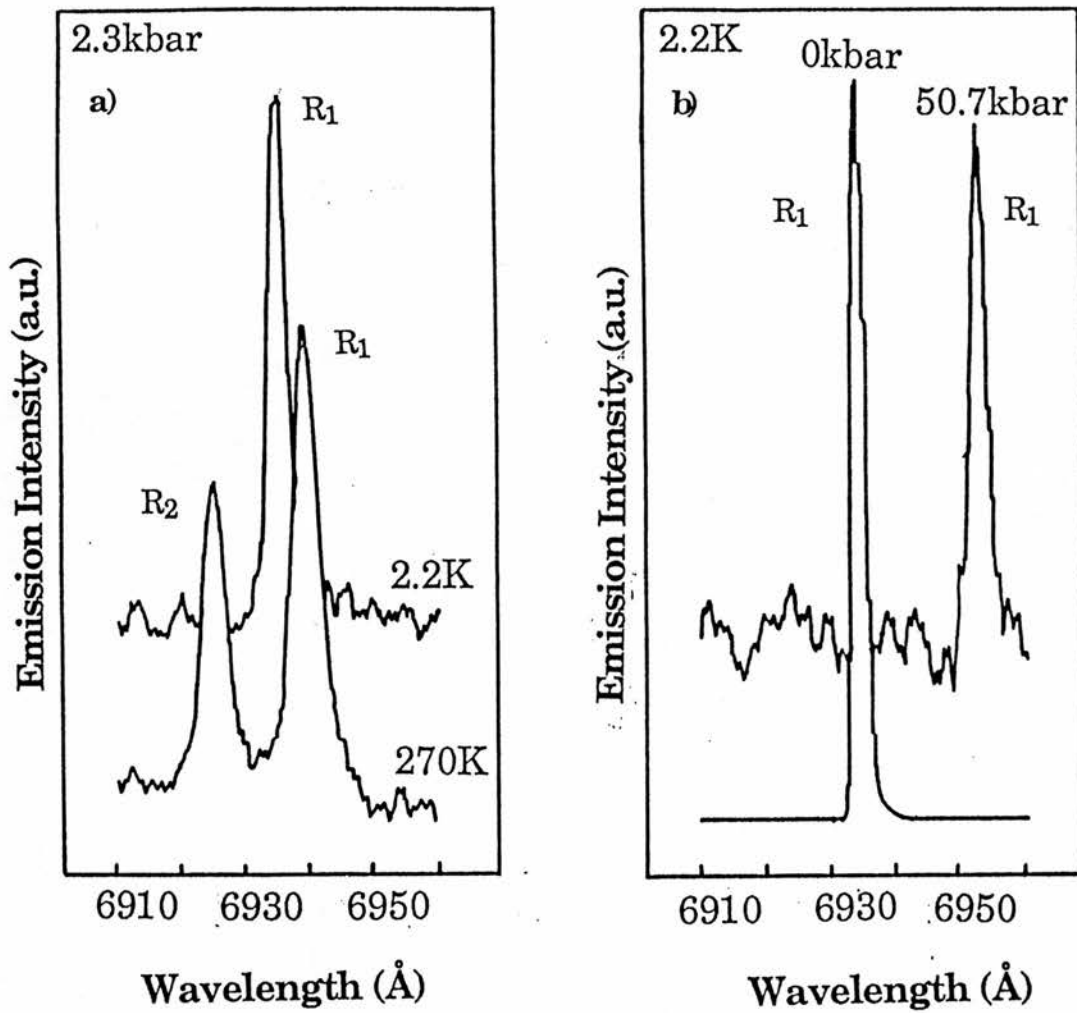


**Figure 2.22** a) Typical room temperature ruby fluorescence is shown. The sample was obtained in the DAC. Note the disappearance of the R<sub>2</sub> branch at low temperature. b) When the ruby is pressurised a 18.5 Å shift occurred in the fluorescence for 50.7 kbar. A ruby sample was mounted outside of the DAC for comparison.

## II Experimental Method

corresponds to a pressure of 50.5 kbar. Accuracy of the ruby fluorescence method is estimated to be  $\pm 0.5$ -2 kbar.

### 2.3.3 Low Temperature Pressure Media

In using the DAC, consideration must be given to the choice of pressure transmitting medium particularly in ensuring that it will be hydrostatic at all pressures and temperatures used. This is most important for semiconductor applications where any uniaxial component to the applied pressure will split the valence band, complicating the observed transitions. A methanol-ethanol mixture in the ratio 4:1 was used, this should remain hydrostatic to 100 kbar (Piermarini et al 1973). The mixture can be used at low temperatures as long as the pressurization is completed at room temperature and then cooled (Jayaraman 1986, 1988). Our own measurements confirm this, as no signs of non-hydrostatic pressures were observed in the ruby fluorescence (section 6.3.1). On cooling, it was observed that the medium remained clear and showed no signs of scatter which is obviously important for optical experiments. It was suggested working range of this medium could be extended to ~145 kbar by adding a small percentage of water to the ethanol-methanol mix (Jayaraman 1983), but this will only be valid for the medium at room temperature (section 6.3.1).

To extend the working range of the DAC the use of condensed gases as the hydrostatic medium must be considered. These require special filling techniques using cryogenic, and remote high pressure filling, of the cell. Condensed gas media such as helium are hydrostatic up to 1 Mbar (Silvera and Wijigarden 1985) and their use is necessary if continuously variable pressures are required at low temperatures. A review of several different organic and condensed gas media including the hydrostatic, homogeneous limit of each, is given by Jayaraman (1983). Argon is considered to be a good medium for low

## II Experimental Method

temperatures since only Van der Waals forces present (Jayaraman 1986) so cryogenic filling of the Diacold cell was explored using liquidified argon in a liquid nitrogen cold cabinet. This method was found to be unsatisfactory, so a high pressure bomb was designed to remotely fill and seal the cell, figure 2.23. It is expected to solve any potential problems of non-hydrostaticity of the alcohol mixture at higher pressures.

### 2.4 Samples used in this work

All the samples used in this work were grown by MBE using a VG Semicon, VG80H reactor. Several growers at different locations donated samples for the project. These were P A Claxton, J S Roberts at the SERC Central Facility for III-V semiconductors, Sheffield, T Kerr at GEC Hirst Research Centre, Wembley, G Scott at British Research Laboratory, Ipswich and T Cheng, C Stanley at Glasgow University Department of Electronics and Electrical Engineering. Tables 2.1 lists the bulk samples, whilst table 2.2 lists the heterostructure and superlattice samples, sample type and structure including any data provided by the growers are given. Sample mobility and carrier density at 77K were found using the Van der Pauw method, this data was mostly provided by Al-Dubuni (1987) and is given when available.

Hex ended rods allow the DAC to be closed once cryo-filled.

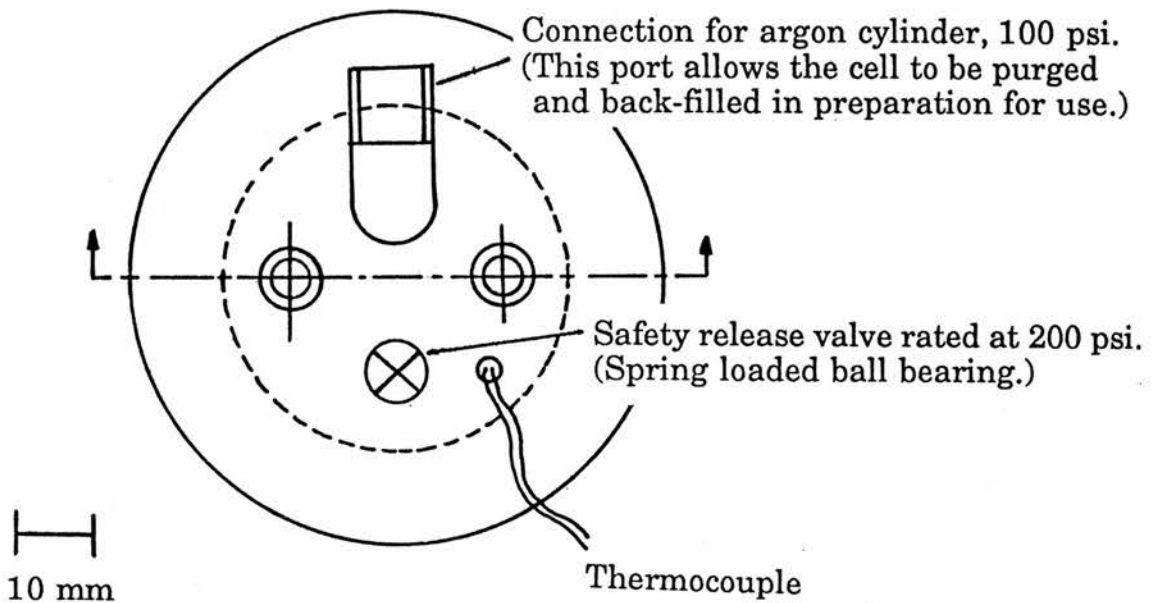
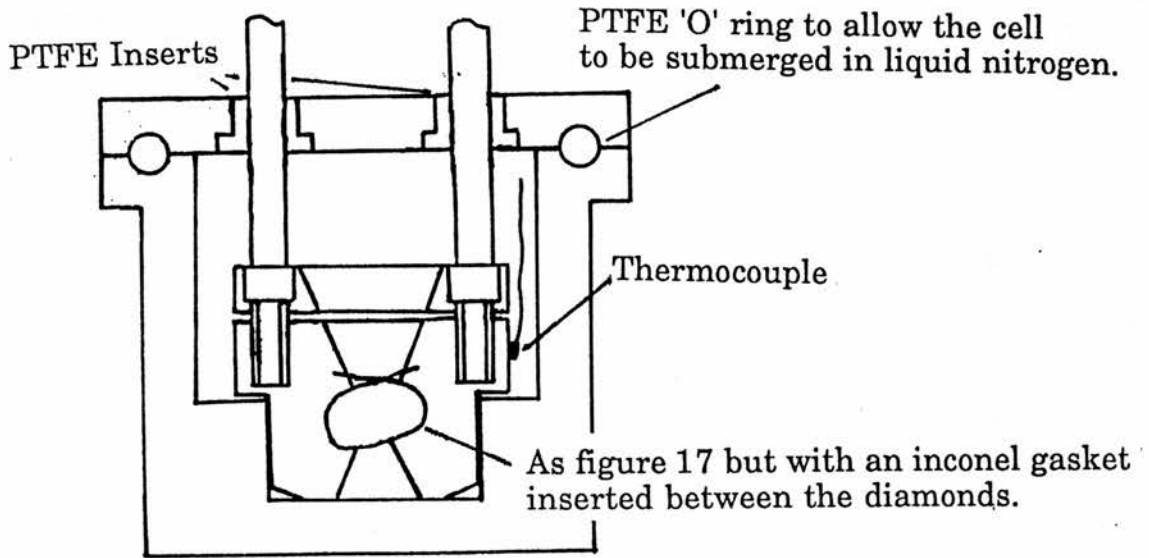


Figure 2.23 A cryo-cell for argon loading the Diacell diamond anvil cell

Sample Name Origin	$\mu \text{ cm}^2 \text{ V}^{-1} \text{ s}^{-1}$ $n_s \text{ cm}^{-3}$ @77K	Layer Thickness ( $\mu\text{m}$ )	Substrate	Other
GaAs MB342 GEC				
InP PMB106 Sheffield	$a_{43,340}$ $a_{2.1 \times 10^{15}}$	2.5	InP:Fe	
InP #203 Glasgow	$a_{42,500}$ $a_{1.5 \times 10^{15}}$	4.8		undoped
InP #254 Glasgow		3.5		Mg doped
InP #273 Glasgow		1		undoped
AlGaAs MB318 GEC	$b_{1 \times 10^{16}}$	2.2		
AlInAs MV402 BT				X(xray)=50.7 % PL-fwhm24.5meV Si doped
$\text{Al}_{1-x}\text{In}_x\text{As}$ MV408 BT	$b_{1 \times 10^{16}}$	1.4		X(xray)=50.3 % PL-fwhm16.9meV
$\text{Al}_{1-x}\text{In}_x\text{As}$ MV409 BT	$b_{0.8-1 \times 10^{16}}$	1.1		X(xray)=51.4 % PL-fwhm14.6meV
$\text{Al}_{1-x}\text{In}_x\text{As}$ MV411 BT	$b_{2-3 \times 10^{15}}$	1.4		X(xray)=51.4 % PL-fwhm15.4meV
$\text{Ga}_{0.47}\text{In}_{0.53}\text{As}$ PMB112 Sheffield	12000 $9 \times 10^{15}$	2.5	InP:Fe	best sample grown 0.785 eV 3.2meV

Table 2.1 Bulk samples used in this work

Sample Name	$\mu \text{ cm}^2 \text{ V}^{-1} \text{ s}^{-1}$	Structure <sup>c</sup>	Other
InP-Ga <sub>0.47</sub> In <sub>0.53</sub> As PMB121 Sheffield	<sup>a</sup> 11,940 <sup>a</sup> 0.125	1000Å InP 25Å × 10 GaInAs 100Å × 10 InP InP:Fe	Cooled shutters 0.9251 eV 7.5 meV
InP-Ga <sub>0.47</sub> In <sub>0.53</sub> As PMB137 Sheffield	<sup>a</sup> 61,520 <sup>a</sup> 0.88	5000Å InP 5×10 <sup>17</sup> Si 100Å InP u/d 10000Å InGaAs 25Å InP u/d InP:Fe	Cooled shutters Modulation doped
Al <sub>0.3</sub> Ga <sub>0.7</sub> As-GaAs MB660 GEC		1.5μm AlGaAs 33Å × 10 GaAs 55Å × 10 AlGaAs 1.5μm AlGaAs 0.08μm GaAs Si doped 5×10 <sup>15</sup>	No luminescence
Al <sub>0.3</sub> Ga <sub>0.7</sub> As-GaAs MB662 GEC		1.25μm AlGaAs 50Å × 10 GaAs 84Å × 10 AlGaAs 1.5μm AlGaAs 0.08μm GaAs Si doped 5×10 <sup>15</sup>	1.5663 eV 1.5644 eV 3.6 meV
Al <sub>0.3</sub> Ga <sub>0.7</sub> As-GaAs MB669 GEC		0.5μm AlGaAs 50Å GaAs 125Å × 10 AlGaAs 50Å × 10 GaAs 0.75μm AlGaAs 500Å GaAs Si doped 5×10 <sup>15</sup>	1.5718 eV 1.5703 eV 5.2 meV
Al <sub>0.3</sub> Ga <sub>0.7</sub> As-GaAs MB670 GEC		0.25μm AlGaAs 100Å GaAs 166Å × 10 AlGaAs 100Å × 10 GaAs 0.25μm AlGaAs 500Å GaAs Si doped 5×10 <sup>15</sup>	No luminescence

Sample Name	$\mu \text{ cm}^2 \text{ V}^{-1} \text{ s}^{-1}$	Structure <sup>c</sup>	Other
InP-Ga <sub>0.47</sub> In <sub>0.53</sub> As	<sup>a</sup> 1,754	1000Å InP	1.0728 eV 21.9 meV
PMB41	<sup>a</sup> 3.1	10Å GaInAs	1.0298 eV 14.2 meV
Sheffield		1000Å InP	0.8815 eV 11.7 meV
		20Å GaInAs	0.8240 eV 20.0 meV
		1000Å InP	
		40Å GaInAs	
		1000Å InP	
		60Å GaInAs	
		5000Å InP	
InP-Ga <sub>0.47</sub> In <sub>0.53</sub> As	<sup>a</sup> 10,680	2000Å InP	0.8052 eV 19.8 meV
PMB78	<sup>a</sup> 2.5	160Å GaInAs	
Sheffield		2000Å InP	
		InP:Fe	
InP-Ga <sub>0.47</sub> In <sub>0.53</sub> As	<sup>a</sup> 986	2000Å InP	0.900 eV 11.5 meV
PMB79	<sup>a</sup> 2.8	50Å GaInAs	
Sheffield		2000Å InP	
		InP:Fe	
InP-Ga <sub>0.47</sub> In <sub>0.53</sub> As	<sup>a</sup> 12,440	2000Å InP	
PMB78	4.97	10Å GaInAs	
Sheffield		2000Å InP	
		InP:Fe	
InP-Ga <sub>0.47</sub> In <sub>0.53</sub> As	<sup>a</sup> 3,660	500Å InP	0.7840 eV 13.1 meV
PMB116	<sup>a</sup> 0.3	160Å GaInAs	
Sheffield		InP	
		InP:Fe	
			green due to InP layer
InP-Ga <sub>0.47</sub> In <sub>0.53</sub> As		1000Å InP	Cooled shutters
PMB117		5Å GaInAs	1.2109 eV 13.1 meV
Sheffield		1000Å InP	1.0862 eV 11.3 meV
		10Å GaInAs	0.9568 eV 7.4 meV
		1000Å InP	0.8863 eV 2.9 meV
		20Å GaInAs	0.8213 eV 5.4 meV
		1000Å InP	
		40Å GaInAs	
		1000Å InP	
		80Å GaInAs	

Sample Name	$\mu \text{ cm}^2 \text{V}^{-1} \text{s}^{-1}$ $n_s \text{ cm}^{-2} (\times 10^{12})$	Structure <sup>c</sup>	Other
Al <sub>0.3</sub> Ga <sub>0.7</sub> As-GaAs MB671 GEC	Dark @77K	0.25 $\mu\text{m}$ AlGaAs 25 $\text{\AA}$ GaAs 125 $\text{\AA}$ $\times 10$ AlGaAs 25 $\text{\AA}$ $\times 10$ GaAs 0.5 $\mu\text{m}$ AlGaAs 500 $\text{\AA}$ GaAs Si doped $5 \times 10^{15}$	More than one well observed in the PL 1.7411 eV 1.7014 eV 1.6519 eV
Al <sub>0.3</sub> Ga <sub>0.7</sub> As-GaAs MB672 GEC		0.25 $\mu\text{m}$ AlGaAs 25 $\text{\AA}$ GaAs 125 $\text{\AA}$ $\times 10$ AlGaAs 25 $\text{\AA}$ $\times 10$ GaAs 0.5 $\mu\text{m}$ AlGaAs 500 $\text{\AA}$ GaAs Si doped $5 \times 10^{15}$	1.6665 eV 1.6633 eV 10.7 meV

a Results from Al-Dubuni (1987)

b  $n_d - n_a$  (cv) @ 297 K

c Growers expected structure

**Table 2.2** Quantum Well samples used in this work

### III LUMINESCENCE FROM BULK III-V SEMICONDUCTORS

	<u>Page</u>
3.1 GaAs	47
3.2 InP	50
3.2.1 Polariton Emission in InP	54
3.2.2 Mg doping of MBE InP	60
3.2.3 The 1.36 eV emission in InP	63
3.3 $\text{Al}_x\text{Ga}_{1-x}\text{As}$	63
3.4 $\text{Ga}_{0.47}\text{In}_{0.53}\text{As}$	67
3.5 Summary	71

#### 3.1 GaAs

GaAs is one of the most technologically important semiconductor materials as is evident by its use in many different applications, consequently it is the most researched of all the III-V compounds. Many books and reviews exist detailing the different aspects of its material and semiconductor properties (see for example Blakemore 1982, GaAs Inspec). An early review and development of the theoretical description of photoluminescence by Williams and Bebb (1972) was firstly successfully applied by them to the different transitions observed in GaAs. However, the myriad of transitions observed in the near band-edge luminescence high purity, lightly doped, GaAs still required explanation (figure 1.3). Heim and Hiesinger (1974) approached this problem by relating spectra from the complementary techniques of photoluminescence, PLE and photoconductivity (PC) to identify unambiguously the excitonic transitions in n- and p- type GaAs. Since there is a small chemical shift between donors in GaAs photoluminescence proved unsuitable for assigning these impurities, but the binding energy of shallow acceptors could be estimated principally from the free-to-bound or donor-acceptor-pair emission. A systematic characterization of the incorporation of acceptors and their binding energies in VPE and LPE GaAs was completed by Ashen et al (1975). Undoped GaAs epilayers grown by different techniques show the same transitions with the emission modified by the dominant impurities incorporated during growth. The discussion here will be restricted to MBE grown material for which Heiblum et al (1983) and others have shown Heim and Hiesinger (1974) assignments are still valid (see table 3.1).

In MBE grown GaAs the dominant residual impurity is normally a carbon acceptor so undoped layers are normally p-type in character with emission in the ( $D^0, A^0$ ) region dominating. However, recent refinements in the growth

<u>Transition (eV)</u>	<u><math>\Delta E</math> (meV)</u>	<u>Assignment</u>
1.5153	-0.3	(F,X) <sub>n=1</sub> upper polariton branch
1.5150	0.0	(F,X) <sub>n=1</sub> lower polariton branch
1.5150-1.5146		(D°,X)*
1.5141	0.9	(D°,X)
1.5133	1.7	(D <sup>+</sup> ,X) or (D,h)
1.5128	2.2	(A°,X) <sub>j=0.5</sub>
1.5124	2.6	(A°,X) <sub>j=1.5</sub>
1.5122	2.8	(A°,X) <sub>j=2.5</sub>
1.5108		two electron transition of a free exciton recombinig in the vicinity of a neutral donor

**Table 3.1** Standard assignments used for the transitions in the excitonic region of GaAs after Heim and Hiesinger (1974)

technique and careful choice of the As<sub>4</sub> source have produced material that is residual n-type with an impurity level of  $\sim 10^{13} \text{ cm}^{-3}$  (Elman et al 1987). The excitonic recombination region for a GaAs epilayer grown at GEC is shown in figure 3.1. The epilayer was doped with silicon to  $5 \times 10^{15} \text{ cm}^{-3}$  so consequently the transitions observed are not as resolved as those shown in figure 3.1. This sample shows the typical bulk luminescence seen at this doping level before material of the same quality was incorporated into a multiple quantum well (MQW) structure. A full discussion relating the luminescence observed from this bulk sample and others to the quasi-two-dimensional luminescence from a multiple quantum well structure is given in section 5.4.1. A qualitative description of the transitions is given here with reference to table 3.3 we can assign the transitions in the excitonic region accordingly. The  $(F,X)_{n=1}$  transition is observed at 1.5150 eV, the structure to higher energy in the exciton-polariton emission is discussed in section 3.2.1. As expected, since the epilayer is doped, donor related transitions dominate,  $(D^+,X)$  at 1.5141 eV is observed as a shoulder on the  $(D^+,X)$  and  $(D^+,h)$  emissions, but it is difficult to discern separate transitions in the peak region due to impurity broadening. An average full width at half maximum over these convoluted, unresolved emissions is relatively meaningless. The splitting of the acceptor related emission  $(A^+,X)$  at 1.5129 eV and 1.5122 eV is due to j-j coupling of the participating states. An unresolved band due to two electron transition leaving the donor in an excited state is centred at 1.5108 eV.

More information can be derived from the emission in the  $(D^+,A^+)$  region, figure 3.2. The insert in this figure shows the relative positions of the near band-edge excitonic emission to that of the  $(D^+,A^+)$  region. The  $(D^+,A^+)$  emission was taken under weak excitation so only transitions due to saturated distant pairs are observed. The amphoteric nature of silicon is clearly visible even at these low

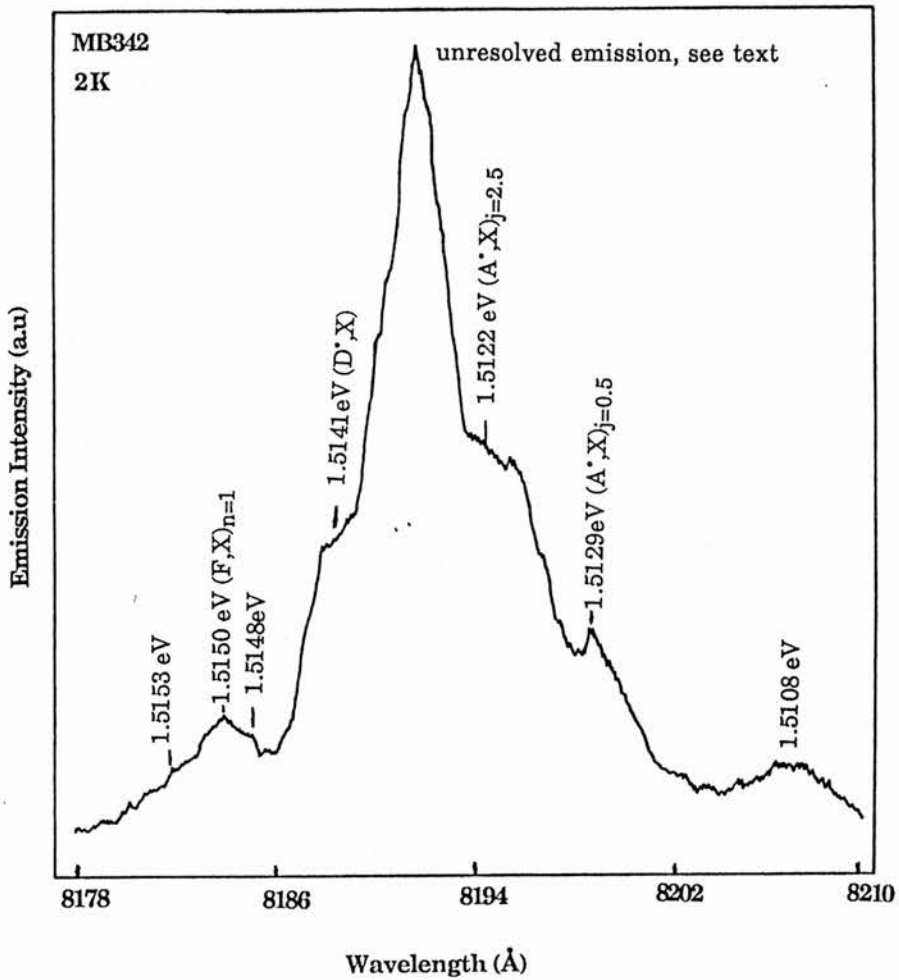


**Figure 3.1** Typical luminescence emission from the excitonic region of MBE grown GaAs used in this work,  $(N_d - N_a) \sim 5 \times 10^{15} \text{ cm}^{-3}$ . Transitions are assigned as in table 3.3.

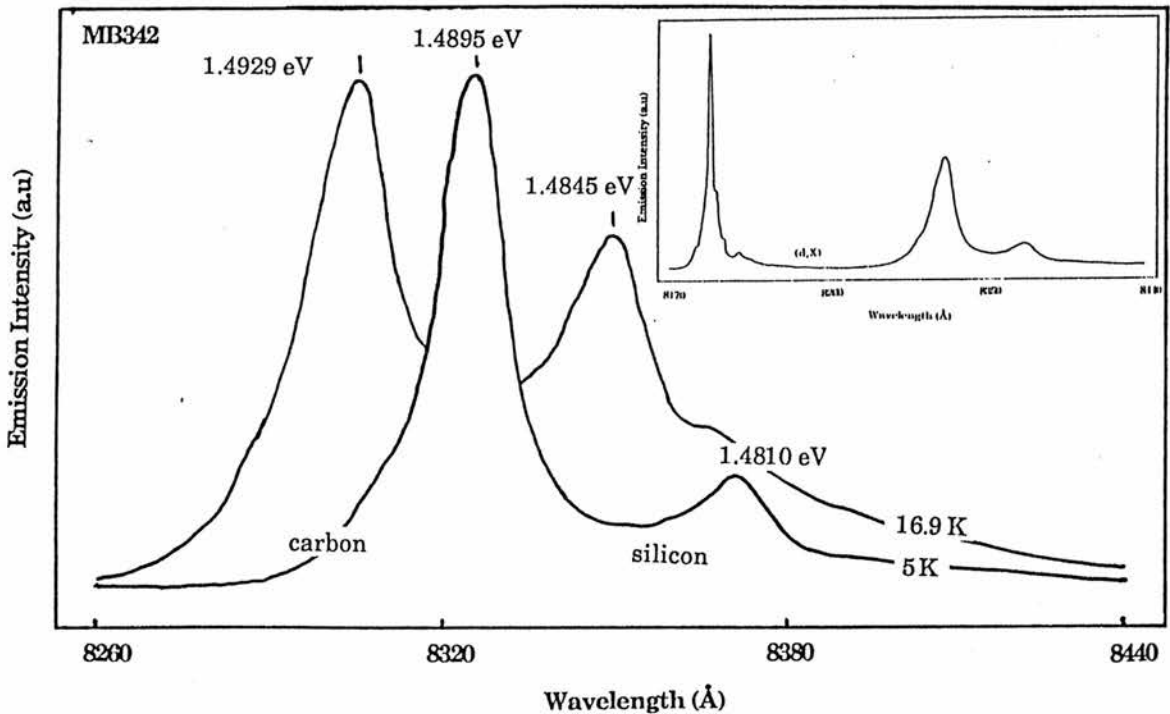


**Figure 3.2** The  $(D^*,A^*)$  region of the GaAs emission clearly shows the amphoteric nature of silicon by the existence of emission at 1.4810 eV. The insert shows the relative position of the excitonic and  $(D^*,A^*)$  region.

### III Luminescence from Bulk III-V Semiconductors

doping levels because apart from residual carbon ( $D^{\circ},A^{\circ}$ ) emission at 1.4895 eV, the transition at 1.4810 eV due to a silicon ( $D^{\circ},A^{\circ}$ ) is observed. As the sample temperature is increased thermalisation of donors means that the ( $D^{\circ},A^{\circ}$ ) transition quenches and that ( $e,A^{\circ}$ ) transitions dominate at 1.4929 eV and 1.4847 eV for carbon and silicon, respectively. Assuming a value of 1.5192 eV for the GaAs band-edge the acceptor binding energy for the impurities can be estimated accordingly,  $E_a=E_g-(e,A^{\circ})$ , for carbon  $E_a=26.3$  meV and for silicon  $E_a=34.5$  meV.

For MBE grown GaAs the luminescence can have some features that are peculiar to this growth technique. This was first observed as structure in the 1.511-1.500 eV region ((d,X) region in figure 3.2) and has become known as the Kunzel-Ploog (KP) lines (Kunzel and Ploog 1980). They were most likely to occur when GaAs is grown from  $As_4$  species, substrate temperatures  $<600^{\circ}C$ , doping levels  $<10^{15} \text{ cm}^{-3}$  and were dominated by the unpolarised g-line at 1.511 eV. The sharpness of the emission lead Kunzel and Ploog (1980) to assign the transitions to recombination of defect-induced bound excitons since on reducing the point defect density associated with particularly Ga vacancies the emission disappeared. The KP lines have become the subject of much research and speculation; Reynolds et al (1984) suggested that it was a consequence of preferential pairing of silicon and carbon, whereas Eaves et al (1984) interpreted the structure as due to excitonic recombination at a pair of shallow acceptors. Later work by Skolnick et al (1985) showed that up to 60 transitions occurred in two groups as determined by their respective polarization. They assigned the emission to defect pairs caused by their preferential orientation because of the inequivalent planar growth of [110] and  $[\bar{1}\bar{1}0]$  directions in the zincblende lattice. An additional emission was also observed in the 1.47-1.49 eV region and a considerable research effort by different groups has tried to prove a correlation with the KP lines (see for example, Contour et al 1983). Many different

explanations and models have been proposed for the origin of this luminescence band.

#### 3.2 InP

It was not until the beginning of the 1970's that sufficiently pure InP became available to allow photoluminescence measurements to become a viable proposition for characterizing its band-edge. Early on, as would be expected, a direct correspondence between the transitions observed in GaAs and InP was noted (White et al 1974). Previous work by White et al (1972) looked at the incorporation of group II acceptors by observing the two hole ( $A^*$ ,  $X$ )<sub>n=2</sub> transitions, their results suggested a deviation for exciton acceptor binding energy from Haynes rule. An accurate measurement of the free exciton energy was made using reflectivity yielding a value of 1.4185 eV (Evangelisti et al 1974). Most of the later optical characterization of InP was dominated by the group at RSRE, Malvern and in the samples grown by VPE. They used resonant SPL techniques to identify residual acceptor impurities from their two hole excited states (Dean et al 1979) and the near band-edge excitonic transitions were labeled using a combination of PL, PLE and PC spectra (Skolnick and Dean 1982). This work was extended with FIRPC and the use of magnetic fields to identify silicon as the dominant impurity in VPE grown InP (Dean and Skolnick 1983).

The growth of InP by MBE proceeds in an analogous fashion to that of GaAs (section 2.1). Normally an InP substrate is brought up to growth temperature using an over pressure of P<sub>2</sub>, non-congruent sublimation is more critical in InP and occurs at lower substrate temperature than in GaAs. Once the oxide has desorbed and a stable (2x4) reconstruction surface obtained, growth can commence. When using an elemental source of red phosphorous the principal donor impurity was found to be sulphur with the residual concentration being

dependant on the magnitude of the phosphorous flux (Martin et al 1985). Consequently, InP epilayers are normally grown with a minimum P over-pressure. However, there is a tendency to form In rich surfaces if growth conditions are not carefully monitored. All early photoluminescence work was completed on refined VPE and as other growth techniques improved similar near band-edge luminescence was observed. The exception to this appears to be solid source MBE grown InP material where the free excitonic emission in some instances appears stronger than that of the bound exciton emission. This is difficult to explain since the higher residual impurity concentration in these materials would act to make free exciton emission more difficult to observe. The luminescence spectra shown here were from samples grown at two laboratories: Sheffield University using an VG V80H machine and at Glasgow University using a home-built reactor. As yet, no detailed analysis of the luminescence from solid source MBE grown InP has been presented in the literature.

A typical luminescence spectra for good quality undoped ( $n \sim 2.1 \times 10^{15} \text{cm}^{-3}$ ,  $\mu = 43340 \text{ cm}^2 \text{V}^{-1} \text{s}^{-1}$  @ 77K) MBE-grown InP is shown in figure 3.3. Increasing the detector sensitivity over the ( $D^0, A^0$ ) region shows the existence of residual acceptor emission. On increasing the excitation power density the 1.3797 eV peak shifts to higher energies and the shoulder at 1.3838 eV becomes a well resolved peak, this labels the emissions as due to ( $D^0, A^0$ ) and ( $e, A^0$ ) transitions, respectively. The ( $e, A^0$ ) emission at  $\sim 1.3840$  eV was found to occur in InP samples grown at three different laboratories (Sheffield, Glasgow and British Telecom). It would be easy to assume that this transition was due to a carbon acceptor analogous to that observed in GaAs. For this reason Tsang et al (1982) suggested that the emission they observed in MBE grown material at 1.3850 eV was due to carbon. However, this may not be the case, since carbon has not been observed as residual impurity in any other growth technique. Moreover, when

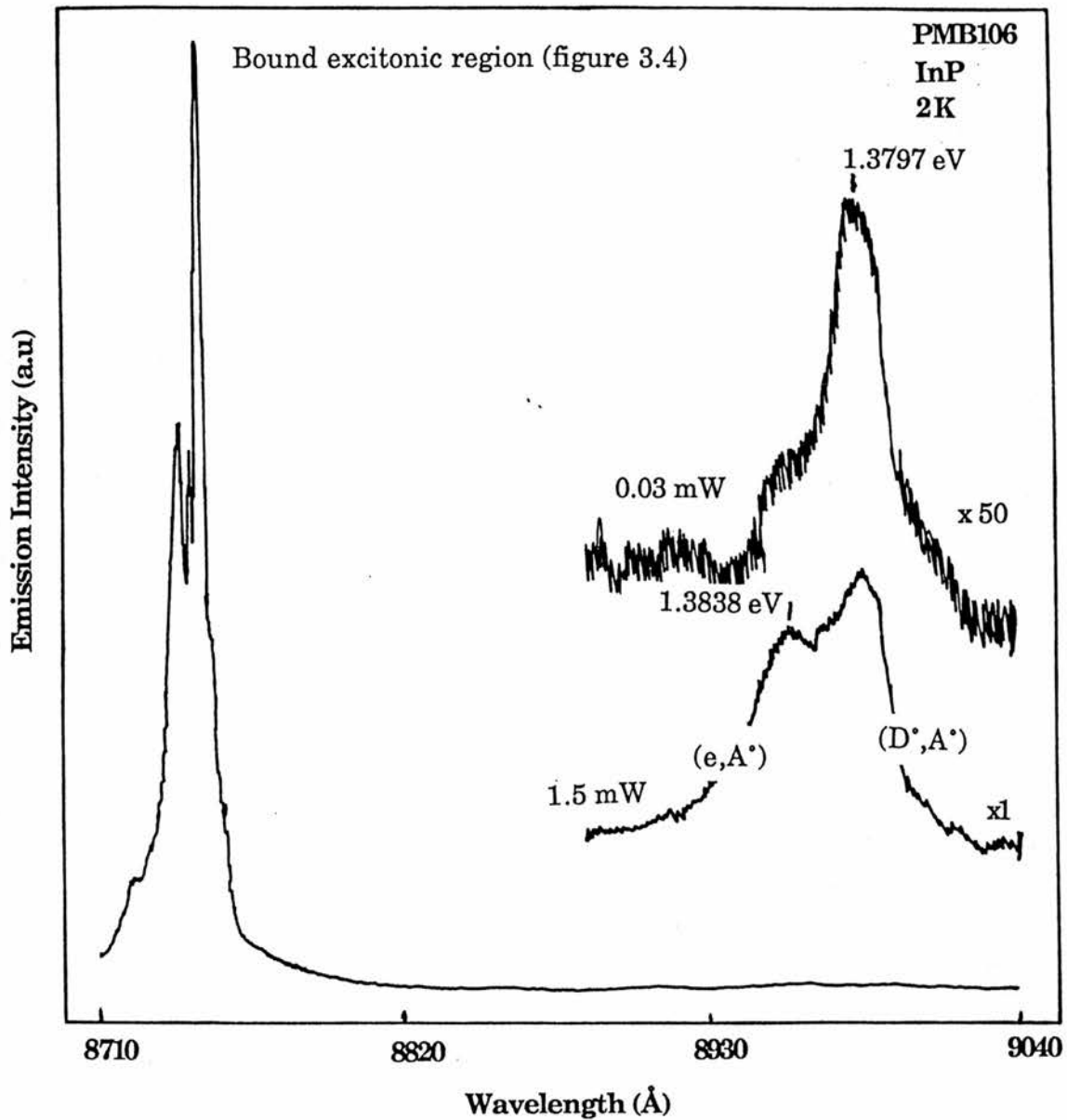


**Figure 3.3** Near band-edge luminescence spectrum for a typical MBE grown InP used in this work showing the relative positions of the excitonic and (D\*,A\*) regions.

carbon was incorporated using ion implantation it was electrically inactive (Stromme et al 1984). If the band-edge is taken at 1.4327 eV then the unknown impurity has a binding energy of  $\sim 40$  meV. Comparing this to values for different acceptor impurity binding energies obtained using various growth techniques in table 3.2 suggests the impurity may be Be or more probably Mg since it is more naturally abundant. It was suggested by Madelung (1982) that the energetic positions of acceptor impurities may depend on growth technique however this seems unlikely when considering the uniformity in the binding energies observed in GaAs. Identification of residual impurities is of crucial importance for the improvement of sample growth. We shall discuss this further in section 3.3.2.

The structure observed in the excitonic emission for sample PMB106 is shown expanded in figure 3.4; the insert shows the same region for a high quality MOCVD sample ( $n=2.5 \times 10^{14} \text{cm}^{-3}$ ,  $\mu=131,600 \text{cm}^2 \text{V}^{-1} \text{s}^{-1}$  @ 77K). Following the standard practice we will assign the emission structure to given transitions by considering the references where it was first correctly assigned, in particular by Skolnick and Dean (1982). Compared to GaAs there is greater variation in the energetic position of transitions from sample to sample and due to different growth techniques, table 3.3. This probably reflects the greater difficulty in growing InP; any slight changes in composition, such as a P vacancy, would change the dielectric constant and so be observed in the excitonic region. So with reference to table 3.3 we assign the transition at 1.4187 eV as the  $n=1$  free exciton emission  $(F,X)_{n=1}$  with the emission at 1.4212 eV from a  $n=2$  level,  $(F,X)_{n=2}$ . Using PLE and sensing at a distant  $(D^*,A^*)$  transition Duncan et al (1984) showed that the transition around 1.419 eV could be ascribed to free excitons. Continuing to lower energies the neutral bound exciton lines  $(D^*,X)$  correspond to recombination from ground and excited states to the final donor  $1s$

	Skrome et al (1984)	Kabota et al (1984)	Pomreke et al (1981)
Mg	41.0	40.4	39.8
Be	41.3	-	-
Ca	-	43.4	-
C	44.6	-	-
Zn	46.1	47.4	45.8
Comments:	Ion implanted LPE No residual C	Synthesis Solute Diffusion doped	Ion implanted VPE

**Table 3.2** Acceptor impurity binding energies in InP obtained from different growth techniques, corrected for the band-edge at 1.4237 eV.

	<u>Skolnick (1982)</u> (VPE)	<u>Zhu (1985)</u> (MOCVD)	<u>Di Forte-Poisson (1985)</u> (MOCVD)	<u>Pomkreke (1981)</u> (LPE)	<u>Tsang (1982)</u> (MBE)
(F,X) <sub>n=2</sub>	1.42230				
(F,X) <sub>n=1</sub>	1.41850 <sup>a</sup>	1.4182	1.4189	1.4187	1.4186 <sup>d</sup>
(D <sup>+</sup> ,X) <sub>n=6</sub>		1.4179			
(D <sup>+</sup> ,X) <sub>n=5</sub>	1.41806	1.4175			
(D <sup>+</sup> ,X) <sub>n=4</sub>	1.41784	1.4174			
(D <sup>+</sup> ,X) <sub>n=3</sub>	1.41738	1.4172			
(D <sup>+</sup> ,X) <sub>n=2</sub>	1.41718	1.4171			
(D <sup>+</sup> ,X) <sub>n=1</sub>	1.41693	1.4169	1.4178	1.4175	1.4174
(D <sup>+</sup> ,h)	1.41627	1.4161 <sup>b</sup>	1.4167	1.4168 <sup>c</sup>	1.4158
(D <sup>+</sup> ,X)	1.41613	1.4166 <sup>b</sup>		1.4168 <sup>c</sup>	
(A <sup>+</sup> ,X)			1.4155	1.4154 1.4136	1.4140

a) Evangelisti (1982) b) assignment reversed c) not resolved and d) unresolved shoulder

**Table 3.3** InP excitonic emission assignment used by other authors.

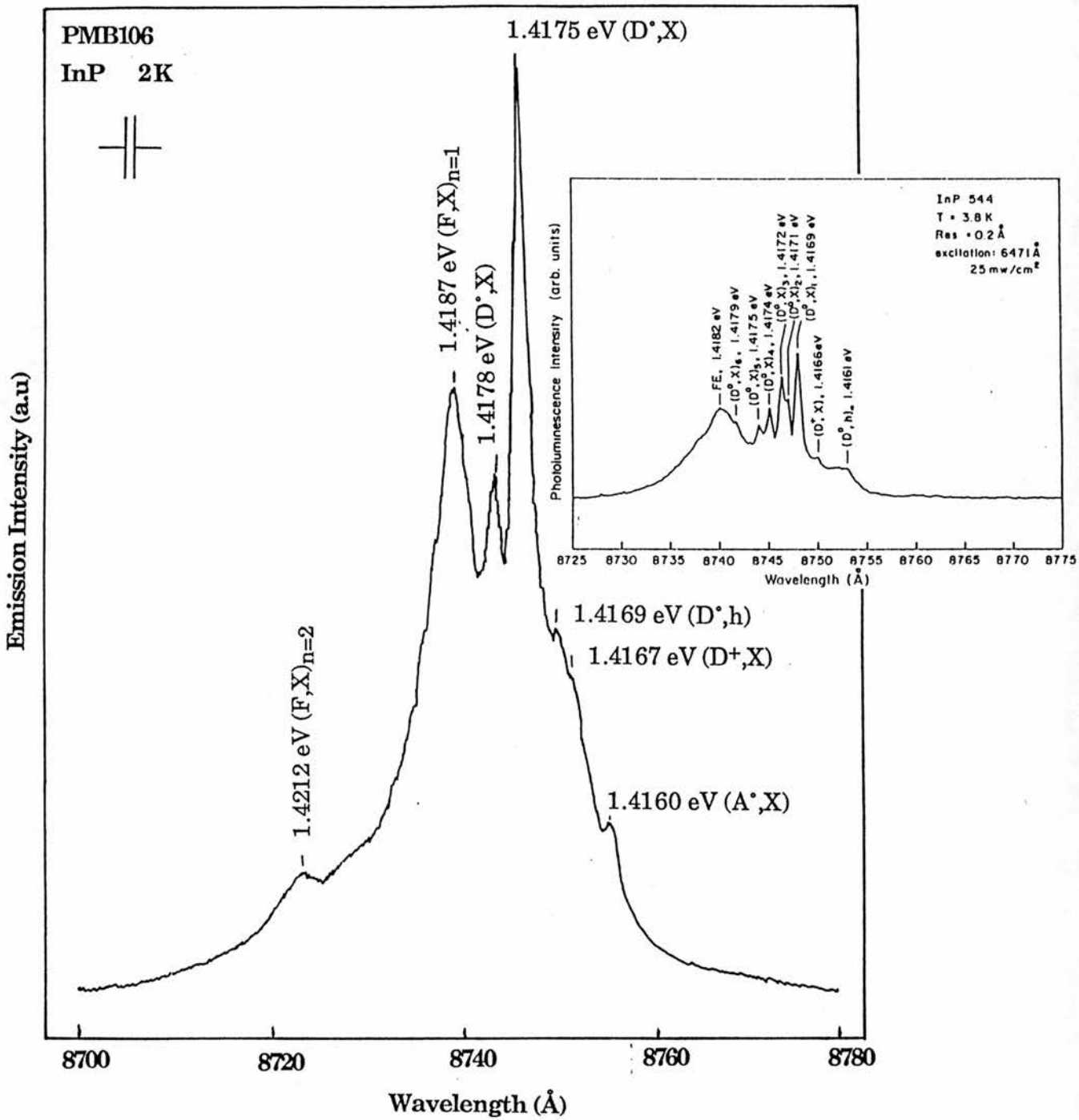


Figure 3.4 The excitonic region from figure 3.5 is shown expanded with the transitions labelled according to the text. The insert shows the luminescence from a high quality MOCVD layer (Zhu et al 1985).

### III Luminescence from Bulk III-V Semiconductors

state. In InP, unlike GaAs, separate transitions are observed for the ( $D^{\circ},h$ ) and ( $D^+,X$ ) transitions, 1.4169 eV and 1.4167 eV respectively, due to higher exciton ( $E_b=5.12$  meV) and donor ( $E_d=7.42$  meV) binding energies. At 1.4160 eV the transition is probably due to an unresolved ( $A^{\circ},X$ ) which is normally observed as a doublet in lightly doped material.

For comparison, figure 3.5 shows the luminescence from the excitonic region from samples grown at Glasgow University. The transitions are not so well resolved and the increased donor structure ( $D^{\circ},X$ )<sub>n=1-6</sub> suggests the layers have a larger residual doping level. Sample #254 shows a clearly defined fine structure with six ( $D^{\circ},X$ ) states resolved, this was exactly reproduced in all the samples screened. Particularly in the Glasgow samples, the ( $F,X$ )<sub>n=1</sub> transition at ~1.4184 eV has approximately the same emission intensity as the ( $D^{\circ},X$ ) transitions. This seems anomalous because as doping levels increase the ( $F,X$ ) transition is usually resolved as a weak shoulder on the emission spectrum since ( $D^{\circ},X$ ) transitions impurity broaden and increase in intensity (in #252  $n\sim 10^{16}$  cm<sup>-3</sup>). Normally the ( $F,X$ ) transition is only fully resolved in lightly doped materials ( $n\sim 10^{14}$  cm<sup>-3</sup>), figure 1.3 and figure 3.4 insert. The low ( $A^{\circ},X$ ) emission intensity in these spectra shows that sample compensation ratio should be low if it is assumed that the ratio is proportional to the intensity ratio of ( $A^{\circ},X$ ) to ( $D^{\circ},X$ ). If ( $A^{\circ},X$ ) had been better resolved it would have been possible to complete some SPL measurements to identify the residual acceptor impurity. Variable power measurements on sample #252 appear to indicate that the emission at 1.4184 eV is excitonic in nature (figure 3.6, section 3.2.1) thus an explanation for the enhanced ( $F,X$ ) emission may come from considering the exact nature of the excitonic luminescence.

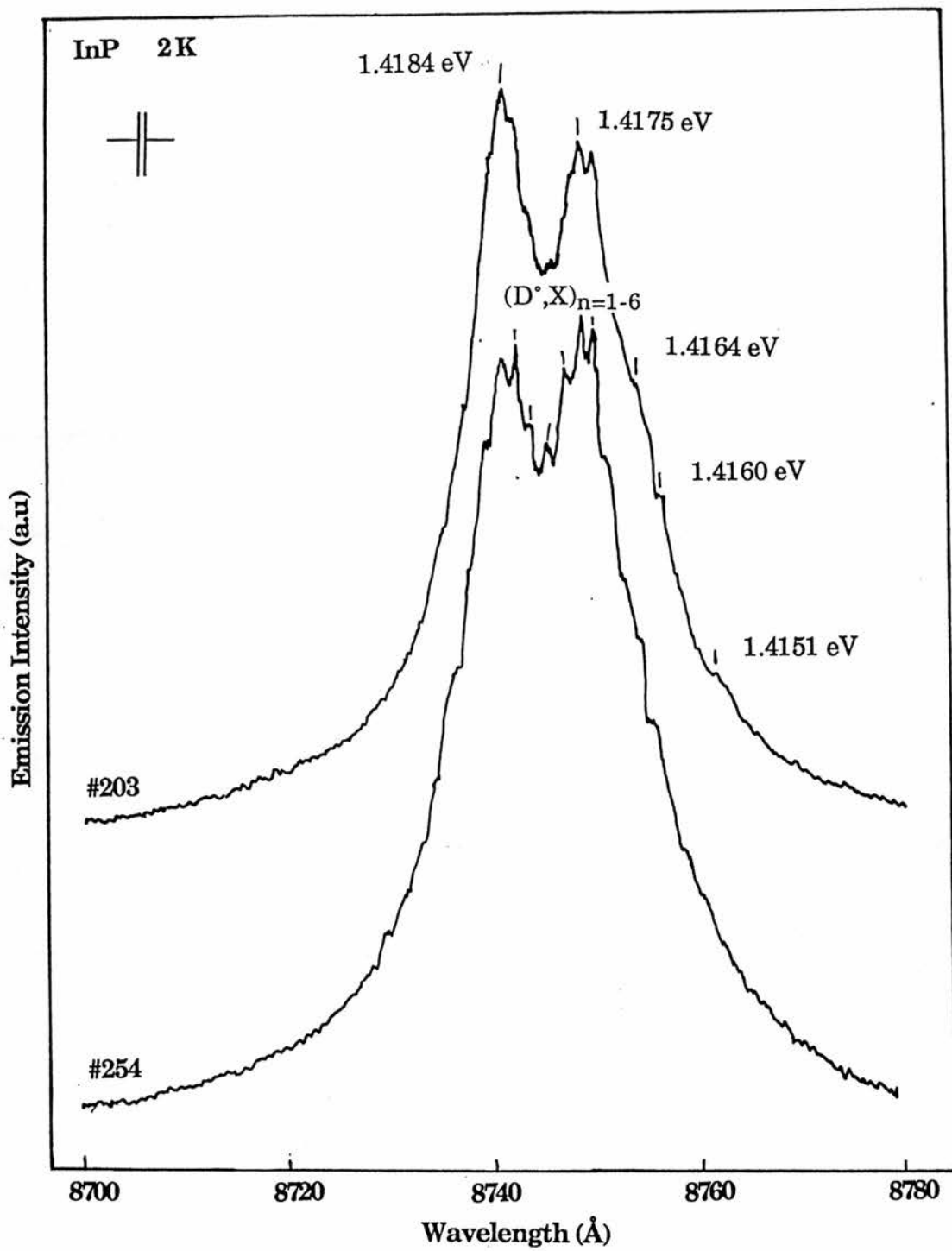


Figure 3.5 The excitonic region for Glasgow grown samples, #203 is undoped and #254 should be Mg doped, see section 3.3.2

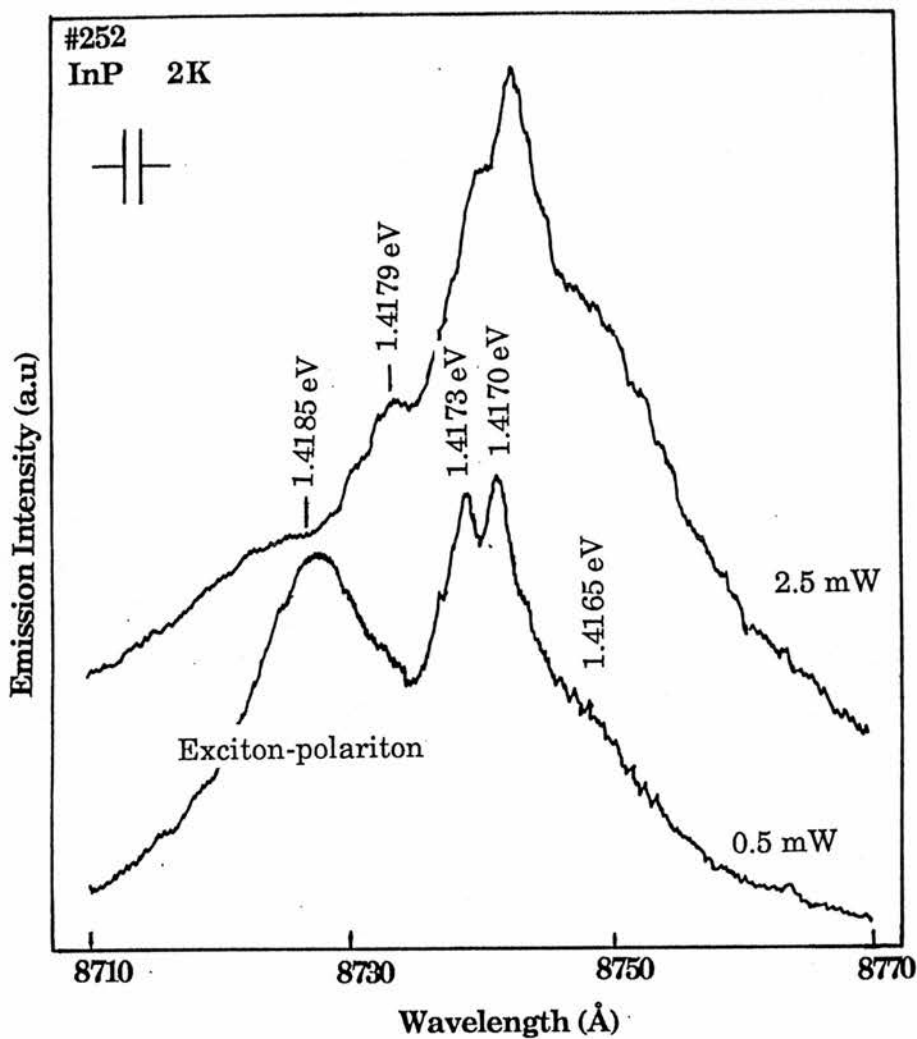


Figure 3.6 As the laser power density is increased the polariton-excitonic emission at 1.4185 eV changes in to a region that appears to be absorbing.

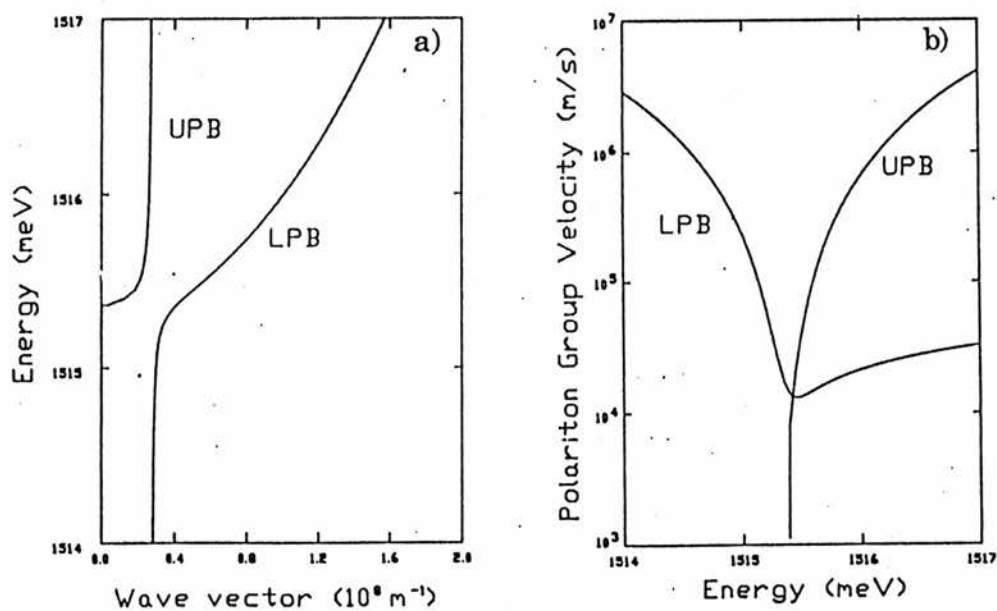


Figure 3.7 a) The polariton dispersion curve for GaAs calculated using equation 3.1. The upper and lower polariton branches are labelled UPB and LPB, respectively. b) Mode group velocity as a function of exciton-polariton energy for both branches (Steiner et al 1985).

### 3.2.1 Polariton Emission in InP

Of interest to us is the interaction between the dipole active exciton and photons of the same energy first considered in detail by Hopfield (1966). The coupling results in a mixed mode excitation called a exciton-polariton. The maximum interaction occurs at the intersection of the photon and exciton dispersion curves, figure 3.7. A gap opens between the dispersion curves resulting in a two-branch polariton dispersion curve given by

$$\left[ \frac{\hbar ck}{E} \right]^2 = \epsilon_0 + \frac{2\epsilon_0 E_{LT} E}{E_0^2(k) - E^2} \quad (3.1)$$

where  $\epsilon_0$  is the dielectric constant in the absence of polaritons,  $E_{LT} = E_L - E_T$  is the splitting between uncoupled longitudinal and transverse excitons at  $k=0$ ,  $E$  is the polariton energy and  $E_0(k) = \frac{\hbar^2 k^2}{2M} + E_T$ , the energy of the uncoupled free exciton of wave vector  $k$  is given by the transverse exciton energy  $E_T$  plus the kinetic energy. On the lower polariton branch (LPB) the polariton is essentially free exciton-like becoming photon-like at small wave vectors just below the point of inflection. The photon-like polaritons interact only weakly with the lattice and are emitted from the crystal.

An accumulation of polariton modes occur on the LPB near the inflection point due to the small density of final states in the photon-like region of the dispersion curve. The quasi-thermal equilibrium of the distribution modes at this point is termed the polariton 'bottleneck'. So the polariton dispersion relationship has a strong effect on the intrinsic lineshape of the exciton-polariton luminescence. When compared to purely excitonic emission the polariton can exhibit a low energy tail beyond the free exciton edge at  $k=0$  since the LPB does not have a minimum energy, figure 3.7. Luminescence is normally obtained when polaritons are scattered from phonons or collide with sample surface.

### III Luminescence from Bulk III-V Semiconductors

In GaAs the exciton-polariton emission can show a doublet structure or dip at the longitudinal free exciton binding energy,  $E_L$ , see figure 1.3 X(n=1) peak. This structure is not repeated in the LO phonon replica or in a second-order processes such as two-electron transitions involving neutral donors. Since these satellites are photon-like they are more representative of the actual bulk exciton-polariton mode distribution expected from the quasi equilibrium polariton population. This structure in the polariton luminescence has not been previously observed in InP. Skolnick and Dean (1982) suggested this could be a consequence of the larger surface recombination velocity in GaAs ( $\sim \times 1000$  of that of InP) producing a much higher probability for non-radiative recombination. We suggest that the structure observed in the spectra of sample #252 at 1.4185 eV is the first observation of this mechanism in InP (figure 3.6), but an explanation is required for why the singlet polariton peak forms a doublet structure with increasing pump power. This type of power dependence has only been observed previously in some slightly n-type doped GaAs samples during time dependent luminescence experiments (Steiner et al 1986).

The existence of a bottleneck region cannot by itself explain the doublet structure observed in the GaAs exciton-polariton luminescence. As any scattering enhanced by the large variation of the polariton group velocity  $v(E) = \hbar \frac{dE}{dk}$  in this region is not large enough to account for it (figure 3.7). A number of different explanations have been proposed for the interpretation of the physical mechanisms causing the structure observed. These include, emission from both polariton branches, intrinsic absorption due to phonons and exciton-electron scattering on the surface. A surface electric field has been found to influence the structure observed in the lineshape accounted for by field-ionised excitons (Schultheis and Tu 1985). Recent experimental and theoretical work interpret the effect as due to exciton-polariton scattering from neutral donor

impurities in the bulk crystal (Lee et al 1985) and further time resolved luminescence experiments appear to support this interpretation (Steiner et al 1986). We will show that the observation in InP is consistent with this interpretation with the spatial distribution of the polariton modes at the surface the most important parameter. Weisbuch and Ulbrich (1979) and others have shown that there was a strong correlation between polariton luminescence, its spatial distribution in the crystal and the density of surface states present. Weisbuch and Ulbrich (1979) enhanced the polariton effect by resonantly exciting at  $E_L$  and observing the luminescence from the back surface of the GaAs sample. Since no structure is observed in the bulk second order processes, this also suggests that the phenomenon is in some way surface related. So the description of polariton luminescence is a transport problem of considerable complexity since the resultant lineshape does not necessarily reflect the polariton distribution in the crystal.

Lee et al (1986) showed that if MBE grown GaAs samples were ordered according to the relative intensity of the  $(h,D^*)$  transition this would determine relative donor concentrations. The donor concentrations were  $\sim 10^{15} \text{ cm}^{-3}$  but no independent electrical measurements were taken due to contact problems. By assuming that the acceptor concentration was constant, the exciton polariton lineshape was found to change from a doublet to a narrower more symmetric singlet as donor concentration decreased. In this way they correlated the existence of the polariton structure as due to the modification of the polariton distribution in the presence of donors as the modes move towards the surface. The process modifying the exciton-polariton lineshape was based on elastic scattering of the exciton-polariton from neutral donor impurities assuming that this process in turn increased the probability of an occurrence of inelastic process. A theoretical calculation showed the neutral donor scattering cross

section for polaritons has a peak in the bottleneck region, figure 3.8. This enhancement of scattering cross section does not occur for the bare exciton because its dispersion and group velocity dependence are different. The spatial distance the modes travel before it reaches the sample surface must therefore be greater than the scattering length otherwise no modification occurs. Steiner et al (1986) again showed that the presence of donors was necessary for any polariton structure to be observed. Time resolved measurements assumed that the process of elastic scattering from neutral donors caused a delay of a polariton appearing at the surface causing a dip. Time dependent intensity measurements showed the luminescence took longer to build up in the dip region. The interpretation of their results showed clearly the spatial distribution of the polaritons was most important.

For a sample under cw excitation the observed polariton photon intensity can be given by the equation

$$I(E) = \sum_{b=1}^2 T_b(E) F_b(x=0,E) v_b(E) \sigma_b(E) \Delta\Omega_b(E) \Delta E \quad (3.2)$$

where  $b$  is the branch index,  $T_b(E)$  is the transmission coefficient of the polariton at the crystal boundary with air,  $F_b(x=0,E)$  is the polariton distribution function at the sample surface,  $v_b(E)$  is the polariton group velocity,  $\sigma_b(E)$  is the density of states and  $\Delta\Omega_b(E)$  is the solid angle through which the luminescence is emitted. The solution of this equation requires a distribution function  $F_b(x,E)$  to be known as the space-energy relaxation function has a dominant effect on the luminescence state (Tranikov and Krivolapchuk 1983). Since,  $T_b(E)$  is given by geometrical considerations and in a spherical approximation  $\sigma_b(E)v_b(E)=(2\pi\hbar)^{-1}k_i^2$  is almost constant except in regions of strong variations of  $k_i^2$ . The distribution function is completely unknown but qualitative results suggest no

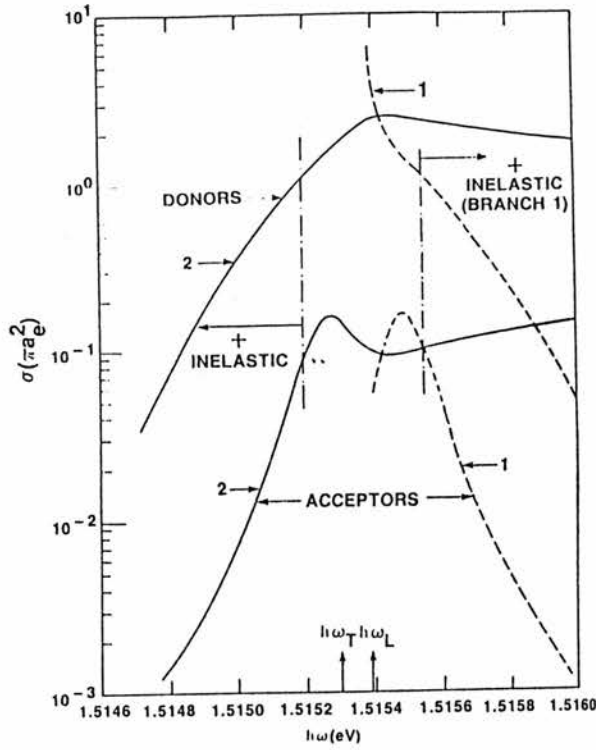


**Figure 3.8** The elastic scattering cross section of exciton-polaritons (in units of  $\pi a_e^2$ ) from neutral acceptors and donors in GaAs as a function of the exciton-polariton mode energy,  $\hbar\omega$  (in eV). The upper and lower polariton branches are labelled 1 and 2, respectively  $\hbar\omega_T$  and  $\hbar\omega_L$  are the transverse and longitudinal exciton energies. The dash-dot vertical lines delimit the energy range for each branch from which elastic scattering is dominant (Lee et al 1985).

great dependence on functional form (Steiner et al 1986). The main simplification in selecting a distribution function is to consider LPB only and assume the function is a product of spatial  $n(x)$  and energy  $f_1(E)$  distribution functions,  $F_1(x,E)=f_1(E)n_b(x)$ , with the spatial distribution given by

$$n_b(x) = \frac{1}{L_0 - L_1} [\exp(-x/L_0) - \exp(-x/L_1)] \quad (3.3)$$

where  $L_0$  is the characteristic generation length of free carriers by the incident light and  $L_1$  is the surface recombination length at the surface that depletes carrier concentration and hence reduces polariton density near the surface. The energy distribution  $f_1(E)$  is independent of coordinate and assuming equilibrium it should peak in energy near the bottleneck region. Hence the observation of polariton structure in InP should be explained by considering the spatial part of the distribution function.

The key to understanding must come from considering why structure is normally observed in GaAs polariton emission and not in InP. Since the absorption coefficient of GaAs and InP is similar, for the same laser pump wavelength, then  $L_0$  would be around the same value. So it must be assumed that surface recombination is the parameter that controls the observation of structure in the polariton luminescence. In GaAs if  $L_1$  is reduced by cleaving in a vacuum to reduce the number of surface states present the polariton structure disappears. Subsequent contamination of the sample surface in air, thus increasing the density of surface states and hence  $L_1$ , sees the reappearance of the structure (Fischer and Stolz 1982). Casey and Beuhler (1977) explained the observation of higher luminescence intensities in InP compared to GaAs as due to much reduced surface recombination velocity in InP. They also noted that Au contacts on n-type InP showed a different distribution or density of surface states compared to other n-type materials such as GaAs. Less surface states may be

seen in InP if there is a greater tendency for the surface to form compensated acceptor/donor pairs. Recently, in LEC samples, Lester et al (1988a) showed the low surface recombination velocity could result in self absorption of the near band-edge luminescence. Intuitively Skolnick and Dean (1982) suggested that no structure was observed in VPE grown InP as a consequence of the reduced surface recombination velocity. This is true if it is assumed the surface recombination velocity is proportional to surface recombination length, hence  $L_1$  is lower in InP compared to GaAs. Now that polariton structure is observed in MBE grown InP (figure 3.6) suggests that  $L_1$  is increased and a higher density of surface states exists compared to that obtained by other growth techniques. This may be related to the defect associated luminescence observed as the 1.36 eV transition in InP since Tranikov and Krivolapchuk (1983) showed there was a correlation between the polariton luminescence and defects in the bulk crystal. This is evident from the difference in the luminescence of the excitonic region of solid source MBE grown InP compared to that of other growth techniques (figure 3.4). The increased polariton emission suggests there may be some enhanced scattering of the exciton-polariton mode producing a greater number of photons that escape the crystal. Obviously further work must be completed to find the exact mechanism responsible. Since an increase in recombination velocity occurs when Ge surfaces were sand blasted (Smith 1978) it may be useful to repeat a similar process with InP to see if polariton structure occurs, in samples grown by other techniques, as a consequence.

Since no polariton structure is observed at low powers this suggests that the peak of the polariton distribution occurs at distances shorter than the neutral donor elastic scattering length  $L_{ds}$ . A similar argument can be used when  $L_1$  is reduced. An estimate of  $L_{ds}$  can be made using  $L_{ds} = \frac{1}{N\sigma_{ds}}$  where  $N$  is the residual donor concentration and  $\sigma_{ds}$  is the scattering cross section. If we

assume that  $\sigma_{ds}$  for InP is similar to that of GaAs, the value of  $\sigma_{ds}$  determined from figure 3.8 to be  $7.698 \times 10^{-16} \text{ m}^2$ , for a residual concentration of  $10^{16} \text{ cm}^{-3}$  for sample #252 gives  $L_{ds} = 0.650 \text{ }\mu\text{m}$ . For InP the extinction coefficient  $k(\nu)$  is 0.431 at  $0.5298 \text{ }\mu\text{m}$ , the laser wavelength. The absorption coefficient  $\alpha(\nu) = \frac{4\pi k(\nu)}{\lambda}$  and at this wavelength is  $\sim 1 \times 10^7 \text{ m}^{-1}$ . Hence assuming an exponential absorption, the penetration depth of the laser light into the crystal is  $0.110 \text{ }\mu\text{m}$  if 95% of the light is absorbed. But the diffusion length of the minority carrier determines the depth from which the luminescence is emitted, in this instance  $L_p = (D_p \tau_p)^{0.5}$ , where  $D_p$  is the hole diffusivity and  $\tau_p$  is the hole lifetime. Normally values of  $1.5\text{-}2.0 \text{ }\mu\text{m}$  are found for InP but recent measurements indicate that due to the large internal quantum efficiency in InP recycling may occur increasing  $L_p$  (Lester et al 1986b). Increasing the excitation power must shift the bulk of the polariton modes beyond  $L_{ds}$  by increasing the carrier profile depth (Williams and Bebb 1975) and neutralising donor impurities, hence scattering occurs and structure is observed (figure 3.6). To estimate the order of magnitude a finely balanced rate equation would need to be solved in which both surface recombination and donor concentration are important.

#### 3.2.2 Mg doping of MBE InP

The normally used p-type dopants of Zn or Cd can not be used in MBE growth of InP as their high vapour pressures means they are not incorporated on the growing surface. Both Be or Mg are expected to have unity sticking coefficients at normal growth temperatures so various groups have tried using these as p-type dopants with different degrees of success (Stanley et al 1985, Kawamura et al 1983). Mg is to be favoured as a dopant since it is relatively non-toxic compared to Be and some preliminary results show that hole mobilities may be higher. At Glasgow University a series of samples were grown where

Mg doping was attempted; sample growth parameters and some Hall data are summarized in table 3.4. Electrical measurements show the doped material is still n-type with an unchanged compensation ratio. The increased background of residual carriers can be accounted for by having the Mg cell operative. Accordingly no enhancement of the intensity of the ( $A^{\circ},X$ ) luminescence was observed, figure 3.5, sample #254. So, doping with this Mg source used does not appear to have been successful. Although if any incorporation of Mg did occur it would be best observed in the ( $D^{\circ},A^{\circ}$ ) region; this is discussed below.

As mentioned previously all the undoped InP layers studied showed an unidentified acceptor which had an ionization energy of  $\sim 40$  meV. In figure 3.9 typical spectra are shown for an undoped sample as its temperature is increased, the ( $D^{\circ},A^{\circ}$ ) transition at 1.3794 eV shifts to higher energies and the ( $e,A^{\circ}$ ) emission at 1.3838 eV dominates by 20K. If it were assumed that the residual acceptor impurity was due to Mg, then doping with Mg should result in an increase of intensity of the ( $D^{\circ},A^{\circ}$ ) or ( $e,A^{\circ}$ ) emissions. This does not happen; instead using this particular Mg cell a new ( $D^{\circ},A^{\circ}$ ) emission at 1.3760 eV is observed (figure 3.10). As the Mg cell temperature was increased no corresponding increase in ( $D^{\circ},A^{\circ}$ ) emission was observed indicating the doping density did not increase.

A number of conclusions can be drawn from the above observations. Firstly, since a new ( $D^{\circ},A^{\circ}$ ) emission was seen as a result of Mg doping this suggests that the residual impurity can be neither Mg or Be as both have approximately the same binding energy. If it is assumed that the new ( $D^{\circ},A^{\circ}$ ) emission at 1.3760 eV is due to a Mg acceptor with binding energy  $\sim 43.7$  meV ( $\Delta E[(e,A^{\circ})-(D^{\circ},A^{\circ})] \sim 4$  meV), then the residual acceptor impurity could be carbon. Scaling accordingly, this agrees qualitatively with the acceptor binding energies of Mg and Be in GaAs. Mg and Be have higher binding energies, 28.8 meV and

	#203	#273	#252	#254	#260
	u/d	u/d	Mg/d	Mg/d	Mg/d
$T_{mg}(^{\circ}C)$	-	-	130	150	300
$T_{sub}(^{\circ}C)$	480	360	480	480	480
Hall77K(n)	$2 \times 10^{15}$	$2 \times 10^{15}$	$\sim 10^{16}$	$\sim 10^{16}$	$\sim 10^{16}$
$\mu_{77K}$	42,700	-	>20,000	-	-
$N_a/Nd(rt)$	0.3	0.3	0.3	0.3	0.3
$N_a/Nd(77K)$	>0.3	-	-	-	-

**Table 3.4** Growth parameters for the Glasgow grown InP samples (Cheng 1988)

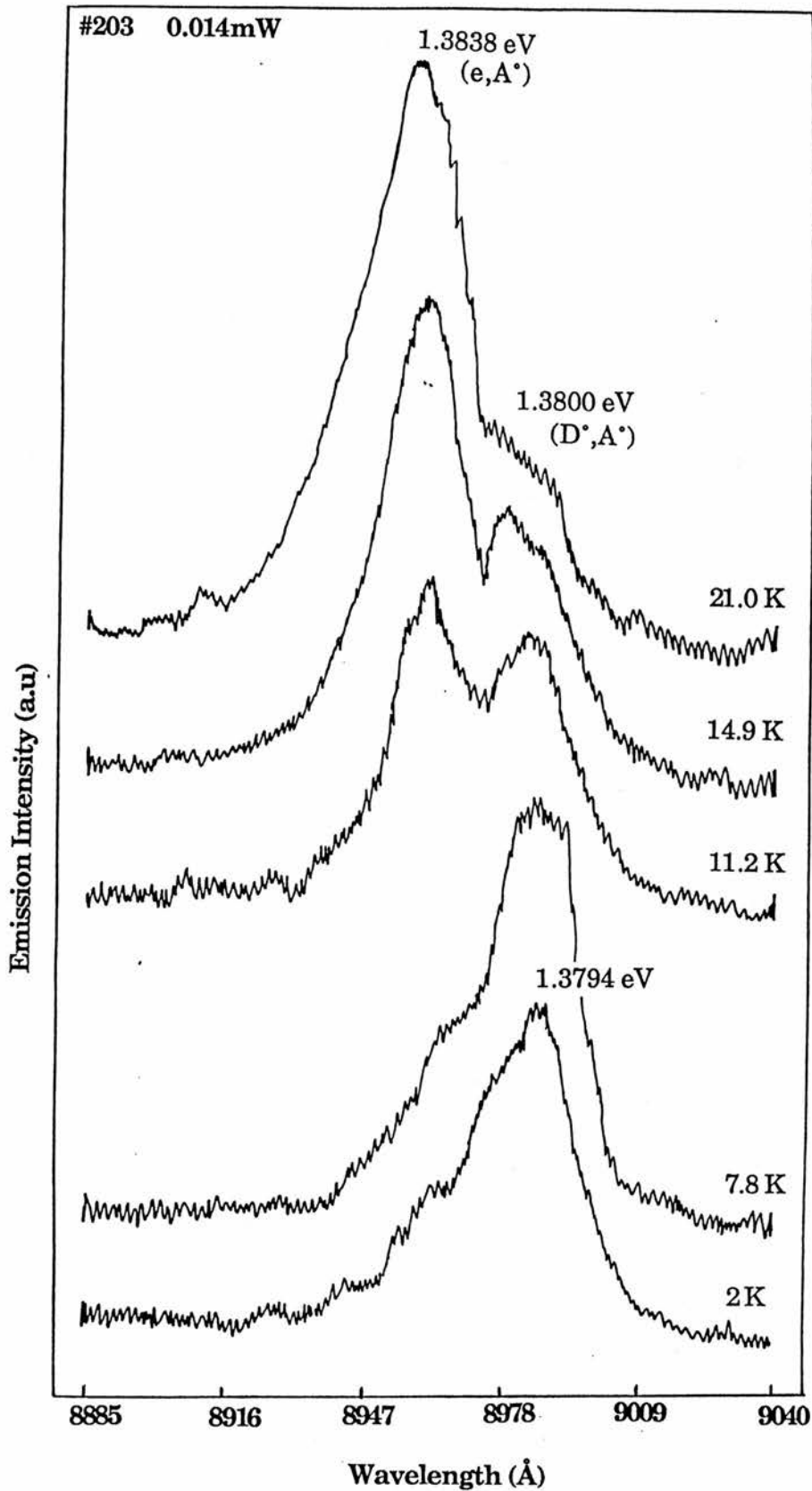


**Figure 3.9** The emission observed in this sample is typical of that observed for nominally undoped InP layers from three different laboratories. The evolution and relative intensities of the (D\*,A\*) and (e,A\*) peaks indicate that sample compensation should be low.

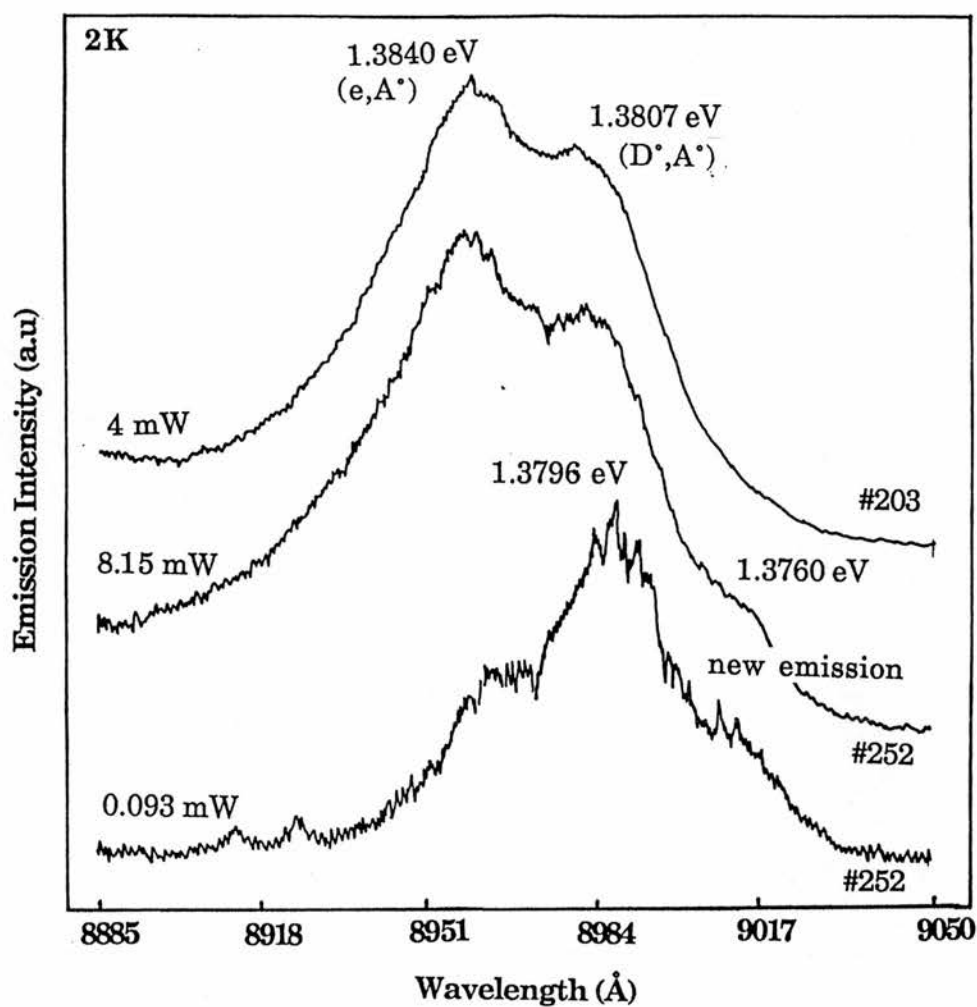


**Figure 3.10** The 1.3760 eV peak occurs as a consequence of using the Mg cell to dope the layer but may not be directly due to Mg incorporation.

### III Luminescence from Bulk III-V Semiconductors

28.0 meV, respectively, compared to carbon at 27.0 meV. However, this assignment does not correspond to the relative binding energies found by Skromme et al (1984) in their ion implanted samples (table 3.2). Unfortunately no other reference could be found where carbon was positively identified so the ion implantation results may be anomalous. Another less likely explanation for the observed luminescence is that the Mg source was contaminated before use, possibly oxidized, so the process of evaporation caused the incorporation of another impurity into the layer during growth (Cheng 1988). Thus, changing the cell temperature had no effect on this incorporation and the acceptor impurity would most likely be assigned to a carbon impurity although Ca may have to be considered as it has approximately the same binding energy, table 3.2.

The donor-acceptor compensation ratio  $\theta$  is important in determining the electrical properties of any semiconductor epilayer. The calculation of compensation ratio from variable temperature Hall measurements requires all the electron scattering processes to be taken into consideration. The estimation of  $\theta$  is a difficult problem in high purity, low compensated III-V compounds such as InP. This was completed by Al-Dubuni (1987) for the InP samples grown by Glasgow and found to be  $\theta \sim 0.3$ . Kamyia and Wagner (1977) showed that  $\theta$  could be determined by lineshape analysis of the ( $D^*, A^*$ ) and ( $e, A^*$ ) peaks in GaAs, appendix A. Luminescence was acquired under conditions of thermal equilibrium and weak excitation so that peaks are resolved and of similar intensity from 10-20 K (c.f. figure 3.9). This model was applied to InP by Pickering et al (1982) and the donor and acceptor impurity concentrations were obtained by fitting to their spectra. They showed there was a good correlation between optical and electrical compensation ratios using the method by Walukiewicz et al (1980) as long as  $\theta \leq 0.4$ . Later work by Rikken et al (1988) using

an model where all the scattering mechanisms were considered in the mobility measurements (Taguchi and Yamada 1987) yielded a better agreement.

#### 3.2.3 The 1.36 eV emission in InP

Duncan et al (1984) noticed the existence of an intense zero phonon line at 1.3608 eV as a consequence of the heat treatment of LEC InP samples. Using Zeeman spectroscopy and strain they showed that the recombination was possibly due to an exciton bound to a deep neutral donor. In figure 3.11 the same emission is observed at 1.3606 eV, just below the ( $D^0, A^0$ ) region, for sample #203. Wavefield et al (1984) found that the transition was observed only under conditions in which a depletion of phosphorous occurred in the epilayer during growth. This appears to be the case here since sample #273 grown at a lower substrate temperature shows little emission at this energy. The 1.36 eV may be ascribed to a P vacancy, probably a complex since a single vacancy would not account for the weak phonon coupling observed. Wavefield et al (1984) noted the emission was less likely to occur for samples with good morphology and electrical properties. We suggest that the modified polariton emission observed in these MBE grown layers may be connected to a P vacancy which could affect the surface state compensation and hence surface recombination properties (see section 3.3.1.).

#### 3.3 $Al_xGa_{1-x}As$

$Al_xGa_{1-x}As$  was one of the first alloys grown by MBE because of its relaxed requirement for lattice match growth onto GaAs. The growth of  $Al_xGa_{1-x}As$  is similar to that of GaAs (see chapter 2.1.4), except higher substrate temperatures (700°C) are required to increase the Al surface mobility so that there is a higher probability of growth from preferred sites. Thus, optimum  $Al_xGa_{1-x}As$  growth temperature is not compatible with that of GaAs at 580°C. A compromise

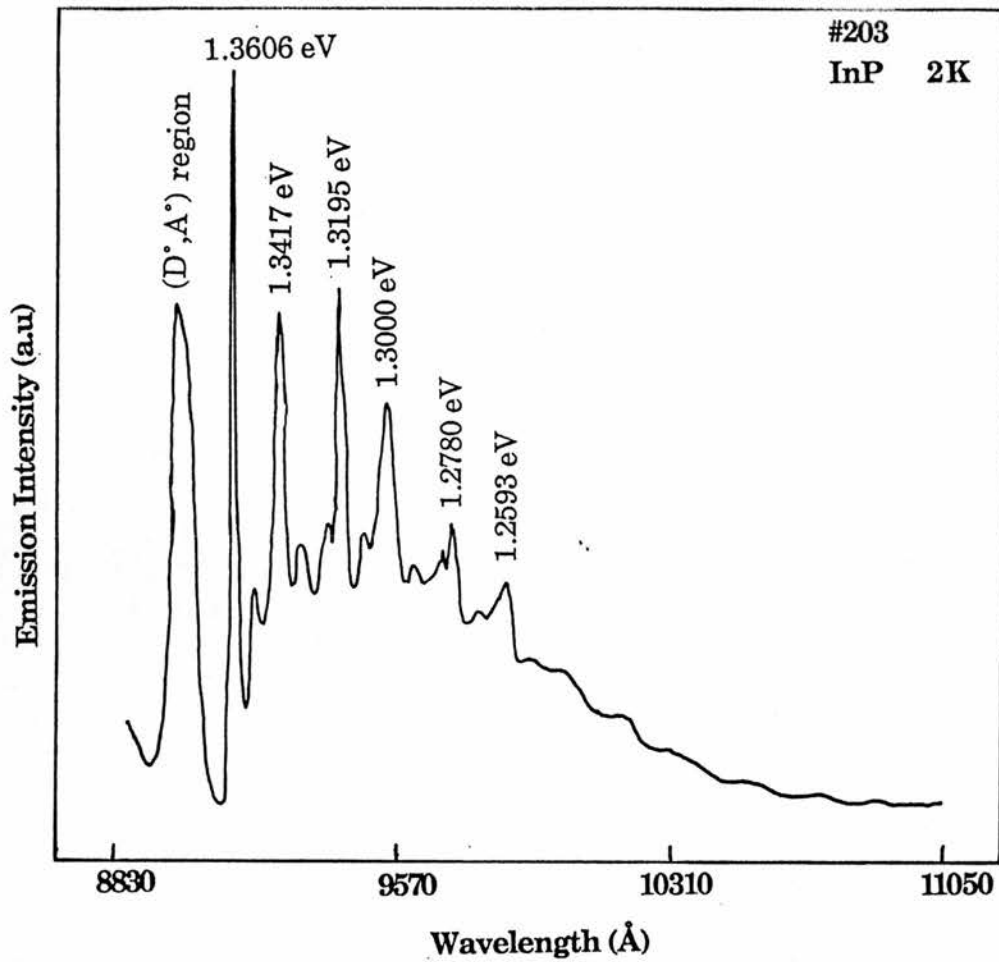


Figure 3.11 The 1.36 eV emission line complete with the weakly bound phonon replicas (Cheng 1988).

### III Luminescence from Bulk III-V Semiconductors

temperature can be used for thin superlattice structures or, alternatively, as Heiblum et al (1983) showed slowing the growth rate to 0.14 $\mu\text{m}/\text{h}$  improved the optical quality of the alloy.

As the Al content is increased from  $x=0$  in  $\text{Al}_x\text{Ga}_{1-x}\text{As}$  the transitions normally observed in GaAs broaden and move to higher energies with the increased band-gap. Around  $x=0.4$  the emission will quench as the material becomes indirect due to the  $\Gamma$ -X cross-over. The increased luminescence FWHM, of excitonic transitions, with increasing  $x$  is caused by potential fluctuations associated with the random distribution of Al and Ga on the group III cation sites resulting in alloy scattering (see section 4.3.1). This minor macroscopic variation of the band-gap energy caused by compositional variations can account for observed linewidths typically of 3 meV (Schubert et al 1984). Alloy disorder additionally results in a smearing of the band-edge similar to impurity tail states in highly doped materials. Assuming a parabolic local density of states in the conduction band of the form:

$$D(E) = \left(\frac{1}{2\pi^2}\right) \left(\frac{2m^*}{\hbar^2}\right)^{1.5} (E-E_c)^{0.5} \quad (3.4)$$

where  $m^*$  is the effective mass. Then the average density of states in the alloy is the convolution of  $D(E)$  with a gaussian function  $p(E)$  describing the randomness of the alloy at a particular composition. Hence:

$$D_A(E) = \int_{-\infty}^{+\infty} D(E-E') p(E') dE' \quad (3.5)$$

So, the normal square root dependence of the density of states is modified around  $E=E_c$  showing an exponential tail and resulting in a band-edge that is not clearly defined.

### III Luminescence from Bulk III-V Semiconductors

In figure 3.12 the luminescence from an AlGaAs layer grown at GEC is shown. Like that of the GaAs in section 3.1 this epilayer was doped to  $\sim 5 \times 10^{15} \text{ cm}^{-3}$  and the quality is typical of the barrier material used in the MQW structures. The bound excitonic emission is centred at 1.9210 eV, a slight shoulder at higher energy,  $\sim 5 \text{ meV}$ , is assigned to a free exciton. The bound excitonic lineshape is a convolution of the different excitonic transitions with a gaussian function reflecting alloy broadening at this composition. The FWHM of 4.9 meV for this doping level indicates good quality material. An estimate of the aluminium mole fraction in the layer was given by Dingle et al (1977) as

$$\text{Mole fraction} = \frac{\text{Exciton energy} - 1.512}{1.245} \quad (3.6)$$

where the energy is in eV. This expression does not include the effects of bowing or exciton binding energy so is limited in its use to  $0 < x < 0.35$ . Recently Lambert et al (1987) tested Dingle's relationship using the correlation of X-ray data for composition and 2K luminescence including a correction for excitonic binding to find  $E_g(x) = E_g(0) + 1.34x \text{ eV}$  ( $x < 0.45$ ); a slight bowing was observed. Using equation 3.6 the Al mole fraction for MB318 was estimated to be  $32.1 \pm 0.5\%$ . Compositional uniformity is always an important consideration in alloys because parameters such as a non-uniform substrate temperature or beam profile can change it. Using the excitonic emission as an indication of alloy composition and averaging across a 6 mm strip, a  $0.2 \pm 0.05\%$  variation was found again indicating good quality material grown under stable conditions. In the (D\*,A\*) region the long energy tail suggests there maybe two bands present. The unresolved emission at 1.8909 eV, in analogy to GaAs, is normally assigned to a (e,A\*) transition due to carbon, the dominant acceptor impurity species. Increasing the sample temperature from 2.2 to 20 K shifts the emission to lower energies by  $\sim 4 \text{ meV}$ . However, on increasing the incident power density the peak shifts

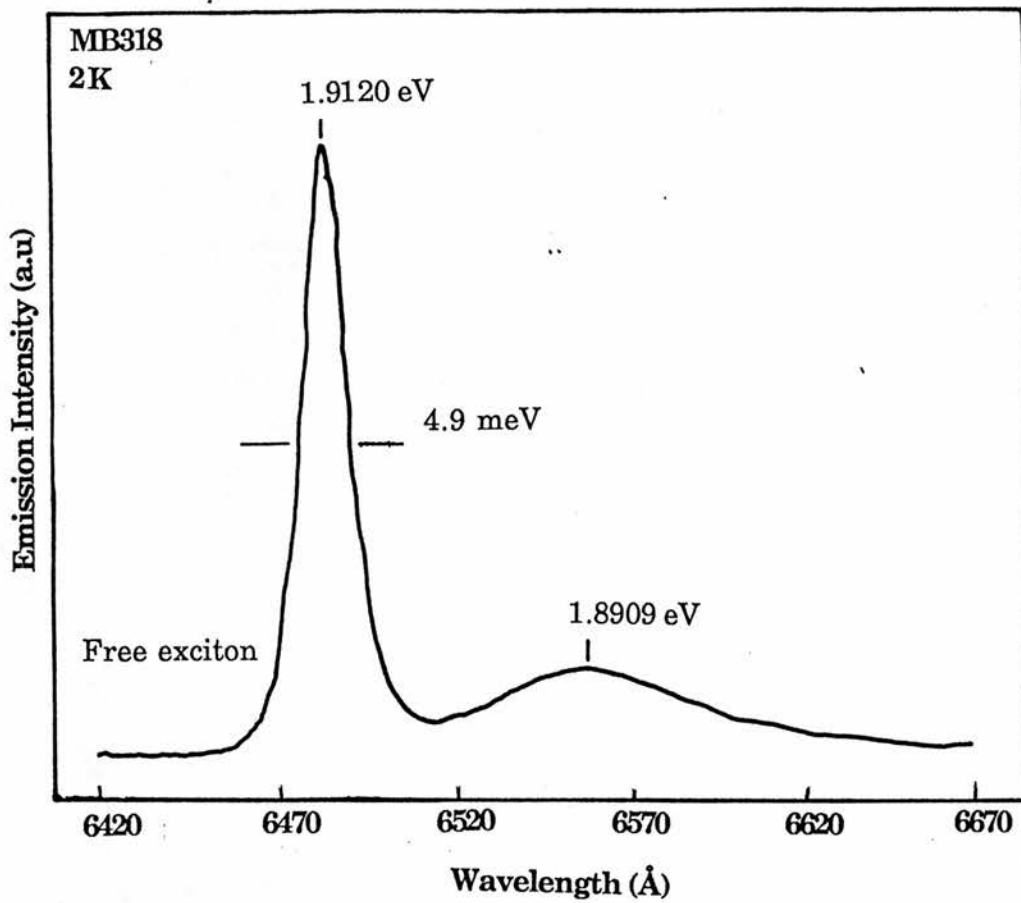


Figure 3.12 The near band-edge luminescence for an AlGaAs sample of composition  $32.1 \pm 0.5\%$  is dominated by bound exciton emission.

### III Luminescence from Bulk III-V Semiconductors

towards higher energies suggesting the emission may be a ( $D^0, A^0$ ) transition, instead.

Acceptor impurities such as carbon or silicon are expected to show a change of effective mass with increasing aluminum content and hence band-gap energy. So, according to the effective mass approximation the acceptor binding energy,  $E_a \sim m^*(x)/\epsilon(x)^2$ , should increase. Early work by Dingle et al (1977) showed the acceptor ionisation energy to be independent of  $x$  for  $0 < x < 0.35$  but they ignored the fact that the exciton binding energy varies from  $\sim 4$  meV at  $x=0$  to  $\sim 10$  meV at  $x=0.3$  (Pearah et al 1985). When this correction was later applied to their results and included in those of other authors a good correlation to the effective mass approximation was found for shallow acceptors such as carbon. For impurities such as silicon a deviation depending on the magnitude of the central cell correction occurred from the effective mass approximation (Swaminathan et al 1982). This explains why only a weak band corresponding to silicon occurs in figure 3.13 compared to the GaAs spectra, figure 3.2. But contrary to the above Schubert and Ploog (1985) used PLE to show the carbon acceptor binding energy was 25 meV at  $x=0.24$ . They also found that PLE measurements on the bound exciton emission indicated that the binding energy of the carbon-related exciton was lower than GaAs at this composition. It is expected that the exciton binding energy should increase with Al content. These results reflect the range of binding energies observed by different groups in this material and even a parameter such as the  $\Gamma$ -X crossover is still not well established, and appears sample dependent (Oelgart et al 1987).

As the aluminium content is increased above  $x=0.2$  the electrical processes in n-type AlGaAs are controlled by a deep donor level and a hydrogenic shallow donor. The origin of this deep level is still being debated, from its X-like character at some compositions it has become known as the DX centre. This

centre has been observed in the luminescence of Si doped tied to the L minima with a optical depth  $E_{DX} \sim 200$  meV (Henning and Ansems 1987). The introduction of a donor impurity should always give rise to localised levels resonant with any of the minima of the conduction band. Henning et al (1988) found the existence of four donor levels in the ( $D^0, A^0$ ) emission the deepest of which may be associated with DX centre.

#### 3.4 $Ga_{0.47}In_{0.53}As$

The ternary alloy  $Ga_xIn_{1-x}As$  grown lattice matched to InP is of growing importance in optoelectronic applications and high frequency FETs. Optimum lattice match conditions can be obtained for  $x_{Ga}=0.468$  at room temperature with layer quality and good device performance depending critically on this composition. Beyond a compositional error of 1-2% dislocations and mismatch strain can occur. Good quality MBE epilayers with optimum lattice match conditions became available once initial problems of InP substrate preparation were solved and the substrate was rotated to improve uniformity (Parker 1985). MBE epilayers show little spatial variation in composition compared to LPE material where the band-gap energy can vary by as much as 15 meV over 1mm of the surface. There obviously exists a strong dependence of the luminescence FWHM and intensity on the In/Ga flux ratio which will be best for lattice match conditions. A relatively high  $As_4$  to In/Ga flux ratio (5:1) appears necessary for producing GaInAs with high luminescence efficiencies in contrast to  $Al_xGa_{1-x}As$ .

The low temperature spectrum of  $Ga_{0.47}In_{0.53}As$  shows two distinct luminescence bands dominated by the near band-edge emission (see figure 3.13). While most authors agree on the assignment of the low energy emission some confusion exists in the literature as to the origin of the high energy peak.

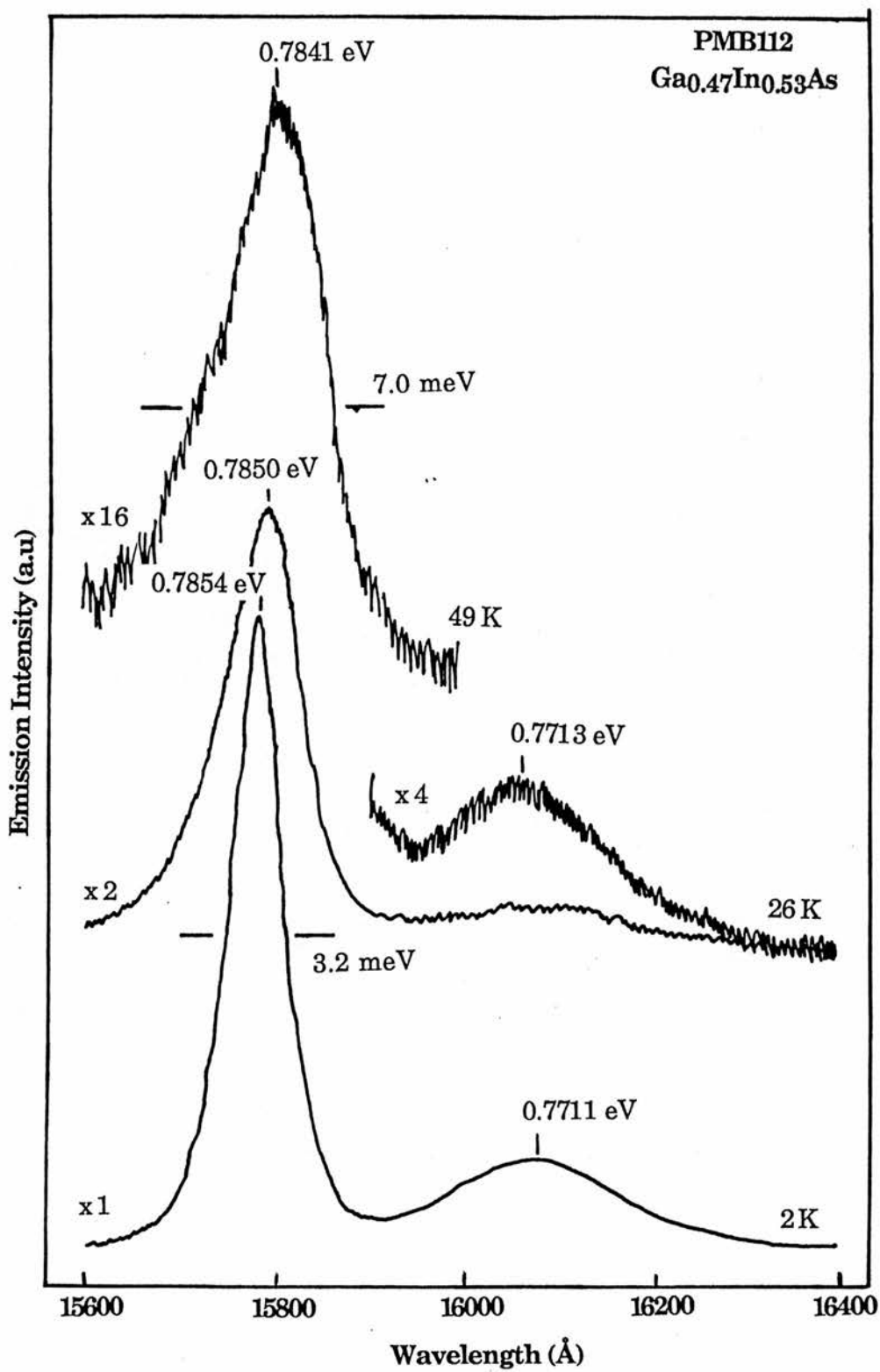


Figure 3.13 Emission spectra of a GaInAs sample ( $x_{\text{Ga}}=0.446$ ) at different temperatures. For peak assignment see text.

### III Luminescence from Bulk III-V Semiconductors

Various assignments have been suggested; a convolution of bound excitons (Goetz et al 1983, Charreaux et al 1986), ( $D^0, h$ ) (Marzin et al 1983), either of these depending on the impurity concentration (Swaminathan et al 1985) and a bound exciton complex (Penna et al 1984). Further confusion arises because the temperature dependence exhibits two distinct activation energies, for example  $E_1=2\pm 0.5$  meV,  $E_2=8\pm 1$  meV (Charreaux et al 1985) or  $E_1=1.6\pm 0.1$  meV,  $E_2=11.6\pm 2$  meV (Goetz et al 1983). The lower activation energy  $E_1$  is normally attributed the exciton ionisation energy estimated to be  $E_x=2$  meV from simple effective mass theory. But the origin of the higher activation energy is unclear since if it was assigned to donor ionisation this would imply a large central cell correction compared to the expected hydrogenic donor binding energy of  $E_d=3$  meV for  $m^*/m_0=0.041$ ,  $\epsilon_r=13.7$ . The assignment of this emission will be considered in more detail as we examine our results.

In figure 3.13 the luminescence spectra obtained from sample PMB112 at various temperatures are shown. The low temperature 2.2 K exhibits two peaks centred at 0.7854 eV with a FWHM of 3.2 meV and at 0.7711 eV. This  $Ga_{0.47}In_{0.53}As$  epilayer was the best grown by Sheffield upto this time. The compositional band-edge variation and bowing parameter of  $Ga_{0.47}In_{0.53}As$  has been obtained by correlating the 2 K luminescence with x-ray measurements around the lattice match conditions by Goetz et al (1983). This work was later extended by Swaminathan et al (1985) using MBE epilayers, the 2K band-gap dependence upon composition was given by

$$E_g(x)_{2K} = 0.4105 + 0.6337x + 0.475x^2 \quad (3.7)$$

from which the optimum lattice match to InP was obtained at  $x=0.465$ , the estimated band-edge position at 2 K is 0.811 eV. Our sample is ~2% In rich since  $X_{PMB112}=0.446$  from equation 3.7 and hence is under compression. This

mismatch, no doubt caused by a compositional variation, explains why the electrical measurements obtained by our laboratory for this sample  $\mu_{rt}=3960$  and  $n\sim 1.5\times 10^{16} \text{ cm}^{-3}$  (Al-Dubuni 1987) are degraded compared to those supplied by the grower  $\mu_{rt}=10000$  and  $n\sim 4\times 10^{15} \text{ cm}^{-3}$ . A heterostructure sample PMB137 grown around the same time as PMB112 has its GaInAs emission peaked at 0.7855 eV suggesting both this sample and MQW structures discussed in section 5.5 may be strained. Varying the laser spot size or position on the sample surface over a few mm resulted in very little change  $\pm 1$  meV in the energetic position of the main emission.

Before considering the assignment of the near band emission at 2.2 K we shall first label the transition observed at 49.6 K. At this temperature, since the donor ionisation energy is small,  $E_d=3$  meV, we would expect the emission at 0.7841 eV to be dominated by band-to-band transitions. The theoretical linewidth for a band-to-band transition at 49.6 K is  $\sim 7.5$  meV ( $\sim 1.8kT$ , see section 4.3.2) agrees well with that observed experimentally, 7 meV. As the sample temperature was increased above  $\sim 60$  K the emission could no longer be resolved from the background due to the limited s/n ratio of the detector.

The main problem with assigning the 2.2 K emission at 0.7854 eV in figure 3.13 is that no definitive experimental data identifying it exists. Swaminathan et al (1985) suggested that the band-edge emission was excitonic below  $n < 5\times 10^{15} \text{ cm}^{-3}$  and  $(D^0, h)$  for  $n > 5\times 10^{15} \text{ cm}^{-3}$ , but with no experimental justification since, in either instance only one emission peak was observed, the luminescence characteristic of which did not change. Most groups consider the emission as due to the convolution of the normal band-edge transitions with a gaussian function associated with the alloy broadening. The energetic positions of the band-edge transitions were estimated using the expected exciton and donor binding energies along with Hayne's rule. Using the model of Schubert et al

### III Luminescence from Bulk III-V Semiconductors

(1984), Charreaux et al (1985) estimated the gaussian broadening function to be  $\sigma=1.6$  meV and when this is convoluted with the expected band-edge transitions a linewidth of  $\sim 3$  meV was obtained, close to the FWHM we observe in our sample. However, another model by Singh et al (1984) for calculating alloy-broadened linewidths gave  $\sigma=3.3$  meV suggesting that the near band-edge emission may be due to only one transition. (A discussion of these alloy broadening models is given in section 4.3.1.) It seems most likely that our GaInAs band-edge luminescence can be assigned to convoluted transitions since Schubert and Tsang (1986) have grown epilayers by CBE with a 1.2 meV linewidth.

As the sample temperature is increased the emission shifts slightly to higher energies before evolving into a band-to-band transition (see figure 3.14). The variation of peak energy with temperature yields an activation energy of  $E_1 \sim 0.5 \pm 0.2$  meV which makes uncertain the determination of the thermalization process occurring in the region 2.2-20 K. Some groups find that the luminescence peak shifts to higher energies by 1-2 meV exhibiting an activation energy that can be related directly to the exciton binding energy. Although from the estimated band-gap variation of lattice matched GaInAs with temperature (Yu and Kuphal 1984):

$$E_g(T) = E(0) - \frac{4.906 \times 10^{-4} T^2}{(T+301)} \quad (3.8)$$

a 0 K energy gap of 0.0788 eV is obtained; this results in an ionisation energy of  $\sim 2.5$  meV for the emission at 2.2 K comparable to the exciton binding energy. As the temperature of the sample is further increased the luminescence quenches with an activation energy of  $E_2 = 10 \pm 1$  meV, as shown in figure 3.15. It is difficult to find a physical mechanism for this activation energy, since, if it assumed the emission is dominated by a  $(D^{\cdot}, h)$  transition above  $\sim 20$  K then  $E_2$  should relate to the donor binding energy. Penna et al (1984) found  $E_2 = 7$  meV and from a

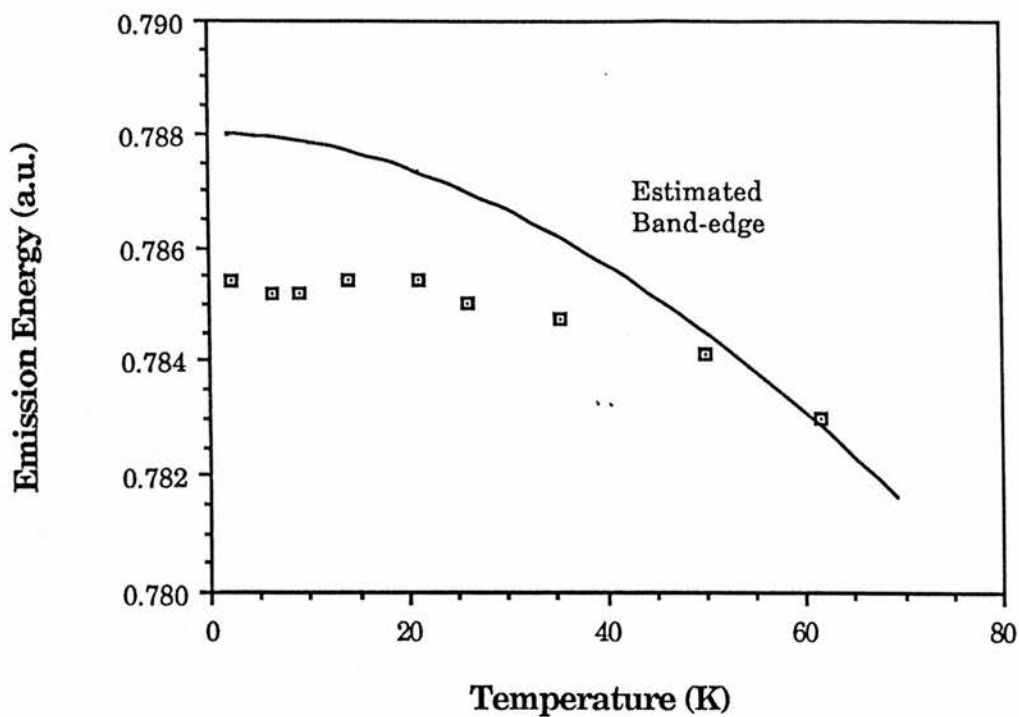


Figure 3.14 The variation of peak emission with temperature for PMB112. The solid line was obtained from the work of Yu and Kuphal (1984).

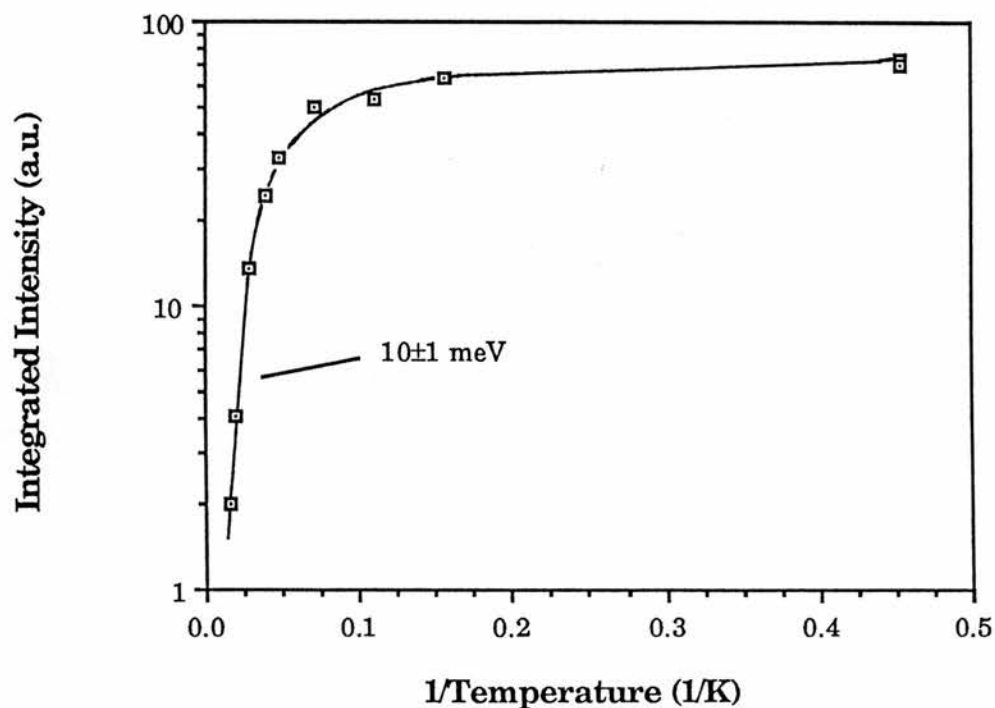


Figure 3.15 Dependence of the emission intensity upon temperature. Two activation energies are obtained  $E_1=0.5 \pm 0.2$  meV and  $E_2=10 \pm 1$  meV.

spectrum at 90 K they deconvoluted a peak shifted by  $\sim 6.5$  meV to higher energies from the peak emission that they then related to  $E_2$ . The asymmetric broadening observed on the high energy side of the emission at 49.4 K could be due to the emission observed by Penna et al at 90 K.

The low energy emission at 0.7711 eV can be assigned to a  $(D^{\circ}, A^{\circ})$  transition since as the excitation power density is increased the peak shifts to higher energies. An acceptor ionisation energy of  $14 \pm 2$  meV ( $E_a \sim E_g - (D^{\circ}, A^{\circ})$ ), estimated from figure 3.13, is due to carbon, the dominant background impurity in most MBE grown layers (Charreaux et al 1985). As the sample temperature is increased the peak shows little energetic movement and no  $(e, A^{\circ})$  transition evolves consistent with the observations of other authors (such as Goetz et al 1983). In the range 25-30 K the  $(D^{\circ}, A^{\circ})$  emission quenches completely as all the shallow donor levels,  $E_d = 3$  meV, are completely ionised. No LO phonon replica associated with the near band-edge emission was observed probably because it was below the detection limit of the germanium detector.

### 3.5 Summary

The luminescence of various MBE grown III-V compounds and alloys is similar to that observed from material of similar quality obtained by other growth mechanisms. In GaAs, impurity related transitions (summarized in section 1.2) dominate the spectral region with the intrinsic free exciton emission only a small percentage of the total emission. InP shows the same characteristics as GaAs but the free exciton emission, observed in material from three laboratories, appears anomalously enhanced either due to selective absorption of the other transitions or some unknown property of the MBE grown material. The first known observation of structure in the InP excitonic emission has tentatively been assigned to polariton effects. An explanation, consistent with the model of

### III Luminescence from Bulk III-V Semiconductors

scattering of the exciton-polariton from a neutral donor is proposed. In a study of Mg doped InP, the  $(D^*,A^*)$  emission shows that Mg may not have been incorporated into the growing layer. The emission from  $\text{Ga}_{0.47}\text{In}_{0.53}\text{As}$  is dominated by a convolution of  $(D^*,X)$  and  $(D^*,h)$  transitions broadened by a Gaussian function reflecting the material's random composition.

In conclusion, the bulk luminescence from all III-V compounds and alloys is dominated by impurity related emission. This is important to note, because in chapter 5 we will show that the luminescence from quantum well structures, such as  $\text{GaAs-Al}_x\text{Ga}_{1-x}\text{As}$  and  $\text{Ga}_{0.47}\text{In}_{0.53}\text{As-InP}$ , reflects that of the bulk. In  $\text{Ga}_{0.47}\text{In}_{0.53}\text{As-InP}$  wells, the quality of the alloy limits the linewidth of the well fabricated from it and the same is true for thin  $\text{GaAs-Al}_x\text{Ga}_{1-x}\text{As}$  wells. A large background doping of the barrier material can result in free carriers transferring into the well, particularly in  $\text{Ga}_{0.47}\text{In}_{0.53}\text{As-InP}$  wells, thus increasing the linewidth observed.

## IV LUMINESCENCE PROPERTIES OF $\text{Al}_{0.48}\text{In}_{0.52}\text{As}$

	<u>Page</u>
4.1 Introduction	74
4.2 Growth of $\text{Al}_{0.48}\text{In}_{0.52}\text{As}$	74
4.2.1 Previous Luminescence Results	77
4.3 Low Temperature Photoluminescence of $\text{Al}_{0.48}\text{In}_{0.52}\text{As}$	79
4.3.1 Linewidth Considerations	80
4.3.1.1 Alloy Broadening in $\text{Al}_{0.48}\text{In}_{0.52}\text{As}$	81
4.3.1.2 The effect of clustering in $\text{Al}_{0.48}\text{In}_{0.52}\text{As}$	84
4.3.1.3 Bimodal ordering in Semiconductor Alloys	86
4.3.2 Lineshape considerations	87
4.4 Temperature Dependence of the emission	90
4.5 Dependence on Excitation Power Density	94
4.6 Selective Photoluminescence Excitation	95
4.7 Summary	99

## 4.1 Introduction

Originally the main motivation for growing semiconductor alloys such as  $\text{Al}_x\text{Ga}_{1-x}\text{As}$  was to produce room temperature luminescence in the visible region.  $\text{Al}_x\text{In}_{1-x}\text{As}$  appeared a good candidate as it was shown to have a  $\Gamma$ -X cross-over  $\sim 100$  meV higher than  $\text{Al}_x\text{Ga}_{1-x}\text{As}$  (Lorenz and Onton 1970, see table 1.2). More recently  $\text{Al}_{0.48}\text{In}_{0.52}\text{As}$ , grown lattice matched to InP and  $\text{Ga}_{0.47}\text{In}_{0.53}\text{As}$ , has become important for optoelectronic devices and heterojunctions where its large band-offset offers a greater confinement for carriers than InP. Unfortunately, in the race to produce good quality superlattice structures of  $\text{Al}_{0.48}\text{In}_{0.52}\text{As}$ - $\text{Ga}_{0.47}\text{In}_{0.53}\text{As}$  with abrupt interfaces, detailed studies of the material and physical properties of  $\text{Al}_{0.48}\text{In}_{0.52}\text{As}$  have been neglected. One such area is the origin of the near band-edge emission. Most authors now appear to accept that the band-edge luminescence results from bound excitonic transitions whose linewidth shows broadening as a consequence of alloy clustering. But experimental proof of this broadening mechanism in the luminescence rests only upon the increased linewidth observed. The motivation for this work was to provide the first detailed study of the luminescence from  $\text{Al}_{0.48}\text{In}_{0.52}\text{As}$ , grown lattice matched to InP, using both PL and PLE, varying sample temperature and excitation power density. Assigning the emission was not only important to determine the position of the band-edge but also for the high pressure work reported in chapter 6.

## 4.2 Growth of $\text{Al}_{0.48}\text{In}_{0.52}\text{As}$

The first report of the growth of  $\text{Al}_x\text{In}_{1-x}\text{As}$  using a modified Bridgman method was made by Lorenz and Onton (1970). Using cathodo-luminescence they found the compositional  $\Gamma$ -X cross-over to be  $x=0.68$  with  $E_g=2.05$  eV at room temperature. Expanding the data obtained by Lorenz and Onton with his own

#### IV Luminescence properties of Al<sub>0.48</sub>In<sub>0.52</sub>As

results Matyas (1979) found the bowing parameter to be 0.24 eV and hence the compositional band-gap energy was described by:

$$\Delta E_{g\Gamma} = 0.36 + 2.35x + 0.24x^2 \text{ eV.} \quad (4.1)$$

The first expitaxial growth of Al<sub>0.48</sub>In<sub>0.52</sub>As onto both InP and GaInAs was reported using MBE at a substrate temperature  $T_s=480$  °C by Ohno et al (1981). It had been recognized by various groups that the large distribution coefficient of Al would make LPE, the most obvious growth method, difficult until it was successfully achieved (Nakajima et al 1982). Although, MBE was not without its own problems, growth proceeds within the misibility gap for  $T_s < 800$  °C, so the alloy is not ideal, originally semi-insulating SI ( $\rho > 3 \times 10^3 \Omega\text{cm}^{-1}$ ) and containing a large density of deep levels and defects as a consequence of the high Al content.

Davies et al (1984) showed that material quality depended primarily on substrate temperature with undoped epitaxial layers having a free electron concentration of  $1 \times 10^{16} \text{cm}^{-3}$  for  $T_s > 560$  °C but SI for  $T_s < 520$  °C. The main constraint on raising the substrate temperature was the congruent sublimation point of Al<sub>0.48</sub>In<sub>0.52</sub>As above which In loss occurs from the growing surface. This was thought to occur around 500-520 °C but Davies et al (1984) showed it was not significant until 580-600 °C. Welch et al (1985) found that material quality, from luminescence linewidth, was best at a specific growth temperature and As<sub>4</sub> overpressure (figure 4.1). With a minimum linewidth around at  $T_s=515 \pm 20$  °C they suggested that lowering  $T_s$  reduced the Al mobility, with the consequence that Al was not incorporated at a preferred lattice site. Increasing  $T_s$  reduced crystalline quality and the density of As vacancies, thus in either case increasing the linewidth. For similar reasons, Juang et al (1987) found as they slowed the growth rate from  $1.3 \mu\text{m h}^{-1}$  to  $0.5 \mu\text{m h}^{-1}$  the luminescence linewidth improved from 40 meV to 19 meV.

Photoluminescence Linewidth of AlInAs  
vs Growth Temperature

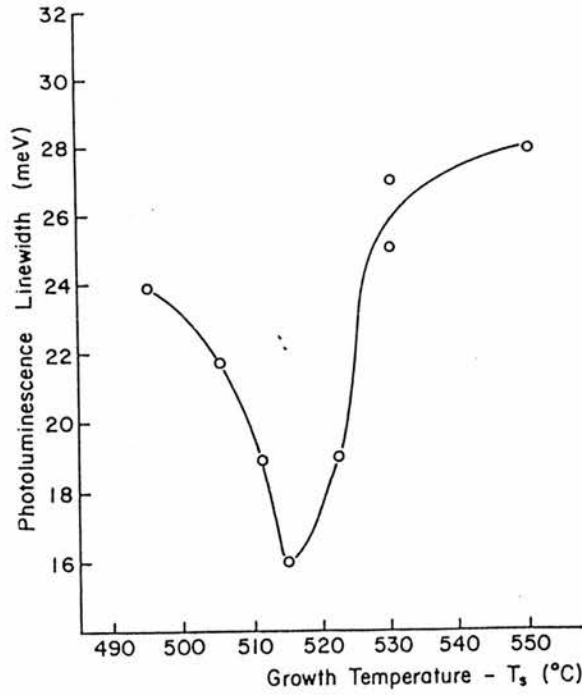


**Figure 4.1** Photoluminescence linewidth of AlInAs against substrate temperature ( $T_g$ ). The minimum linewidth of 16 meV occurs at 515 °C. (Welch et al 1985)

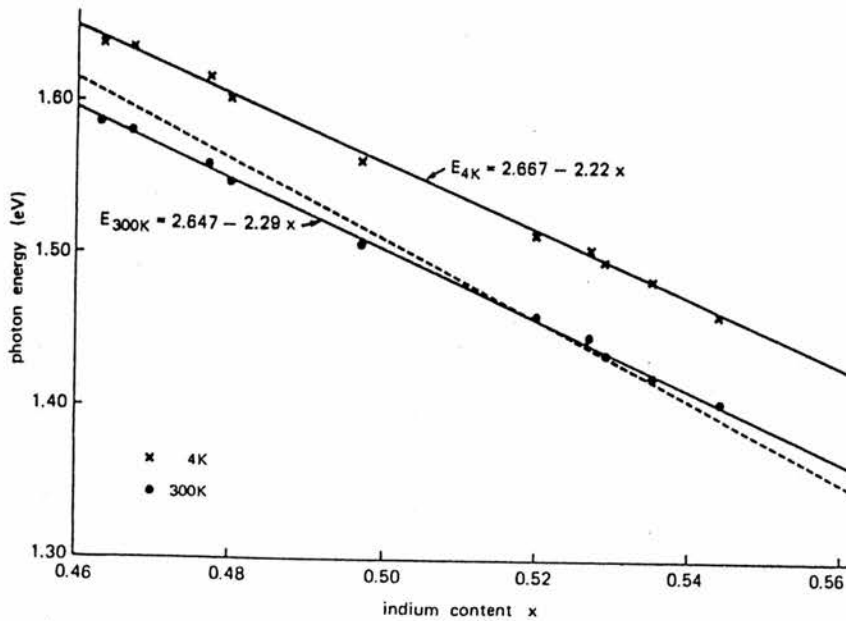


**Figure 4.2** Variation of the band gap of  $Al_{1-x}In_xAs$ , grown on (100)InP, with In content ( $x$ ) at room temperature and at 4 K. The dashed line is the relationship at room temperature in the absence of mismatch. (Wakefield et al 1984)

#### IV Luminescence properties of $\text{Al}_{0.48}\text{In}_{0.52}\text{As}$

Using a Monte Carlo computer simulation Singh et al (1986) studied the MBE growth dynamics of  $\text{Al}_{0.48}\text{In}_{0.52}\text{As}$  on a  $40 \times 40$  crystal lattice with up to 20 monolayers deposited. They found that since growth proceeds in the miscibility gap, for some  $\text{III}_a\text{III}_b\text{V}_c$  alloys this thermodynamically favours phase separation. They concluded that under normal MBE growth conditions producing a high quality alloy and abrupt interfaces required for heterostructures were incompatible. In their model they found evidence for clustering in  $\text{Al}_{0.48}\text{In}_{0.52}\text{As}$ , so they defined a short range order parameter  $C$  to describe the structural quality of the alloy. They found that the alloy was random at low  $T_s = 130^\circ\text{C}$  becoming clustered and hence showing degraded physical properties as the growth temperature increased to  $T_s \sim 470^\circ\text{C}$ . Unfortunately Singhs' model must be called into doubt since unrealistic growth temperatures were used thus predicting results that contradict many of those observed experimentally (see section 4.3.1.2).

The  $\text{Al}_{0.48}\text{In}_{0.52}\text{As}$  used in this work (see table 4.1) was grown by Scott et al (1987) who found that the best optical material quality was obtained at the highest  $T_s$  below the onset of In loss from the substrate. They found this point by increasing the substrate temperature above  $530^\circ\text{C}$ , the growing surface appeared rough for 30 to  $40^\circ\text{C}$  until it smoothed out again at  $560$  to  $570^\circ\text{C}$ , growth was then initiated. Our epitaxial layers have been grown at a higher  $T_s$  than any other group (see above and Juang et al (1987)  $500^\circ\text{C}$ ; Praseuth et al (1987)  $520^\circ\text{C}$ ). Consequently, the  $\text{Al}_{0.48}\text{In}_{0.52}\text{As}$  has shown the best luminescence linewidths of  $14\text{ meV}$  and low defect densities,  $200\text{ cm}^{-2}$ . The InP substrate was raised to growth temperature in a over-pressure of As thus resulting in a InP(As)-AlInAs interface. By the use of a glancing-incidence scattering geometry with a triple crystal diffractometer, the interface region of  $20 \pm 1\text{ \AA}$  thickness, was found not to scatter suggesting that it was polycrystalline (Hatton 1988) but the epitaxial layer had excellent crystalline quality over the top even for layers as thin as  $200\text{ \AA}$

**Table 4.1** Summary of the AlInAs samples luminescence properties

<u>Sample</u>	<u>Emission (eV)</u>	<u>FWHM (meV)</u>	<u>n(C-V) @ 297 K (cm<sup>-3</sup>)</u>	<u>Doped</u>
MV401	1.5362	-	-	-
MV402	1.5252	24.5	-	Si
MV408	1.5498	16.9	1.0x10 <sup>16</sup>	u/d
MV409	1.5460	15.6	0.9x10 <sup>16</sup>	u/d
MV411	1.5333	17.4	2.3x10 <sup>15</sup>	u/d

(Lucas et al (1988), sample MV494). It was therefore evident, from the narrow luminescence linewidth and the good crystalline quality of the epitaxial layer, that the interface region does not influence the luminescence properties.

#### 4.2.1 Previous Luminescence Results

No detailed study of the luminescence from  $\text{Al}_{0.48}\text{In}_{0.52}\text{As}$  has been found to exist in the literature. When Onho et al (1981) first produced lattice-matched  $\text{Al}_{0.48}\text{In}_{0.52}\text{As}$  they observed the 2 K emission at 1.542 eV with FWHM of 25 meV. Since the luminescence was broad and weak, they suggested that it was probably not near band-edge and that it indicated a high density of non-radiative transitions present. Using cathodo-luminescence Wakefield et al (1984) assumed the luminescence of FWHM 24 meV was band-edge (or at least a measure of it) since, the band-edge position obtained by photovoltage spectroscopy and the luminescence emission agree within experimental error. This assumption may not be valid since there can be large errors associated with determining the band-edge from a photovoltage spectrum. By varying the In composition from  $x=0.46$  to 0.55 for  $\text{Al}_{1-x}\text{In}_x\text{As}$  grown on InP they found, based on the above assumption, the lattice match band to be at 1.508 eV at 4 K. Around the lattice match composition the band-edge at 4 K and room temperature was given by:

$$E_g(4\text{K}) = 1.508 + 2.22 \Delta x \quad (4.2a)$$

$$E_g(\text{RT}) = 1.450 + 2.29 \Delta x \quad (4.2b)$$

where  $\Delta x=(0.52-x)$  (see figure 4.2). They also noticed that the  $\text{Al}_{0.48}\text{In}_{0.52}\text{As}$  emission intensity was approximately a tenth of that for  $\text{Ga}_{0.47}\text{In}_{0.53}\text{As}$  grown in the same reactor.

No improvements were made in the optical quality of the material until Welch et al (1985) obtained linewidths of 16 meV for a 3% In rich epitaxial layer

grown during a systematic study of growth parameters. Observing a smooth change in emission energy with increasing sample temperature they assumed this to indicate a band-to-band transition. Correlating their PL results to Raman scattering data they suggested that the broadening mechanism for the emission linewidth was due to a degraded crystal structure and not impurities. Intuitively this does not seem correct because the low temperature luminescence is normally dominated by impurity related emission. This also contradicts the work of Praseuth et al (1987) who find no correlation between the optical and crystalline properties. Good luminescence linewidths were obtained for samples whose x-ray rocking curve measurements showed poor crystal quality. A TEM micrograph of  $\text{Al}_{0.48}\text{In}_{0.52}\text{As}$  grown directly onto a InP substrate showed a rough surface with a high density of dislocations and stacking faults, luminescence linewidths of 16 meV at 1.545 eV were still obtained. Using PLE, a 60 meV shift occurred between the PL and PLE spectra which they attributed to a deep, acceptor type state (see section 4.6).

It had been noted by a number of authors that the linewidths observed in  $\text{Al}_{0.48}\text{In}_{0.52}\text{As}$  were much larger than those of any other III-V alloys, typically 1-7 meV, see chapter 3. No attempt was made to explain the increased linewidth until Singh et al (1986) suggested that the broadening may be caused by clustering, a detailed discussion of this model is given in section 4.3.1.2. Experimental proof for clustering was found during variable temperature Hall measurements (Hong et al 1987) where in the region 400-600 K the mobility increased for some low mobility samples (FWHM 40meV). Since alloy scattering was the dominant scattering mechanism above 200 K they postulated that ordering resulting in a compositional fluctuation of 150 meV and a cluster size of 70 Å could account for the increased mobility.

### 4.3 Low Temperature Photoluminescence of $\text{Al}_{0.48}\text{In}_{0.52}\text{As}$

For  $\text{Al}_{0.48}\text{In}_{0.52}\text{As}$  grown lattice-matched to InP it was expected to find the band-edge emission around 1.5 eV (see section 4.2.1). A summary of the low temperature luminescence results and  $n(c-v)$  measurements supplied by Dr E G Scott are given in table 4.1 for all the  $\text{Al}_{0.48}\text{In}_{0.52}\text{As}$  samples screened. Figure 4.3 shows a typical spectrum where, two main emissions are observed one peaking at 1.5334 eV with a FWHM of 17.4 meV and the other, a very broad band emission peaking at 1.5007 eV. They were assigned to the  $\text{Al}_{0.48}\text{In}_{0.52}\text{As}$  epitaxial layer and the InP substrate, respectively. This assignment was tested by etching off the  $\text{Al}_{0.48}\text{In}_{0.52}\text{As}$  epitaxial layer leaving only the InP substrate. Both sides of the sample were then chemically polished and only emission at 1.5007 eV was observed. The best linewidth we observed for our  $\text{Al}_{0.48}\text{In}_{0.52}\text{As}$  was 15.6 meV compared to that obtained by Dr Scotts group of 14 meV, the slight difference can easily be accounted for by sample uniformity.

The InP substrate luminescence is consistent with that expected for heavily sulphur doped substrate,  $n > 10^{18} \text{ cm}^{-3}$ . The emission linewidth corresponds to the lowest acceptor impurity binding energy terminating at the Fermi energy within the conduction band. Its luminescence and temperature dependence properties are well described by the configurational co-ordinate model (Williams 1968). A thin 25Å GaAs cap was used to reduce oxidization of the  $\text{Al}_{0.48}\text{In}_{0.52}\text{As}$  layer thus improving surface quality for electrical contacts. Lucas et al (1988) showed that the GaAs was oxidised and a low electron density suggested that water could be absorbed in a GaO-GaAs complex on the surface; this would not be observed in the luminescence. A further low energy emission could also be observed at 1.35  $\mu\text{m}$ , FWHM  $\sim 90$  meV, probably due to deep level analogous to that ascribed to oxygen at 1.3  $\mu\text{m}$  in GaAs (Ilegem 1985).

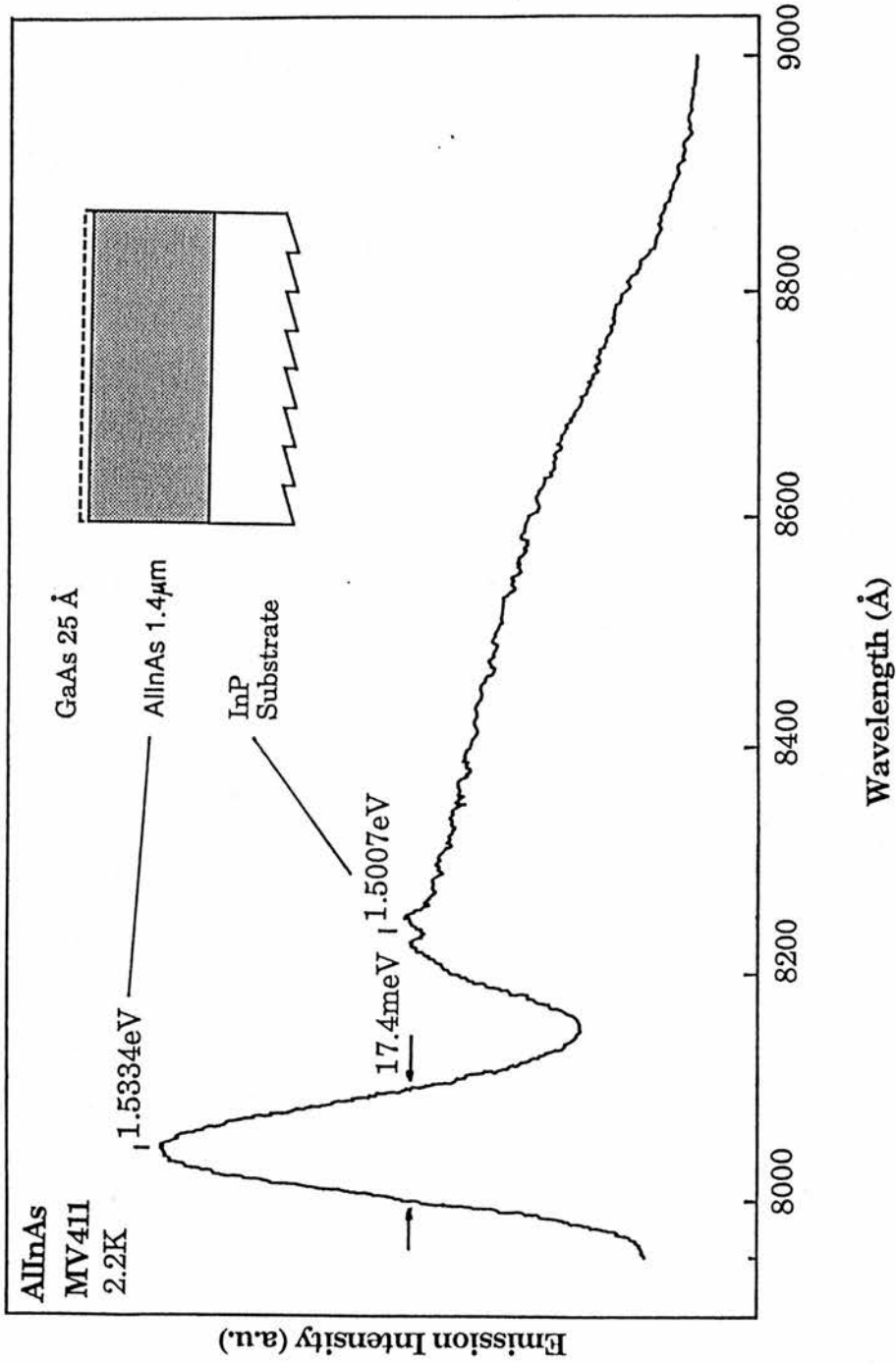


**Figure 4.3** A typical luminescence spectrum is dominated by the  $A_{0.48}In_{0.52}As$  emission, but in this instance the spectrum shows an unusually large emission intensity from the substrate.

## IV Luminescence properties of $\text{Al}_{0.48}\text{In}_{0.52}\text{As}$

The characteristic  $\text{Al}_{0.48}\text{In}_{0.52}\text{As}$  emission had a gaussian-like lineshape, was asymmetrically broadened to the low energy side and had no splitting or shoulders. The lineshape of our spectra are similar to those reported in the literature (see figure 4.4), suggesting that we are observing the same emission. Although it has been suggested that the emission is due to band-to-band transitions or bound excitons (see section 4.2.1), other assignments such as free-to-bound and donor-acceptor-pair transitions have not been considered. The correct assignment of the  $\text{Al}_{0.48}\text{In}_{0.52}\text{As}$  emission is crucial since an accurate estimate of the lattice matched band-gap energy depends on it. This is complicated in alloys such as  $\text{Al}_{0.48}\text{In}_{0.52}\text{As}$  as the near band-edge luminescence does not show the sharp excitonic transitions observed in binaries such as GaAs.

### 4.3.1 Linewidth Considerations

In semiconductor alloys of the form  $\text{A}_x\text{III}\text{B}_{1-x}\text{III}\text{CV}$  the low temperature luminescence linewidth of any transition contains contributions from many different scattering mechanisms. Linewidth broadening can be associated with ionized impurity scattering resulting from potential fluctuations associated the random distribution of ionized impurities. Since room temperature C-V measurements show the number of ionized impurities cannot exceed  $\sim 10^{16} \text{ cm}^{-3}$  this contribution to the linewidth is expected to be less than 1 meV (Larsen et al 1973). Accordingly, linewidth contributions due to impurities will be small and thermal broadening,  $\sim kT$ , is also negligible at 2K. In undoped binary compounds the linewidth of the bound exciton is normally smaller than  $kT$ , about 0.1 meV in GaAs. By far the dominant broadening mechanism is alloy scattering caused by the random compositional disorder on the atomic scale. In the case of  $\text{Al}_{0.48}\text{In}_{0.52}\text{As}$  it is the random distribution of the Al and In on the group III cation sites, which will be discussed below.

Photoluminescence (4°K) of AlInAs  
 growth rate = 5000 Å/hr

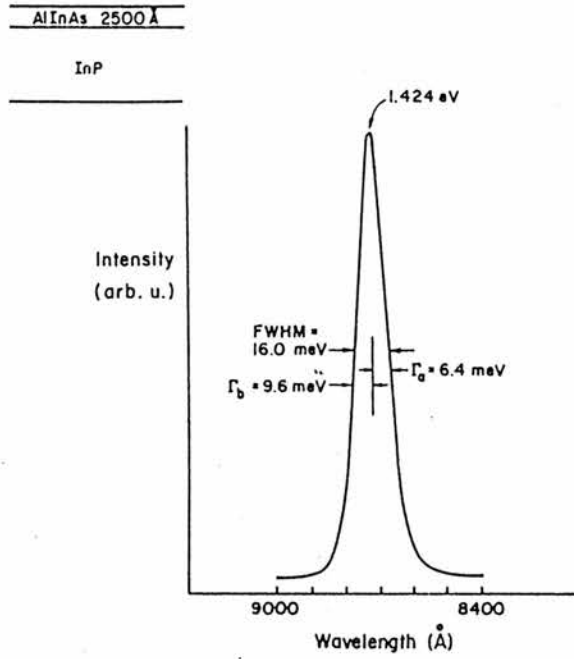


**Figure 4.4** Photoluminescence spectrum (4K) of AlInAs. The emission energy of 1.424 corresponds to 3 % In rich. The linewidth of the 16 meV is the narrowest line shape in the literature to date. The inset shows the structure studied. (Welch et al 1985)

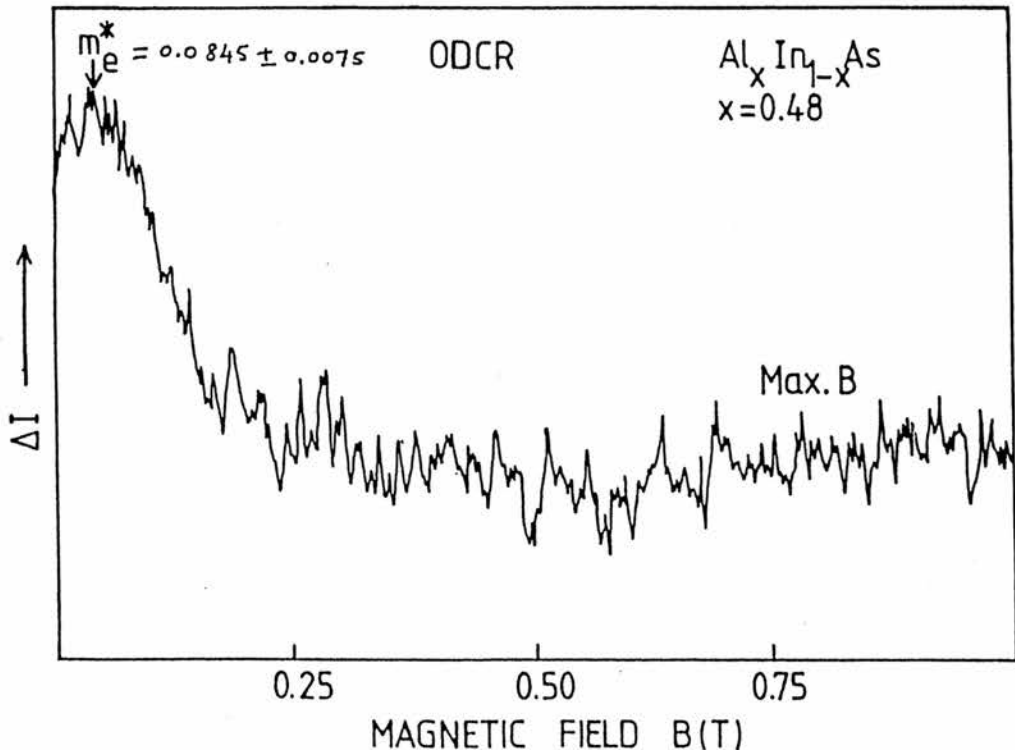


**Figure 4.5** ODCR spectrum of Al<sub>0.48</sub>In<sub>0.52</sub>As showing the resonance due to electrons. The effective mass  $m_e^*$  obtained is larger than previously reported (Kama'ah 1988).

### 4.3.1.1 Alloy Broadening in $\text{Al}_{0.48}\text{In}_{0.52}\text{As}$

A formalism to describe the effects of alloy scattering on the luminescence linewidth by the random distribution of group III cations was derived independently by Schubert et al (1984) and Singh et al (1984). Essentially the material was treated as a classical system with an exciton of radius  $a_{\text{exc}}$  determining a crystal volume of  $V_{\text{exc}}=4/3\pi a_{\text{exc}}^3$ . Only this limited volume of the crystal determined the emitted photon energy. The compositional variation in the crystal was treated as a statistical distribution of the group III cations on their respective lattice sites. Hence the probability of finding a particular atom was proportional to its concentration in  $\text{A}^{\text{III}}_x\text{B}^{\text{III}}_{1-x}\text{C}^{\text{V}}$  and the linewidth of an excitonic or free to bound transition  $\sigma$  varied as  $(V_{\text{exc}})^{-0.5}$ .

Schubert (1984, 1986) calculated the minimum theoretical linewidth due alloy scattering in an ideal semiconductor assuming that a hydrogenic approximation was valid for donor and acceptor impurities. The group III atoms (cations) density in a zincblende lattice is given by  $K=4a_0^{-3}$ , where  $a_0$  is the lattice constant. Thus the probability of finding  $n$   $\text{A}^{\text{III}}$  atoms within a volume  $V$  can be approximated by a Gaussian distribution if the total number of  $\text{KV}$  cations in the volume is high. The mean value of the distribution is  $xKV$  and the standard deviation for the alloy composition within the same volume is

$$\sigma_x = \left[ \frac{x(1-x)}{KV} \right]^{0.5} \quad (4.3)$$

This results in local changes in the band-gap sensed by the excitonic volume  $V_{\text{exc}}$ , therefore

$$\sigma E_g = \frac{dE_g}{dx} \left[ \frac{x(1-x)}{KV_{\text{exc}}} \right]^{0.5} \quad (4.4)$$

where  $dE_g/dx$  is the variation of band-gap with alloy composition. So the random occupation of the cation sites results in a broadening of the

#### IV Luminescence properties of $\text{Al}_{0.48}\text{In}_{0.52}\text{As}$

luminescence transition caused by this variation. The FWHM of a Gaussian distribution is  $2.36\sigma$ , so for a bound exciton recombination

$$\Delta E_{\text{exc}} = 2.36 \frac{dE_g}{dx} \left[ \frac{x(1-x)}{4a_0^{-3} \left(\frac{4}{3}\right) \pi a_{\text{exc}}^3} \right]^{0.5} \quad (4.5)$$

Assuming the exciton is hydrogenic, the effective mass approximation is valid yielding an estimate for  $a_{\text{exc}}$ :

$$a_{\text{exc}} = \epsilon_r \left( \frac{m_0}{m_r^*} \right) a_B \quad (4.6)$$

where  $\epsilon_r$  is the dielectric constant of the material and  $a_B$  is the Bohr radius of  $0.527 \text{ \AA}$ . The reduced mass  $m_r^*$  of the exciton is given by

$$m_r^{*-1} = (m_e^{*-1} + m_{hh}^{*-1})^{-1} \quad (4.7)$$

where  $m_e^*$  and  $m_{hh}^*$  are the electron and heavy-hole effective masses respectively.

We can now make an estimate of the alloy broadened linewidth for bound excitonic transition in  $\text{Al}_{0.48}\text{In}_{0.52}\text{As}$ . Olego et al (1982) determined the electron effective mass in  $\text{In}_{1-x-y}\text{Ga}_x\text{Al}_y\text{As}$  from the plasma frequencies measured using Raman scattering as

$$m_e^* = (0.0427 \pm 0.0015) + (0.0683 \pm 0.0007) y \quad (4.8)$$

so,  $m_e^* = 0.0755$  in  $\text{Al}_{0.48}\text{In}_{0.52}\text{As}$ . The value of  $m_r^*$  in equation 4.7 is relatively insensitive to  $m_{hh}^*$  so it was assumed this would have approximately the same value as for GaAs,  $m_{hh}^* = 0.450$ . Calculating  $m_r^*$  and substituting it into equation 4.6 with  $\epsilon_r = 12.7$ , extrapolated from the binaries (table 1.2), gives  $a_{\text{exc}} \sim 103 \text{ \AA}$ . From equation 4.1  $dE_g/dx$  can be found as  $2.59 \text{ eV}$ .  $a_0 = 5.860 \text{ \AA}$  is interpolated from the binaries (table 1.2). Using these values in equation 4.5 we find  $\Delta E_{\text{exc}} \sim 10 \text{ meV}$  for  $\text{Al}_{0.48}\text{In}_{0.52}$ . Before commenting on this value for the

alloy broadened linewidth in  $\text{Al}_{0.48}\text{In}_{0.52}\text{As}$  we will consider the linewidth broadening estimated by the model of Singh et al (1984).

Singh et al consider an alloy system  $A(C_A^\circ)B(C_B^\circ)$  where A and B are components of the alloy and  $C_A^\circ$  and  $C_B^\circ$  is the mean composition. The electronic structure is assumed to be described within the virtual crystal approximation (VCA) to represent extended electronic states treating the potential fluctuation associated with compositional variations as a perturbation. If the global concentration of A and B are  $C_A^\circ$  and  $C_B^\circ (1-C_A^\circ)$  then the probability of a local concentration  $C_A$  to occur over the exciton volume  $P(C_A, a_{\text{exc}})$  was given by (Lifshitz 1965) as

$$P(C_A, a_{\text{exc}}) = \exp \left[ -\frac{a_{\text{exc}}^3}{r_c^3} \left( C_A \ln \frac{C_A}{C_A^\circ} + C_B \ln \frac{C_B}{C_B^\circ} \right) \right] \quad (4.9)$$

where  $r_c$  is the radius of the smallest distance over which fluctuations occur; if the alloy is random  $r_c=r_0$ , the interatomic distance, otherwise it is the size of a cluster (see section 4.3.1.2). This results in a shift in the exciton energy which will be observed as an increased linewidth thus

$$\sigma_0 = 2 \left[ 1.4 C_A^0 C_B^0 r_c^3 / a_{\text{exc}}^3 \right]^{0.5} \Delta_1 \quad (4.10)$$

Here  $C_A^0$  and  $C_B^0$  are the mean composition of the binary components AlAs and InAs, and  $\Delta_1$  is the difference in the band-gap of the two components of the alloy. Using a more rigorous quantum mechanical formalism, a variational-statistical approach developed later showed that the right-hand side of equation 4.9 should be multiplied by a factor of 0.327 (Singh et al 1986b). An estimate was made of the expected  $\text{Al}_{0.48}\text{In}_{0.52}\text{As}$  alloy scatter limited linewidth by Singh et al (1986) as  $\sim 4$  meV, although  $a_{\text{exc}}=200 \text{ \AA}$  was assumed. If  $a_{\text{exc}}=200 \text{ \AA}$  is substituted into equation 4.5 with the other parameters used previously then Schuberts model also gives  $\Delta E_{\text{exc}} \sim 4$  meV.

#### IV Luminescence properties of $\text{Al}_{0.48}\text{In}_{0.52}\text{As}$

In these linewidth calculations the result depends critically on the estimate of  $a_{\text{exc}}$  and hence in turn  $m_e^*$ . The effective mass determined by Olego et al (1982) was an extrapolation from  $\text{In}_{0.5}\text{Ga}_{0.24}\text{Al}_{0.26}\text{As}$  and not actually from a  $\text{Al}_{0.48}\text{In}_{0.52}\text{As}$  sample. Recently, Wright et al (1989) measured  $m_e^*=0.10\pm 0.01m_0$  (figure 4.5) by ODCR on BT sample MV398. They obtained  $m_e^*$  from a curve fit to their data because  $\omega\tau=0.73$ , so a peak did not occur at  $\omega_c (=eB/m^*)$ . Substituting as before we find  $a_{\text{exc}}\sim 94 \text{ \AA}$ . This value does not agree with the estimate made by Singh et al of  $a_{\text{exc}}=200 \text{ \AA}$  which seems difficult to justify. But in either case the linewidths predicted by both models, 4-10meV, fail to account for those observed in  $\text{Al}_{0.48}\text{In}_{0.52}\text{As}$ . Singh et al suggested that the compositional clustering found in their growth model (see section 4.3.1.2) could account for the increased linewidth. Schubert et al (1984) have also used their model to explain the effect of alloy broadening in  $\text{Al}_x\text{Ga}_{1-x}\text{As}$  free-to-bound transitions. This was later extended by Charreux et al (1985) to explain the effects of alloy broadening on donor-acceptor-pair transitions in  $\text{Ga}_{0.47}\text{In}_{0.53}\text{As}$ . In both instances the linewidths estimated for donor-acceptor-pair and free-to-bound transitions are closer to those reported in  $\text{Al}_{0.48}\text{In}_{0.53}\text{As}$ .

##### 4.3.1.2 The effect of clustering in $\text{Al}_{0.48}\text{In}_{0.52}\text{As}$

Both equations 4.5 and 4.10 have been obtained for an alloy without considering the effects compositional clustering. Monte Carlo simulations show that the MBE growth mechanism of random impingement with surface migration at temperatures within the miscibility gap can thermodynamically favour clustering or phase separation. Singh et al (1986) extended their linewidth broadening model to include clustering into calculations of excitonic linewidth and electron mobility. It was assumed that the bulk alloy was formed by two clusters with concentrations  $C_A^1$  and  $C_A^2$  containing  $n_c$  atoms in the smaller cluster. Thus regions exist where the alloy composition is different to

#### IV Luminescence properties of $\text{Al}_{0.48}\text{In}_{0.52}\text{As}$

that of the bulk. In a perfectly random alloy  $n_c=1$  and  $C_A^1=1(0)$ ;  $C_B^2=0(1)$ . For clustering a short range order parameter  $C$  was defined and within the cluster  $C_{\max}$  was given by  $Z(C_A^1 - C_A^2)$ , where  $Z$  is the co-ordination number. The excitonic linewidth  $\sigma$  for an alloy with compositional clustering was then given by:

$$\sigma = \sigma_0 n_c^{1.5} |C_A^1 - C_A^2| \quad (4.11)$$

where  $\sigma_0$  was calculated using equation 4.10. It is assumed the largest scale over which correlations exist,  $r_c=n_c r_0$ , is not larger than  $a_{\text{exc}}$  otherwise multiple peaks would be observed in the luminescence. The values of  $C_A^1$  and  $C_A^2$  were estimated from their growth simulations as 0.3 and 0.7, respectively, and were given without any physical justification. When the order parameter  $C$  is related to growth temperature it was found the luminescence linewidth increases monotonically, having a value of  $\sim 10$  meV at 800K (figure 4.6).

Although this theory goes some way to show that including the effects of compositional clustering can give excitonic linewidths similar to those observed in  $\text{Al}_{0.48}\text{In}_{0.52}\text{As}$ , it is mostly a theoretical formalism which provides a phenomenological explanation of the observed luminescence linewidth. Experimentally a minimum luminescence linewidth is obtained at a specific growth temperature (figure 4.1, see also Kerr 1984). Later work by Juang et al (1987) showed that the linewidth improves with increased growth temperature, both contrary to the predictions of Singh et al (1986). Using variable temperature mobility measurements Juang et al found  $|C_A^1 - C_A^2| \sim 4\%$  contradicting the estimated values by Singh et al above, which suggest that they used a 30 to 70 % compositional variation within the cluster to obtain the results in figure 4.6. Juang et al only observed the effects of clustering in a sample that showed the largest linewidths  $>40$  meV, thus, it can be assumed that clustering was not the dominant mechanism in their better samples which had FWHM  $\sim 19$  meV. It

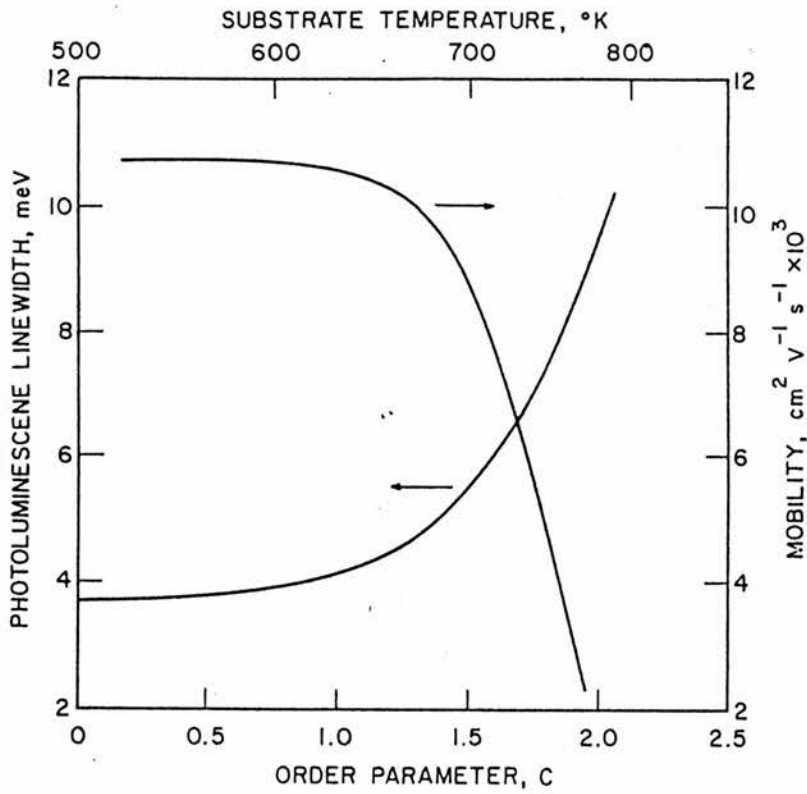


**Figure 4.6** Variation of alloy limited low temperature PL linewidth and 300-K electron mobility in  $\text{Al}_{0.5}\text{In}_{0.5}\text{As}$  as a function of alloy clustering or substrate temperature. Note that the improvement at low temperatures may be reduced by the intrinsic defects that may be produced due to the poor growth front quality (Singh et al 1986)

#### IV Luminescence properties of $\text{Al}_{0.48}\text{In}_{0.52}\text{As}$

would thus appear that the model derived by Singh et al (1986) has been largely proved inadequate by recent experimental results. Since our samples have better FWHM than Juang et al's we can assume that linewidth broadening due to clustering is minimal and possibly included within the normal alloy broadening.

##### 4.3.1.3 Bimodal Ordering in $\text{A}_{0.5}\text{B}_{0.5}\text{C}$ Semiconductor Alloys

$\text{Al}_{0.48}\text{In}_{0.52}\text{As}$  is more likely to show bimodal or structural ordering similar to that first observed in  $\text{Ga}_{0.5}\text{In}_{0.5}\text{As}$  (Nakayama and Fujita 1985) and later in other ternary and quaternary alloys. Hull et al (1986) have found evidence for a non-random distribution of Al and In on the cation sub-lattice in  $\text{Al}_{0.48}\text{In}_{0.52}\text{As}$ . A number of authors have considered the possibility of long range order in pseudo-binary alloy semiconductors suggesting that at equilibrium an ordered state was more likely to occur than clustering because different bond lengths could be accommodated without strain (Shahid and Makajan 1987). This could not be predicted using the virtual crystal approximation since average bond lengths weighed by the concentration of the different binaries are used. Ito (1986) considered the disorder contribution in  $\text{A}_{0.5}\text{B}_{0.5}\text{C}$  ternary semiconductors for bond length, lattice parameter and mixing entropy using a pseudopotential approach. He suggested that the bimodal distribution of anion-cation bond lengths could be responsible for the lattice parameter obeying Vegard's law. In bimodal ordering the normal zincblende crystal structure shows atomic ordering on the [110] planes when viewed parallel to the growth direction. This is observed in the TEM electron diffraction pattern as superstructure spots with twice the period of the lattice and indicates an ordered superlattice on the column III sub-lattice. Although a number of possible structures have been suggested it is still not clear which one is correct.

The one to one relationship between alloy composition  $x$  and energy gap in  $\text{A}_x\text{III}\text{B}_{1-x}\text{III}\text{C}^{\text{V}}$  alloys may have to be questioned. In MOVPE  $\text{Ga}_{0.5}\text{In}_{0.5}\text{P}$ , grown

lattice-matched to GaAs, under certain growth conditions (substrate temperature and III/V source ratio) a reduction of the band-gap energy of 50 meV can occur. The different band-gaps have been shown to exist for lattice matched material depending on whether it was grown randomly,  $E_g=1.9$  eV or an ordered state,  $E_g=1.85$  eV. This ordered state may have already inadvertently been observed in  $\text{Al}_{0.48}\text{In}_{0.52}\text{As}$  since Welch et al (1984, figure 4.1) observe their best linewidths at a 3% In rich composition, corresponding to a  $\sim 80$  meV shift for  $E_g$  to lower energy compared to our data and that of other groups. In sample MV402 a higher energy emission is observed at  $\sim 70$  meV above the main transition (figure 4.7). Its assignment is uncertain but it indicates that the normally observed  $\text{Al}_{0.48}\text{In}_{0.52}\text{As}$  emission may not be band-to-band or excitonic. The new emission may be a consequence of Si doping of the  $\text{Al}_{0.48}\text{In}_{0.52}\text{As}$  sample but, since growth is occurring within the rough region (section 4.2) the crystal may be forming an ordered state. So we suggest the emission could be due to bimodal ordering in the crystal since the shift in energy agrees qualitatively with that observed in  $\text{Ga}_{0.5}\text{In}_{0.5}\text{P}$  of 80 meV (Gomyo et al 1987) and  $\text{Ga}_{0.5}\text{As}_{0.5}\text{Sb}$  of 70 meV (Boguslowski and Baldereschi 1988).

It was concluded from a pseudopotential calculation that since the GaAs-InAs and AlAs-InAs atomic volume ratios were similar, then they should have similar order and disorder effects (Ito 1985). This is obviously not the case when considering the difference in linewidths from the near band-edge luminescence obtained from these material systems. Consequently, factors other than the compositional or structural properties of  $\text{Al}_{0.48}\text{In}_{0.52}\text{As}$  will be required to account for the increased linewidth compared to other III-V alloys.

#### 4.3.2 Lineshape considerations

Before attempting any fit to  $\text{Al}_{0.48}\text{In}_{0.52}\text{As}$  luminescence, the lineshape characteristics of the emission obtained should be compared to the theoretical

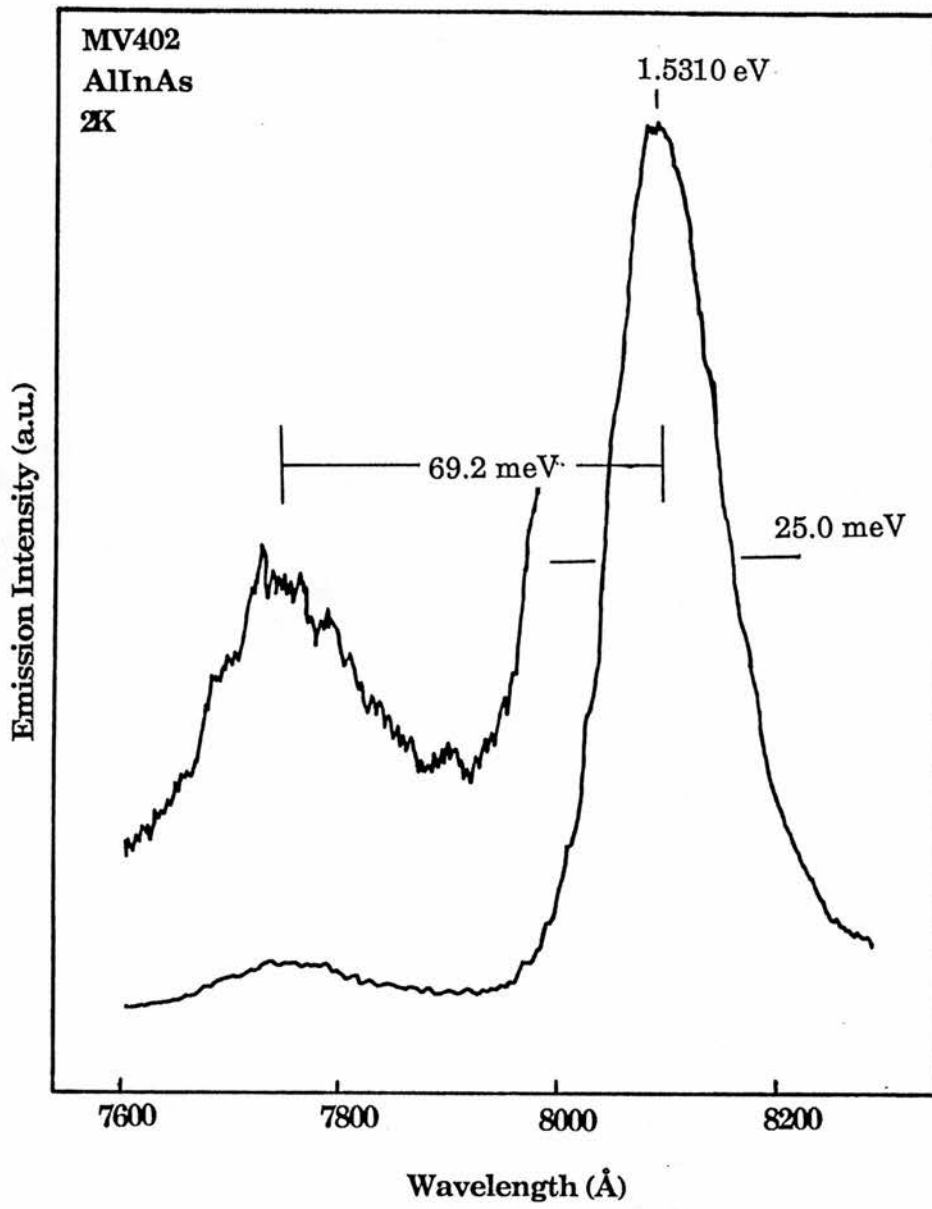


**Figure 4.7** Emission of sample MV402. A peak is observed 69.2 meV away from the main emission (see text for a discussion).

lineshapes for different transitions. All the samples used in this work have produced spectra whose lineshape is Gaussian and asymmetrically broadened to the low energy side. The lineshape of bound excitonic emission in compound semiconductors should be a Lorentzian function whose linewidth is approximately  $kT$  since the transition has no kinetic energy associated with it. Schubert et al (1984) showed that in ternary alloys the emission lineshape can be approximated by a Gaussian with the linewidth  $\sigma$  reflecting the alloy scattering (see section 4.3.1.1). If a Gaussian function were convoluted with the near band-edge transitions, as was done in  $\text{Ga}_{0.47}\text{In}_{0.53}\text{As}$  (see section 3.5), it would produce another broader Gaussian. Therefore, to first approximation the lineshape of the emission cannot be due to a simple bound exciton or convolution of excitonic transitions.

In some alloys such as  $\text{GaInAsP}$  the near band-edge luminescence has been ascribed to band-to-band transitions without considering the effects of alloy scattering. From a simple parabolic band theory the lineshape intensity  $I(\hbar\omega)$  is given by (Pearsall 1985)

$$I(\hbar\omega) \sim (\hbar\omega - E_g)^{0.5} \exp[-(\hbar\omega - E_g)/kT] \quad (4.12)$$

From this expression the low energy side of the emission increases as  $(\hbar\omega - E_g)^{0.5}$  and the high energy side decreases exponentially,  $\exp[-(\hbar\omega - E_g)/kT]$ . The emission peak maximum occurs at  $\hbar\omega_{\text{max}} = E_g + kT/2$  and the luminescence linewidth is proportional to  $1.8kT$ . So at  $\sim 4\text{K}$  the intrinsic band-to-band emission should have a linewidth of  $\sim 5\text{ meV}$  increasing monotonically with temperature to  $\sim 45\text{ meV}$  at  $300\text{K}$ . This simplified model does not take into consideration the effects of doping or impurity related emission. The low energy side of the emission spectrum normally shows an exponential increase instead of the expected parabolic dependence. Since at low temperatures ( $<10\text{K}$ ) the luminescence tends to be dominated by impurities the exponential lineshape

#### IV Luminescence properties of $\text{Al}_{0.48}\text{In}_{0.52}\text{As}$

suggests that impurity states or disorder-induced processes (Oelgart et al 1987) are present. The low energy is fitted using  $\exp(\hbar\omega - E_g)/\epsilon_t$  where  $\epsilon_t$  is the tail state parameter giving an indication of how large the tail is. The low temperature emission in most semiconductors is impurity related and since  $m_e^* = 0.10 \pm 0.01 m_0$  in  $\text{Al}_{0.48}\text{In}_{0.52}\text{As}$  then significant band-to-band transitions would not be observed until these donor levels are ionized  $>60$  K.

When using the emission lineshape given by the relationships 1.2 or 1.5 for the free-to-bound and donor-acceptor-pair, the linewidths obtained are much narrower than those in semiconductor alloys (Goetz et al 1983, Chareaux et al 1986). The effects of broadening due to alloy fluctuations has to be taken into consideration just as they have been in excitonic transitions. This was achieved by convoluting the relationship obtained for the free-to-bound donor-acceptor-pair emission with a Gaussian curve of standard distribution  $\sigma$ :

$$I(\hbar\omega) \sim \int_{-\infty}^{+\infty} \bar{I}(\hbar\omega) \exp[-0.5(E-E')^2/\sigma^2] dE \quad (4.13)$$

When this was fitted to the luminescence spectra for a particular transition a value for  $\sigma$  can be found. This value for  $\sigma$  has been found to compare well with the value estimated by Schubert's model for alloy scattering taking both conduction and valence band fluctuations into account (Charreaux et al 1986). The unfortunate consequence of the resulting convolution is that the predicted luminescence is Gaussian and featureless. Hence it is impossible to deduce the expected transition from considering lineshape alone. Therefore a theoretical fit to the spectra can only be attempted if the origin of the luminescence transition is determined from further experimental work.

Since the luminescence transitions in most alloys will show a Gaussian lineshape a fit was attempted to sample MV408 (figure 4.8). An excellent fit was

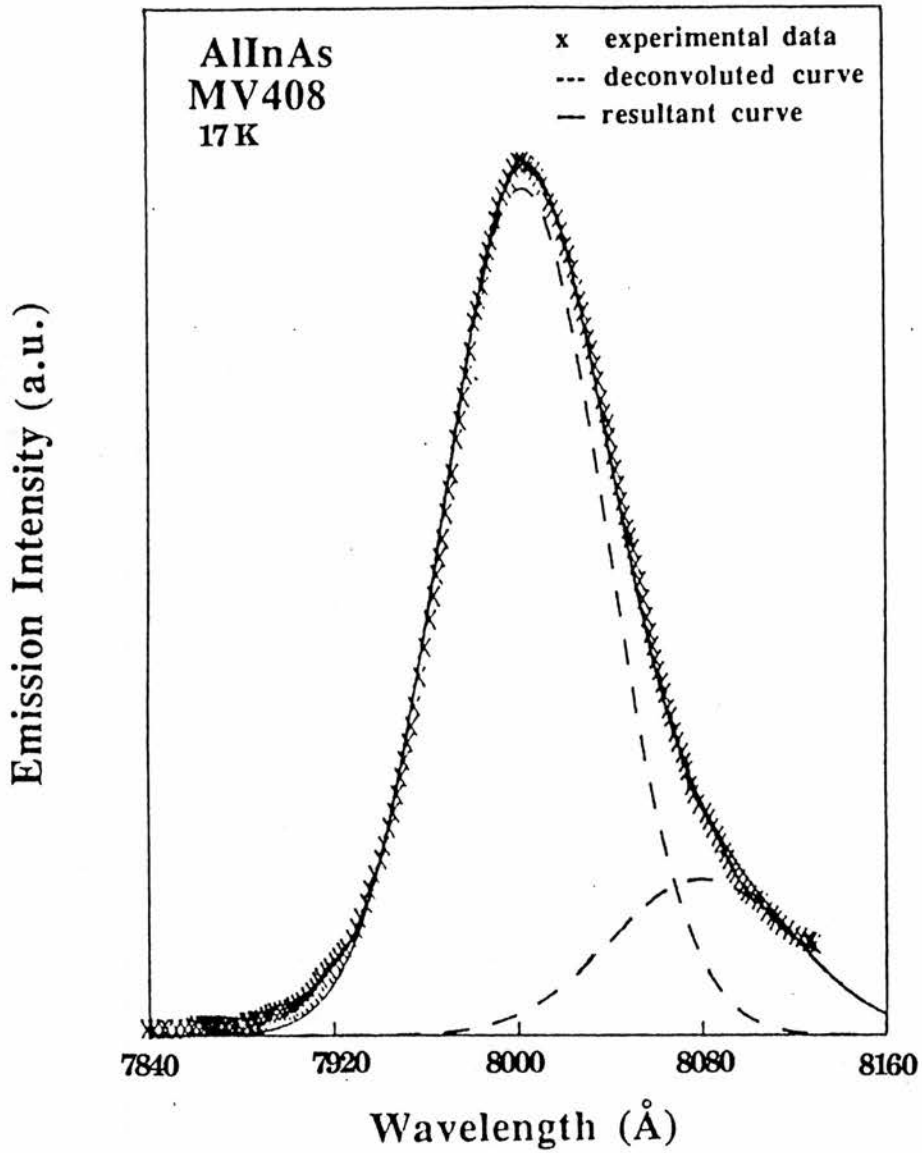


**Figure 4.8** Deconvolution of the 17 K emission spectrum using two gaussian functions. The existence of another emission occurring ~14 meV below the main emission is shown.

#### IV Luminescence properties of $\text{Al}_{0.48}\text{In}_{0.52}\text{As}$

obtained on the high energy side of the emission with a Gaussian lineshape. The asymmetrically broadened emission was deconvoluted into two Gaussian functions producing another emission, labeled peak A, separated by  $\sim 14$  meV from the main transition. No significant reduction in the linewidth occurred as a result of this deconvolution. Goetz et al (1983) showed that for  $\text{Ga}_{0.47}\text{In}_{0.53}\text{As}$  the near band-gap emission lineshape could be explained as the convolution of all the excitonic transitions normally observed in the binary. But this is difficult to justify in this instance because of the much larger  $\text{Al}_{0.48}\text{In}_{0.52}\text{As}$  linewidth. Hayne's rules states that the dissociation energy of neutral excitonic impurity complexes is approximately 10% of the impurity binding energy. So if the  $\text{Al}_{0.48}\text{In}_{0.52}\text{As}$  emission were ascribed to bound excitons the deconvoluted peak 14 meV below the main emission could not be ascribed to donor or acceptor impurities and would more likely be defect or disorder related.

On the other hand, if the main emission is assigned to donor-acceptor-pairs or free-to-bound transitions then the additional transition can easily be accounted for by another acceptor impurity. Normally photoluminescence spectra from undoped MBE grown materials are dominated by carbon related impurity emission (see section 2.1). The luminescence of most alloys also shows emission due to other impurities, such as Be or Si, which have a larger binding energy than carbon. It would not be unreasonable to expect  $\text{Al}_{0.48}\text{In}_{0.52}\text{As}$  to exhibit similar characteristics. It was found that as a consequence of Si doping the  $\text{Al}_{0.48}\text{In}_{0.52}\text{As}$  the linewidth of the emission increased to 25 meV suggesting that Si was incorporated during growth (figure 4.7).

#### 4.4 Temperature Dependence of the Emission

On increasing sample temperature the  $\text{Al}_{0.48}\text{In}_{0.52}\text{As}$  emission at 1.533 eV for sample MV411 (figure 4.3) shifts to lower energies and thermally quenches (figure 4.9). The linewidth increases monotonically with temperature and by 50

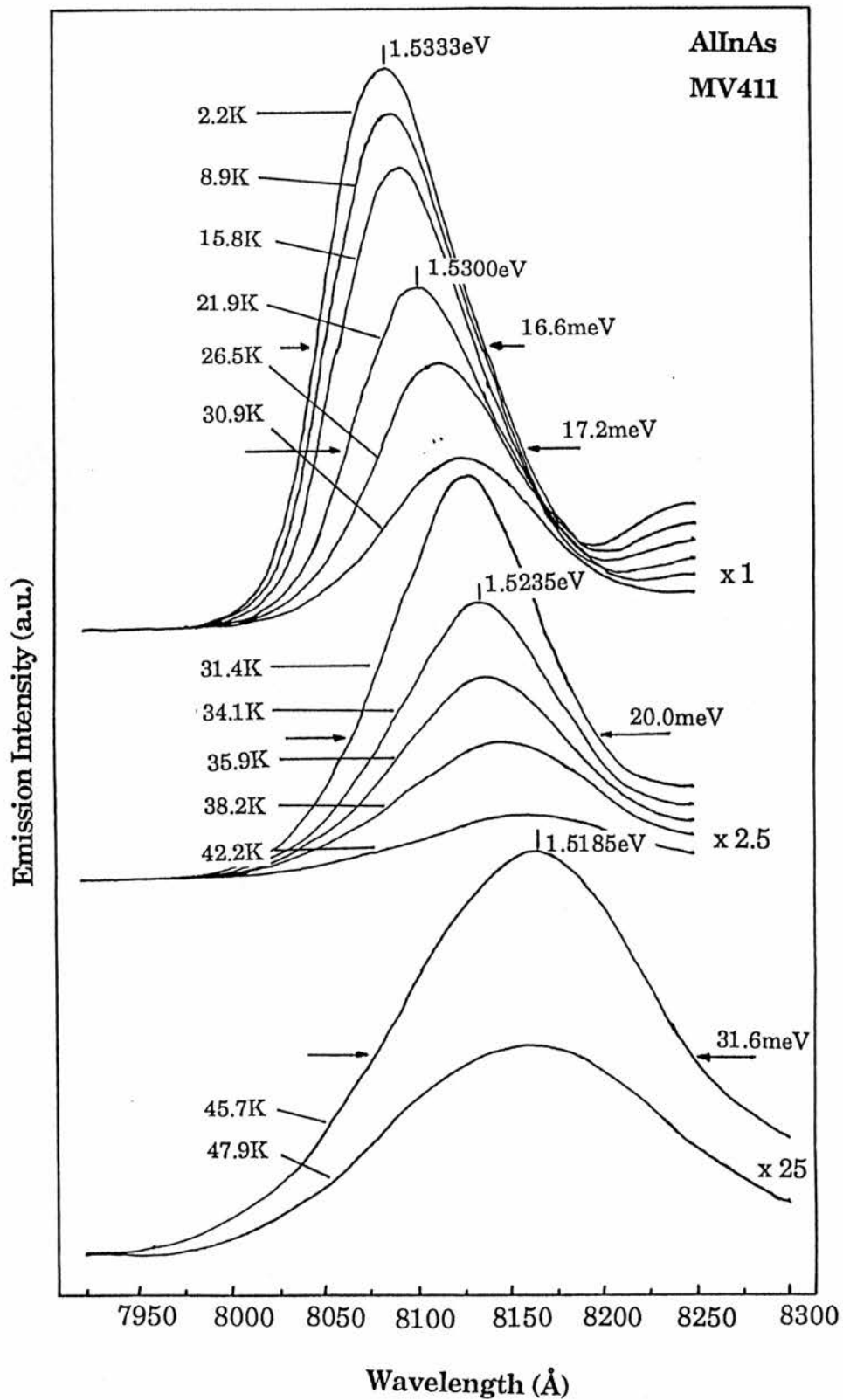


**Figure 4.9a** Temperature dependence of the  $\text{Al}_{0.48}\text{In}_{0.52}\text{As}$  emission. As the 2.2 K emission thermally quenches at 50 K an unresolved, combined peak emerges around 1.518 eV.

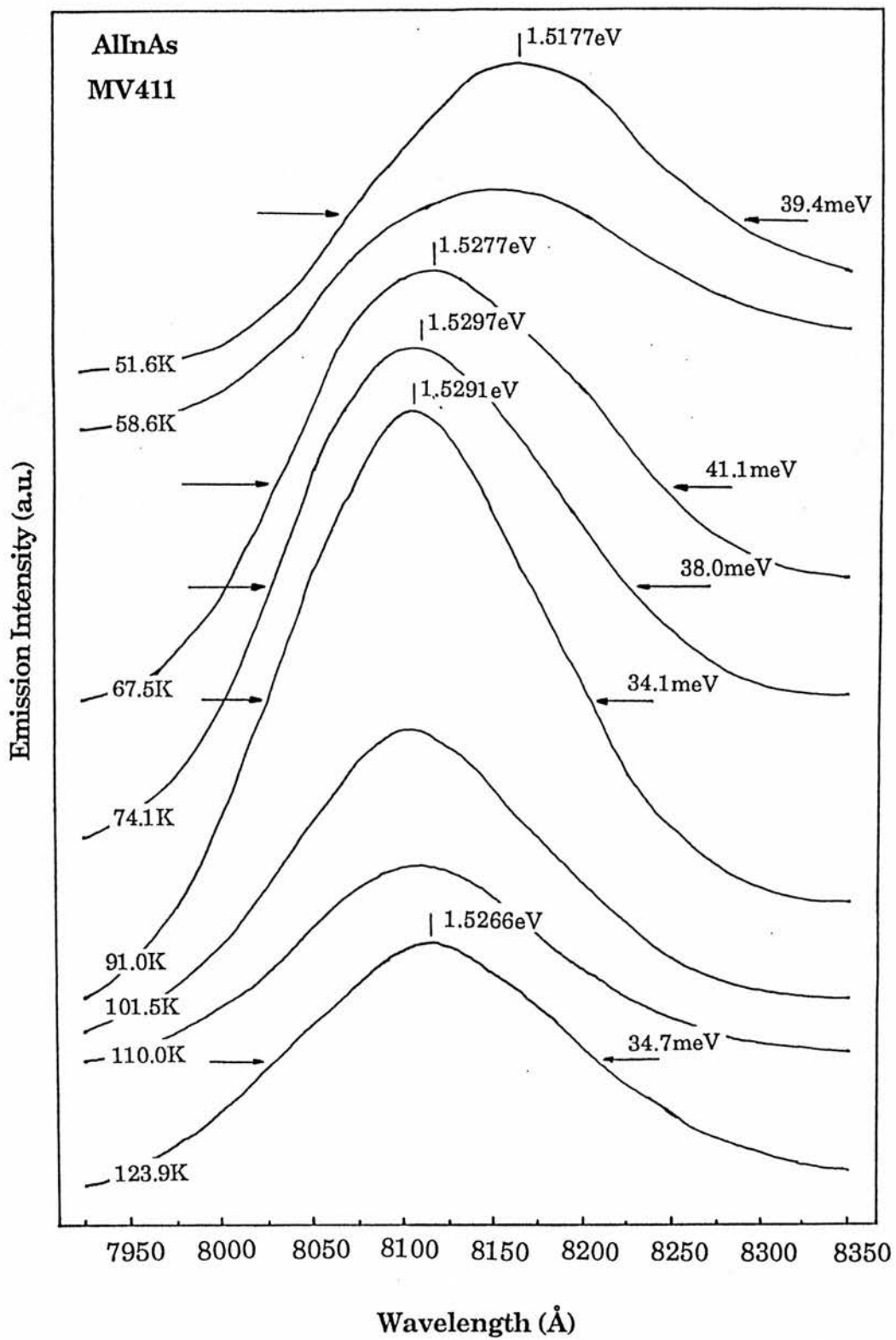


**Figure 4.9b** Temperature dependence of the  $\text{Al}_{0.48}\text{In}_{0.52}\text{As}$  emission. On increasing the temperature further to 80 K, the 2.2 K emission quenches completely leaving a new transition dominating at 1.529 eV.

#### IV Luminescence properties of $\text{Al}_{0.48}\text{In}_{0.52}\text{As}$

K the emission at 1.5177 eV is the convolution of more than one transition. Increasing the sample temperature further to 90 K apparently causes the emission to move to higher energies at 1.5291 eV. However, this is due to the low temperature transition quenching completely leaving a new transition at higher energies to dominate the emission spectrum. The same process also occurs for sample MV409 (figure 4.10). To our knowledge this is the first report of this higher energy emission in  $\text{Al}_{0.48}\text{In}_{0.52}\text{As}$ .

An attempt was made to fit the emission peak energy to the expected band-edge dependence upon temperature when compared to the empirical expression derived by Varshni (1967):

$$E_g(T) = E(0) + \frac{\alpha T^2}{(\beta + T)} \quad (4.14)$$

where  $\alpha$  is a constant (eV/K) and  $\beta$  is a constant that can be related to the Debye temperature,  $\theta_D$ . The equation is based on the assumptions that the energy gap should be proportional to  $T$  at high temperatures and proportional to  $T^2$  at low temperatures. Interpolating the Debye temperature for  $\text{Al}_{0.48}\text{In}_{0.52}\text{As}$ , assuming the validity of Vegard's law with  $\theta_D(\text{AlAs})=417$  K and for  $\theta_D(\text{InAs})=254.5$  (Madelung 1982),  $\theta_D(\text{Al}_{0.48}\text{In}_{0.52}\text{As})=335$ K was obtained. However, a plot in the form  $T^2/(335+T)$  against emission peak energy did not yield the expected straight line. Varying the value of  $\beta$  did not improve the fit except in increasing the bowing below 335 K. Fitting the emission peak energy temperature dependence to Varshni's equation gave a value of  $2.5 \times 10^{-3}$  eV/K for  $\alpha$  which is approximately an order of magnitude larger than those observed for any other III-V semiconductor. If a more realistic value is estimated for  $\alpha$  as  $\sim 5 \times 10^{-4}$  eV/K (Thurmond 1975) and this is substituted into equation 4.14 it can be seen that the  $\text{Al}_{0.48}\text{In}_{0.52}\text{As}$  emission does not follow the expected band-edge dependence with temperature (figure 4.11). Thus the low temperature emission

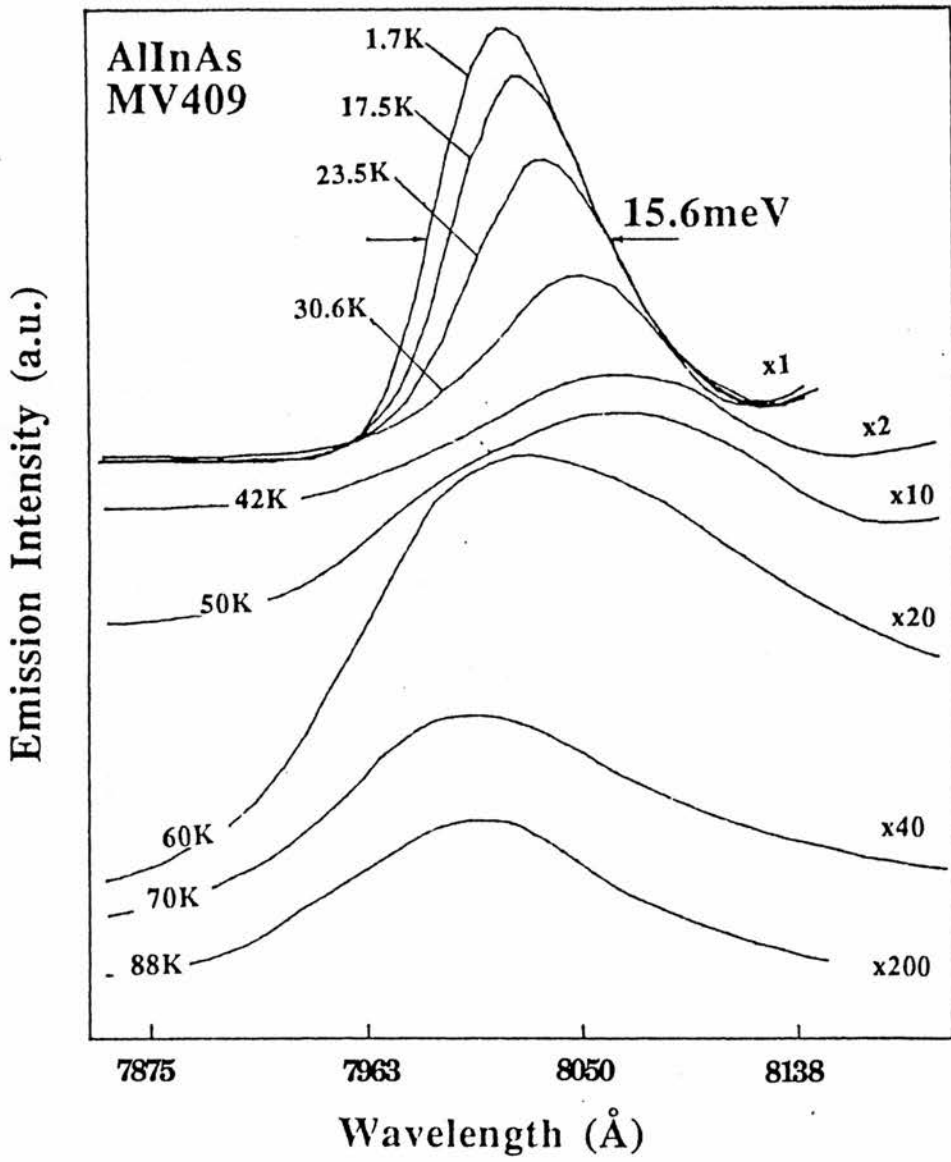
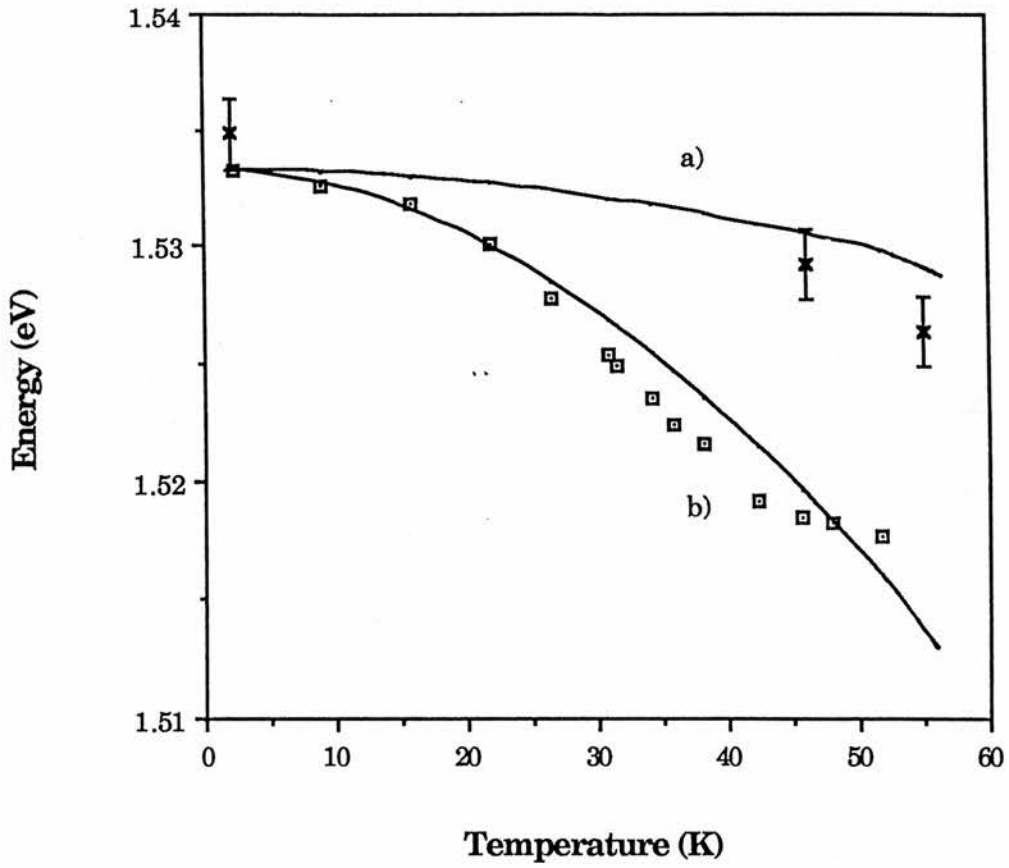


Figure 4.10 Temperature dependence of  $\text{Al}_{0.48}\text{In}_{0.52}\text{As}$  (MV409).



**Figure 4.11** Temperature dependence of the emission energy. The solid lines are fits using the expression by Varshni (1967) with a)  $\alpha=2.5 \times 10^{-3} \text{ eVK}^{-1}$  (least square fit) and b)  $\alpha=5 \times 10^{-4} \text{ eVK}^{-1}$ .

#### IV Luminescence properties of $\text{Al}_{0.48}\text{In}_{0.52}\text{As}$

is unlikely to arise from band-to-band, free-to-band or bound excitonic transitions as all these should follow the expected band-edge dependence with temperature.

The dominant 2K emission has quenched completely by 90 K (figures 4.9 and 4.10). A thermal activation energy can be determined for this process from the integrated intensity versus the reciprocal temperature (figure 4.12). The temperature dependence of the integrated intensity  $I(T)$  can be described by

$$\frac{I(T)}{I(0)} = [ 1 + C \exp(E_a/kT) ]^{-1} \quad (4.15)$$

where  $E_a$  is the activation energy and  $C$  is a temperature independent constant related to the radiative lifetime of the transition,  $\tau_r$ . An excellent agreement is obtained with equation 4.15 and the experimental points in figure 4.12 giving  $E_a=20\pm 2$  meV and  $C=1954$  eV for MV411. In the high temperature limit data can be described using  $I(T)\sim\exp(E_a/kT)$ , yielding for samples MV408, MV409 and MV411  $E_a=15.0, 20.0$  and  $17.5$  meV, respectively, giving an average of  $E_a=17\pm 3$  meV.

When equation 4.15 is applied to emission associated with donor-bound excitons the activation energy can be related to the donor ionization energy. However, in both  $\text{Ga}_{0.47}\text{In}_{0.53}\text{As}$  (see section 3.5) and GaAs (Williams and Bebb 1975) the thermalisation process for donor-bound emission shows two distinct activation energies associated with exciton and donor ionization energies. This is not the case for  $\text{Al}_{0.48}\text{In}_{0.52}\text{As}$  in which only one activation energy is observed (figure 4.12). The estimated donor ionization energy  $E_D=13.6x(1/\epsilon_0)^2(m^*/m_0)$  eV was calculated using  $m^*=0.10\pm 0.01m_0$  to give  $E_D=7.1$  meV. If  $E_a=17\pm 3$  meV were related to a donor ionization energy this would imply an unreasonably large central cell correction.  $E_a$  can only be directly related to  $E_D$  if the thermal release of carriers is a rate-limited process. If this occurs in thermal equilibrium then

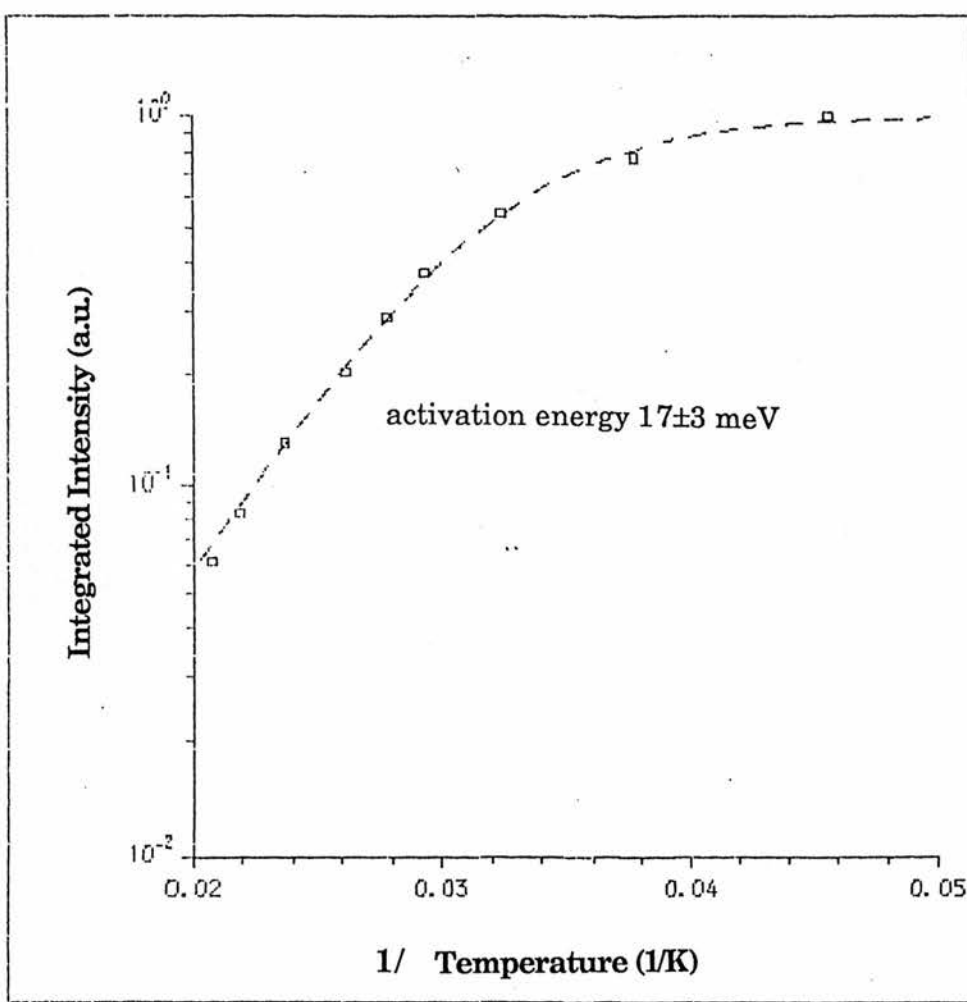


**Figure 4.12** The integrated emission intensity against inverse temperature for the AlInAs sample MV411. A theoretical fit is made using equation 4.14 to give  $c=1959$  and the activation energy  $E_a=20 \pm 2.5$  meV.

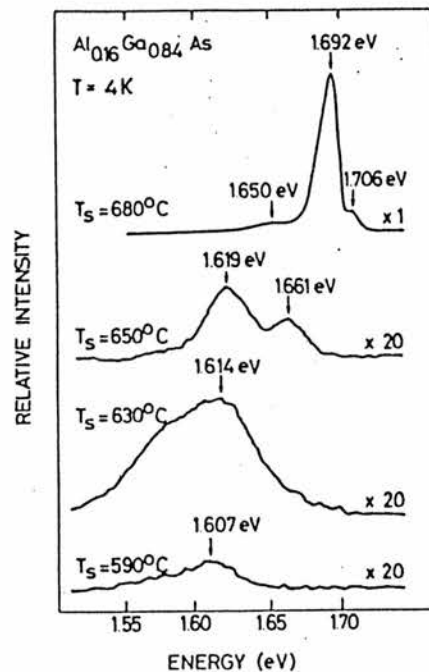


**Figure 4.13** Effect of growth temperature ( $T_s$ ) on the 4 K luminescence of  $\text{Al}_{0.16}\text{Ga}_{0.84}\text{As}$  films (Wicks et al 1981)

#### IV Luminescence properties of $\text{Al}_{0.48}\text{In}_{0.52}\text{As}$

$E_a$  is less, perhaps as low as  $E_D/2$ , depending on doping concentration (Dean 1973).

Thus, it is unlikely that the dominant emission in  $\text{Al}_{0.48}\text{In}_{0.52}\text{As}$  can be ascribed to a bound exciton transition particularly when in  $\text{Al}_x\text{Ga}_{1-x}\text{As}$  samples with high Al content the  $(D^*,A^*)$  transition dominates with the bound exciton emission observed more as a shoulder (Henning 1987). Many authors (such as Wicks et al 1981) have shown the sensitivity of the bound excitonic emission in MBE samples to substrate growth temperature (figure 4.13). Since the growth of  $\text{Al}_{0.48}\text{In}_{0.52}\text{As}$  is far from optimised (see section 4.2) the good surface morphology observed in our samples may not necessarily be an indication of material quality. Praseuth et al (1987) presented evidence that a deep acceptor-like level could be responsible for the luminescence at 2 K. When a series of  $\text{Ga}_{0.47}\text{In}_{0.53}\text{As}$  quantum wells were grown onto the InP substrate to trap impurities during growth the PL spectrum showed a shoulder due to  $(D^*,h)$  in the better epitaxial layer. Deconvolution of the emission yields an activation energy of 7 meV which corresponds well with the donor ionization energy estimated previously. We suggest that the low temperature emission in our samples does not arise from bound excitons.

If the dominant emission from  $\text{Al}_{0.48}\text{In}_{0.52}\text{As}$  is due to  $(D^*,A^*)$  then the activation energy derived would still be associated with donor ionization. It has been found that as  $\text{Al}_x\text{Ga}_{1-x}\text{As}$  approaches the  $\Gamma$ -X cross-over, the activation energy associated with donor ionization increases and the optically active donor becomes L-like for  $x > 0.35$  (Dingle et al 1979). Similarly, Pearah et al (1985) showed that the free exciton binding energy increased sharply above  $x > 0.25$ , well away from the  $\Gamma$ -X cross over, due to multi valley contributions to the effective mass. Evidence already exists for non  $\Gamma$  contributions to the donor effective mass in  $\text{Al}_{0.48}\text{In}_{0.52}\text{As}$  since high pressure Hall measurements find the electron

#### IV Luminescence properties of $\text{Al}_{0.48}\text{In}_{0.52}\text{As}$

concentration to decrease with applied pressure with a corresponding shift in the  $E_D$  of  $\sim 3 \text{ meV kbar}^{-1}$  (Ben Amor et al 1988) or  $\sim 2.5 \text{ meV kbar}^{-1}$  (Holmes 1988). Holmes (1988) postulated that applying pressure populates an electron trap but no carrier freeze out to a deeper level was observed with increasing temperature, although a metastable state was shown to exist during pressure cycling. We suggest that our emission and the activation energy are not due to a simple  $\Gamma$ -type donor level. This is confirmed by recent ODMR measurements where, at maximum electric field and s/n ratio, an effective mass of  $m^*=0.1704 m_0$  was obtained (Kamah'am 1988). Using the effective mass approximation as before this corresponds to a donor ionization energy of 14.2 meV which is within the error range of  $E_a=17\pm 3 \text{ meV}$ . Ben Amor et al (1988) found the donor activation energy to be small  $<30 \text{ meV}$  and decrease rapidly with increased doping density, 26 meV at  $4 \times 10^{16} \text{ cm}^{-3}$  to 6.3 meV at  $6.3 \times 10^{17} \text{ cm}^{-3}$  corresponding to the donor level impurity broadening. We tentatively assign the low temperature emission in our samples to a  $(D^*, A^*)$  which implies that the higher energy transition at increased temperatures will be a  $(e, A^*)$  transition. This transition dominates  $\text{Al}_{0.34}\text{Ga}_{0.66}\text{As}$  emission above 50K (Henning and Ansems 1987).

#### 4.5 Dependence on Excitation Power Density

The interpretation of data obtained varying the CW excitation power density while monitoring the integrated luminescence intensity can prove difficult, mainly because the competing non-radiative transitions are unknown. In alloys such as  $\text{Al}_{0.48}\text{In}_{0.52}\text{As}$  with a high Al content it is further complicated as many deep levels exist providing many alternative channels other than the near band-edge luminescence. The emission integrated intensity  $PL(I)$  varies with incident excitation power density  $P_{in}$  according to the relationship (Zhongying et al 1987)

$$PL(I) = c P_{in}^s \quad (4.16)$$

#### IV Luminescence properties of $\text{Al}_{0.48}\text{In}_{0.52}\text{As}$

where  $c$  is a constant and it is assumed that no saturation occurs. At 2.2 K the emission for samples MV409 and MV411 has an excitation power density that is slightly less than unity  $s=0.95$  and  $0.99$ , respectively (figure 4.15). Many authors show the excitonic emission to have  $s \geq 1$  depending on the unknown non-radiative channels, and for weak excitation the  $(D^{\circ}, A^{\circ})$  transition has  $s=1$  (Dean 1973). The  $(D^{\circ}, A^{\circ})$  emission intensity is expected to saturate with increased excitation power density, in our sample this behaviour was not observed probably because the excitation power density was too low. Based on the observation of  $s < 1$  we suggest that the main emission arises from  $(D^{\circ}, A^{\circ})$  transitions at low temperatures. The exponent  $s$ , in equation 4.16 depends on the temperature for the new high energy emission (see figures 4.9 and 4.10), for MV411  $s=1.86$  at 59.2 K and  $s=2.05$  at 79.8 K. In this case when  $s > 1$  it indicates a transition that is free-carrier-associated such as free-to-bound or band-to-band. The  $\sim P_{in}^2$  power dependence occurs at much reduced radiative efficiencies compared to the transition at 2.2 K.

If the low temperature transition were  $(D^{\circ}, A^{\circ})$  then as the excitation power density increases the emission peak should move to higher energies. Only the emission from sample MV411 is observed to move by  $\sim 0.95 \pm 0.25$  meV/decade (figure 4.16). This result may be sample dependent or alternatively since the  $\text{Al}_{0.48}\text{In}_{0.52}\text{As}$  linewidth is large a slight energy shift of a relatively deep  $(D^{\circ}, A^{\circ})$  transition would not be resolved (see section 4.6). It should also be pointed out that since  $s \sim 1$  for MV411 at 2.2 K then it is more likely to show an energy shift.

#### 4.6 Selective Photoluminescence Excitation

By using the narrow bandwidth of dye lasers, structure normally unresolved in PL spectra can be enhanced by excitation techniques. The method of selective excitation can be used to increase the intensity of exciton luminescence and their associated two-electron and two-hole transitions,

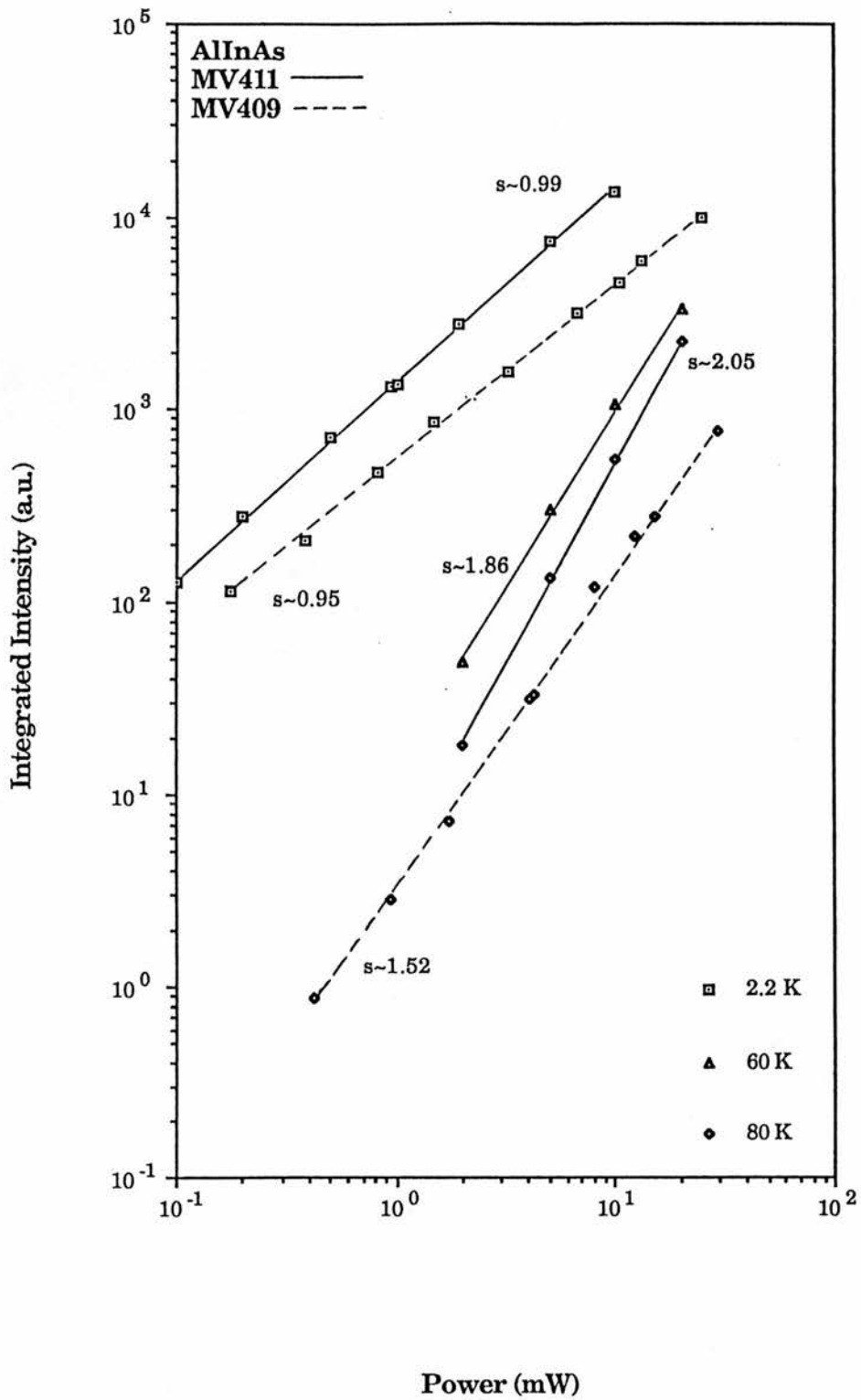


**Figure 4.15** Dependence of the integrated emission intensity upon excitation power density. At 2.2 K,  $s < 1$ , suggests that the emission might not be due to bound excitons since  $s \geq 1$  for them. The higher energy emission has  $s \geq 1.5$  and increases with temperature indicating the transition is due to free carriers.

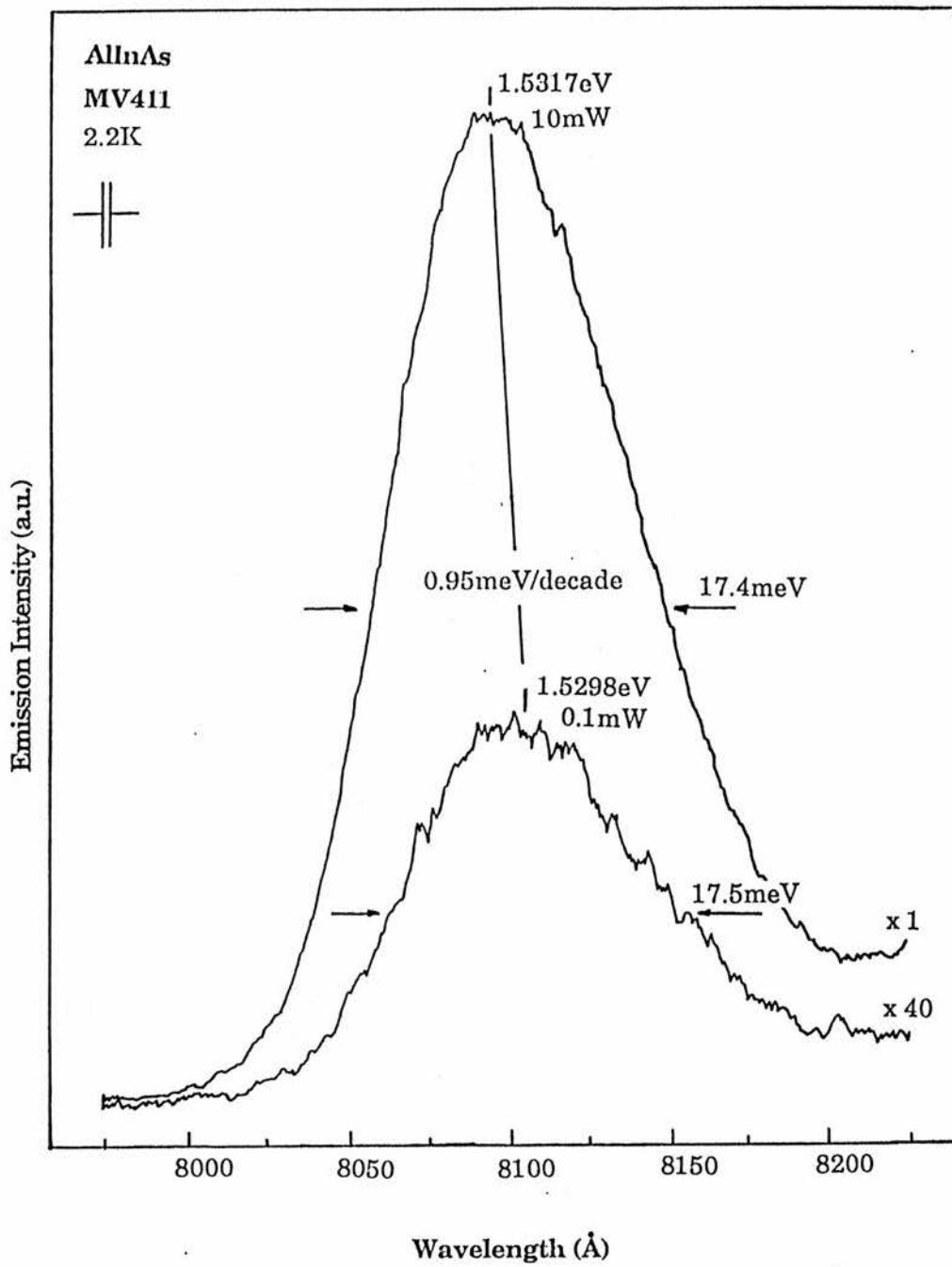


**Figure 4.16** Shift in the emission peak for MV411 to higher energies as the excitation power density is increased.

#### IV Luminescence properties of $\text{Al}_{0.48}\text{In}_{0.52}\text{As}$

particularly those of the minority species. The use of photoluminescence excitation (PLE) is most powerful for  $(D^{\circ}, A^{\circ})$  transitions in which unresolved emission can show the fine structure described by equation 1.3. In PLE the luminescence is sensed in a ground state,  $(D^+, A^+)$  as the laser excitation energy increases and donors and acceptors are observed in their excited states. In the excitation process of a  $(D^{\circ}, A^{\circ})$  photons are absorbed through three types of process: a) a direct transition within the donor-acceptor pair, b) excitation via the conduction band and c) band-to-band transitions (figure 4.17). The observation of transitions within the donor-acceptor band requires impurity concentrations  $<10^{16} \text{ cm}^{-3}$  as a higher concentration of impurities cause broadening of the excited states and merging of the peaks into a structureless background. This background is a consequence of energy transfer between  $(D^{\circ}, A^{\circ})$  with different  $r_{DA}$ . It seems unlikely that  $\text{Al}_{0.48}\text{In}_{0.52}\text{As}$  will show any fine structure in its PLE spectra since C-V measurements gave  $n \sim 10^{16} \text{ cm}^{-3}$  and alloy scattering will further increase linewidth broadening. Non-selective excitation of distant pairs, sensed towards the low energy part of  $(D^{\circ}, A^{\circ})$  emission, causes a broad threshold to appear near  $E_g - E_A$  (Dean 1973). Here an electron is excited into the conduction band leaving a hole in the acceptor (1S) state which migrates and is bound into the donor ground state (Figure 4.17b). Hence the excitation process  $(D^+, A^+) \rightarrow [D^+, A(1S)] + e$  occurs at a photon energy  $\hbar\omega_e$ , assuming  $E_A > E_D$  from equation 1.3 we find

$$E_g - E_A + \frac{e^2}{4\pi\epsilon_0\epsilon_r r_{DA}} \leq \hbar\omega_e \quad (4.17)$$

so for distant  $r_{DA}$  the lowest photon energy for an excitation process is  $E_g - E_A$  therefore  $E_A$  can be estimated if  $E_g$  is known.

The PLE apparatus is the same as the photoluminescence apparatus shown in figure 2.5 but the dye laser was used as the excitation source with Stiryl 9 dye

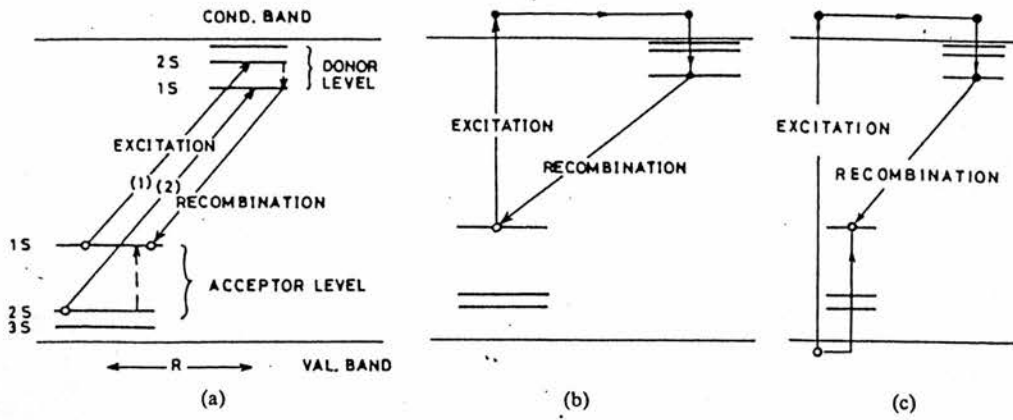


**Figure 4.17** Excitation processes for the donor-acceptor pairs in semiconductors. a) Transition within the pair, b) bound-to-free transition, and c) band-to-band transitions (Nakajima and Yamaguchi 1979)

#### IV Luminescence properties of $\text{Al}_{0.48}\text{In}_{0.52}\text{As}$

which had a tuning range of 800-890 nm. The laser wavelength was calibrated to a micrometer using the monochromator to give  $\lambda_{\text{laser}}(\text{\AA})=6916.7+3128.7x$  ( $0.35 < x < 0.65$ ); this calibration was checked periodically. Since the PLE spectra were obtained on a steadily rising background of dye laser power (10-150 mW), the spectra were taken point by point, along with a laser power reading, and deconvoluted accordingly. As the dye laser wavelength was varied it was not found necessary to optimise the emission indicating that no movement of the laser spot on the sample occurred.

A PLE spectrum was first taken of sample MV402 since it had shown the highest luminescence efficiency of all the samples screened. In figure 4.18 both the photoluminescence spectrum peaking at 1.5252 eV and the PLE spectrum sensed at 1.5176 eV are superimposed: a large shift of ~35 meV occurs between the PL and PLE spectrum. This virtually rules out the emission being due to bound excitons since in  $\text{Al}_{0.24}\text{Ga}_{0.76}\text{As}$  using PLE and sensing at the bound exciton transition the exciton binding energy was found to be 2.4 meV (Schubert and Ploog 1985). Our samples have shifts between the PL and PLE spectra similar in magnitude to those observed by Schubert and Ploog for a  $(e, A^{\circ})$  transition with a binding energy of 25 meV for a carbon acceptor. In figure 4.18 the emission threshold of 1.534 eV was obtained by extrapolating the curve to zero as done by Nakashima et al (1979). The difference between the sensing energy at 1.5176 eV and the threshold at 1.534 eV is 16.4 meV which is consistent with the activation energy of  $17 \pm 3$  meV obtained previously. To estimate a value for  $E_A$  the band-gap energy needs to be known. Due to the limited tuning range of the dye laser only the onset of band-to-band transitions are observed at 1.575 eV. As would be expected, the approximate energetic width of the PLE shoulder, which is ascribed to  $(e, A^{\circ})$  transitions, is similar to the linewidth of the sensing luminescence transition. In order to increase the energetic tuning range and observe band-to-band transitions the dye laser was replaced by a stabilized white

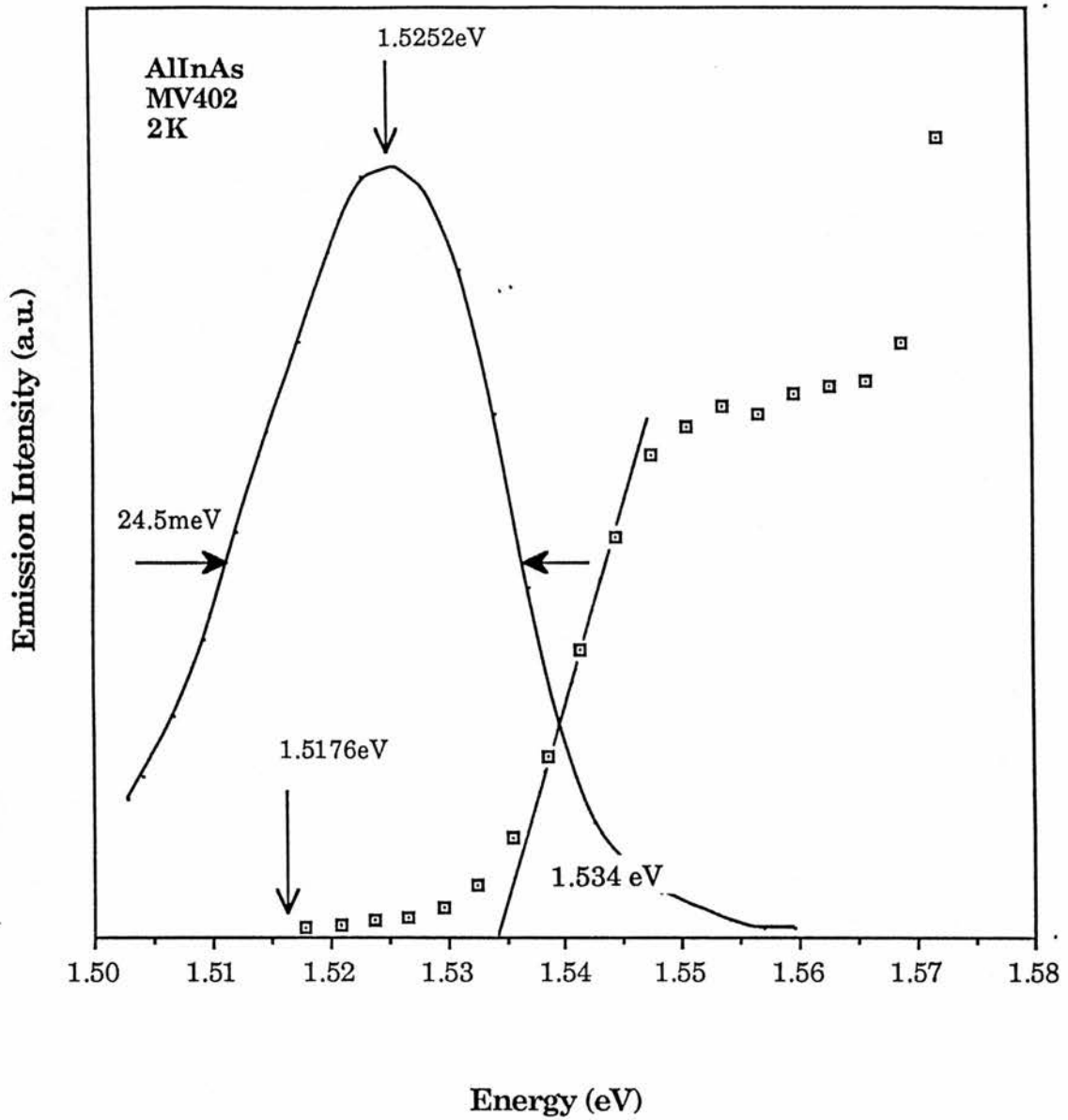


**Figure 4.18** 2 K photoluminescence ( $D^*,A^*$ ) and PLE (taken point by point) of  $Al_{0.48}In_{0.52}As$  (MV402). A shoulder shifted by  $\sim 35$  meV from the sensing position at 1.5176 eV can be seen.

light source and mini monochromator. But no signal could be observed from the sample possibly due to the low power density of the source. Praseuth et al (1987) using a similar arrangement to ours obtained PLE spectra for their samples and found the band-to-band transition to occur at 1.62 eV. If we use this value for  $E_g$  in our samples then the acceptor binding energy is 86 meV consistent with the results Praseuth et al obtained. This implies that the emission from our samples is due to 'deep' ( $D^0, A^0$ ) transitions. This has important implications when estimating  $E_g$  from PL spectra and for the magnitude of confinement calculated in superlattice structures.

Leaving the sensing position unchanged at 1.5176 eV and increasing the sample temperature then the PLE emission, assigned to a ( $e, A^0$ ) transition, should follow the expected band-edge temperature dependence (figure 4.19). Since the acceptor impurity distribution should reflect the compositional variation of the band-edge due to alloy fluctuations (section 4.3.1.1) then the acceptor emission-edge in the PLE spectra can be approximated by a Gaussian function. A best fit to the emission-edge of the spectra in figure 4.19 gives the equivalent FWHM as  $2.36\sigma$  and peak energy,  $E_p$ , as shown in figure 4.20. The increase of the linewidth with temperature, 5.8 meV, is consistent with that associated with thermal broadening of the emission. Plotting the values obtained for  $E_p$  on figure 4.11, shifted accordingly in energy, shows a reasonable agreement with that of the expected band-edge temperature dependence. But the observed emission shift with temperature is the product of two effects; the band-edge shrinkage and a change in the sensed  $r_{DA}$ . As the temperature is increased the PL emission shifts to lower energies (figure 4.9) causing the energy to see smaller  $r_{DA}$ , so, the coulombic term in equation 4.17 becomes more important accounting for an additional shift of the emission of 4-5 meV (c.f. Nakashima et al 1979). Thus, the emission shift is slightly larger than that of the expected band-edge dependence in figure 4.11.

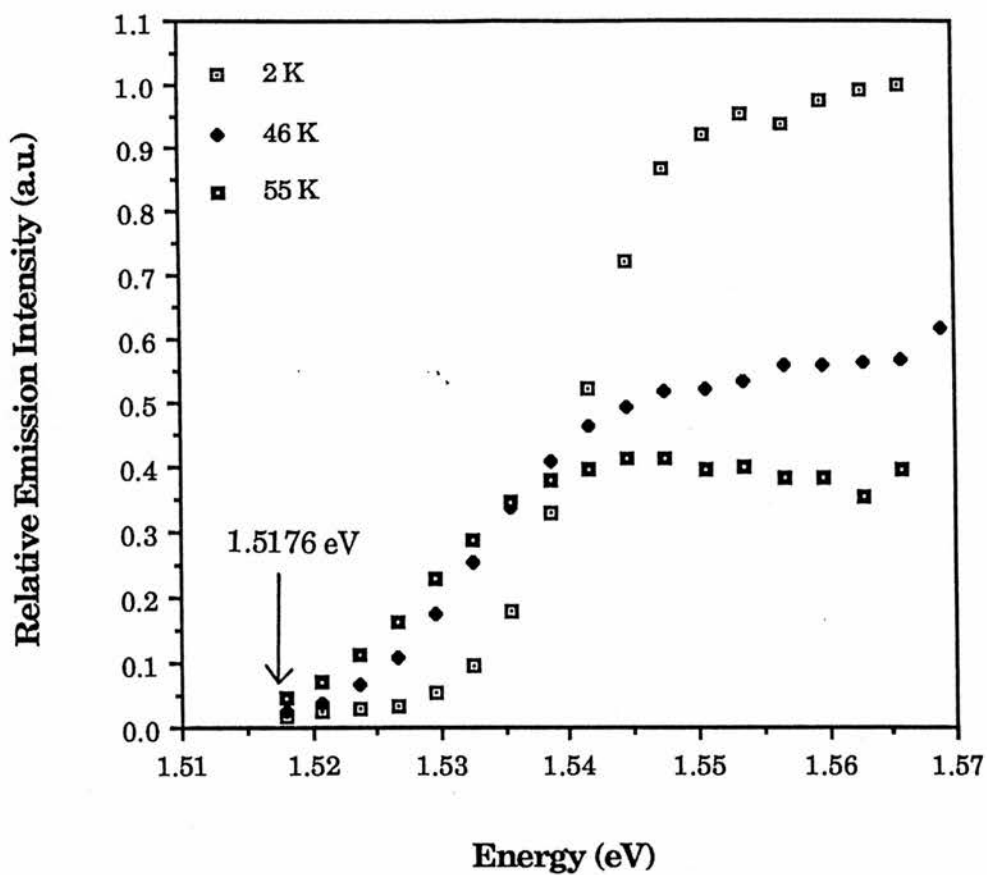


**Figure 4.19** The temperature dependence of the PLE emission leaving the sensing position unchanged at 1.5176 eV. The spectra are scaled relative to the 2 K spectrum showing the emission does not quench like the (D\*,A\*) transition (figure 4.9).

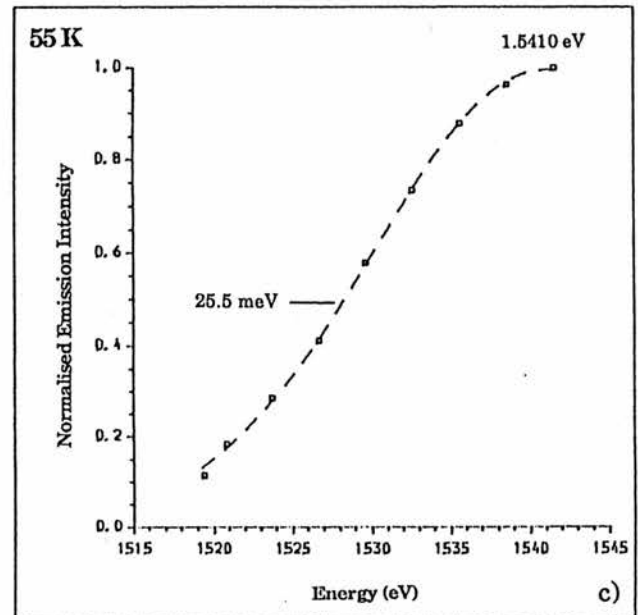
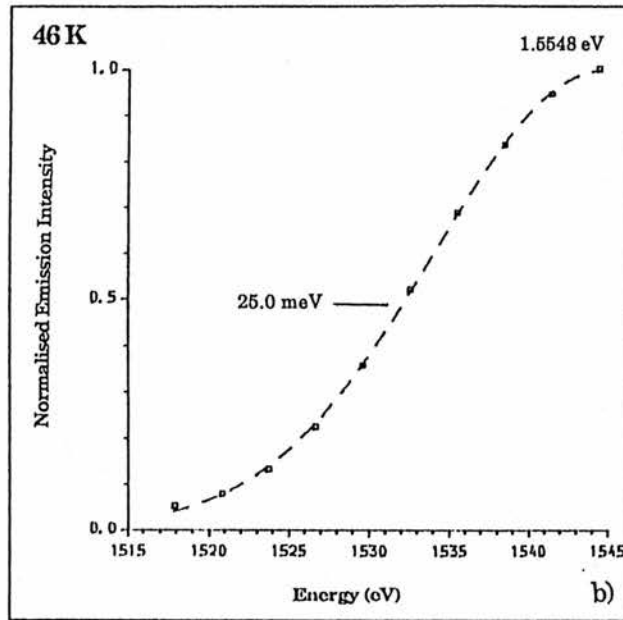
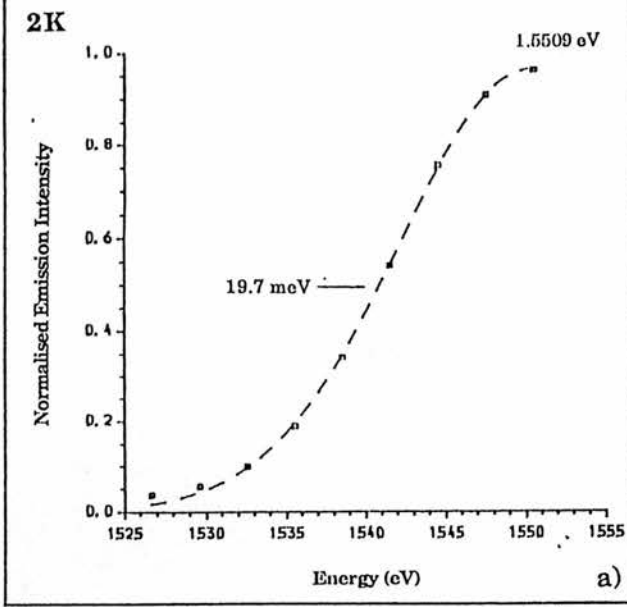


**Figure 4.20** Fitting a Gaussian function to the emission-edge in figure 4.19 gives an equivalent FWHM and peak maximum for the emission.

Sample MV402 was Si doped and the increased linewidth for PL emission suggests that Si has been incorporated during growth (figure 4.18). When PLE spectra were taken for MV411 the  $(e, A^*)$  transition shoulder was no longer clearly defined (figure 4.21). The shallow rising edge could be due to Si impurities with the main emission plateau at 7950 Å due to carbon, the background impurity. Changing the sensing wavelength from the emission peak at 8086 Å in MV411 to longer wavelengths at 8160 Å did not shift the relative position of the shoulder showing that the emission at the peak is due to  $(D^*, A^*)$  at distant  $r_{DA}$  (equation 4.17).

### 4.7 Summary

Until this work was completed no detailed study of the near band-edge luminescence of  $\text{Al}_{0.48}\text{In}_{0.52}\text{As}$  was available to the best of our knowledge. The main problem in assigning the emission was linked to the much broadened linewidth compared to that of other alloys. The conventional broadening mechanism of alloy scattering that accounts for the observed linewidths in  $\text{Al}_x\text{Ga}_{1-x}\text{As}$  and  $\text{Ga}_{0.47}\text{In}_{0.53}\text{As}$  does not suffice in the case of  $\text{Al}_{0.48}\text{In}_{0.52}\text{As}$ . An additional broadening mechanism of statistical alloy scattering was postulated. However, this mechanism seems unlikely since evidence exists for bimodal (structural) ordering in many alloys including  $\text{Al}_{0.48}\text{In}_{0.52}\text{As}$ . The results presented here suggest that the low temperature emission in  $\text{Al}_{0.48}\text{In}_{0.52}\text{As}$  is not excitonic but due to relatively 'deep'  $(D^*, A^*)$  transitions thereby explaining the large linewidths reported previously. The experimental evidence for this transition is:

a) the emission does not follow the expected temperature dependence of the band-edge,

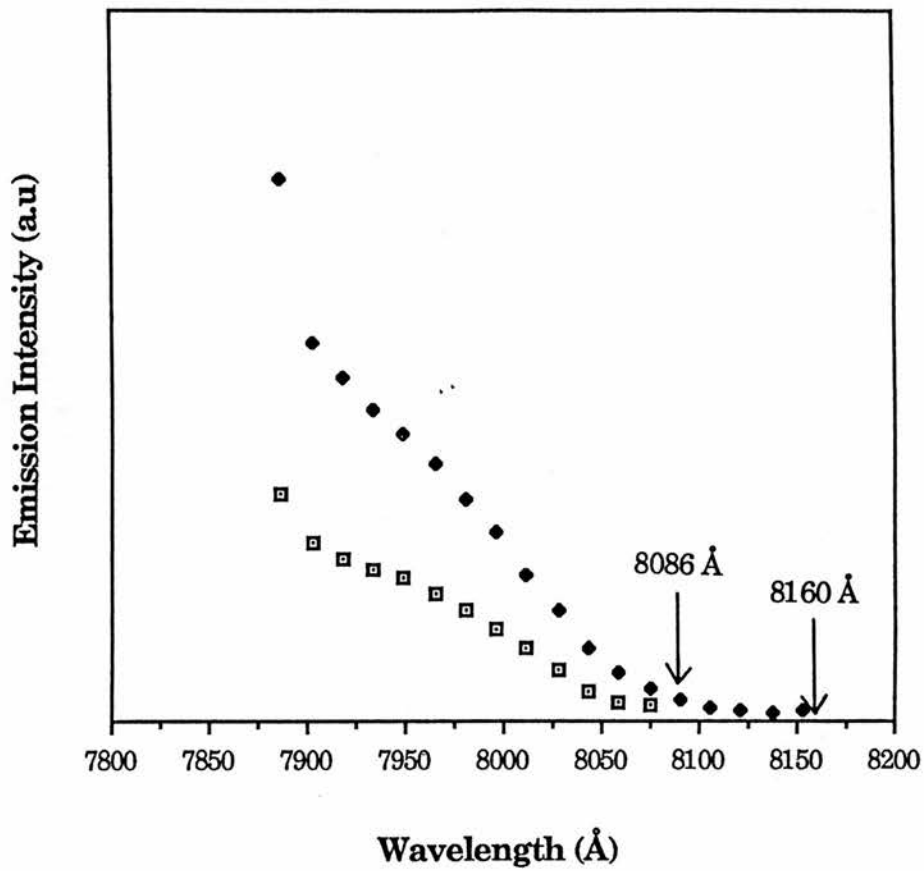


**Figure 4.21** Varying the energetic position of the sensing the PLE emission (c.f. figure 4.3) does not change the emission threshold showing that distant rDA are being sensed.

#### IV Luminescence properties of $\text{Al}_{0.48}\text{In}_{0.52}\text{As}$

b) the emission quenches with an activation energy,  $E_a=17\pm 2.5$  meV, which cannot be attributed to a simple  $\Gamma$ -type donor but possibly to a L-X mixed donor level,

c) on quenching a new high energy emission is observed, the linewidth of which is not consistent with band-to-band transitions and since the band-edge does not appear to be observed in the PLE spectra the emission is ascribed to a  $(e, A^\circ)$  transition.

d) A large shift is observed between the PL and PLE spectra,  $\sim 35$  meV, again showing that the emission is not excitonic and that it is consistent with a relatively deep acceptor of  $\sim 85$  meV.

## V LUMINESCENCE FROM QUANTUM WELL STRUCTURES

	<u>Page</u>	
5.1	Introduction	102
5.2	Review of previous work	103
5.2.1	Impurity and Exciton Binding Energy	104
5.2.2	Interfacial Disorder and Growth Interruption	107
5.2.3	Band Offset	109
5.3	Lineshape and Linewidth Considerations	110
5.4	GaAs-Al <sub>x</sub> Ga <sub>1-x</sub> As	115
5.4.1	Intrinsic and Extrinsic Emission	115
5.4.1.1	Temperature dependence	118
5.4.1.2	Excitation Power Density Dependence	119
5.4.1.3	Doping Study	120
5.4.2	Carrier Capture	121
5.4.3	Growth on Misorientated Substrates	124
5.4.3.1	Barrier of composition x=0.3	127
5.4.3.2	Barrier of composition x=0.4	129
5.4.3.3	Barrier of composition x=0.2	130
5.5	Ga <sub>0.47</sub> In <sub>0.53</sub> As-InP	130
5.5.1	Review	131
5.5.2	Temperature dependence	132
5.5.3	Some Comments	135
5.6	Pseudomorphic HEMTs	135
5.7	Summary	137

## 5.1. Introduction

In considering the optical properties of GaAs-Al<sub>x</sub>Ga<sub>1-x</sub>As and Ga<sub>0.47</sub>In<sub>0.53</sub>As-InP quantum well structures we will concentrate mainly on impurity incorporation and interface quality. Using photoluminescence, while varying excitation power density and sample temperature, is a sensitive probe of the quantum well material quality, in particular of the interface region from which monolayer fluctuations in the well thickness have been observed by many groups. It was shown before (chapter 1) that the low temperature emission should be dominated by a free exciton transition. In a brief review of the extensive literature in the area of GaAs-Al<sub>x</sub>Ga<sub>1-x</sub>As quantum wells we will present our own data as it is representative of the physical mechanisms of the luminescence observed by other groups. We also include, to the best of our knowledge, the first complete description of all the scattering mechanisms affecting luminescence linewidth in quantum well structures.

The assignment of the various transitions observed in the excitonic region of our GaAs-Al<sub>x</sub>Ga<sub>1-x</sub>As samples was made by varying sample temperature and excitation power density along with careful deconvolution of the spectra. A later comparison of the emission from Si-doped and undoped well structures justified the initial assignment. In a study of carrier capture of a quantum well the temperature dependence of the well emission was considered in more detail. This provided the background necessary for a study of the growth of quantum structures on [100] substrates off-cut in [110] direction. A brief summary of emission data obtained from some Ga<sub>0.47</sub>In<sub>0.53</sub>As-InP quantum well samples has also been included for comparison.

## 5.2 Review of previous work

It is beyond the scope of this work to give a comprehensive review of all the relevant and related literature in the area of the optical properties of GaAs- $\text{Al}_x\text{Ga}_{1-x}\text{As}$  quantum wells. In this section we will summarize the main points covered by the most important review articles and then concentrate on the question of impurity incorporation and interface quality that is explored in this work. When reviewing the literature it should be noted that some groups may have presented results that are sample dependent with an interpretation based accordingly on them.

Miller and Kleinman (1985) considered the properties of excitons in GaAs- $\text{Al}_x\text{Ga}_{1-x}\text{As}$  quantum wells including the topics of exciton binding energy, modulation doped structures and band-gap discontinuities. In their review they include a summary of most of the original work completed in this area at Bell Laboratories. Delande (1986) provides the background to PLE applied to well structures, makes some comment on the contentious issue of room temperature excitonic emission and discusses the luminescence obtained from various material systems. In the most recent review of the optical properties of quantum wells, Weisbuch (1987) covers the problems of impurity related emission and interface disorder, which can have important consequences for laser diodes. The application of quantum well structures in optoelectronics including the fabrication of laser diodes and other novel devices is presented by Okamoto (1987) and the recombination dynamics of excitons and free carriers is considered by Fouquet and Burnham (1986). An excellent review, mainly of the electrical properties, of the physics of quantum structures has been given by Kelly and Nicholas (1985) with Drummond et al (1986) providing further information on the device applications of modulation doped structures.

Two parameters have a dominant effect on the luminescence, doping and quantum well width, generally with wider wells being more bulk like and narrow wells showing a single Gaussian like peak. A two-peak structure has been observed by many groups (figure 5.1) with low energy emission assigned, on occasions, to biexcitations (Cingolani et al 1988), exchange interaction splitting (Bauer et al 1987), impurities (Shanabrook and Comas 1984) and interface islands (Deveaud et al 1986).

### 5.2.1 Impurity and Exciton Binding Energy

Although we noted in chapter 1 that the intrinsic free-exciton emission can dominate the luminescence from GaAs quantum wells, impurity related emission still provides an important contribution to the spectrum. It has been shown that for a strictly 2D hydrogenic impurity of binding energy  $E_b$ , this will tend to  $4 E_b$  ( $0.25 E_b$ ) at well centre (edge). Bastard (1981) first calculated the binding energy of a donor or acceptor as a function of well thickness and impurity position in a quantum well with infinite barrier height. It was found that as the well width increases from zero, the 2D limit, the binding energy of an impurity placed at the well centre (edge) will decrease from  $4 E_b$  to  $1 E_b$  ( $0.25 E_b$ ) and that impurity degeneracy with respect to impurity position in the well was lifted leading to band formation. The resulting density of states can exhibit two peaks associated with impurities at well centre (statistically dominant) and well edge (Lane and Greene 1983). But donors in a well of finite barrier height were found to have a maximum binding energy at some critical well width,  $\sim 15\text{-}60 \text{ \AA}$ , as shown in figure 5.2 (Mailhiot et al (1982), Greene and Bajaj (1983a)). Since, as the well width is further increased, the impurity wavefunction penetrates the barrier material, the impurity binding energy tends to the bulk value of the barrier material.

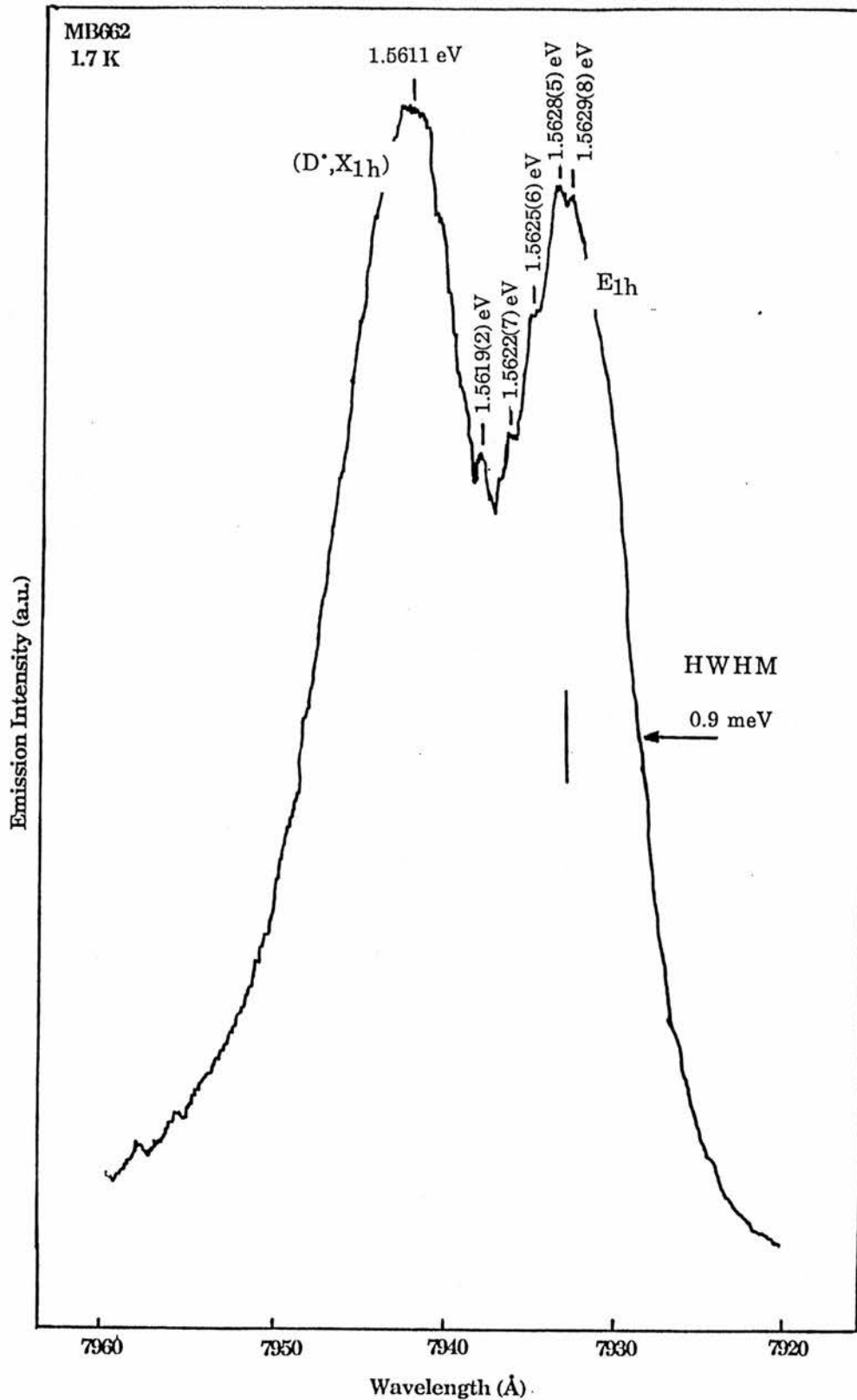


**Figure 5.1** Typical luminescence spectrum, obtained from a GaAs-Al<sub>0.3</sub>Ga<sub>0.7</sub>As 84 Å multiple quantum well sample. The two-peak structure has been observed by many groups and assigned to interface fluctuations, donor bound impurities, biexcitons and exchange interaction splitting.

## V Luminescence from Quantum Well Structures

Photoluminescence has been used to probe donors levels in quantum wells of various widths (Shanabrook and Comas (1984), Reynolds et al (1984)). Shanabrook and Comas (1984) consistently found an emission peak  $\sim 1-2$  meV below that of the  $E_{1h}$  transition in wells that have been Si-doped either at the well centre or edge. Edge-doped samples showed an additional transition  $\sim 2$  meV above  $E_{1h}$  due to the reduced binding energy of these donors (figure 5.2). This work was extended to include Raman scattering and far infrared absorption measurements of donor binding energy which produced results that were less ambiguous and in good agreement with theoretical predictions discussed above (Chaduri and Bajaj (1984), Shanabrook (1986)).

Photoluminescence is a better probe of acceptor impurities as there is proportionally less error in estimating acceptor binding energies from emission spectra than donor's. The binding energy of an acceptor impurity  $E_{A^*}$  can be estimated using

$$E_{A^*} = E_{1h} + B_{exc} - E_{(e,A^*)} \quad (5.1)$$

where  $E_{1h}$  is the measured value of the heavy-hole exciton transition,  $B_{exc}$  is the exciton binding energy and  $E_{(e,A^*)}$  is the measured emission energy for the electron to neutral acceptor recombination. In figure 5.3 the acceptor related emission obtained from one of our samples (MB662) at different excitation power densities is shown. At low excitation, emission is obtained from both  $(D^*,A^*)$  and  $(e,A^*)$  transitions. Since  $(D^*,A^*)$  emission is rarely obtained from wells of this width this suggests the well material is compensated. Increasing the excitation power density causes two  $(e,A^*)$  related transitions to dominate at 1.5400 eV and 1.5517 eV. Theoretical calculations of the binding energy of acceptor in quantum wells taking into consideration valence band coupling in the well and barrier has been completed by Masselink et al (1986). Calculating the acceptor binding energy for these transitions using equation 5.1, from the energetic position of the

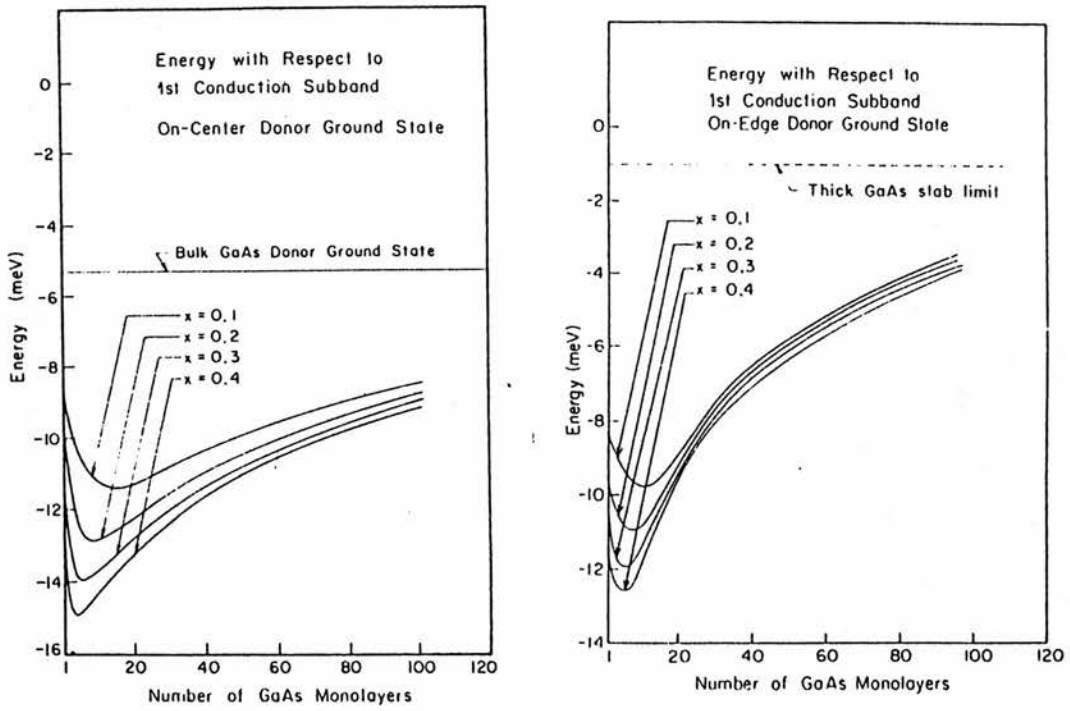


**Figure 5.2** The energy of on-centre and on-edge donor ground state with respect to the first conduction subband as a function of GaAs well thickness and alloy composition  $\text{Al}_x\text{Ga}_{1-x}\text{As}$  (Mailhot et al 1982).

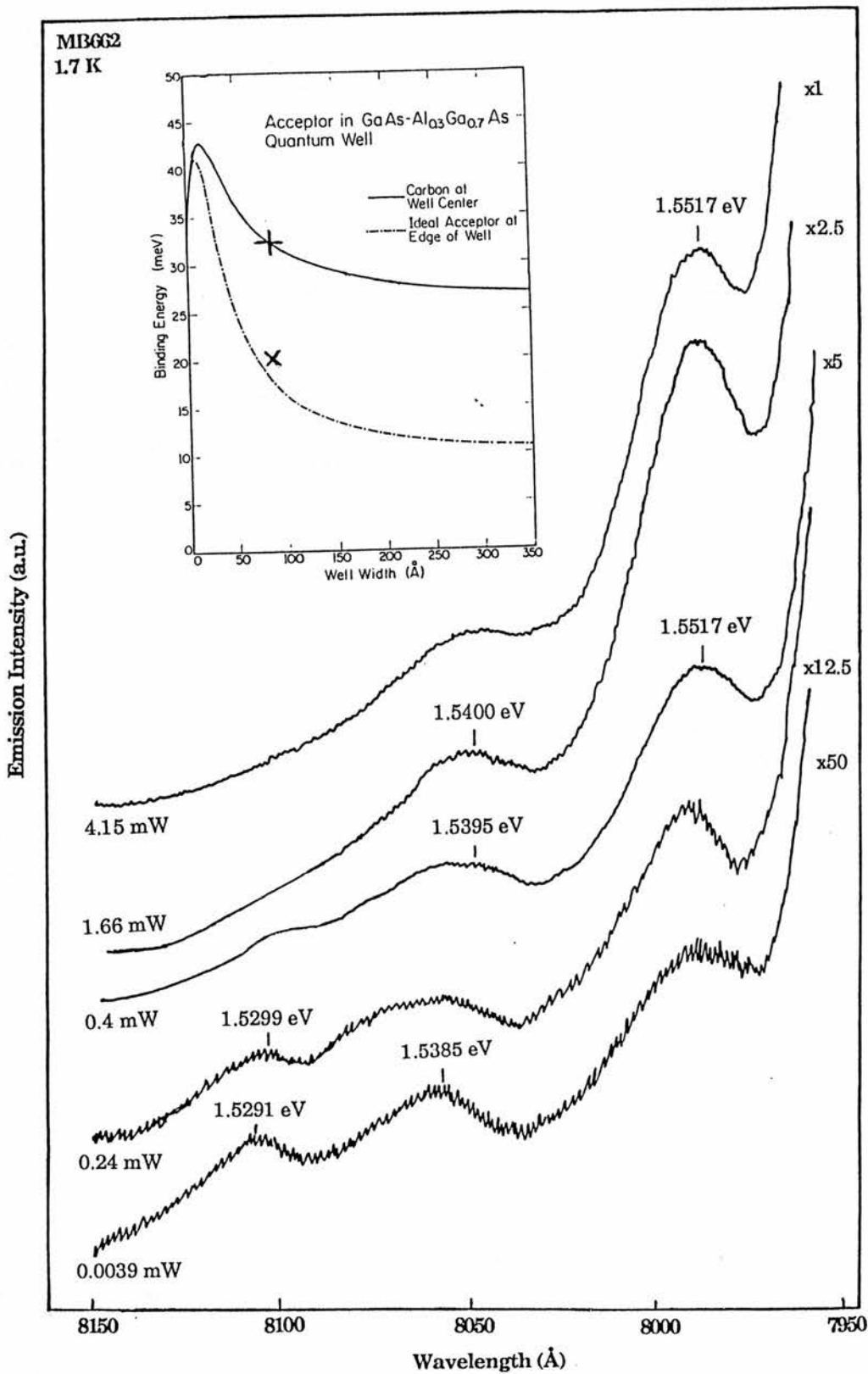


**Figure 5.3** Excitation power density dependence of the emission showing the existence of ( $D^*, A^*$ ) and ( $e, A^*$ ) transitions in the well. The emission intensity is much reduced (x60) compared to the excitonic emission in figure 5.1. Calculating the acceptor binding energy shows that the emission can be assigned to acceptors at the well centre and edge (insert).

peak in figure 5.3, with the exciton binding energy obtained from figure 5.4. A good agreement with binding energies estimated by Masselink et al (1986) is obtained (see insert figure 5.3). So the transitions at 1.5400 eV and 1.5517 eV can be assigned to carbon acceptors, the background impurity, at the well centre and well edge respectively. Since a higher density of states exist at the well centre, peak ratio  $(e,A^*)_c/(e,A^*)_i$  should be 2.2/1 (Bastard 1981), we would expect the transition associated with it to dominate. This is not the case here suggesting that carbon may be gettered at one of the well interfaces.

The question of light and heavy hole binding energy in a quantum well has provoked much experimental and theoretical work. Dingle (1975) first estimated the exciton binding energy to be  $\sim 9$  meV for  $L_z \sim 100$  Å by extrapolating the exciton peaks observed in absorption spectra to zero confinement. In PLE spectra obtained by Miller et al (1981) a shoulder was seen on the high energy side of the  $E_{1h}$  and  $E_{1l}$  transitions. This was assigned to a 2s excited state of the exciton, consistent with oscillator strengths and polarization, thus providing a direct measure of the 1s-2s splitting of the exciton. They found that since the in-plane light hole mass was larger than the heavy hole mass it had a larger binding energy. Dawson et al (1986) resolved these shoulders as actual peaks in their spectra allowing an accurate estimation of the binding energy of the heavy hole exciton as 13.0-10.1 meV for well widths of 75-92 Å. Magneto-optical measurements, from which the heavy hole exciton binding energy was estimated by extrapolating to zero field, have been reported (Rogers et al (1986), Petrou et al (1987)). Rogers et al (1986) found the estimated binding energies from high field measurements were slightly larger than those obtained from the low field measurements giving a binding energy of 16-9 meV for wells of 22-160 Å.

Much of the theoretical work in calculating excitonic binding energies has been completed within the effective mass approximation (Greene and Bajaj (1983b), Bauer and Ando (1986)). A calculation by Greene et al (1984), using a

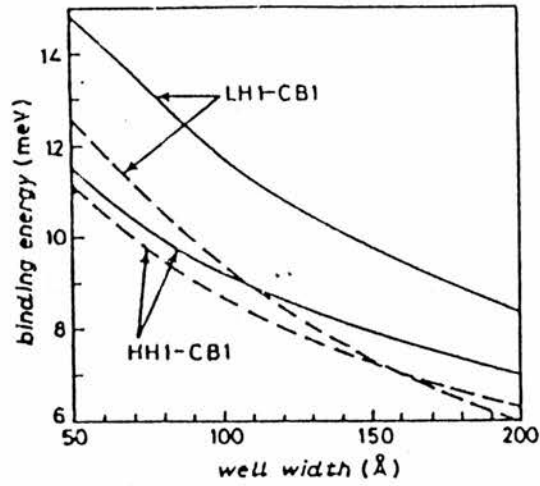


**Figure 5.4** The binding energy of the heavy (HH1-CB1) and light (LH1-CB1) exciton as a function of GaAs well thickness for an alloy composition of  $\text{Al}_{0.4}\text{Ga}_{0.6}\text{As}$ . The solid line shows the inclusion of coupling between the valence bands (Andreoni and Pasquarello 1988).

0.85/0.15 band-offset, showed the light and heavy hole binding energy to increase monotonically with decreasing well width until the wavefunction penetration in the barrier becomes significant. More accurate calculations including the effects of non-parabolicity of the conduction band and valence band degeneracy (Ekenberg and Alterelli (1987), Andreoni and Pasquarello (1988)) have shown increased oscillator strengths and produced binding energies that are within 1 meV of those reported experimentally (figure 5.4).

### 5.2.2 Interfacial Disorder and Growth Interruption

The interface quality of a quantum well can have important consequences on the observed luminescence and for the properties of devices fabricated from it (section 5.3). Generally, as the well thickness decreases a corresponding increase in the linewidth occurs as a consequence of intra-well thickness variations (Weisbuch et 1981). It is convenient to consider an infinite square well with energy levels  $E_n$ , of effective mass  $m^*$  and well width  $L_z$

$$E_n = \frac{\hbar^2 \pi^2}{2m^*} \left[ \frac{n}{L_z} \right]^2 \quad (5.2)$$

where  $n=1,2,3\dots$ . So, an uncertainty in well width  $\Delta L_z$  will result in an uncertainty in the  $E_1$  energy level of  $\Delta E_1$  thus

$$\Delta E_1 = \frac{\hbar^2 \pi^2}{m^* L_z^3} \Delta L_z \quad (5.3)$$

where  $\Delta L_z$  is normally considered as a monolayer fluctuation, so as the well width decreases then  $\Delta E_1$  increases as does the linewidth. In fact infinitely large, atomically flat interfaces do not form during growth and interface islands that may be limited in size by the Ga and Al diffusion length (section 2.15) are produced. The lower Al diffusion length, typically 40 Å, compared to Ga, typically 40 Å, suggests the GaAs on  $Al_xGa_{1-x}As$  (inverted) interface may be rougher than the  $Al_xGa_{1-x}As$  on GaAs (normal) interface. Thus, the quasi two dimensional

## V Luminescence from Quantum Well Structures

exciton,  $a_{\text{exc}} \sim 250 \text{ \AA}$  (Greene and Bajaj 1983b), will essentially average over the interface region when  $L_z \leq a_{\text{exc}}$ . But if the well interface has an island size greater than  $a_{\text{exc}}$  then discrete peaks associated with monolayer fluctuations in the well width are observed.

These monolayer fluctuations were first proposed by Goldstein et al (1983) as an explanation for fine structure seen in the luminescence from a GaAs-AlAs superlattice at 77 K. Using a particle in a box model a good correlation between monolayer well thickness and the energetic position of emission peaks was obtained. The monolayer fluctuations have been confirmed by many other workers using PLE (Deveaud et al 1986), photoreflectance (Yu et al 1987), TEM (Tanaka et al 1987) and time resolved spectroscopy which gave an exciton transfer time of  $\sim 250 \text{ ps}$  between island regions (Deveaud et al 1987). Since GaAs and  $\text{Al}_x\text{Ga}_{1-x}\text{As}$  share a common cation at abrupt interfaces 1/2 monolayer fluctuations are meaningful and have been reported by Reynolds et al (1985) as fine structure in the luminescence.

RHEED intensity oscillations are recognized as a useful, real time, technique of monitoring growth parameters and interface quality during MBE. In GaAs growth, when the Ga shutter is opened to the substrate in a As stabilized atmosphere RHEED oscillations are observed. But their original amplitude decreases rapidly since the required 2 D growth mechanism no longer occurs as a consequence of increased surface roughness and proceeds instead from vicinal planes. When the Ga shutter is closed the RHEED intensity recovers to its original value (Neave et al 1983). This is regarded as proof that interrupting the growth results in a smoothing of the As stabilized surface since Ga atoms can find their preferred lattice sites. RHEED measurements showed that growth interruption should have the greatest effect at the inverted interface. A more detailed study of the oscillations by Lewis et al (1985) showed that two processes may be present, a fast smoothing of the growth front over  $\sim 1$  second and followed

by slow rearrangement of terraces' geometries over a few minutes. It should be noted however, that the use of growth interruption to smooth interfaces can be strongly dependent on growth parameters (Turco et al 1987, Kohrbroch et al 1989).

Many authors have reported drastic linewidth narrowing and the observation of monolayer fluctuations (see above) as a consequence of interface smoothing that results from growth interruption. Miller et al (1986) found up to seven discrete lines in their luminescence assigned to 7-12 monolayers with a decrease of  $\Delta E_{1h}$  from 24.8 meV at 5 ML to 13.7 meV for 11 ML. Slight low energy tails are formed due to impurity incorporation at the interface but no change in the radiative efficiency occurred, contrary to the findings of Bimberg et al (1986, 1987) who observed a factor of three decrease which they assigned to the formation of non-radiative centres. Tu et al (1987) found that growth interruption only at the inverted interface resulted in the formation of interface islands but mobility measurements on growth interrupted inverted HEMTs structure proved inconclusive. Tanaka and Sakaki (1987) suggested that growth interruption results in smoothing at both interfaces but when  $x > 0.5$  the inverted interface cannot be smoothed at all. They showed that island formation only occurred with growth interruption at the normal interface for GaAs-AlAs quantum wells. So, it can be concluded that the linewidth must be predominantly determined by the inverted interface.

### 5.2.3. Band offset

One area where luminescence techniques, particularly PLE, has made a large contribution to the understanding of quantum well structures is the determination of the band-edge discontinuity from the observed energy levels. The magnitude of the band-edge discontinuity at a GaAs-AlGaAs heterostructure, its dependence upon Al mole fraction, deposition sequence and even measurement technique is a controversial subject (see for example Duggan

et al 1985). Experimental data obtained from PLE (Miller et al 1984) first questioned the band-edge discontinuity derived by Dingle (1975) from interband absorption. In the PLE spectra, weakly allowed  $\Delta n=2$  transitions were found experimentally to be very sensitive to band-offset compared to the  $\Delta n=0$  transitions. This coupled to a more sophisticated model to describe sub-band minima energy levels (Bastard 1982) produced a reappraisal of the band-edge discontinuity showing it to divide 60%/40% to the conduction and valence bands, respectively. The problem of band-edge discontinuity has been the source of much experimental (Meynadier et al 1985, Tsang and Miller 1985) and theoretical work (Kane 1986, Chomette et al 1986) and there still remains a controversy (Shum et al 1988).

### 5.3 Lineshape and Linewidth Considerations

In this section we will consider the factors that contribute to the luminescence linewidths in quantum well structures. We will show that luminescence linewidth from quantum well structures fabricated from GaAs- $\text{Al}_x\text{Ga}_{1-x}\text{As}$  and  $\text{Ga}_{0.47}\text{In}_{0.53}\text{As-InP}$  can be described by a similar formalism but including the effects of alloy scattering, in the barrier or the quantum well, as necessary. We will find that the dominant mechanism that increases the linewidth can be interface roughness (section 5.4.3). The linewidth of the excitonic emission reflects an average composition of the interface therefore photoluminescence is a sensitive probe of interface quality.

Lee et al (1986) calculated a minimum linewidth as a function of temperature for light and heavy hole associated emission in GaAs- $\text{Al}_x\text{Ga}_{1-x}\text{As}$  quantum well structures. Contributions to the excitonic linewidth were attributed to interaction with polar optical phonons, acoustic phonons (via deformation and piezoelectric potentials), ionized impurity scattering and well width fluctuations. A transition rate  $\omega^i$  was calculated using Fermi's Golden

## V Luminescence from Quantum Well Structures

rule for the various scattering mechanisms which contribute to the linewidth  $\Gamma_i$  given by  $\omega^{1/2}$ . Lee et al showed the half width half maximum (HWHM) for the heavy hole emission from a 200 Å well as a function of temperature could be expressed as

$$\Gamma_{\text{tot}}^+ = \Gamma_0^+ + (1.47 \times 10^{-3})T + \frac{4}{\exp(\hbar\omega/kT) - 1} + \Gamma_{\text{imp}}^+ \exp^{-\langle E_b \rangle/kT} \quad (5.4a)$$

and for light hole emission (HWHM)

$$\Gamma_{\text{tot}}^- = \Gamma_0^- + (1.19 \times 10^{-3})T + \frac{2.45}{\exp(\hbar\omega/kT) - 1} + \Gamma_{\text{imp}}^- \exp^{-\langle E_b \rangle/kT} \quad (5.4b)$$

where  $\Gamma_0^\pm$  is the linewidth due to the homogeneous fluctuations of the well thickness (see later) and  $\Gamma_{\text{imp}}^\pm$  is the linewidth due to fully ionized impurity scattering. The second term in 5.4 represents the linewidth due to acoustical phonon scattering while the third term is the contribution from optical phonon scattering. The variation of these different components of the linewidths with temperature is shown in figure 5.5. Acoustic phonon scattering is found to be dominant at low temperatures; above 20 K ionized impurity scattering makes an significant contribution to the linewidth; on increasing the sample temperature further, by 200 K, polar optical scattering dominates. These scattering mechanisms however do not account for the total low temperature luminescence linewidth. In addition, Lee et al (1986) did not consider the effects of alloy scattering in their model limiting its validity to well width,  $L_z$ , greater than the excitonic diameter,  $a_{\text{exc}}$ .

Singh and Bajaj (1985) extended a formalism they had derived to study alloy disorder in bulk III-V compounds (outlined in section 4.3.1.1) to consider quantum well structures where an alloy forms the barrier or the well. In GaAs- $\text{Al}_x\text{Ga}_{1-x}\text{As}$  wells the exciton only senses a fraction,  $F_0^{\text{exc}}$ , of the alloy in the barrier and hence, the volume over which a fluctuation  $C_A$  occurs is now  $a_{\text{exc}}^3 F_0^{\text{exc}}$  so equation 4.10 becomes

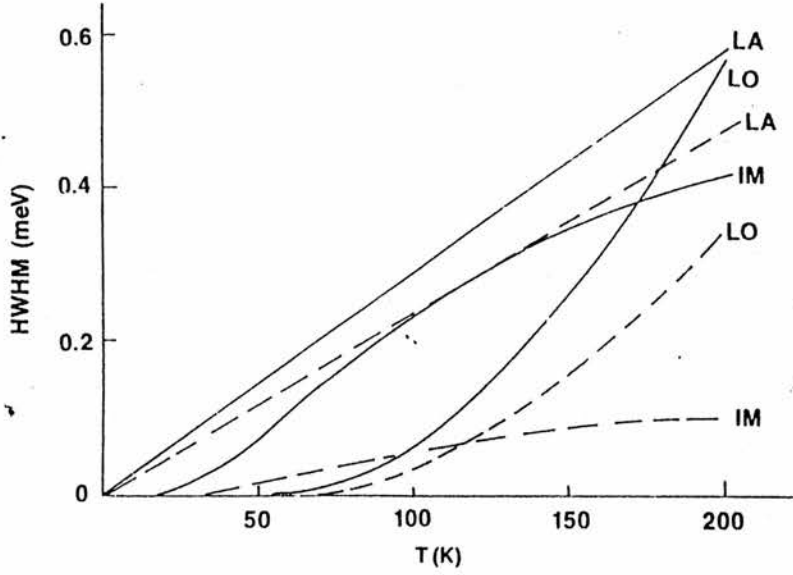


**Figure 5.5** Contributions to light-hole (dashed line) and heavy-hole (solid line) exciton linewidth (HWHM) from acoustic phonons (LA), polar optical phonons (LO) and impurities (IM) (Lee et al 1986).

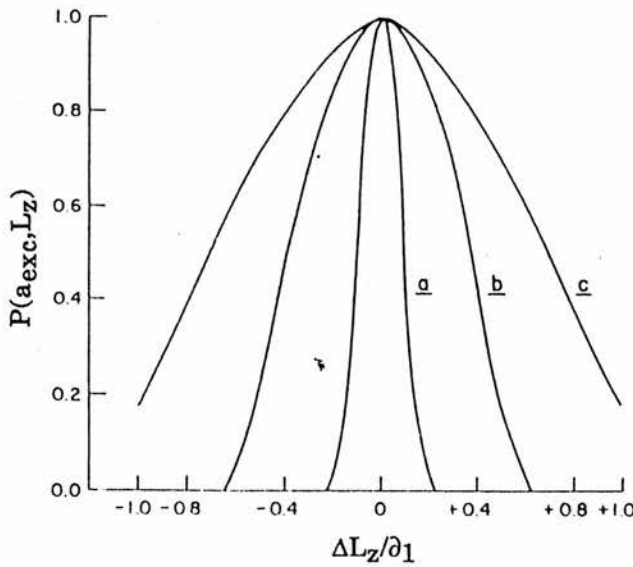


**Figure 5.6** Probability distribution of fluctuation in well size  $P(a_{exc}, L_z)$  as function of  $\Delta L_z/\partial_1$  for values of  $\partial_2$  equal to a) 20 Å, b) 80 Å and c) 160 Å (Singh et al 1984).

## V Luminescence from Quantum Well Structures

$$\sigma_{W(\text{GaAs-Al}_x\text{Ga}_{1-x}\text{As})} = 2 \left( \frac{1.4C_A^0 C_B^0 r_c^3}{a_{\text{exc}}^3 F_0^{\text{exc}}} \right)^{0.5} \Delta_{\text{QW}} \quad (5.5)$$

where

$$\Delta_{\text{QW}} = \frac{\partial E^{\text{eh}}}{\partial C_A} \Big|_{C_A} ; E^{\text{eh}} = E^{\text{e}} - E^{\text{h}} + E_{\text{g}}^{\text{w}} - E_{\text{b}} \quad (5.6)$$

here  $E^{\text{e}}$  and  $E^{\text{h}}$  are the electron and hole sub-band energies and  $E_{\text{b}}$  is the exciton binding energy and  $E_{\text{g}}^{\text{w}}$  the band gap of the well material. We can write equation 5.5 in terms of the excitonic linewidth in the bulk alloy forming the barrier thus

$$\sigma_{W(\text{GaAs-Al}_x\text{Ga}_{1-x}\text{As})} = \sigma_0 \frac{\Delta_{\text{QW}}}{\Delta_1} (F_0^{\text{exc}})^{-0.5} \quad (5.7)$$

where  $\sigma_0$  is the linewidth given by equation 4.10. So, in wells with  $L_z$  greater than  $a_{\text{exc}}$ ,  $F_0^{\text{exc}}$  goes to zero, but  $\Delta_{\text{QW}}/\Delta_1$  approaches zero faster, leading to a zero contribution to the linewidth from the alloy barrier as a consequence. When the alloy forms the quantum well and a binary forms the barrier as in  $\text{Ga}_{0.47}\text{In}_{0.53}\text{As-InP}$  then  $F_0^{\text{exc}}$  can be replaced by  $(1-F_0^{\text{exc}})$  in equation 5.7 and the contribution to the linewidth is

$$\sigma_{W(\text{Ga}_{0.47}\text{In}_{0.53}\text{As-InP})} = \sigma_0 \frac{\Delta_{\text{QW}}}{\Delta_1} (1-F_0^{\text{exc}})^{-0.5} \quad (5.8)$$

and in this instance as  $L_z$  increases alloy disorder effects becomes more important. In  $\text{Ga}_{0.47}\text{In}_{0.53}\text{As-InP}$  wells above  $100\text{\AA}$  the linewidth of the luminescence will be essentially the same as that of bulk  $\text{Ga}_{0.47}\text{In}_{0.53}\text{As}$ .

When the barrier region is doped the luminescence can show broadening due to band filling when electrons transfer into conduction sub-bands up to a Fermi energy,  $E_{\text{f}}$ , known as modulation doping. If the total number of carriers transferred is constant, then the density of electrons in the well increases with decreasing well thickness. Assuming the density of states at the ground state energy in the well is equivalent to,  $\rho_{3\text{D}}$ , the bulk density of states (equation 1.12),

## V Luminescence from Quantum Well Structures

then,  $n_s/L_z$ , where  $n_s$  is the sheet carrier density, divided by the density of states at the sub-band confinement energy,  $E^e$ , results in band filling  $\Delta E (=E_f - E_c)$

$$\Delta E = n_s \pi^2 \hbar^3 / L_z m_e^* (2m_e^* E^e)^{0.5} \quad (5.9)$$

where  $m_e^*$  is the effective mass of the electron. As the well thickness decreases then  $\rho_{3D}$  tends to  $\rho_{2D}$  and equation 1.11 is valid so

$$\Delta E = n_s / \rho_{2D} = n_s \pi \hbar^2 / m_e^* \quad (5.10)$$

and in either case the luminescence will exhibit an increased linewidth proportional to  $\Delta E$ .

The interface region of a quantum well structure does not form infinitely flat layers and can best be described in terms of random microscopic fluctuations of the well width,  $\partial_1$ , and island size  $\partial_2$  (Singh et al 1984). So, there will be regions where, for example in a GaAs-Al<sub>x</sub>Ga<sub>1-x</sub>As heterojunction, small islands of GaAs and Al<sub>x</sub>Ga<sub>1-x</sub>As will be formed, in addition to the variation of Al composition discussed above. If it assumed that Al concentration is constant then interface roughness is only due to island formation. This can be described on a global scale by  $C^o_a$  and  $C^o_b$  representing the concentration of islands and valley regions of lateral size  $\partial_a$  and  $\partial_b$ , respectively. So the exciton of diameter  $a_{exc}$  extending over the well will average the microscopic nature of the interface determining the excitonic lineshape and emission energy. The probability of finding a concentration fluctuation  $C_a$  and  $C_b$  over  $a_{exc}$  is then

$$P(C_a, C_b, a_{exc}) = \exp \left[ -\left( \frac{a_{exc}^2}{\partial_a^2} C_a \ln \frac{C_a}{C^o_a} + \frac{a_{exc}^2}{\partial_b^2} C_b \ln \frac{C_b}{C^o_b} \right) \right] \quad (5.11)$$

with the average width of the quantum well given by

$$L_z = L_{z0} + \partial_1 (C_a - C^o_a) \quad (5.12)$$

## V Luminescence from Quantum Well Structures

assuming the emission is dominated by one interface which is the case in GaAs-Al<sub>x</sub>Ga<sub>1-x</sub>As where the inverted interface is normally the rougher. As an illustration figure 5.6 shows the probability distribution of finding a fluctuations in well size  $P(a_{exc}, L_z)$ , for  $a_{exc}=250 \text{ \AA}$  and  $\partial_1=1$  monolayer step height for different values of  $\partial_2$ . It is obvious that as the island size  $\partial_2$  increases towards  $a_{exc}$  then the half width of the probability distribution increases and hence the luminescence linewidth increases. As  $\partial_2$  increases it approaches a value as if the well size had changed to  $L_z \pm 0.6\partial_1$ , hence it should be possible to identify  $\partial_1$  and  $\partial_2$  as they have different functional forms (see section 5.4.3).

The above contributions to luminescence linewidth have been described with the emphasis placed on GaAs-Al<sub>x</sub>Ga<sub>1-x</sub>As and Ga<sub>0.47</sub>In<sub>0.53</sub>As-InP well structures but is valid for similar heterojunction systems. The only difference between GaAs-Al<sub>x</sub>Ga<sub>1-x</sub>As and Ga<sub>0.47</sub>In<sub>0.53</sub>As-InP is the inclusion of alloy scattering in the barrier or the well, respectively. But in either instance the contribution to the linewidth will never be larger than the equivalent bulk linewidth,  $\sigma_0$ . We noted that since the heterojunction interface is not perfect its properties will in most instances dominate the linewidth. As sample temperature is increased other contributions to the linewidth such as optical phonon scattering have to be considered.

The lineshape of the excitonic emission from quantum well samples has been shown by various groups (Bimberg et al 1987) to be modeled accurately by a Gaussian distribution function. The excitonic lineshape as a function of energy  $I(E)$  can be described in general terms as

$$I(E) \sim \int_0^{\infty} f(E, E') D(E_n, E') B(E', E) dE' \quad (5.13)$$

where  $f(E)$  is a thermal distribution function which can be approximated to a Maxwell-Boltzmann distribution under low excitation densities,  $D(E)$  is the two

dimensional density of states (equation 1.11) and  $B(E)$  is a broadening function. At low sample temperatures and doping density the contribution from  $f(E)$  will not make a significant contribution, so the lineshape will reflect the inhomogeneous broadening of  $B(E)$  alone. The function  $B(E)$  will be a Gaussian function reflecting the statistical distribution of well thickness, interfacial islands and alloy composition described above. Although, it has also been suggested that only lifetime broadening should contribute to the final state so  $B(E)$  would appear Lorentzian (Christen et al 1988). In either case the excitonic volume will essentially sense many levels close together thus the lineshape observed  $I_{obs}$  will be the result of a statistical average

$$I_{obs} = \int_v I[E(v)] dV \quad (5.14)$$

Equation 5.14 is modified for the case of growth interruption since it results in the observation of discrete energy levels due to interfacial islands. Then

$$I_{obs} = \sum_{v=1}^n I_v(E) \quad (5.15)$$

where  $n$  is the total number of monolayer fluctuations observed.

## 5.4 GaAs-Al<sub>x</sub>Ga<sub>1-x</sub>As

### 5.4.1 Intrinsic and Extrinsic Emission

The samples initially studied are all uncoupled multiple wells of various thicknesses, nominally 25 -100 Å, with an Al composition of  $x=0.3$  in the barrier region and uniformly doped throughout with Si to mid  $10^{15} \text{cm}^{-3}$  (see table 2.2). The exact well width,  $L_z$ , is not important in most instances but it was checked against the growers estimate using a finite square well model (Kirby 1989) with the parameters given by Miller and Kleinman (1985). In the excitonic region of

the emission all samples showed either two or three separate transitions convoluted together (figures 5.1 and 5.7). Two samples MB662 and MB669 are considered in detail since they give the best resolved emission and are of a similar well width.

A typical high resolution spectrum of MB662 is shown in figure 5.1, it consists of two main transitions separated by  $\sim 1.9$  meV. The fine structure on the high energy peak is not observed from all parts of the sample, the possible origin of this is discussed later. The high energy emission, centred around 1.5629 eV, can be assigned to a  $n=1$ , free exciton, heavy hole recombination,  $E_{1h}$ . The linewidth of the  $E_{1h}$  transition,  $\sim 1.8$  meV, is amongst the best reported for a well of this width. The linewidth probably reflects the quality of the alloy barrier as much as that of the interface region (section 5.3). Although this sample is Si doped it is impossible to assign the low energy emission at 1.5611 eV to a donor related transition. Since, a strong reduction from the impurity related emission compared to that of the free exciton is normally observed and the energetic separation of the peaks is similar to that expected for monolayer fluctuations due to interface islands,  $\sim 2$  meV.

Still, it seems obvious to assign the peak at 1.5611 eV to a donor bound exciton transition since this is dominant in bulk GaAs doped at mid  $10^{15}\text{cm}^{-3}$ , (section 3.1). Hayne's rule should apply in principle in quantum well samples, with donor bound excitons binding at some proportion of the donor binding energy,  $E_d$ . From figure 5.2, a 88 Å quantum well will have a donor of binding energy  $\sim 12$  meV at well centre and  $\sim 8$  meV at the well boundary. If the 1.5611 eV transition is due to bound excitons, then as a consequence of Hayne's rule a 0.4-0.6 meV split in the emission should be observed. This is not the case, even though the acceptor related transition ( $e, A'$ ) shows a strong recombination associated with the interface region. As the laser spot is scanned across the sample surface a continuous shift of the emission is observed (4-6 meV)

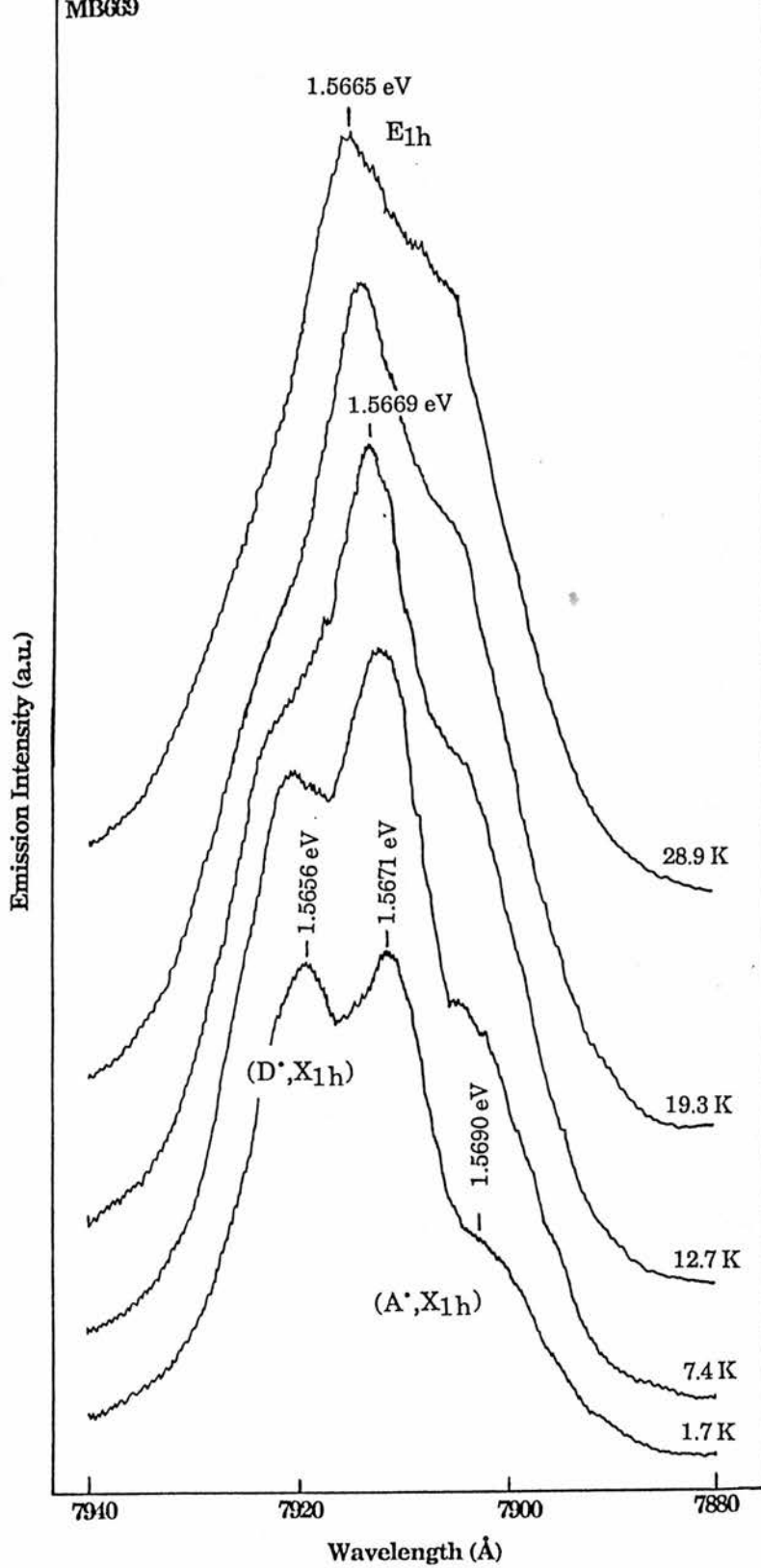


**Figure 5.7** Emission spectra of GaAs-Al<sub>0.3</sub>Ga<sub>0.7</sub>As multiple quantum well (sample MB669) for various temperatures. The excitonic region shows emission due to three transitions (see text).

corresponding to variation in Al composition found previously (section 3.3.), although, at a particular power density the relative peak intensity ratio remains unchanged. This is contrary to that expected from a well with a distribution of islands at the interface as two or three peaks which change relative to each other in intensity is normally observed (Deveaud et al 1986). In MB669 the problems of emission assignment is complicated by the appearance of another transition, figure 5.7. This sample may provide further evidence for interface islands or a further impurity related transition, either an acceptor bound exciton or increased emission from donors bound at the well interface. It should be noted the emission from the  $\text{Al}_{0.3}\text{Ga}_{0.7}\text{As}$  barrier in MB669 has a much larger linewidth, 8.0 meV, than MB662, 3.7 meV, suggesting a larger impurity concentration.

In section 5.3 it was shown that the low temperature lineshape of an excitonic transition from a quantum well sample can be described by a Gaussian function. It is obvious the emission at 1.5629 eV is in fact an average of many transitions so equation 5.12 is valid. The lineshape of the 1.5611 eV emission appears Lorentzian so it still may be assigned to a donor bound exciton (Christen et al 1988). Fitting a Lorentzian function proves unsuccessful (figure 5.8a) possibly because the donor binding energy will be distributed with respect to the donor atom position in the well (Bastard 1981). The emission lineshape is successfully fitted by a convolution of two Gaussian functions centred at 1.5606 eV and 1.5625 eV of linewidth 1.8 meV and 1.6 meV, respectively, showing that interface roughness and alloy scattering in the barriers are dominant. This means the low energy tail may be associated with acceptor related impurities. Assuming the 1.5606 eV transition is due to donors then it appears likely that the recombination is due to a heavy hole with an electron of a neutral donor ( $D^0, hh$ ). So emission from donors situated at the well interface would occur  $\sim 2$  meV above the  $E_{1h}$  transition. This emission would suffer a strong reabsorption from the

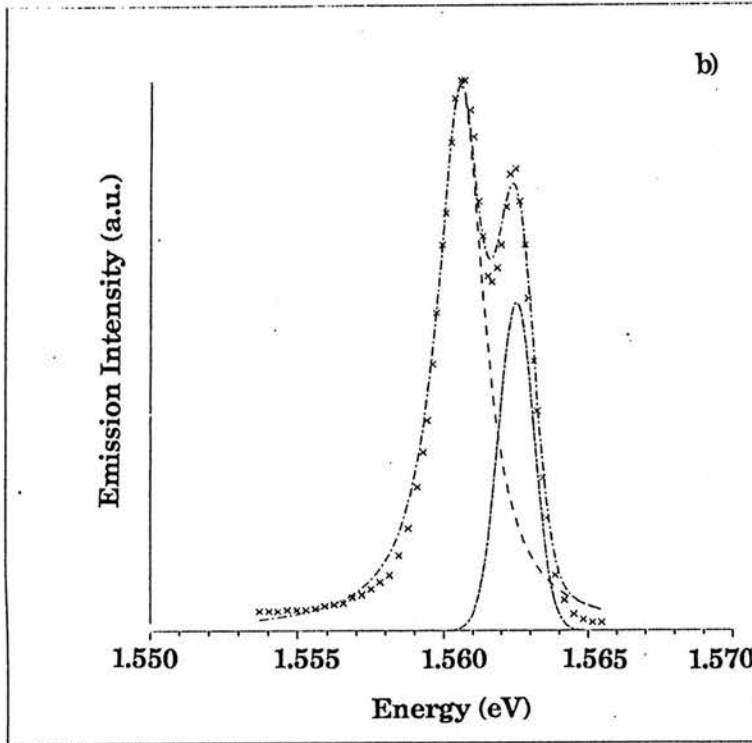
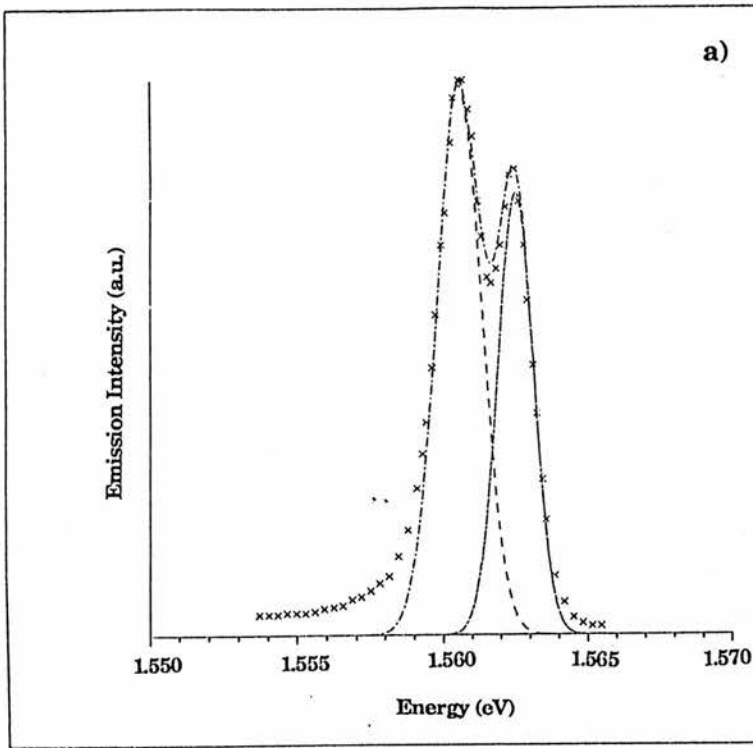


**Figure 5.8** a) The low temperature emission spectra of MB662 is deconvoluted and best fitted by Gaussian functions. b) An attempted fit of a Lorentzian to the low energy peak did not prove successful suggesting that the tail emission is due to impurities.

lower nearby  $E_{1h}$  transition thus explaining why there is only a slight evidence for this emission in the deconvoluted spectrum, figure 5.8b.

Monolayer fluctuations only appear in the luminescence when the island size is greater in scale than  $a_{exc}$  otherwise the exciton feels an average of the interface roughness. However, an intermediate case can occur; Bastard et al (1984) showed, by considering a semi Gaussian interface defect, that the density of states can exhibit a fluctuation depending on the ratio of island size to  $a_{exc}$ . This could explain the fine structure seen on the 1.5629 eV transition within the normal monolayer fluctuation.

### 5.4.1.1 Temperature dependence

As the temperature of sample MB662 is increased the transition at 1.5611 eV thermally quenches (figure 5.9) with a corresponding increase in the intensity of the  $E_{1h}$  emission at 1.5629 eV (see insert figure 5.9). When the spectra is deconvoluted, as in figure 5.8, a thermal activation energy of  $0.7 \pm 0.1$  meV is obtained for the 1.5611 eV transition. In bulk GaAs, the  $(D^*,X)$  transition dissociates into a neutral donor  $D^*$  and a free exciton with a dissociation energy of  $\sim 1$  meV (Williams and Bebb 1972). Since, the 1.5611 eV emission has a similar activation energy to this and an increase of the  $E_{1h}$  free exciton recombination occurs, then the transition may be assigned to a neutral donor bound to a heavy-hole exciton  $(D^*,X_{1h})$ . The fact that the activation energy is lower than that of the bulk suggests that the donor may be situated at the interface. The  $(D^*,hh)$  transition can be virtually ruled out since in the bulk  $(D^*,h)$  dissociates into an ionized donor  $D^+$  and a free  $(e,h)$  pair with a dissociation energy of  $\sim 7$  meV. Sample MB669 behaves similarly to MB662 with the lowest energy transition quenching and increasing temperature favouring the higher energy transitions (figure 5.7). Above  $\sim 30$  K the emission can no longer be resolved as two distinct transitions.

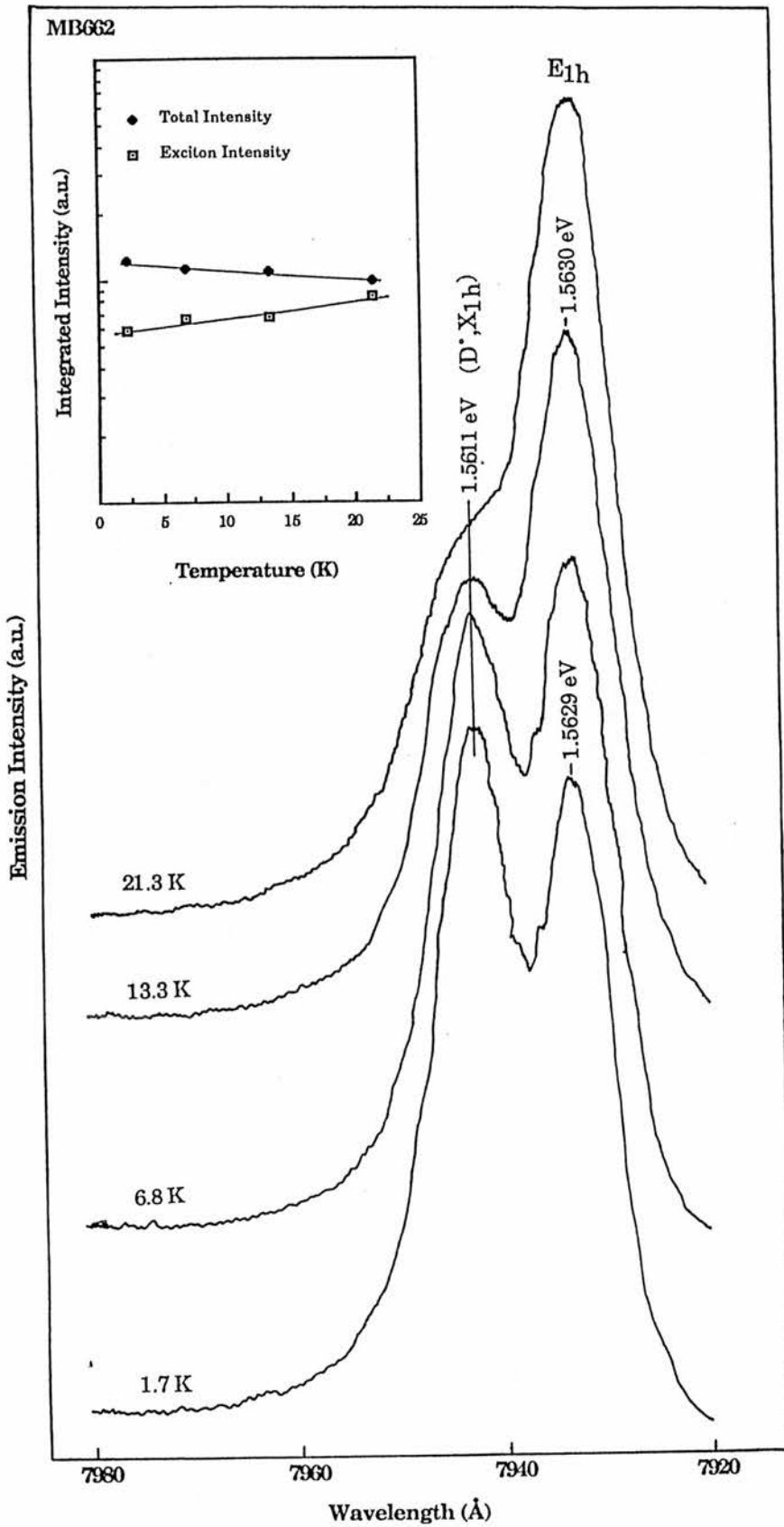


**Figure 5.9** The temperature dependence of the emission from GaAs- $\text{Al}_{0.3}\text{Ga}_{0.7}\text{As}$  MQW (sample MB662). As the sample temperature is increased the low energy emission quenches with a corresponding increase in the high energy emission.

#### 5.4.1.2 Excitation Power Density Dependence

Increasing excitation power density favours the high energy transition at 1.5657 eV in sample MB662 (figure 5.10). The low energy emission at 1.5638 eV has an exponent  $s=0.89$  (equation 4.16) while the transition at 1.5657 eV has an exponent  $s=1.07$ . The quasi-superlinear power dependence of the transition at 1.5657 eV can be taken as direct evidence of its free exciton nature thus justifying the  $E_{1h}$  assignment (Juang et al 1985). Figure 5.11 shows the excitation power density dependence of MB669, a careful deconvolution of the spectra is required (figure 5.12) so that the relative intensity of each transition can be obtained (figure 5.13). The high energy transitions at 1.5688 eV and 1.5669 eV have exponents of 1.08 and 0.91, respectively, which agree well with those obtained from MB662 above. So it seems reasonable to assign these transitions to the same recombination pathways as those in MB662, that is  $(D^*,X_{1h})$  and  $E_{1h}$ , for the transitions at 1.5688 eV and 1.5669 eV, respectively. The emission at 1.5652 eV has an exponent  $s=0.72$ . Since the ratio of donor binding energies at the well interface and centre (8 meV/12 meV) is not the same as the binding energy relative to  $E_{1h}$  (1.9 meV/3.6 meV), as would be expected applying Hayne's rule, then it is unlikely that its origin involves a donor. So, this transition was tentatively assigned to a neutral acceptor bound to a heavy-hole exciton  $(A^*,X_{1h})$ .

Shanabrook and Comas (1984) assignment of their donor related emission to a  $(D^*-hh)$  transition must now be revised (section 5.2.1). Their assignment was suggested because they argued that if the donor emission was involved in the capture of an exciton then both peaks, in a sample similar to MB662, should exhibit the same power density dependence. However, as we have shown it is also possible that doping at the well interface in their samples may result in the binding to an acceptor due to autocompensation. Thus our assignment of the transitions in MB669 will be valid for their samples. It should be noted that if interface islands were present in our samples they would exhibit the same

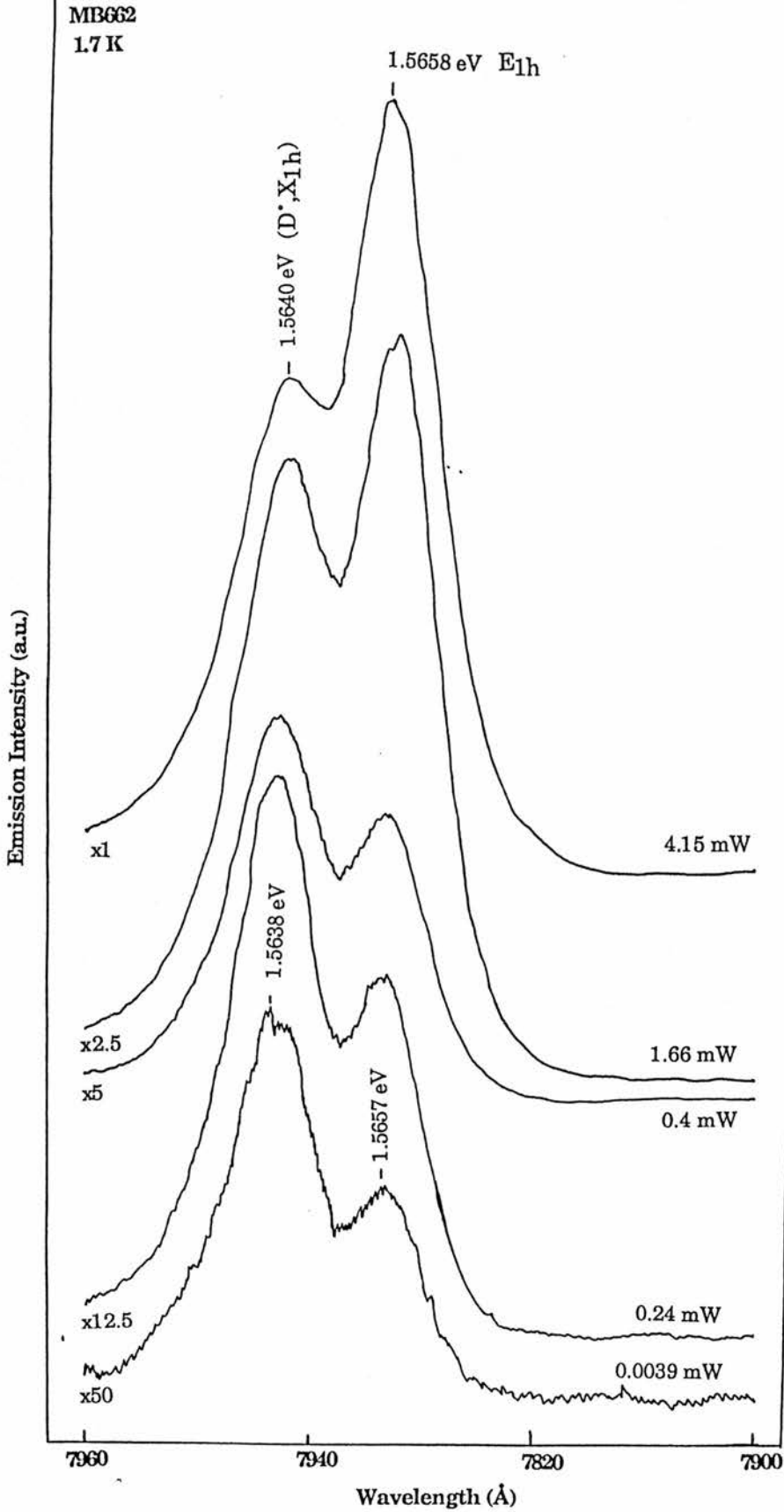


**Figure 5.10** Excitation power density dependence of the low temperature emission from GaAs- $Al_{0.3}Ga_{0.7}As$  MQW (sample MB662). Increasing the excitation power density favours the high energy emission.

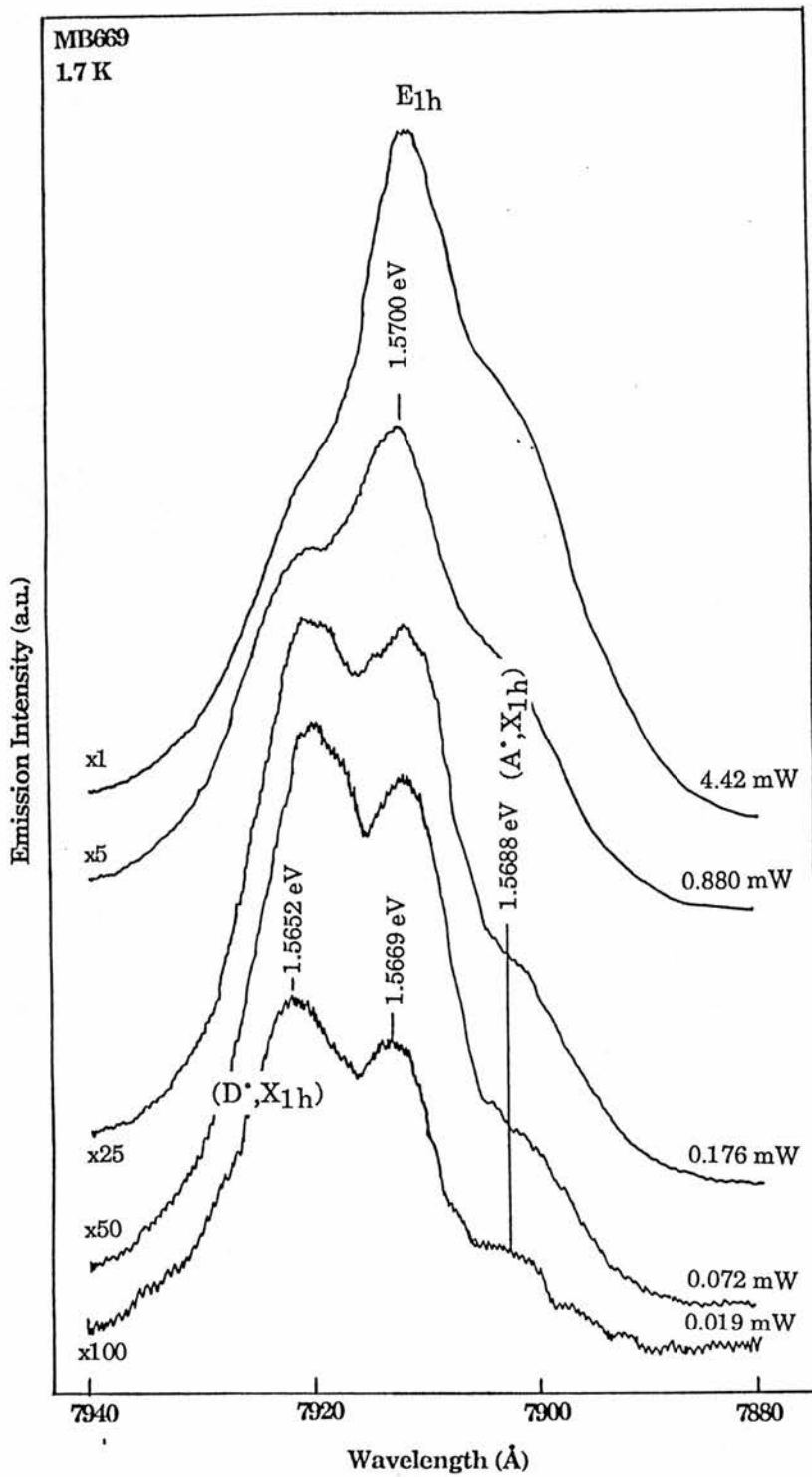


**Figure 5.11** Excitation power density dependence of the low temperature emission from GaAs-Al<sub>0.3</sub>Ga<sub>0.7</sub>As MQW (sample MB669). As with increasing the sample temperature, increasing the excitation power density appears to favour the transition at 1.5669 eV.

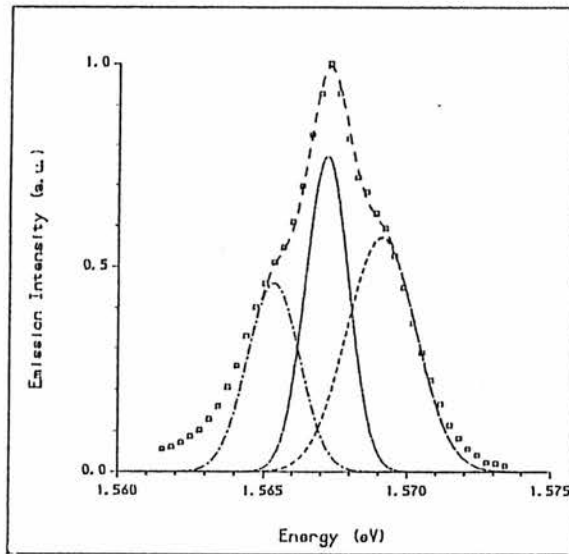
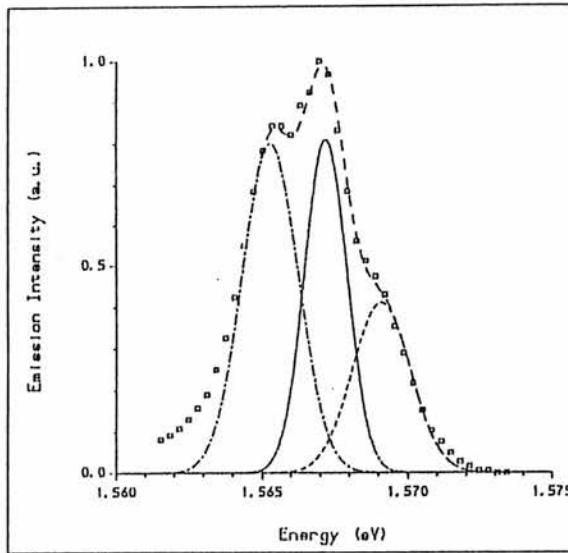
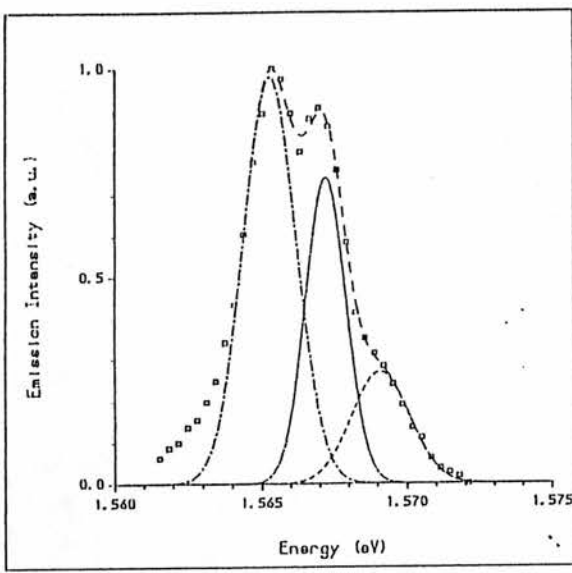


**Figure 5.12** A deconvolution of the MB669 spectra taken at different excitation powers a) 0.072 mW b) 0.880 mW and c) 4.42 mW shows the actual relative emission intensity of the transitions. The high energy emission appears superlinear (figure 5.13) suggesting it may be due to free excitons.

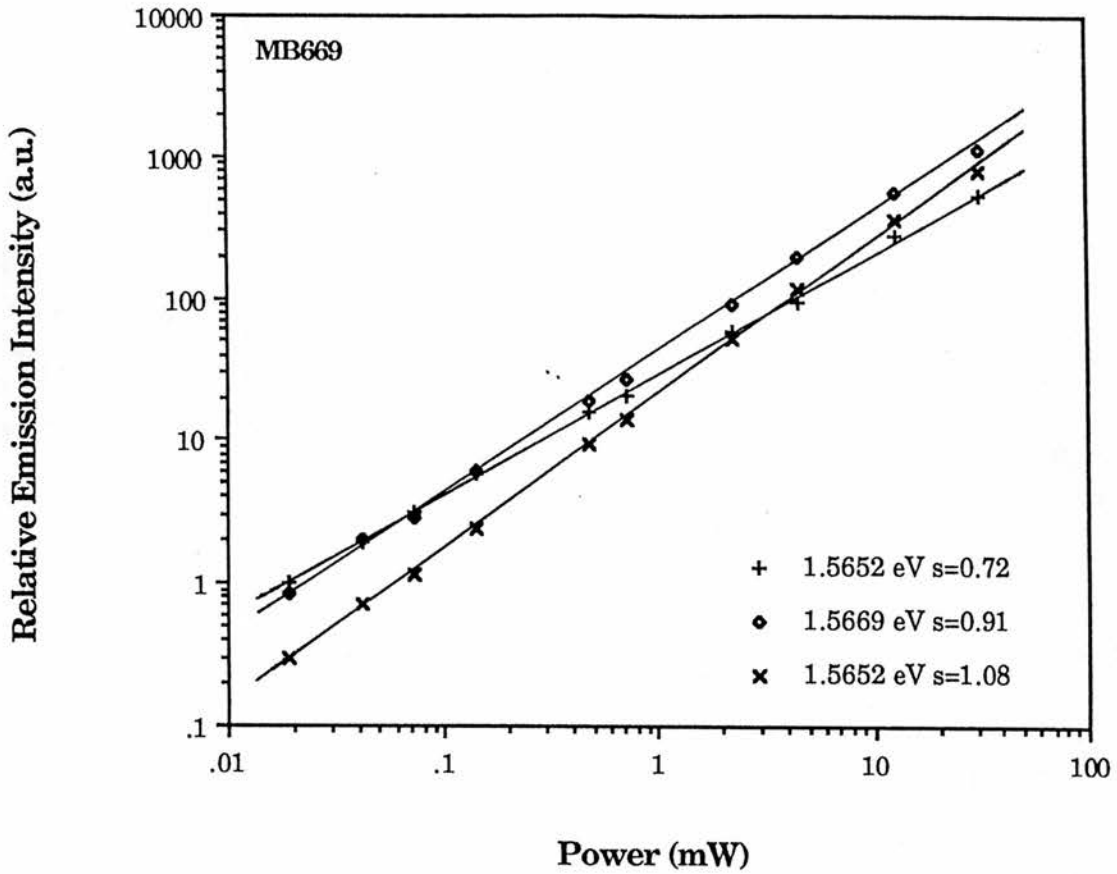


**Figure 5.13** Emission intensity dependence of the three peaks observed in sample MB669 as a function of exciting power density. Since the transition at 1.5669 eV and 1.5688 eV in MB669 (figure 5.11) have the same dependence on excitation power density as MB662 (figure 5.10) they can be assigned to  $(D^*, X_{1h})$  and  $E_{1h}$ , respectively.

functional dependence upon temperature and excitation power density as we observed (Deveaud et al 1986).

### 5.4.1.3 Doping Study

In order to prove that the emission below the  $E_{1h}$  transition was due to donor related impurities and not interface islands two single quantum well structures were grown. These samples were doped, one with Si to mid  $10^{15} \text{ cm}^{-3}$  (MB1240) and the other nominally undoped (MB1241), with well widths of 50 Å, 100 Å and 150 Å separated by a 200 Å  $\text{Al}_x\text{Ga}_{1-x}\text{As}$  barrier of  $x=0.3$ . It is obvious from figure 5.14 comparing the spectra from MB1240 and MB1241 that the emission at 1.5443 eV below the  $E_{1h}$  transition must be related to the incorporation of Si donors. The difference in peak energy between MB1240 and MB1241 will be due to a slight compositional variation. In the ( $D^*$ ,  $A^*$ ) region of the bulk GaAs emission from MB1241 an additional defect related emission at 1.4817 eV was also observed (section 3.1).

The 150 Å well did not exhibit a specific transition in either MB1240 or MB1241, only a broad band emission,  $\sim 8 \text{ meV}$ , centred around 1.522 eV appears. Impurity gettering is known to occur at heterojunctions under similar growth conditions thus superlattices are sometimes grown in the buffer layer to remove impurities from the growth front (Jung et al 1985). This could account for the enlarged linewidth of the first well in this sample implying that impurities are segregated on the growth front and donors observed in the luminescence could then be from the interface.

In MB1241, as the excitation power density is increased the  $E_{1h}$  transition moves to lower energy, within a monolayer fluctuation, with a decreasing linewidth. Decreasing the excitation power only results in a further increase of the linewidth which may be explained by any resolved donor related emission being proportionally more important (see figure 5.10). During growth,

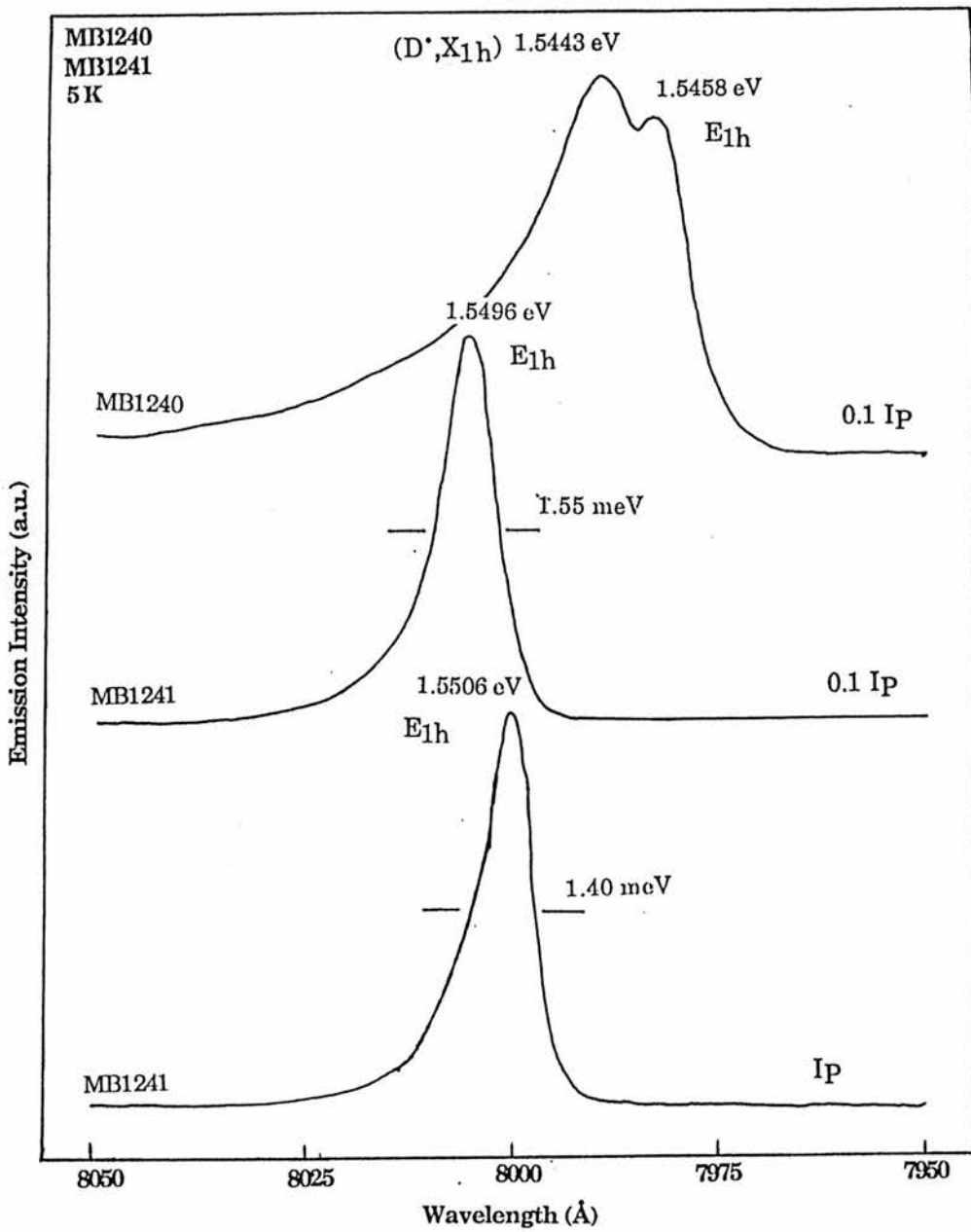


**Figure 5.14** Comparison of a Si doped ( $5 \times 10^{15} \text{cm}^{-3}$ , MB1240) and u/d (MB1241) emission from  $100 \text{ \AA}$  wells provides clear evidence that the low energy emission is due to donor impurities. Decreasing the excitation power density causes the undoped well emission to move to higher energies with an increase in linewidth.

fluctuations of the well thickness across the interface can cause the effective band-gap to have a periodic modulation in energy,  $E_{1h}^{\max}$  to  $E_{1h}^{\min}$ , similar to that reported in  $\text{Ga}_{0.47}\text{In}_{0.53}\text{As}$  (Schubert and Tsang 1986). At low excitation power density recombination occurs from  $E_{1h}^{\min}$  as photogenerated carriers can relax to  $E_{1h}^{\min}$ . At high excitation power density the recombination lifetime is short so an apparent shift in energy towards  $E_{1h}^{\max}$  occurs.

### 5.4.2 Carrier Capture

In this section the temperature dependence of the integrated intensity of the luminescence from MB662, under direct and indirect excitation is considered with respect to carrier capture in the quantum well. Additional information is required about the well interface to answer why interface islands are not seen in the luminescence even though the observed linewidth indicates good material quality. Large interface islands comparable to the exciton diffusion length could explain this, but it is unlikely they would be produced without growth interruption.

Luminescence from a quantum well can be excited by either pumping directly into the well, below the band gap of the  $\text{Al}_x\text{Ga}_{1-x}\text{As}$  barriers, or indirectly via the  $\text{Al}_x\text{Ga}_{1-x}\text{As}$  barriers. In MB662, which has a  $x=0.3$  barrier, this can be achieved by using excitation at 1.6476 eV (7525 Å) and 1.9160 eV (6471 Å) for direct and indirect excitation, respectively. As a consequence of direct pumping the total luminescence intensity is reduced by a factor of 3.6 (figure 5.15). This can be accounted for by, the ratio of the corresponding thicknesses of the absorbing  $\text{Al}_{0.3}\text{Ga}_{0.7}\text{As}$  and GaAs layers (88Å/50Å) and the number of energy levels, which the absorption is proportional to (section 1.5.1), is now halved (see figure 1.8), leading to factor of ~3.4. The strong  $\text{Al}_{0.3}\text{Ga}_{0.7}\text{As}$  emission from this sample is due to thick 1.25 μm capping layer. The  $\text{Al}_{0.3}\text{Ga}_{0.7}\text{As}$  emission quenches with an activation energy of  $42 \pm 2$  meV which is less rapid than that observed by other

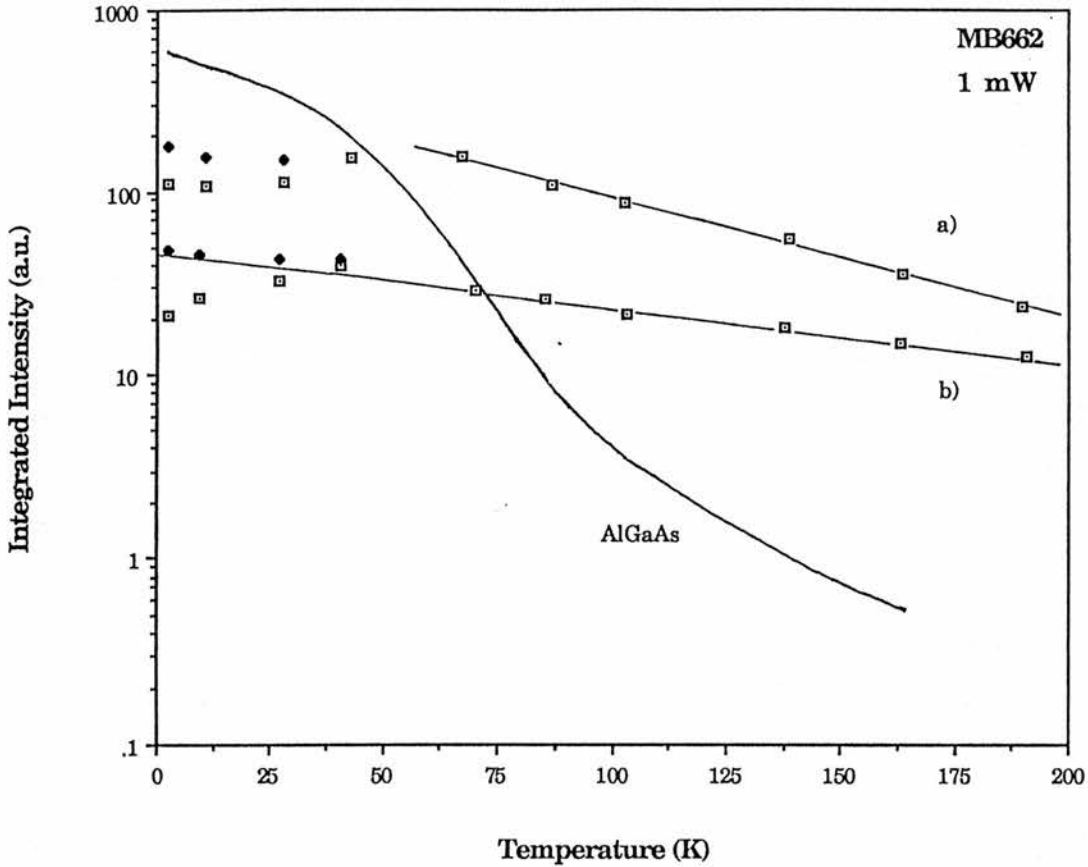


**Figure 5.15** Well carrier capture processes are considered by pumping the quantum well structure with a) an energy greater than the  $\text{Al}_{0.3}\text{Ga}_{0.7}\text{As}$  barrier height (6471 Å) and b) directly into the well (7525 Å). The difference in luminescence intensity can be directly related to the number of energy levels pumped and the  $\text{Al}_{0.3}\text{Ga}_{0.7}\text{As}$  barrier thickness. As the impurity related emission quenches, a corresponding increase in the free exciton emission occurs. The total integrated intensity of the total emission does not increase with temperature although there is evidence of a interface trap releasing carriers in the 25 to 70 K region.

groups (Delalande and Voos 1986, Jaing et al 1988). Contrary to expectations, the emission shows a functional dependence on the excitation energy with  $E_{1h}$  ( $D^*, X_{1h}$ ) transition dominant for indirect (direct) excitation. The enhanced free exciton emission  $E_{1h}$ , caused by direct pumping, must be a consequence of carriers from the barrier relaxing into the well.

As the sample temperature is increased a continuous decrease of the well emission intensity mainly due to the participation of non-radiative processes occurs (Jaing et al 1988). The total recombination rate is equal to the sum of the radiative  $R_r$  and non-radiative  $R_n$  recombination channels thus

$$R = R_r + R_n = \frac{\Delta n}{\tau_r} + \frac{\Delta n}{\tau_n} \quad (5.16)$$

where  $\Delta n$  is photogenerated excess carrier concentration, and  $\tau_r, \tau_n$  are the radiative and non-radiative carrier lifetimes, respectively. Assuming the non-radiative recombination is due to defects of density  $N_t$ , with capture cross-section  $\sigma_c$ , then

$$\tau_n = 1 / ( \sigma_c N_t (3kT/m^*)^{0.5} ) \quad (5.17)$$

when using c.w. excitation the stationary equilibrium generation rate  $G$  must equal the recombination rate and  $\Delta n$  will be constant. Assuming  $\sigma_c$ ,  $N_t$  and  $\Delta n$  are not temperature dependent then the radiative recombination rate as a function of temperature is given from equations 5.16 and 5.17 as

$$R_r = G - C\sqrt{T} \quad (5.18)$$

where  $C$  is constant. So under direct excitation the total integrated intensity should follow a  $\sqrt{T}$  dependence (see figure 5.16). This is the case, except in the range 25-70 K, where an increase in integrated intensity is observed (figure 5.15). This increase during indirect excitation cannot be only from carrier transfer from the  $Al_{0.3}Ga_{0.7}As$ , alone. We suggest the excitons must be bound to defects

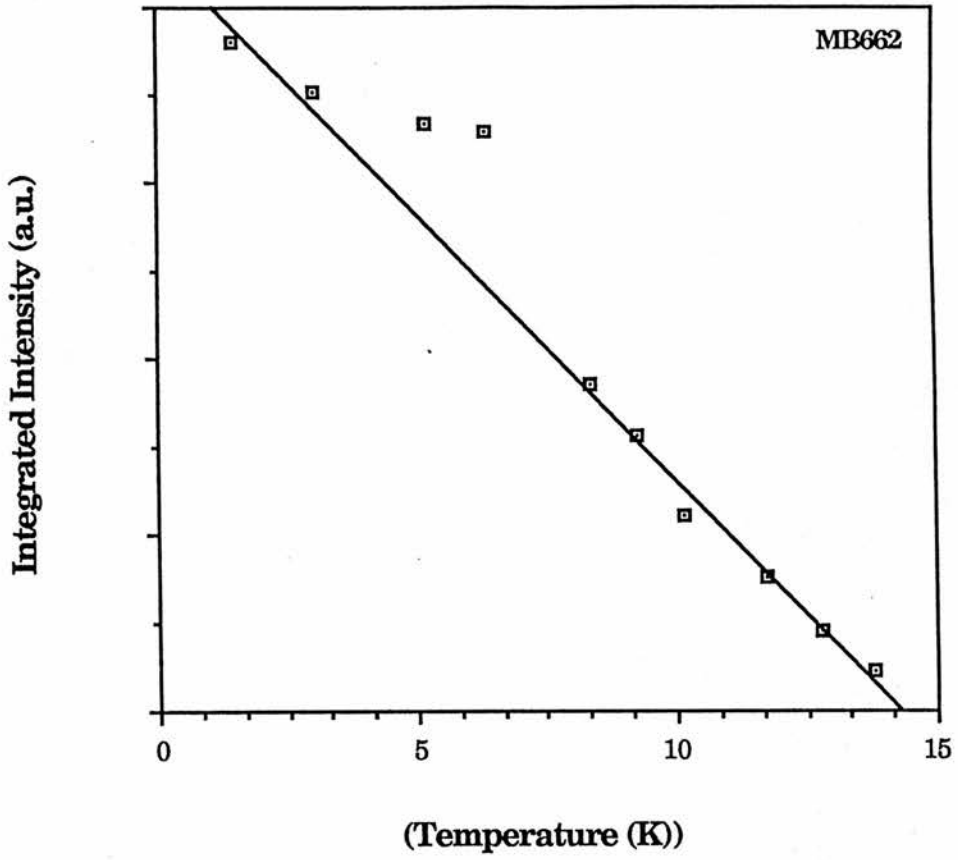


**Figure 5.16** Temperature dependence of the total integrated intensity showing a linear decrease due to the non-radiative processes. The radiative recombination rate is proportional to  $(T)^{0.5}$  as shown in text.

at the well interface (Bastard et al 1984) which are then thermally released as the temperature is increased. Therefore, consistent with our previous results, interface islands  $> a_{exc}$  do not occur in these samples and the exciton will always average over a pseudo-rough interface most probably dominated by the inverted interface (section 5.4.3). Consequently, it must be assumed, except under high excitation power densities (section 5.4.1.3), that photocreated carriers relax rapidly to the bandedge at  $E_{1h}^{min}$ . The linewidth of the  $E_{1h}$  transition under direct excitation is accurately modeled by equation 5.4a assuming that the inhomogeneous linewidth  $\Gamma_0^+$  is 1.8 meV which will include contributions from both the interface and the alloy barrier (section 5.3). This appears as the solid line on figure 5.17 that is bowed since, optical phonon scattering has the dominant temperature dependence (figure 5.5). Under indirect excitation the linewidth shows a linear dependence as a consequence of carrier transfer from the barrier (figure 5.17). This shows the importance of using direct excitation of a quantum well when completing lineshape analysis of luminescence.

The  $E_{1h}$  transition is found to follow the GaAs band-edge temperature dependence extrapolated to the well energy regardless of excitation energy (figure 5.18). As the sample temperature increases the  $E_{11}$  transition which is thermally suppressed at low temperatures is observed. The energetic separation of the transitions  $E_{11}-E_{1h}=14.2\pm 0.5$  meV agrees with that estimated by Shum et al (1988) of 14 meV. The  $E_{1h}$  transition is found to initially dissociate with an activation energy of 9.3 meV which can be related directly to the exciton binding energy in figure 5.4. At higher temperatures the  $E_{1h}$  and  $E_{11}$  transitions both quench with an activation energy of  $38\pm 2$  meV (figure 5.19 meV). This is similar to the behaviour of the  $Al_{0.3}Ga_{0.7}As$  barrier emission suggesting that the same thermally activated non-radiative centre may be responsible for the quenching of the emission from the well and barrier. At 190 K the emission dependence on

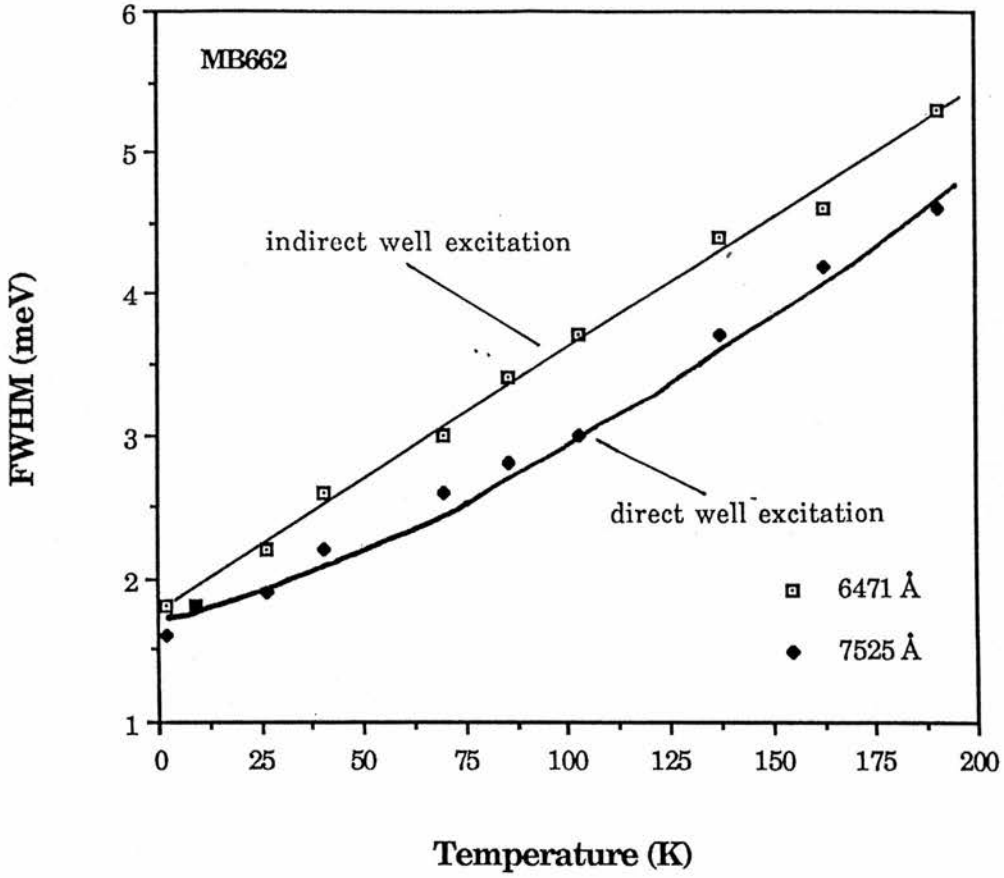


**Figure 5.17** Exciton linewidth dependence on temperature. The linewidth  $E_{1h}$  under direct excitation is described by the scattering processes considered in equation 5.4a. When indirect excitation is used a increased linewidth due to carrier transfer from the barrier is observed.

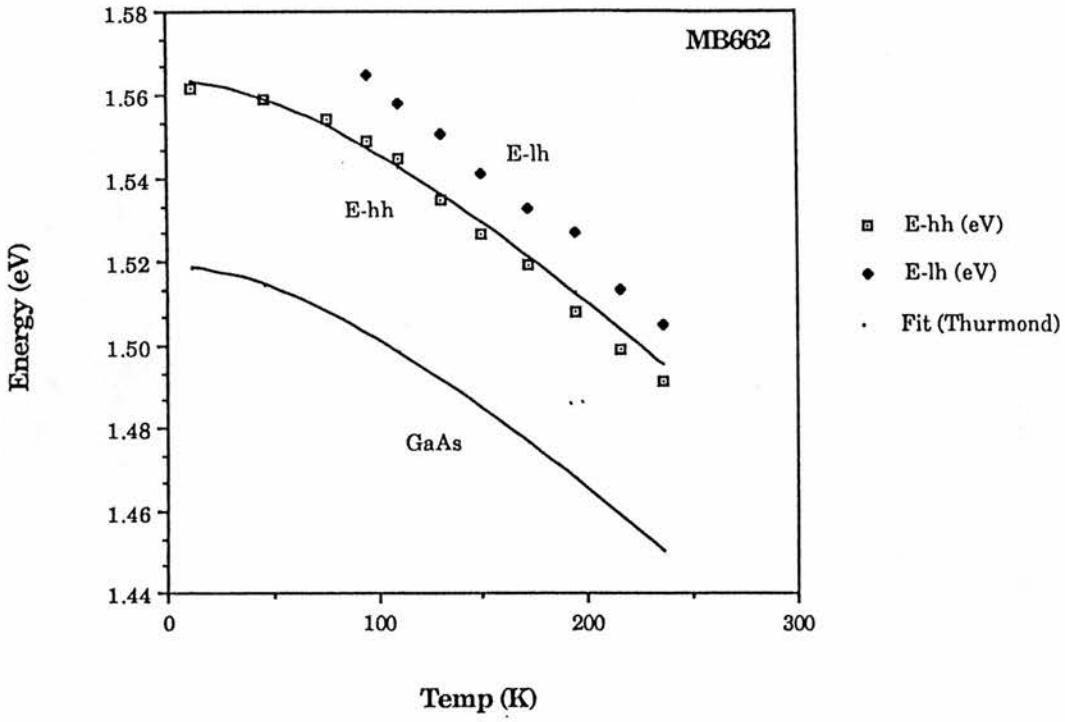


**Figure 5.18** Increasing sample temperature causes the light-hole state to become thermally populated. Both transitions follow the expected band-edge temperature dependence extrapolated to the well energy regardless of pump wavelength.

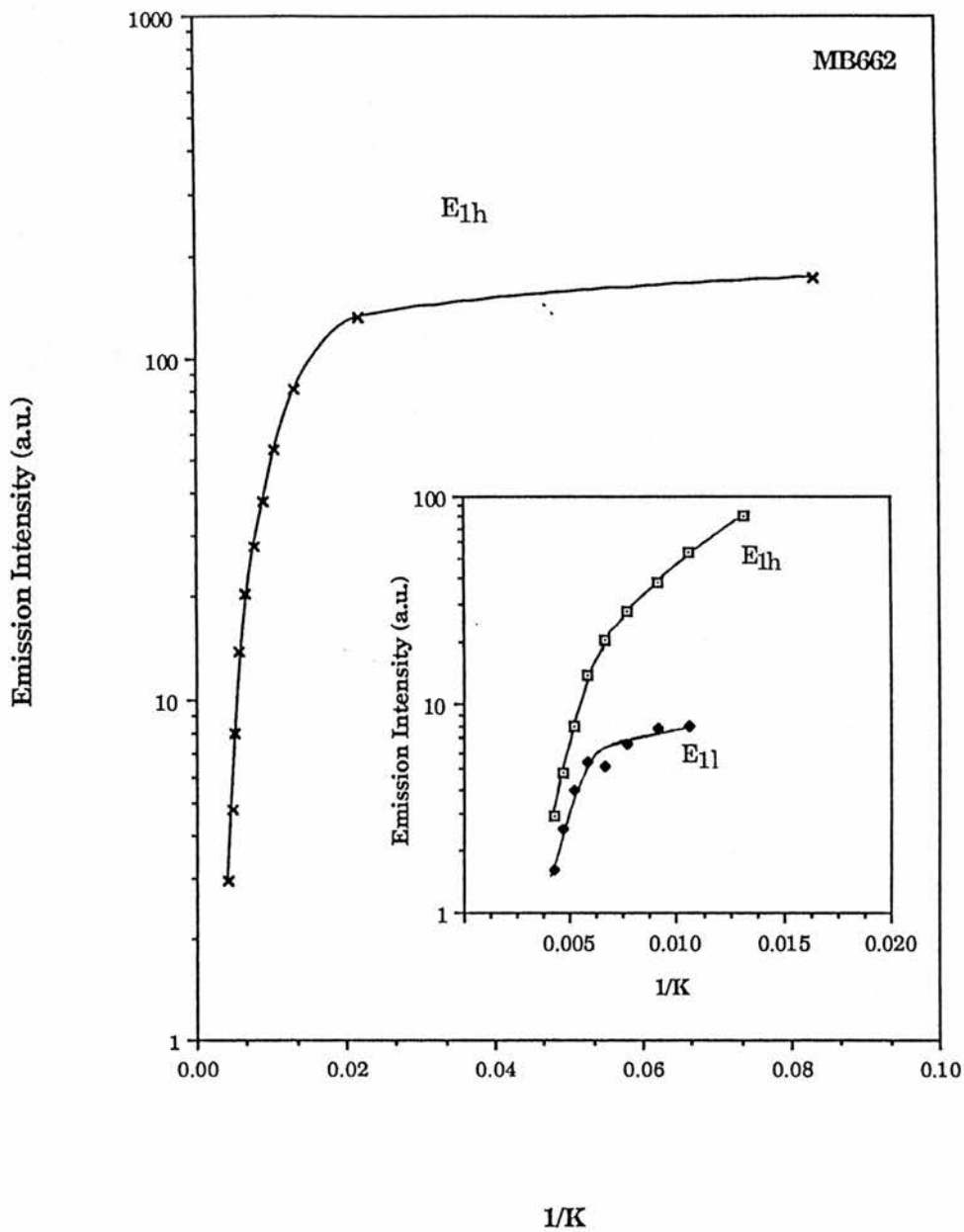


**Figure 5.19** Temperature dependence of the emission from the heavy and light hole excitons. The heavy hole  $E_{1h}$  emission quenches with an activation energy of  $9.3 \pm 0.5$  meV that can be related to the heavy-hole excitonic binding energy. As the the temperature further increases the  $E_{1h}$  and  $E_{1l}$  dissociate with an activation energy of  $38 \pm 2$  meV.

excitation power density has an exponent  $s=1.11$  suggesting it is still essentially excitonic at this temperature.

### 5.4.3 Growth on Misorientated Substrates

As discussed above a quantum well interface does not form an infinitely flat heterojunction but can be described in terms of well width fluctuations  $\partial_1$  and interface island size or vicinal step width  $\partial_2$  (section 5.3). Photoluminescence is a sensitive probe of the interface quality but the sensing exciton averages over both, the well width fluctuations and interface islands. The narrow linewidths observed from our well samples make them particularly suited to sensing an increased interface roughness. It has been suggested by Wada et al (1989) that the growth interruption smoothing technique is limited by the vicinal step width. So, [100] substrates misorientated from  $0^\circ$  to form different vicinal step widths should show different luminescence linewidths for the same well width (figure 5.6) hence separating the functional dependence of  $\partial_1$  and  $\partial_2$ . The quantum well samples grown at GEC exhibit amongst the best linewidths, for a particular well thickness, either with or without growth interruption. However, when growth interruption was attempted at our normal and inverted well interfaces, a further narrowing of the linewidth did not occur (section 5.2.2), but instead the luminescence linewidth increased by a factor of 3-4. An increase in linewidth for growth interrupted samples has been observed by Hayakawa et al (1987) who assigned it to compositional changes as a consequence of Ga desorption due to the high substrate temperature  $T_s=720^\circ\text{C}$ . This argument is not valid in this instance as no Ga desorption would occur since a relatively low  $T_s=600^\circ\text{C}$  was used. This study was initiated to look for a functional dependence of the luminescence linewidth on  $\partial_2$ , to provide an answer for the increased linewidth in growth interrupted samples and to clarify the work of other authors who have used growth interruption (section 5.2.2).

2" [100] GaAs wafers with a misorientation of 2°, 4° and 6°, labeled -011/-019, -015, -017, respectively, towards the nearest [110] were used as substrates. The orientation of the wafers were checked using X-ray rocking measurements and were found to be accurate within  $\pm 5'$ . The mean vicinal step width is given by  $a_0(\cot\alpha)/2$ , where  $\alpha$  is the misorientation angle,  $a_0$  is the lattice constant of GaAs and  $a_0/2$  is the monolayer step height, 2.83 Å. So a 2°, 4°, and 6° misorientation corresponds to a vicinal step width  $\partial_2$  of 81.1 Å, 40.5 Å and 26.9Å, respectively which can be compared to the Al diffusion length 40 Å (section 2.1.5). It was reported recently (Wada et al 1989) that vicinal step height may be greater than one monolayer, extended step widths and clustered step heights, so the  $\partial_2$  estimated should be regarded as a minimum.

Nominally undoped, mid  $10^{13} \text{ cm}^{-3}$ , well structures of 5 (14.2 Å), 10 (28.3 Å), 20 (56.6 Å) and 40 (113.2 Å) GaAs monolayers separated by 200 Å  $\text{Al}_x\text{Ga}_{1-x}\text{As}$  barriers of composition  $x=0.2, 0.3$  or  $0.4$  were grown on the substrates. This well structure was grown both, with and without, a growth interruption of 2 minutes at each interface. Relatively thin wells were chosen as they will show the greatest dependence on  $\partial_2$ . The top  $\text{Al}_x\text{Ga}_{1-x}\text{As}$  layer was grown thick enough so that carrier capture by the wells did not deplete the layer allowing the Al mole fraction to be estimated using equation 3.6. A large excitation power density was used to excite the luminescence such that the  $E_{1h}$  emission from the wells should normally dominate the spectra. The model used to estimate well widths from emission spectra (Kirby 1989) was modified to account for the exciton binding energy for very thin wells using the values given by Greene and Bajaj (1983b).

The substrates were prepared for growth in the normal manner using a fast etch to preserve the step width (section 2.1.7). Four substrate pieces of different 2" wafers of orientation, two with 2°, one with 4° and another with 6° were mounted on to a Mo block which was then transferred to the MBE machine. Two different 2° misorientated substrates ( -011 and -019) were used to check any

differences in sample preparation, indium mounting and system dependent variables such as beam uniformity did not affect the results obtained. The samples were brought up to 600 °C, under an As over-pressure and growth commenced immediately to stop any thermal decomposition of the vicinal planes on the substrate. A GaAs buffer layer was grown to clean the substrate but this was kept thin, 1000 Å, to prevent smoothing of vicinal planes. After growth, some samples showed a fluctuation on the sample surface (figure 5.20), this appeared randomly with no dependence on orientation and did not affect the luminescence properties. Surface roughness is due to the energetic instability at the growth front which depends on the interplay of anion desorption, cation migration and surface reconstruction (Tsui et al 1985).

Two well structures with  $x=0.3$  (MB1256) and 0.38 (MB1158) were grown on a normal  $0^\circ$  [100] substrate, to check misorientation growth runs were consistent with previous results and for peak assignment. The 20 and 40 monolayer wells always showed a two or three peak emission spectra with the thinner wells 5 and 10 monolayers having a Gaussian lineshape since the exciton is more sensitive to interface roughness and impurity related emission quenched. In figure 5.21, spectra for the 113.2 Å well for MB1156 and for MB1158 are shown. The spectra here indicate that a better material quality is produced than in the doping study (section 5.4.1.3) since the first well does not show any signs of impurity gettering. The emission at 1.5360 eV (1.5371 eV) is assigned to  $E_{1h}$  since it should be dominant (section 5.4.1) and the emission at 1.5375 eV (1.5385 eV) is assigned to a  $(D^0, X_{1h})$  transition. The recombination at 1.5343 eV is most probably a  $n=2$  excited state of the  $E_{1h}$  transition. The linewidths of MB1156 and MB1158 show a monotonic increase of FWHM with decreasing well width. This corresponds to an effective interface roughness of 0.2 monolayer (figure 5.22), similar to that reported by Tanaka et al (1987) who used growth interruption in their samples. The luminescence linewidths are comparable with the best previously reported of

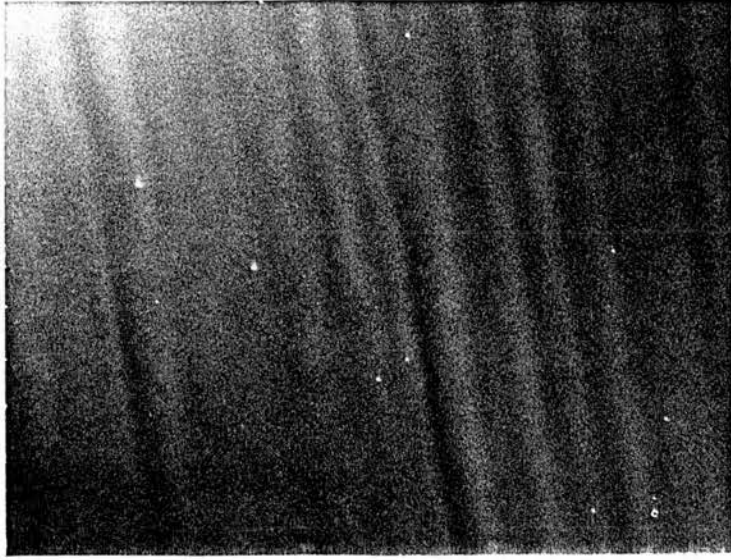


**Figure 5.20** Random modulation of the sample surface of misorientated substrates. The grown layers here is viewed under x50 magnification.

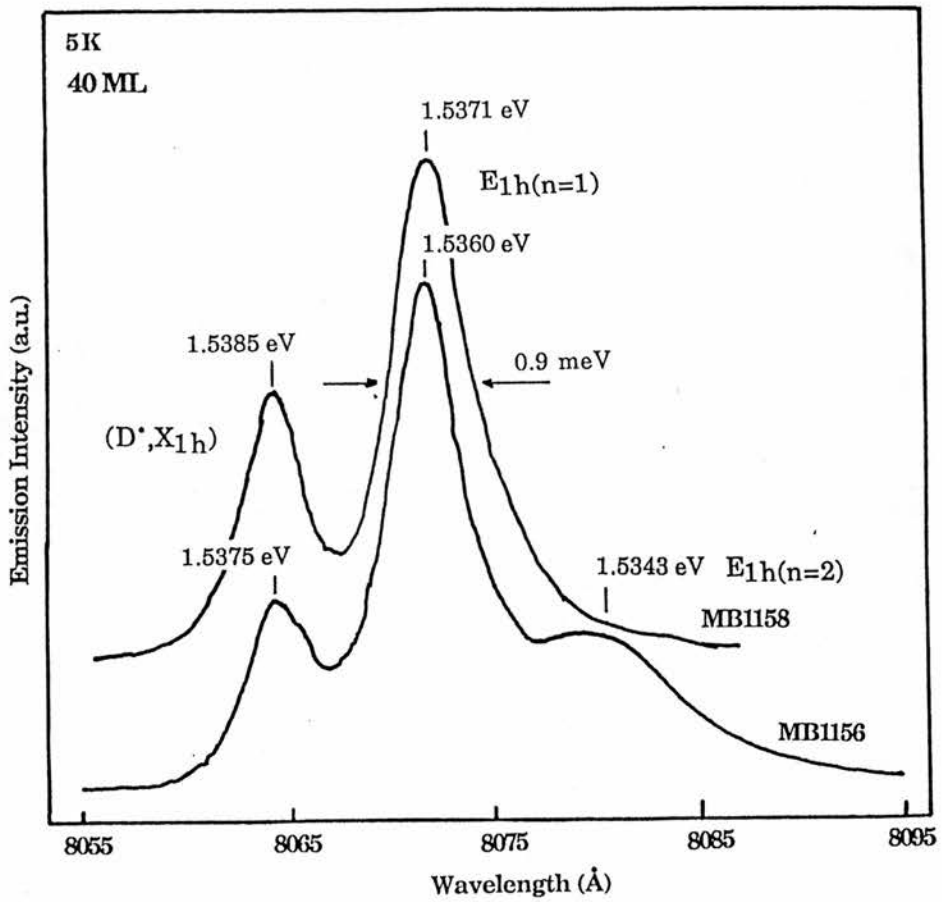


**Figure 5.21** Emission spectra of the 113 Å well (~40 monolayer thickness) with a  $\text{Al}_x\text{Ga}_{1-x}\text{As}$  barrier composition of  $x=0.4$  (MB1158) and  $x=0.3$  (MB1156). Although very narrow linewidths of 0.9 meV were observed it was impossible to assign the emission to interfacial islands.

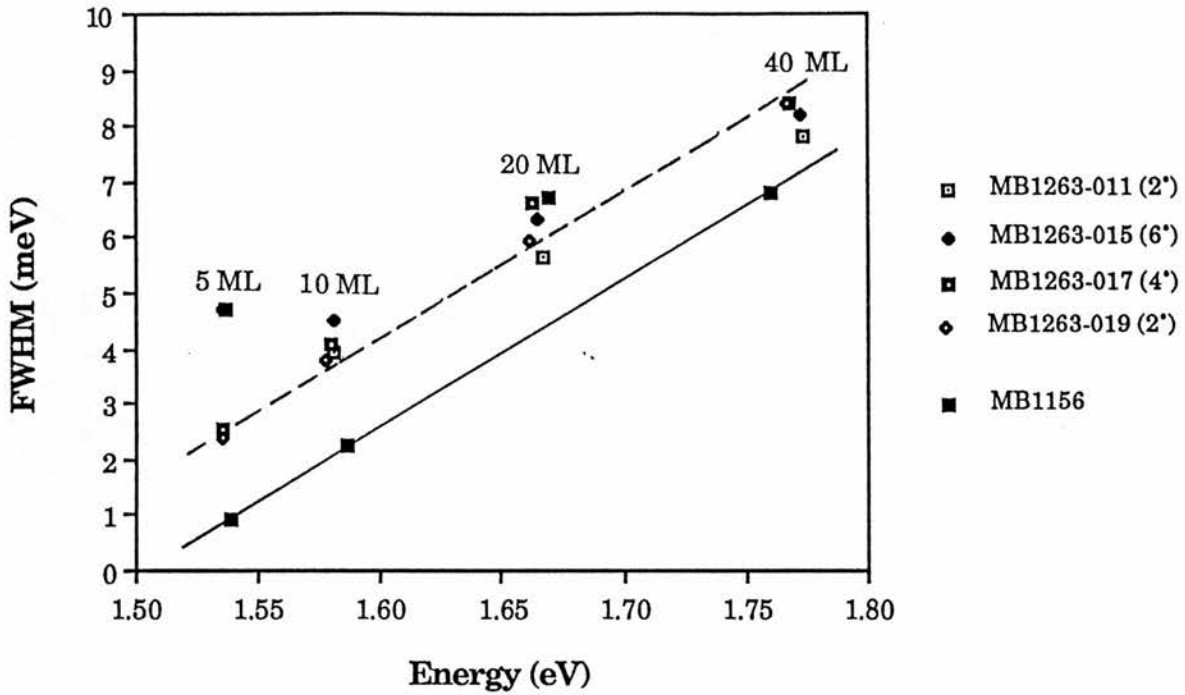


**Figure 5.22** Linewidth (FWHM) and the peak positions for wells grown on various misorientated substrates without growth interruption. Even without the use of growth interruption to smooth well interfaces with linewidths comparable to best produced by any other group have been produced. The slightly increased linewidths obtained from the wells grown on misorientated substrates suggest that greater impurity incorporation has occurred.

6.0 meV achieved by Tu et al (1987) comparing favourably with 6.7 meV for our 5 monolayer well (MB1156).

### 5.4.3.1 Barrier of composition $x=0.3$

The well structure described in section 5.4.3 was grown on misorientated substrates, of angle  $2^\circ$ ,  $4^\circ$  and  $6^\circ$ , with a barrier composition of  $x=0.3$  (MB1263). The linewidths obtained for MB1156 and the linewidths of the wells on the misorientated substrates are plotted for comparison in figure 5.22. Alloy composition and growth rate are expected to vary with orientation (Heonk et al 1989), but the well emission has the same energy regardless of orientation suggesting these growth parameters did not change. The substrate orientation does not show a functional difference on the luminescence linewidths of the wells. All the samples, regardless of orientation, exhibit the same monotonic increase in linewidth corresponding to interface roughness of  $\sim 0.2$  monolayer. Thus, MBE growth, even at a  $T_s=600^\circ\text{C}$ , results in smoothing of the vicinal planes formed on the misorientated substrate, producing a similar island size for all samples. Emission spectra from the wells are less well resolved on the misorientated substrates, with slightly increased linewidth,  $\sim 1.5$  meV, reflecting an increased impurity incorporation. The spectra obtained from the wells on  $4^\circ$  and  $6^\circ$  substrates have the largest linewidths suggesting that the substrates for these samples may be more difficult to clean.

Repeating sample MB1263, but now with growth interruption at each interface results in a drastic increase in linewidth again with no dependence on vicinal step width (figure 5.23). The observed linewidths are now equivalent to a one monolayer well width fluctuation in energy. When Tu et al (1987) used growth interruption on a  $50 \text{ \AA}$  well this resulted in a reduction of the linewidth from 4 meV to 1.6 meV; in our  $56.6 \text{ \AA}$  well the linewidth increases from 2.2 meV to 7.2 meV. This increase in linewidth, as a consequence of growth interruption,

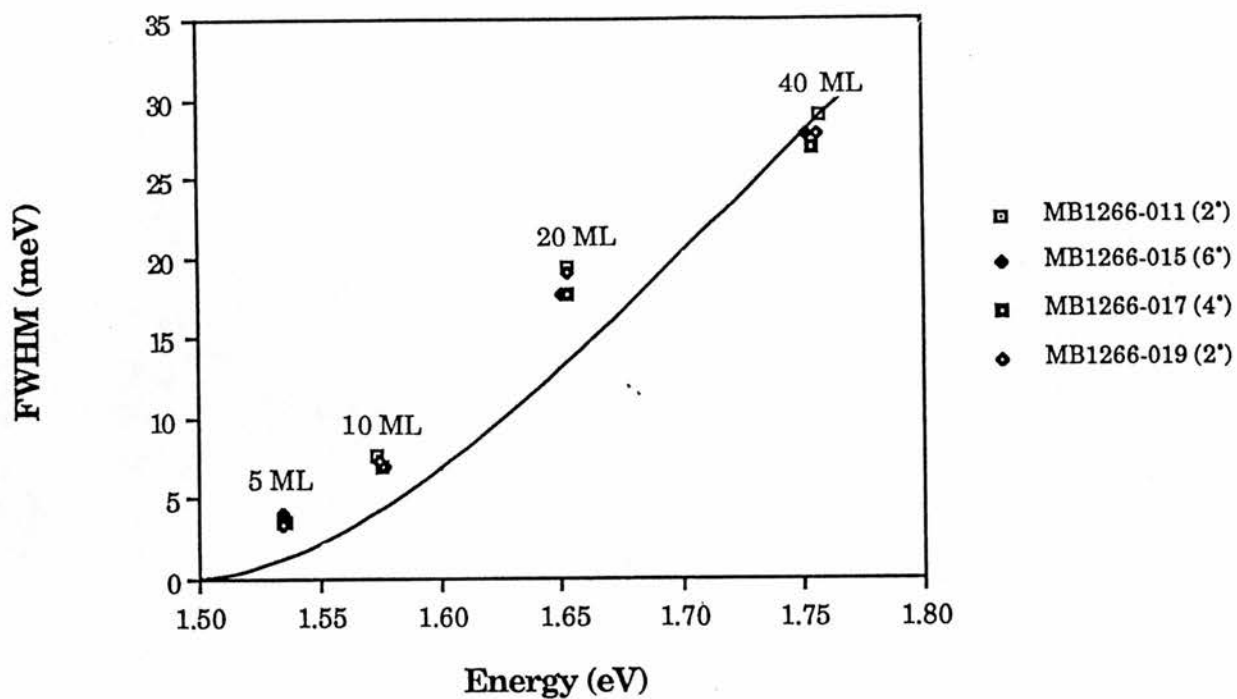


**Figure 5.23** Linewidth (FWHM) and the peak positions for wells grown on various misorientated substrates with growth interruption. Growth interruption instead of producing narrower linewidths as consequence of smoothing the interface region has increased the linewidth by a factor of ~3-4. The solid line corresponds to a monolayer well width fluctuation in energy.

has not previously been reported in the literature. Comparing the spectra obtained for MB1263 and MB1266 (figure 5.24) only one peak associated with a single transition is observed and there is no emission structure due to interface islands. The increasing intensity of the emission in the spectra of sample MB1263 suggests the growth front is smoothing as the epitaxial layer depth increases. This contrasts the trend in MB1266 where growth interruption at the first well results in an increased emission intensity and an apparently immediate improvement in the growth front. Compared to MB1156 both samples MB1263 and MB1266 have a peak intensity an order of magnitude lower.

A model for the broadening of luminescence linewidths in a quantum well as a consequence of interface roughness is given in section 5.3. The effect of alloy scattering from the barrier is ignored since Singh and Bajaj showed that for a 28 Å well of FWHM 8.3 meV (c.f. 6.7 meV for our 28.3 Å well), 5.8 meV of the linewidth is accounted for by interface roughness. The estimated luminescence linewidth was plotted as a function of well thickness for island sizes of 20 Å, 40 Å, 80Å, 160 Å and 200 Å with the linewidths obtained for samples MB1256, MB1263 and MB1269 overlaid. Wells grown without growth interruption have a linewidth that is dominated by pseudo rough surface with an island size of 40 Å. Therefore, it must be concluded that the luminescence linewidth is dominated by the inverted interface (figure 5.26a) which is limited by the Al diffusion length of ~40 Å (section 2.1.4). So, growth interruption results in a partial smoothing of the inverted interface, with a corresponding reduction in vicinal step density, (section 5.2.2) increasing the island size to ~200 Å, regardless of orientation, (figure 5.26b) and thus explaining the increased linewidths observed. This is contrary to the suggestion by Wada et al (1989) of interface smoothing being limited by vicinal step width. The interface structure of the normal interface is not clear, if it contributed to the luminescence then larger linewidths would be expected since  $\sigma^2_{\text{total}} = \sigma^2_{\text{inverted}} + \sigma^2_{\text{normal}}$ . So the interface must be assumed

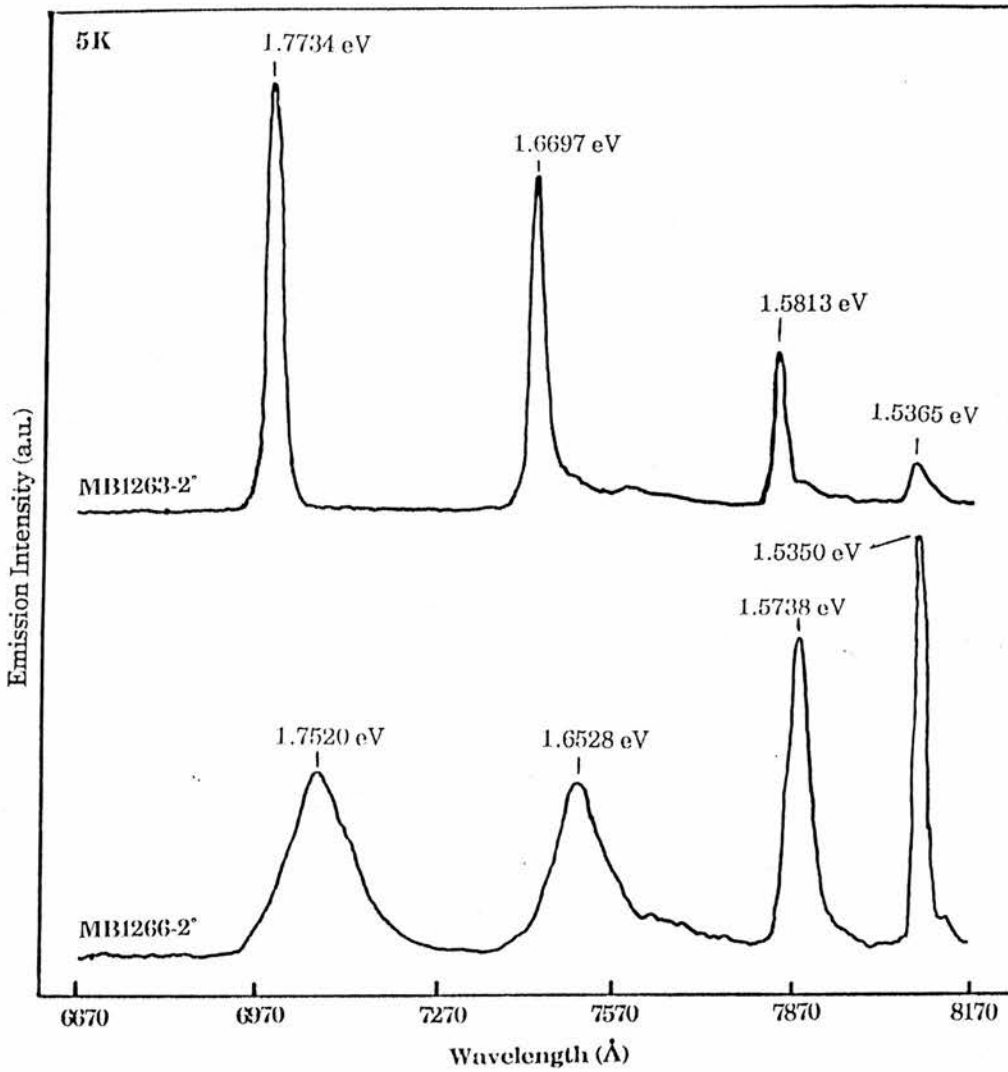


**Figure 5.24** Typical spectra for GaAs- $\text{Al}_x\text{Ga}_{0.7}\text{As}$  MQW  $x=0.3$  with (MB1263) and without growth interruption (MB1266).

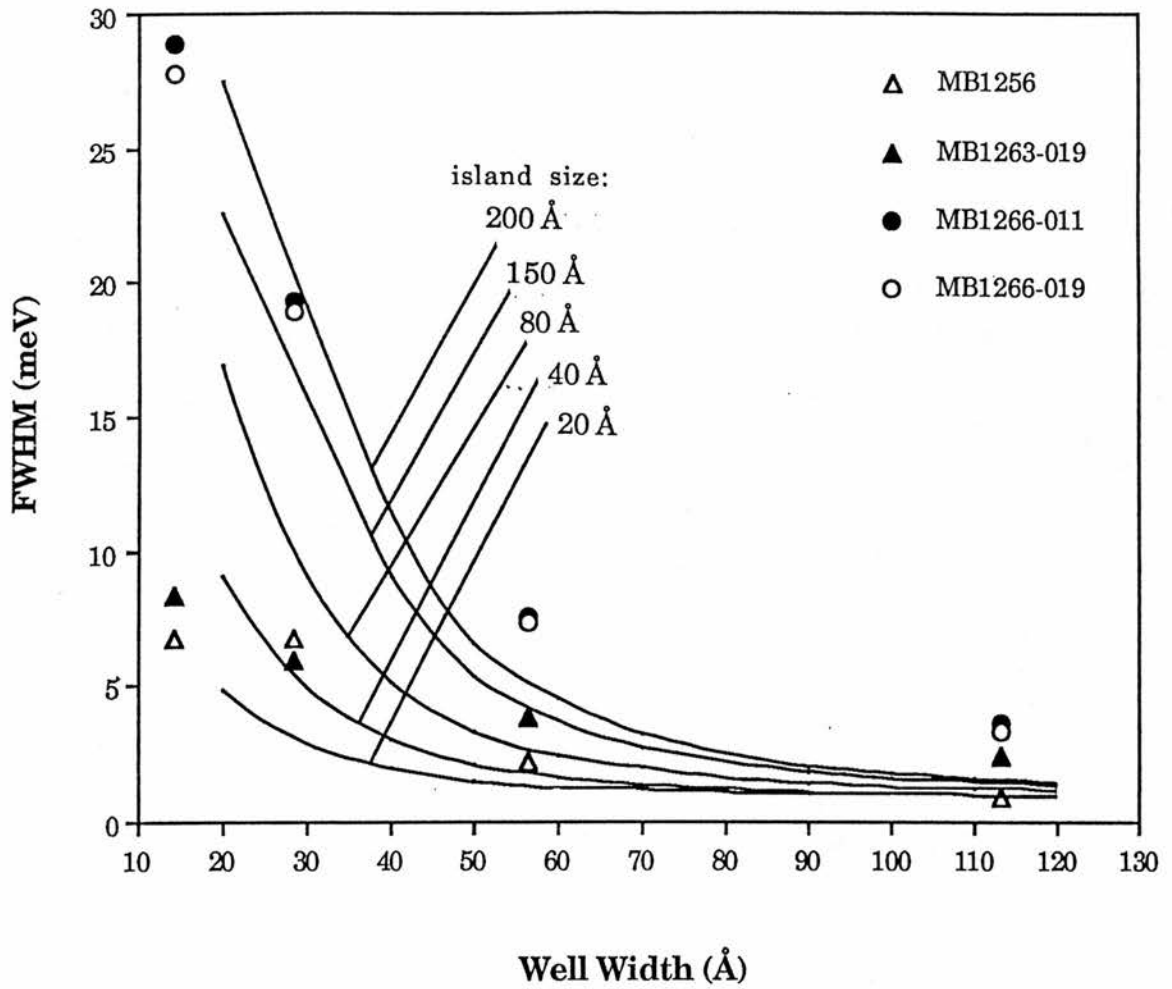


**Figure 5.25** Calculated luminescence linewidth due to interface roughness for various widths of atomic island size. Our data shows that the MB1256 and MB1263 exhibit an islands size of  $\sim 40$  Å and the growth interrupted sample has an island size closer to the excitonic diameter,  $a_{exc}$ .

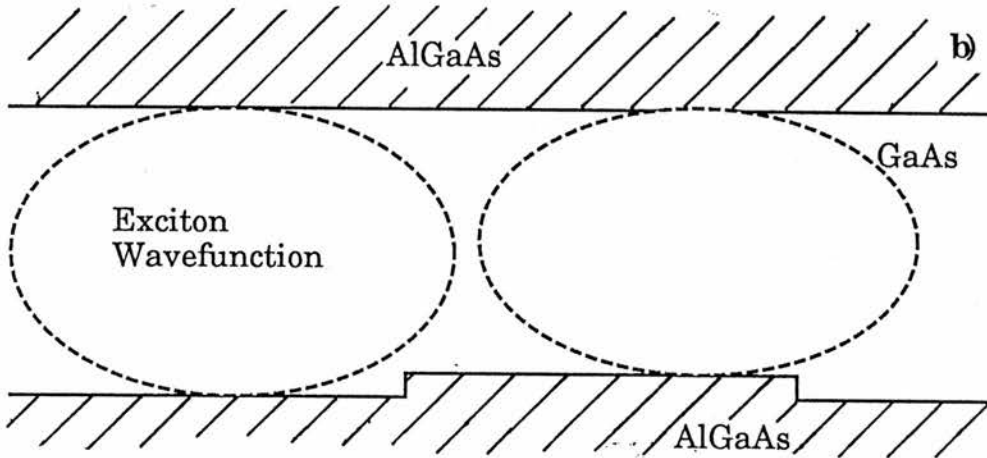
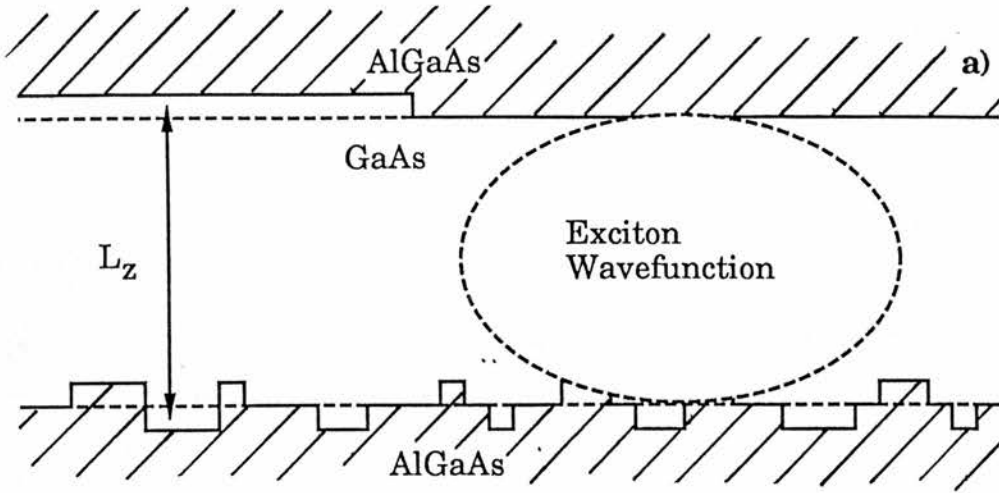


**Figure 5.26** Since the samples exhibit very good linewidths it is assumed that smoothing occurs only at the inverted interface. a) Prior to growth interruption the surface appears pseudo-smooth with the exciton averaging over 40 Å islands. b) Growth interruption causes the interface islands to enlarge with a corresponding increase in the luminescence linewidth, figure 5.25.

to be smooth to the sensing exciton (figure 5.26) and probably reflects the compositional variation of the alloy layer observed in section 5.4.1.3, consequently with no island formation at the well interface

### 5.4.3.2 Barrier of composition $x=0.4$

Sample MB1269 was grown with a barrier composition of  $x=0.4$  and growth interruption of two minutes at each interface. A remarkable increase in the linewidth compared to MB1158, and even the previous growth interrupted sample MB1266, is obtained (figure 5.27). It would be tempting to assign the increased linewidths to an interface fluctuation of greater than one monolayer. But both, the GaAs emission (figure 5.28) and the  $\text{Al}_{0.4}\text{Ga}_{0.6}\text{As}$  emission (not shown), into which the well wavefunction will have significant penetration, are dominated by a  $(D^{\circ}, A^{\circ})$  transition. An examination of the well luminescence in MB1269 shows that the emission is not excitonic (figure 5.28) and the difference in energy between the spectra in MB1158 and MB1269 (figure 5.27) can be related to an acceptor binding corresponding to different well widths (section 5.2.1). So the well emission will be due to an acceptor transition, most probably  $(e, A^{\circ})$  at the excitation power density used.

It is interesting to note the linewidth now has a functional dependence on vicinal step width but not that shown in figure 5.25. This provides proof that the substrate orientation was not changed during sample preparation or initial growth stages. The  $4^{\circ}$  misorientated substrate, with a vicinal step width similar to that of the Al diffusion length, exhibits linewidths closest to a monolayer fluctuation, particularly the  $14.2 \text{ \AA}$  well whose emission appears excitonic. It may be that better material quality with a less rough interface occurs in this instance, because Al can migrate easily to a vicinal plane without rearrangement of terrace geometries required for the  $2^{\circ}$  and  $6^{\circ}$  substrates. In MOCVD samples grown on substrates with a  $4^{\circ}$  orientation produce the best

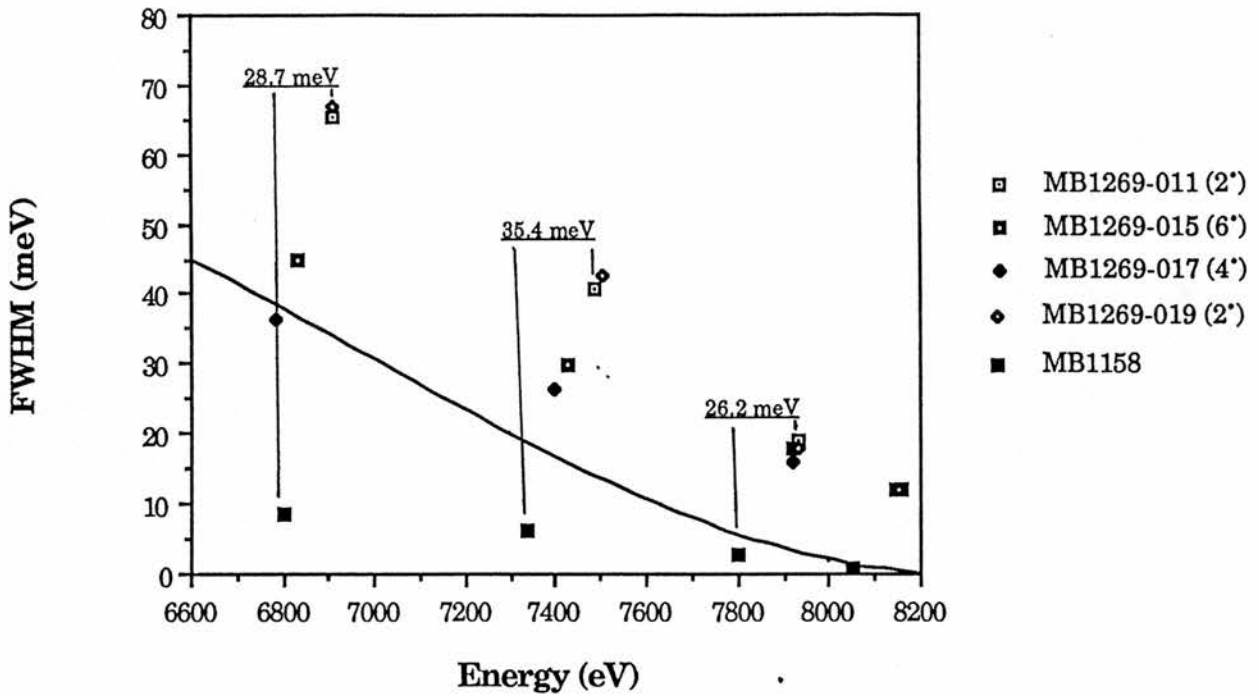


**Figure 5.27** Growth interruption on a well structure with  $x=0.4$  (MB1269) results in luminescence linewidths that are approximately an order of magnitude larger than those obtained without (MB1158). It would be tempting to assign these increased linewidths to interface fluctuations of greater than a monolayer when compared to the well width fluctuation (solid line). But a closer examination of the luminescence spectra and the emission energy suggests the luminescence is dominated by ( $D^0, A^0$ ) transitions, figure 5.28.

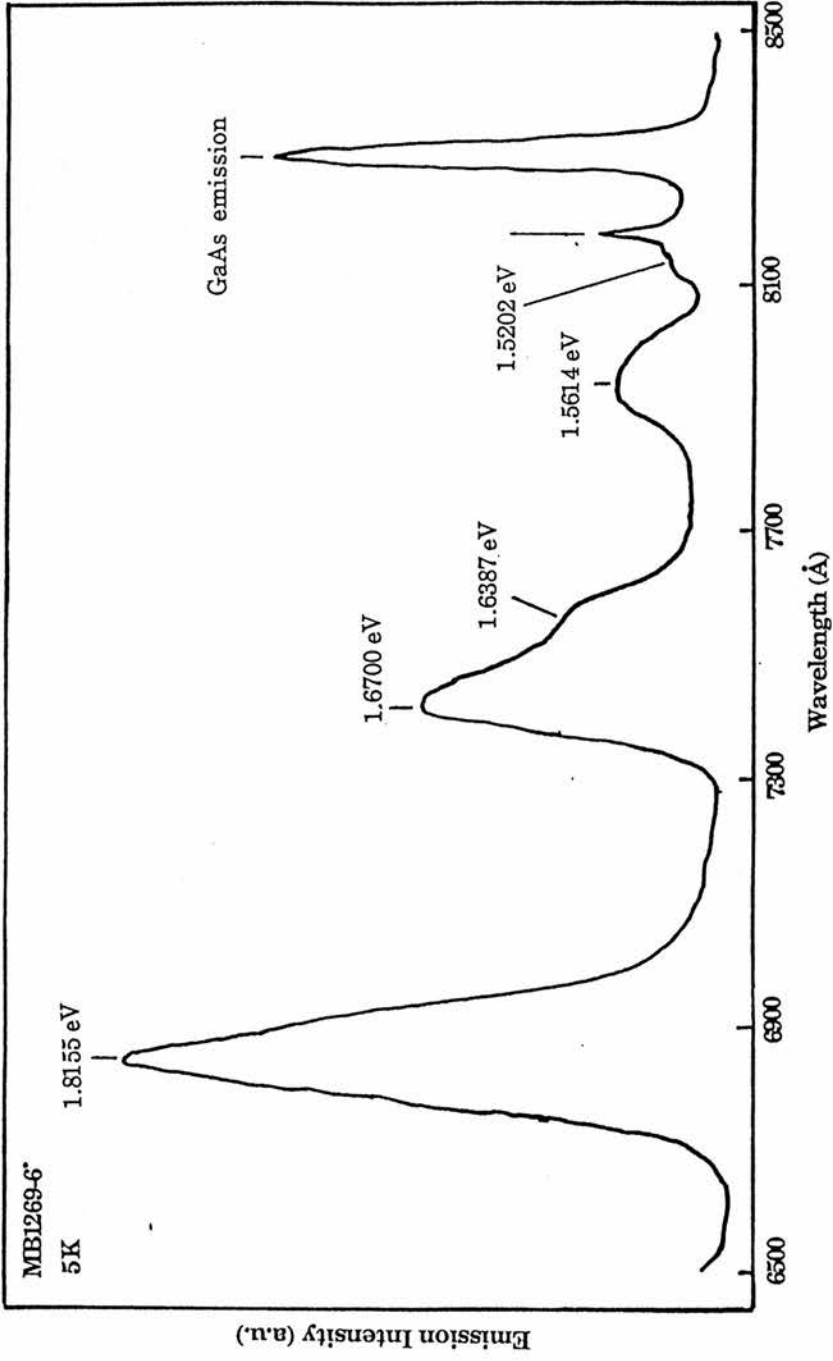


Figure 5.28 A typical spectrum obtained from MBI269 for a growth interrupted samples with barriers of  $x=0.4$  grown on a  $6^\circ$  orientated substrate. The GaAs ( $D^0, A^0$ ) emission due to a carbon acceptor dominates the spectrum.

quality material (Claxton 1989). Since alloy composition or growth rate does not vary with substrate orientation (section 5.4.3.1) then the Al and Ga surface diffusion length and not desorption rate is dominant in controlling material quality. On the misorientated substrate surface the Ga and Al should have different diffusion lengths parallel and perpendicular to the vicinal planes. Since growth interruption is used in this sample it is possible that elongated islands along the vicinal planes could be formed. Unfortunately the exciton would not be able to sense this.

### 5.4.3.3 Barrier of composition $x=0.2$

A reduction in barrier composition  $x=0.2$  did not result in the change of linewidth and lineshape reported by Tanaka et al (1986) for their growth interrupted samples, figure 5.29. Instead the emission was the same as the  $x=0.3$  samples (section 5.4.3.1) dominated by a  $E_{1h}$  transition and the linewidth again showing a  $\sim 0.2$  monolayer fluctuation, figure 5.30. A slight compositional variation of the Al content in the barrier was observed, 0.2%, but could not be correlated to substrate orientation so was assigned to non-uniformities in the growth system. The excitonic well emission of the 113.2 Å well mirrors exactly that of the bulk GaAs (figure 5.31) corroborating the assignment of the well emission made in section 5.4.1. In addition, the substrate orientation can change the amphoteric nature of an impurity (Wang et al 1985). Figure 5.32 show the appearance of a  $(D^0, A^0)$  transition, on the  $2^\circ$  orientated substrate, at 1.4831 eV which is assigned to silicon. This suggests the previously unknown donor in our samples could be silicon.

## 5.5 $Ga_{0.47}In_{0.53}As-InP$

$Ga_{0.47}In_{0.53}As-InP$  based heterostructures are becoming of greater importance in optoelectronic applications since the band-gap can be tuned to 1.3 or 1.55  $\mu m$ , the windows of low loss and minimum dispersion of silica fibres.

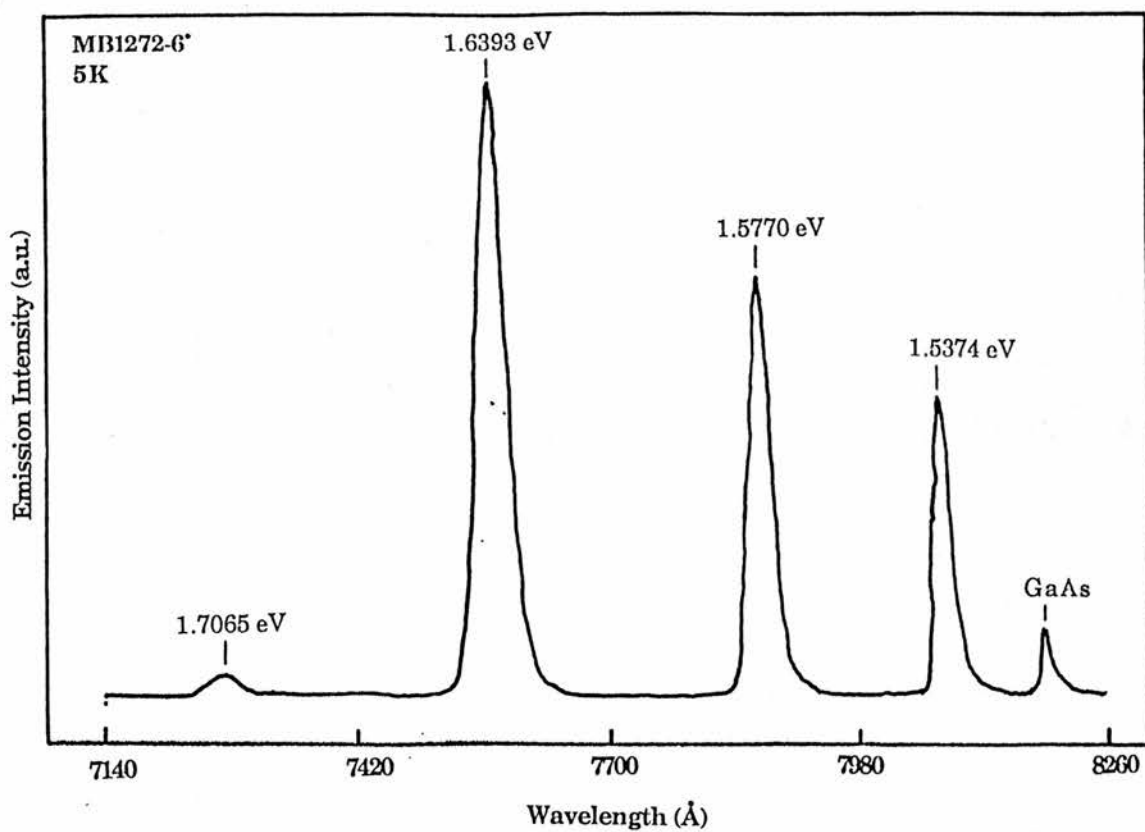


**Figure 5.29** Typical emission spectrum obtained from MB1272 grown on a  $6^\circ$  orientated substrate. The luminescence intensity increases for the wells closer to the sample surface although, the 5 ML shows an anomalous decrease in well intensity.

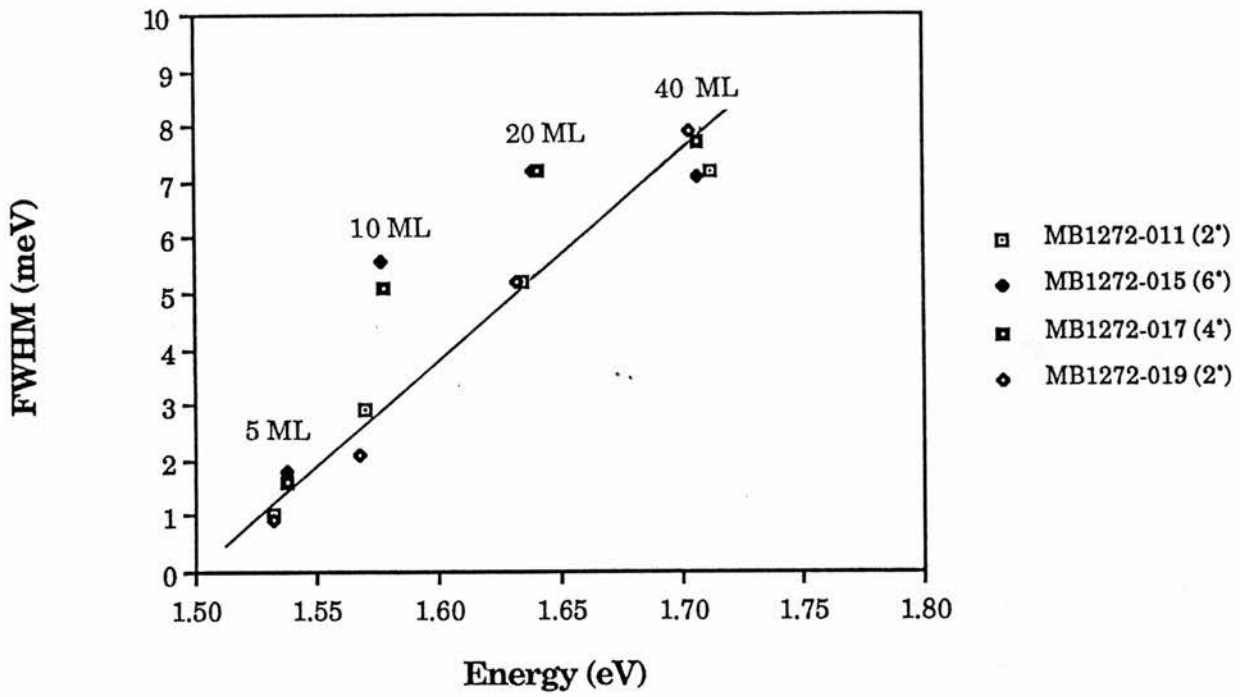


**Figure 5.30** Linewidth (FWHM) and the peak positions for wells grown on various misorientated substrates without growth interruption. Lower Al content in the barriers,  $x=0.2$ , does not result in smoother inverted interfaces since linewidths are similar to those observed before (c.f. figure 5.22).

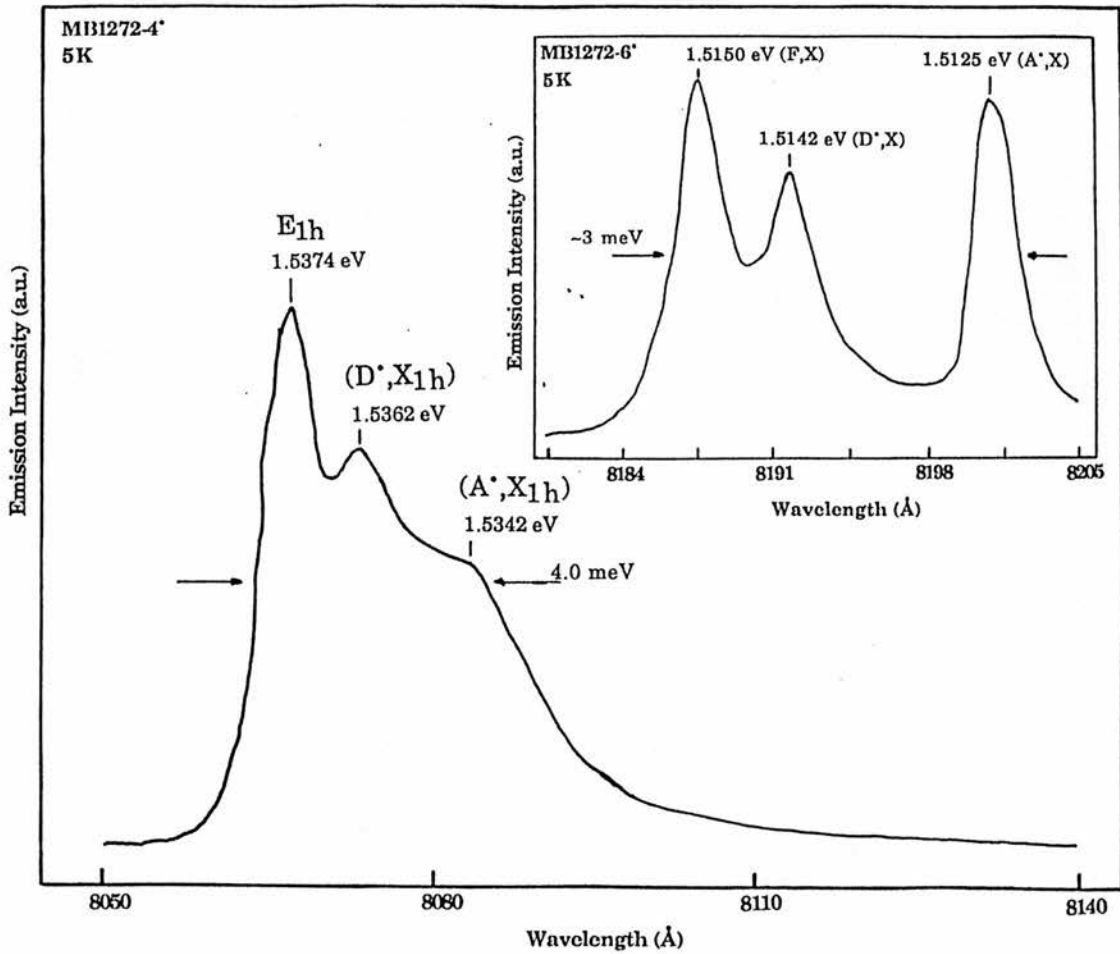


**Figure 5.31** Luminescence obtained from the 113 Å (40 ML) well grown on a misorientated substrate without growth interruption. It mirrors that obtained for the undoped GaAs buffer layer (insert). This supports the earlier assignment of the lower energy well transitions as being due to donor and acceptor bound impurities.

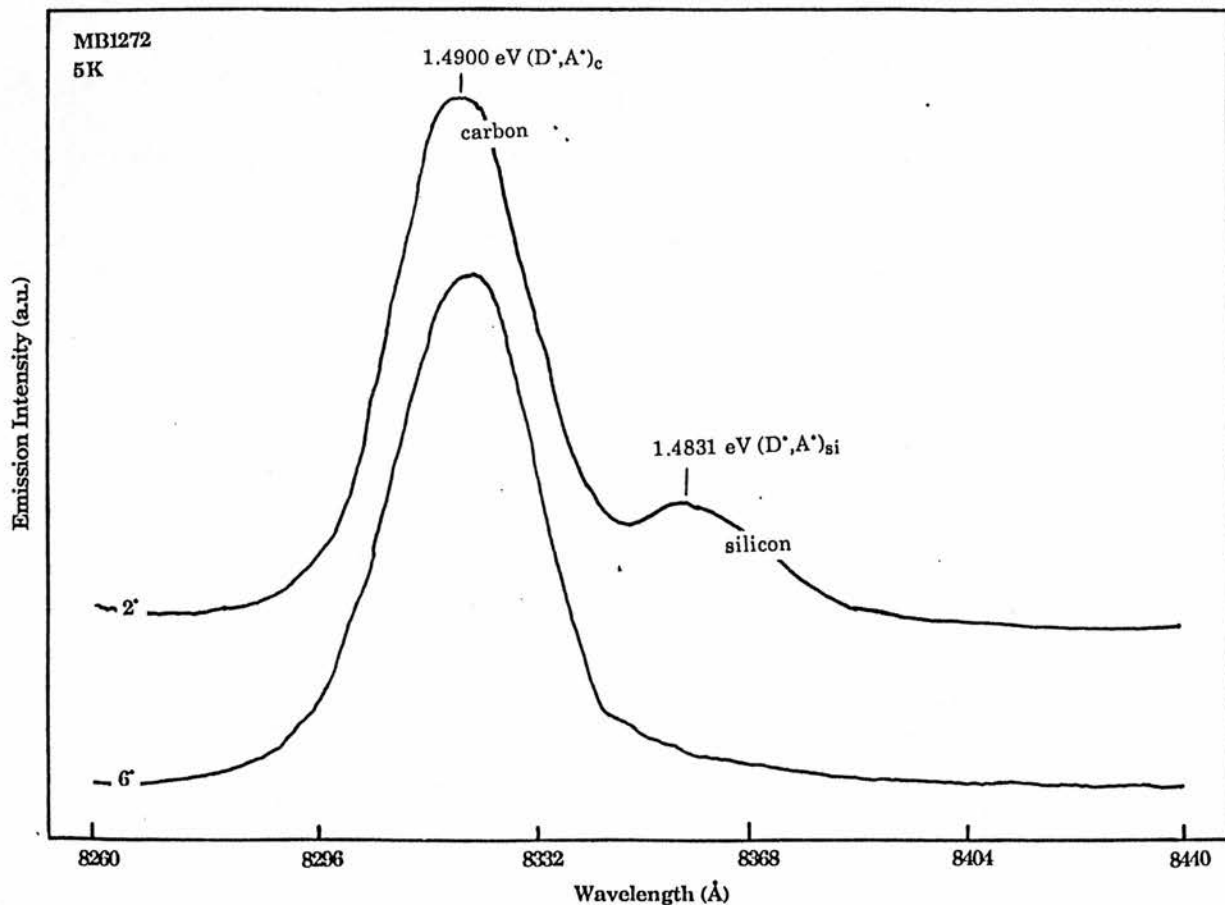


**Figure 5.32** The luminescence shows evidence that the sample off-cut angle effects the amphoteric nature of silicon. Although this sample is nominally undoped strong (D\*,X) emission is always observed in the spectra, figure 5.31. The fact that a Si transition (1.4831 eV) is seen in the (D\*,A\*) region means that it can be assigned to this previously unknown donor.

The growth of  $\text{Ga}_{0.47}\text{In}_{0.53}\text{As-InP}$  by solid source MBE (SSMBE) has proved difficult due to interface control of the group V species As and P. A simple mechanical shutter cannot be used to control the fluxes consequently an interruption to growth of 8 minutes is required at each interface during the group V flux change (Marsh et al 1985). Most groups have used other growth methods or grown  $\text{Al}_{0.52}\text{In}_{0.48}\text{As-Ga}_{0.47}\text{In}_{0.53}\text{As}$  (Scott et al 1986) which only requires the control of one group V flux, but there are difficulties associated with  $\text{Al}_{0.52}\text{In}_{0.48}\text{As}$  material quality (section 4.2). Claxton et al (1986) solved these problems by using a nitrogen cooled aperture to collimate the group V beam fluxes thus increasing the beam extinction ratio. This now allowed the use of mechanical shutters which resulted in an improvement in interface quality with a corresponding decrease in linewidth (figure 5.33). In this section a brief review of the relevant literature of the optical properties of  $\text{Ga}_{0.47}\text{In}_{0.53}\text{As-InP}$  heterostructures is given with a short summary of some of our data for SSMBE grown samples. Much of this experimental work was completed in parallel with the group at RSRE. The results obtained here corroborate their findings.

### 5.5.1 Review

Skolnick et al (1986a) completed a detailed analysis of MOCVD grown  $\text{Ga}_{0.47}\text{In}_{0.53}\text{As-InP}$  heterostructures using PL, PLE, photoconductivity and photoreflectance. They found typically, for a 150 Å well with a FWHM of 5.3 meV, that extrinsic processes determine the linewidth below 10 K. On raising the sample temperature from 2 K excitons become unbound from potential fluctuations in the well and populate the higher energy free exciton state. As a result the emission is observed to move to higher energies with an increase in linewidth since the exciton now senses the well interface (figure 5.35). A similar conclusion was drawn for the excitonic emission observed from  $\text{Al}_{0.52}\text{In}_{0.48}\text{As-Ga}_{0.47}\text{In}_{0.53}\text{As}$  wells by Davey et al (1987). Their modulation doped well samples were found to have an anomalous lineshape which was strongly skewed towards

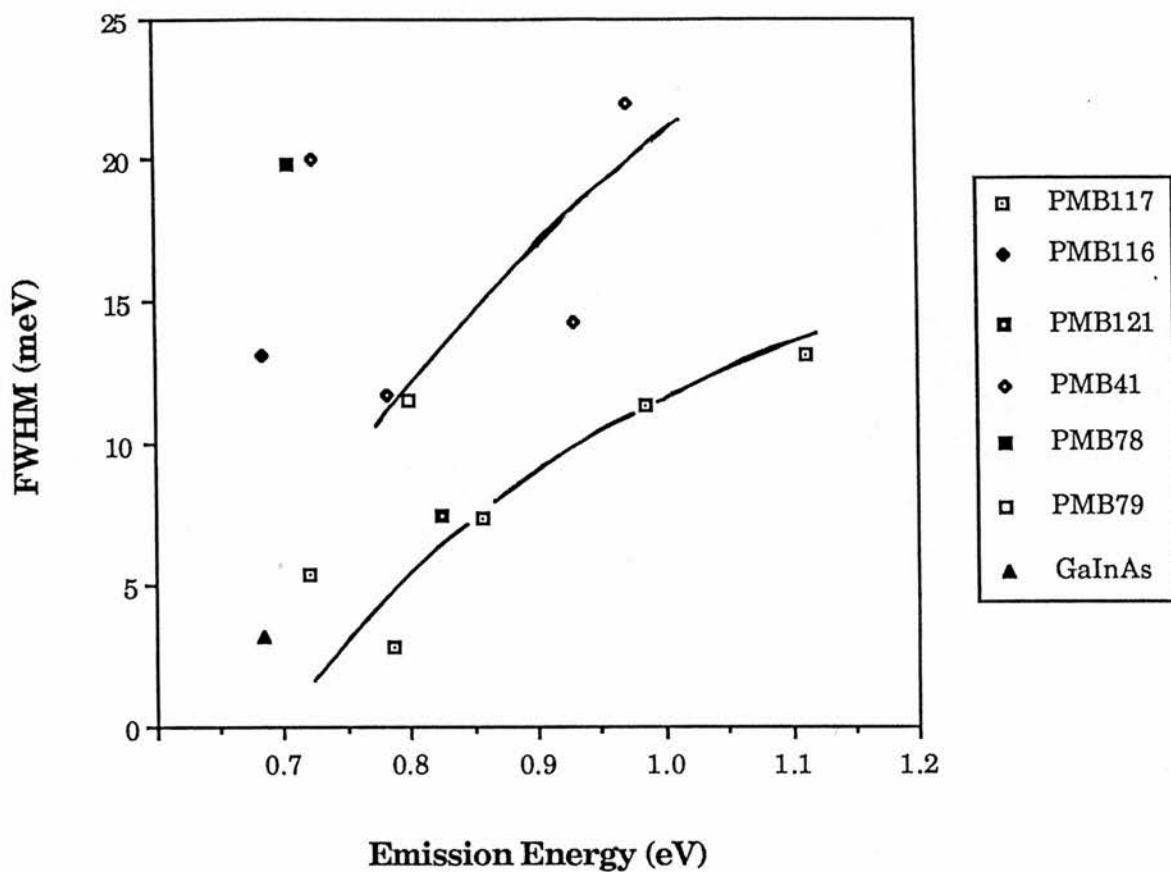


**Figure 5.33** The linewidths of all the  $\text{Ga}_{0.47}\text{In}_{0.53}\text{As-InP}$  quantum well structures at 2 K considered in this work (see Table 2.2 for sample summary). A reduction in FWHM is observed for PMB116, PMB117 and PMB121 grown with a liquid nitrogen cooled shutters. Some of the wells show an increased linewidth due to free carrier broadening.

higher energies (Skolnick et al 1986b). This is interpreted by Nash et al (1988) as a consequence of a Fermi edge singularity as photo-created holes are strongly localized. Even in undoped wells free carrier broadening can have a dominant effect on the observed lineshape (Saker et al 1988) so, Schottky barrier depletion or a magnetic field have been used to observe the inhomogeneous linewidth of the luminescence (Skolnick et al 1987a).

The best quality  $\text{Ga}_{0.47}\text{In}_{0.53}\text{As-InP}$  heterostructures, to date, have been produced by CBE with an estimated effective interface roughness of 0.12 monolayers (Tsang et al 1986). Structure has been observed in well spectra and assigned to both, compositional variations of the  $\text{Ga}_{0.47}\text{In}_{0.53}\text{As}$  barrier (Sauer et al 1984) and monolayer thickness fluctuations (Kawaguchi and Asahi 1987). Using thermally modulated photoluminescence technique Gal et al (1986) found the exciton binding energy to vary from 8-10 meV for wells of 100-65 Å. The question of the band offset is again a contentious issue (section 5.2.3), fitting to PLE and absorption spectra has given the conduction:valence band offsets as 50:50, 45:55 and 35:65 (Westland et al 1987). In general, many of the physical principles discussed in section 5.2 still apply to  $\text{Ga}_{0.47}\text{In}_{0.53}\text{As-InP}$  heterostructures.

### 5.5.2 Temperature dependence

The results presented here are mainly from sample PMB117 as it is representative of the data obtained from all the samples (table 2.2). PMB117 consists of five  $\text{Ga}_{0.47}\text{In}_{0.53}\text{As}$  layers of thickness 10 Å, 20 Å, 28 Å, 50 Å and 110 Å, labeled PMB117a-e respectively, separated by 1000 Å barriers of InP grown by SSMBE with cooled nitrogen shutters (section 5.3). The 110 Å well, PMB117e, has an increased linewidth, 5.4 meV, as a consequence of free carriers in the well and has been studied in detail elsewhere (Saker et al 1988). They used a Schottky gate to vary the free carrier density in the well and showed the lineshape to

narrow from the high energy side as the free carrier density decreased. Free carrier broadening is not important for the wells considered here as they are within the surface depletion layer. Since the emission shows narrow linewidths, approximately unity excitation power density dependence and no shifts in energetic position, it can be assumed to be excitonic, compared to convolution band edge transitions observed in the bulk (section 3.4). In analogy to GaAs-Al<sub>x</sub>Ga<sub>1-x</sub>As it is assumed the emission is from a E<sub>1h</sub> transition. The linewidths of the 28 Å and 50 Å wells, 2.9 meV and 7.4 meV, are comparable to those observed by Tsang et al (1986) and almost equivalent to alloy scattering in the bulk, 3.2 meV (figure 3.13).

As the temperature of PMB117 is increased the emission from all the wells, except PMB117a, shift to higher energy (figure 5.34 and 5.35) with a corresponding increase in linewidth. As discussed in section 5.2.1, this provides clear evidence that the emission is essentially extrinsic, since, intrinsic or free exciton emission would follow the band-edge as in GaAs-Al<sub>x</sub>Ga<sub>1-x</sub>As (figure 5.18). The shift to higher energy occurs when the exciton becomes unbound and populates the free exciton transition. This also observed, but to lesser extent, in bulk Ga<sub>0.47</sub>In<sub>0.53</sub>As (figure 3.14). As a consequence the thermal activation energies derived from the well emission does not reflect exciton binding energy as in GaAs-Al<sub>x</sub>Ga<sub>1-x</sub>As (figure 5.19). Above 150 K the emission linewidth corresponds to ~1.8 kT (figure 5.34) suggesting a band to band transition now dominates. As the sample temperature is increased another transition, ~8 meV below the E<sub>1h</sub> is observed (figure 5.37). The exact assignment of this recombination is uncertain since during thermalisation it shifts to lower energies. It has been suggested it is due to a defect related band (Saker et al 1988) although, it seems more likely it is acceptor related transition exhibiting a distribution of binding energies as it may be located at the well interface and also at the well centre (section 5.2.1).

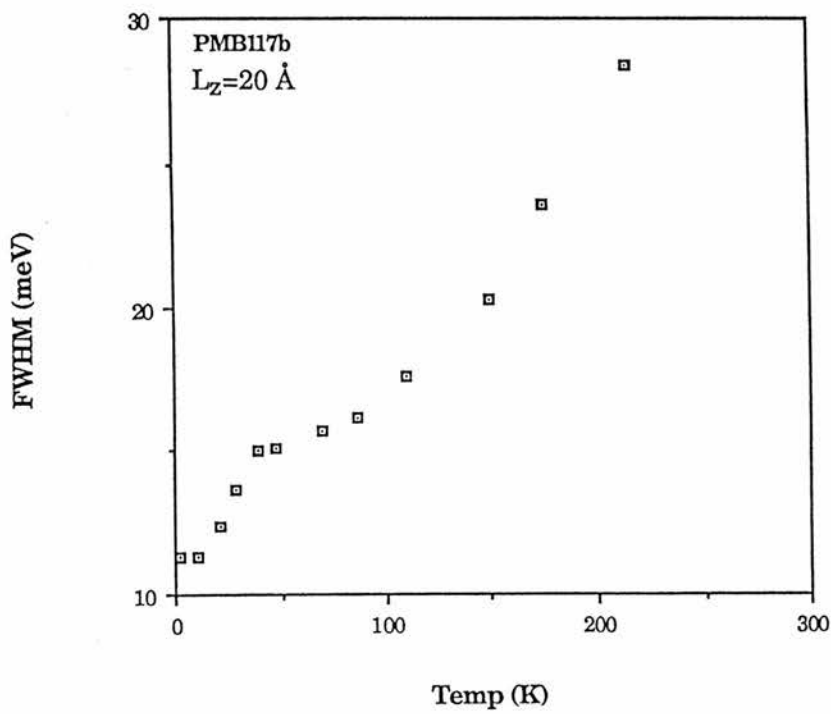
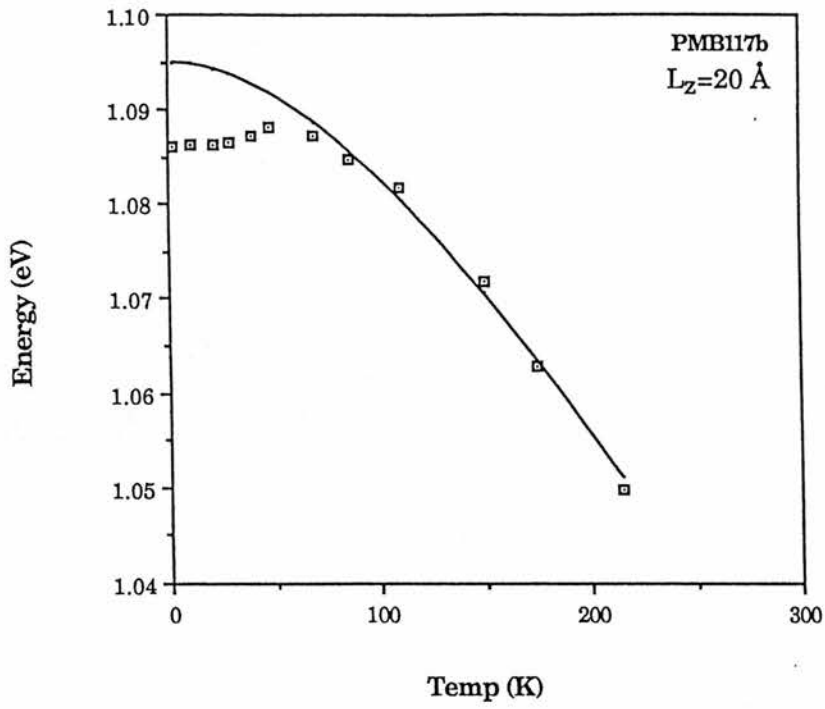


**Figure 5.34** The dependence of the emission energy and linewidth of the 20 Å well in PMB117b and its variation of linewidth with temperature. The solid line shows the Ga<sub>0.47</sub>In<sub>0.53</sub>As band-edge dependence extrapolated to the well energy.

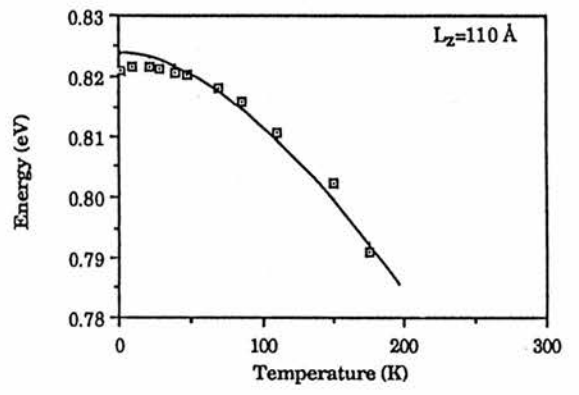
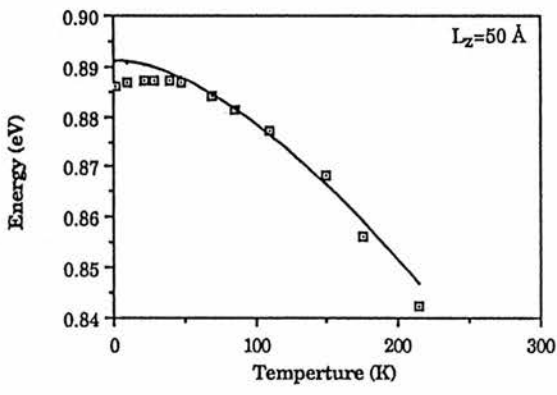
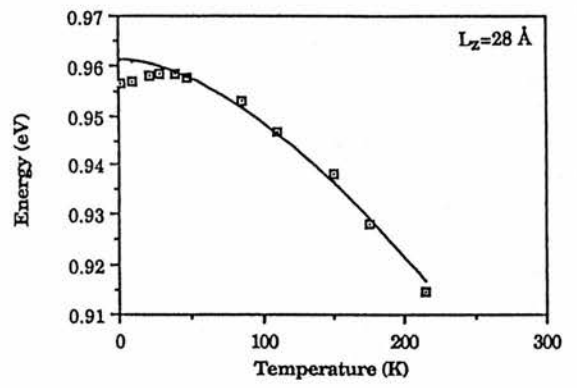
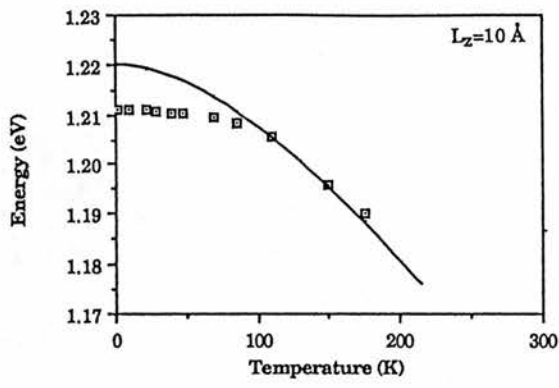


**Figure 5.35** Temperature dependence of emission for the other wells in PMB117 along with expected band-edge dependence.

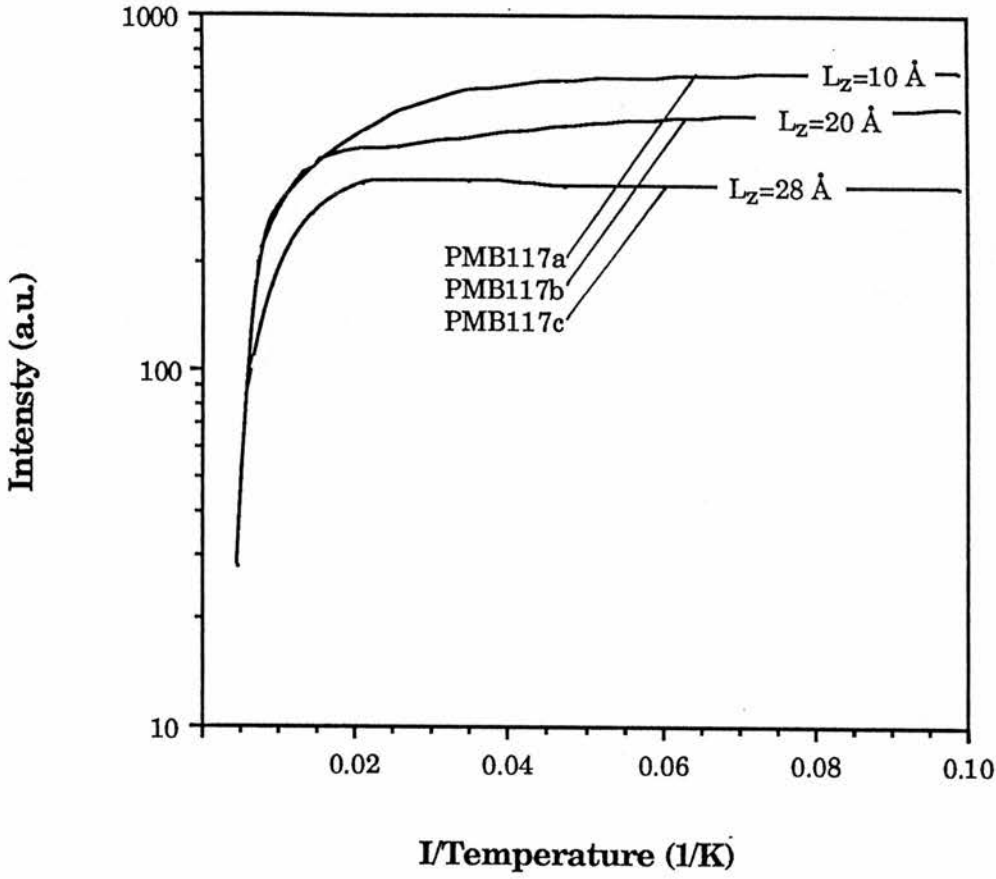


**Figure 5.36** Temperature dependence of various  $\text{Ga}_{0.47}\text{In}_{0.53}\text{As}$  wells emission intensity. Since the exciton is localised by alloy fluctuations, the estimated activation energy for dissociation of the exciton does not correspond to the exciton binding energy. As the sample temperature is increased all well transitions quench with the same dissociation energy.

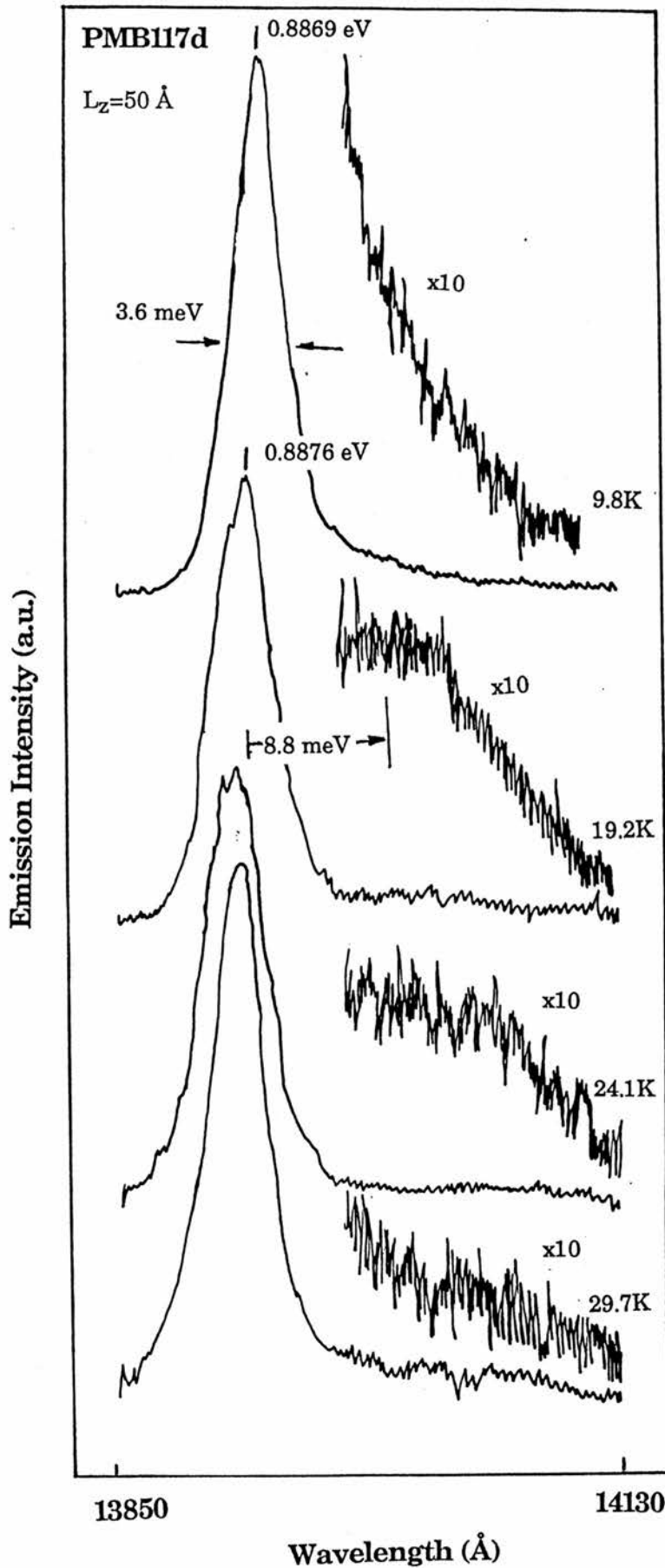


**Figure 5.37** Above 10K, defect related band,  $\sim 9 \text{ meV}$  below the  $E_{1h}$  emission is observed in PMB117d ( $L_z = 50 \text{ \AA}$ ). This emission moves to lower energy with increasing temperature until it quenches.

LO phonon emission is not observed in the PL spectra from GaAs-Al<sub>x</sub>Ga<sub>1-x</sub>As well because coupling is weak for free exciton transitions. But in Ga<sub>0.47</sub>In<sub>0.53</sub>As-InP since the exciton is essentially localized due to potential fluctuations in the well LO phonon so coupling is stronger and a the LO phonon replica is observed (figure 5.38). Here the 10 Å, PMB117a, well exhibits phonon emission due to a InP LO phonon at 1.2454 eV, 41.2 meV away from the main transition. The resolution of the emission did not allow a GaAs-like LO phonon at ~33.5 meV to be observed. It has been suggested this could be due to free carrier screening (Skolnick et al 1987b) or photo-created carriers in the well (Mowbray et al 1987) but neither of these arguments are valid in this instance because the well is within the surface depletion layer and the excitation power density was low. This suggests very efficient coupling of the 10 Å Ga<sub>0.47</sub>In<sub>0.53</sub>As well into the InP barrier due to interface disorder and thus a relaxing of selection rules. The interface region has a greatest effect in the narrowest well and disorder in the 10 Å well is reflected in the larger than expected linewidth, 13.3 meV, compared to the extrapolated value, 9 meV, from the 28 Å and 50 Å wells (c.f. Tsang et al 1986).

The superlattice structure PMB121 is a periodic array of 25 Å Ga<sub>0.47</sub>In<sub>0.53</sub>As wells separated by 100 Å InP, originally grown to check interface roughness. PLE was completed on this sample using a white light source and monochromator (figure 5.39). The spectra obtained confirms absorption measurements taken previously (Claxton et al 1986) and shows the E<sub>1l</sub> transition ~82 meV below the E<sub>1h</sub> transition reflecting the larger valence band confinement compared to GaAs-Al<sub>x</sub>Ga<sub>1-x</sub>As. A peak associated with E<sub>1h</sub> was not resolved because the detector bandwidth was similar to the luminescence linewidth. Sample PMB116, a 230 Å Ga<sub>0.47</sub>In<sub>0.53</sub>As well, shows bulk like emission which may be free carrier broadened (figure 5.40). As the sample temperature is increased peaks to higher energy are observed due to strong compositional

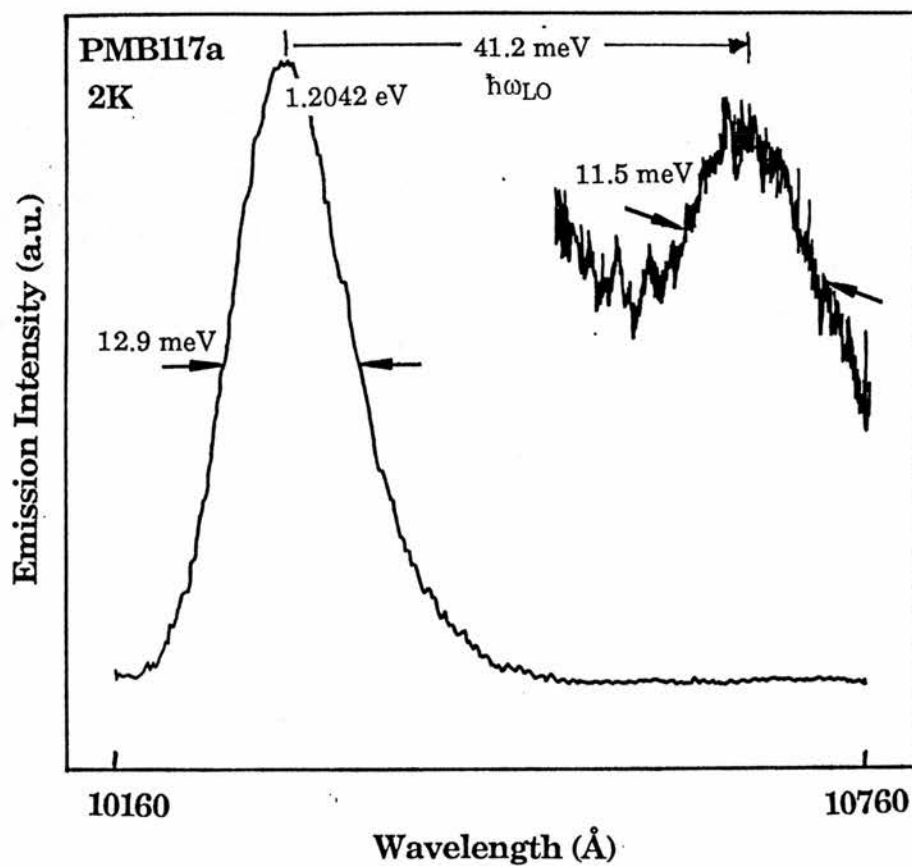


**Figure 5.38** The 10 Å well exhibits a strong InP LO phonon possibly due to efficient coupling of the well into the barrier. The lower energy GaAs-like phonon at 33.5 meV is not resolved.

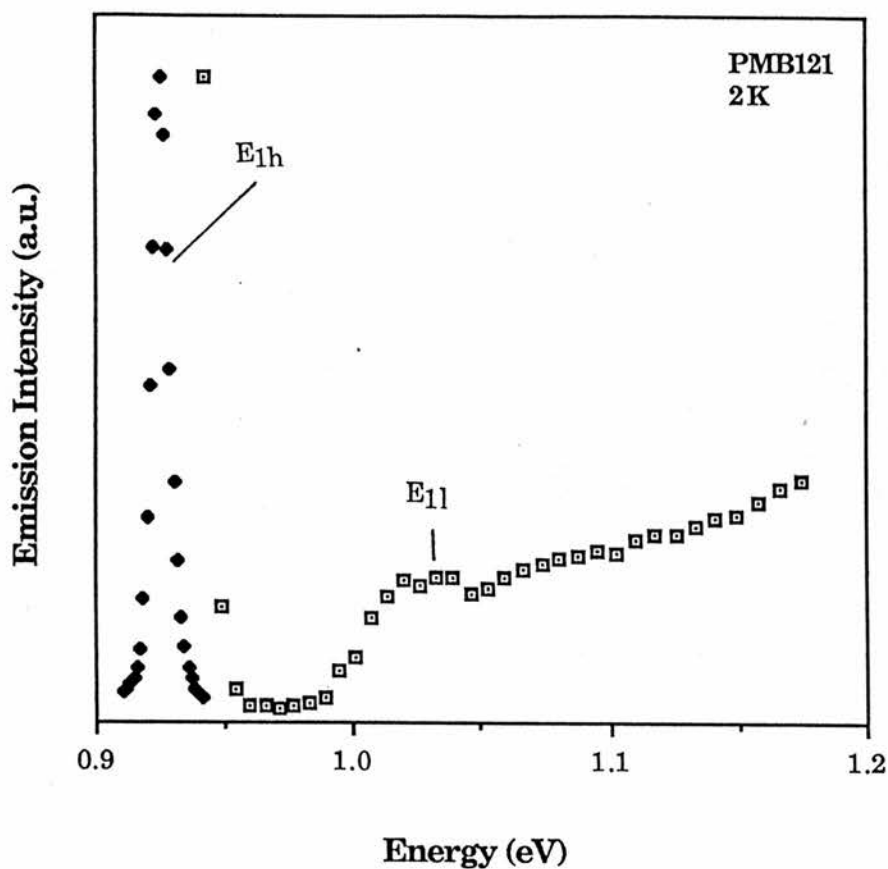


**Figure 5.39** PLE spectra of a MQW of 50x 25 Å Ga<sub>0.47</sub>In<sub>0.53</sub>As and 100 Å InP (PMB121). The E<sub>1h</sub> transition is not observed since its FWHM is similar to the detector bandwidth and coincides with the luminescence band. The E<sub>1l</sub> transition at ~82 meV above the E<sub>1h</sub> transition is seen.

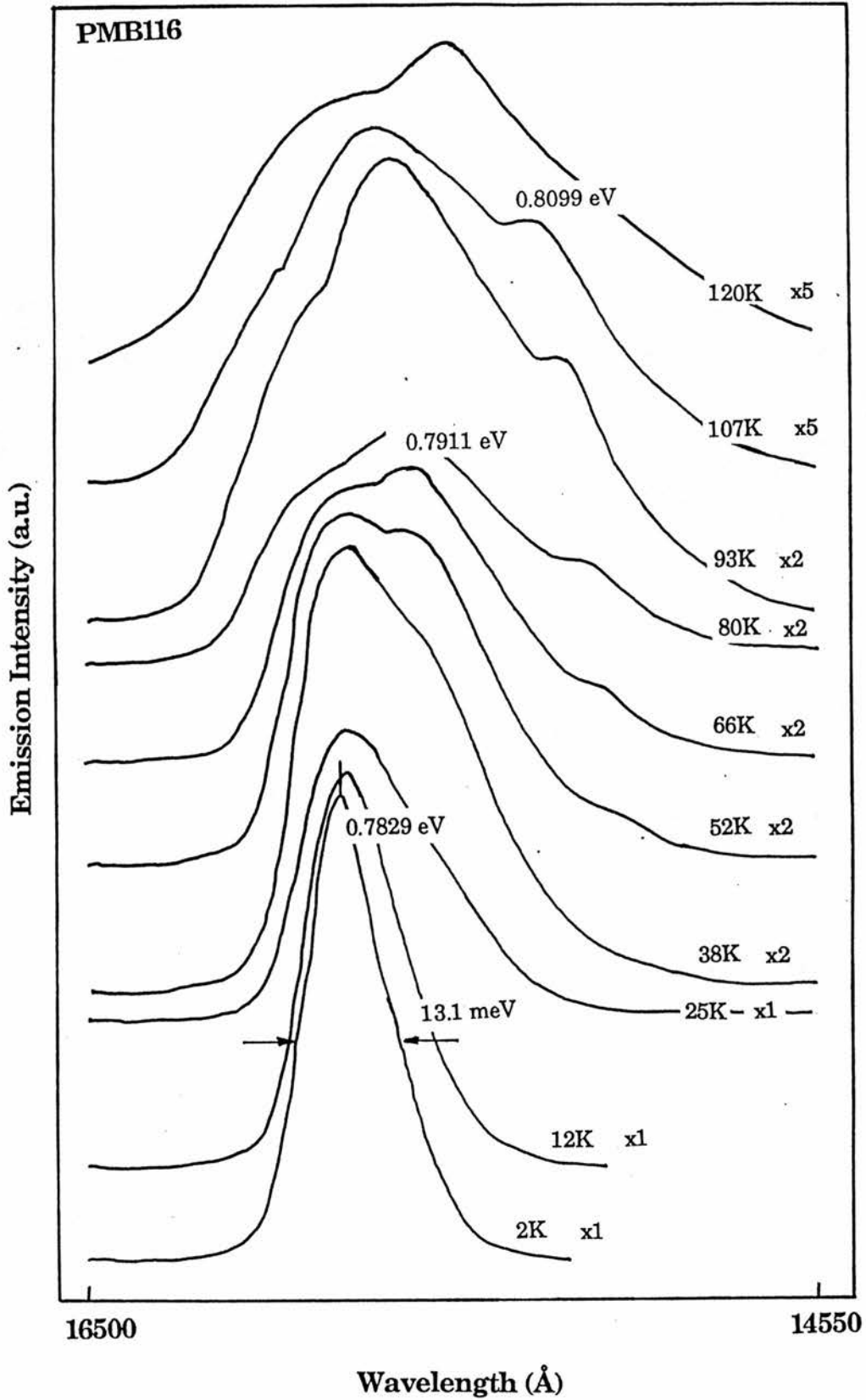


**Figure 5.40** 2 K luminescence spectra from a 230 Å Ga<sub>0.47</sub>In<sub>0.53</sub>As quantum well (PMB116), moving to lower energies due to band gap shrinkage. The new emission bands emerging at higher energies, 0.711 eV at 66 K and 0.8099 eV at 107 K, are due to Ga<sub>0.47</sub>In<sub>0.53</sub>As compositional variations rather than impurities.

variations, 2-3%, in the  $\text{Ga}_{0.47}\text{In}_{0.53}\text{As}$  layer. A 2% compositional mismatch was also reported in section 3.4 for the bulk  $\text{Ga}_{0.47}\text{In}_{0.53}\text{As}$ .

### 5.5.3 Some Comments

Comparing the emission spectra obtained from  $\text{Ga}_{0.47}\text{In}_{0.53}\text{As-InP}$  with  $\text{GaAs-Al}_x\text{Ga}_{1-x}\text{As}$  quantum wells, alloy scattering in  $\text{Ga}_{0.47}\text{In}_{0.53}\text{As}$  increases the luminescence linewidth, particularly in the wider wells. As well widths are reduced, interface roughness is dominant linewidth broadening mechanism in both systems. In  $\text{Ga}_{0.47}\text{In}_{0.53}\text{As-InP}$  wells emission arises from excitons bound to compositional alloy fluctuations probably as a result of hole localization due to the large  $\Delta E_v$  in this system compared to  $\text{GaAs-Al}_x\text{Ga}_{1-x}\text{As}$ . Screening effects are more pronounced in  $\text{Ga}_{0.47}\text{In}_{0.53}\text{As}$  because it has a higher density of states per unit area than  $\text{GaAs}$ , allowing the observation of many-body interactions observed by the RSRE group. Carrier screening not only affects the lineshape of the emission but also the electron-phonon interaction as was demonstrated by RSRE and our group (Watt et al 1987), namely reducing the strength of the  $\text{GaAs}$ -like phonon in the high carrier density (modulation doped or optically pumped) regime.

## 5.6 Pseudomorphic HEMTs

The high electron mobility transistor, HEMT, is formed using a heterojunction between two latticed materials, such as  $\text{Al}_x\text{Ga}_{1-x}\text{As}$  and  $\text{GaAs}$ . There exists a two dimensional electron gas (2-DEG) at the interface due the difference in band-gap energy and the electrostatic attraction of transferred carriers from the remotely doped barrier (Esaki 1970). Modulation doping has increased the low temperature mobility mostly due to a reduction in impurity scattering. Unfortunately, the high Al content,  $x=0.3$ , required to give the 2-DEG confinement results in the formation of traps. These are principally associated with DX centres in the  $\text{Al}_x\text{Ga}_{1-x}\text{As}$  leading to the collapse of the drain current-

voltage (I-V) characteristics in devices. The insertion of a  $\text{Ga}_{1-y}\text{In}_y\text{As}$  layer between that of the  $\text{Al}_x\text{Ga}_{1-x}\text{As}$  and GaAs can be used to maintain the band offset while reducing the Al content typically to  $x=0.15-0.22$  (figure 5.41). When a 15% In content is used, the  $\text{Ga}_{1-y}\text{In}_y\text{As}$  layer has a lattice mismatch of 1% and for a critical thickness  $< 200\text{\AA}$  no misfit dislocations are formed. The resulting strain is taken up completely by the  $\text{Ga}_{1-y}\text{In}_y\text{As}$  layer hence the term pseudomorphic. Not only does the pseudomorphic HEMT eliminate the effects of DX centres by reducing the Al concentration in the barrier but it also has larger sheet carrier density, higher mobility and saturation velocity than a normal HEMT (Swanson 1987). This enables it to operate at higher frequencies with improved gain and noise parameters (Liu et al 1987).

A pseudomorphic HEMT series was grown at GEC based on a  $400\text{\AA}$   $\text{Al}_x\text{Ga}_{1-x}\text{As}$  capping layer, Si doped to  $\sim 2 \times 10^{18}\text{ cm}^{-3}$ , and varying the parameters of well thickness ( $40-180\text{\AA}$ ), composition ( $x=0.18-0.22$ ,  $y=0.11-0.15$ ) and doping spacer layer ( $20-150\text{\AA}$ ). Preliminary results, for structures that are far from optimised, are encouraging with 4 K Hall mobilities higher than  $130,000\text{ cm}^2/\text{Vs}$  for a 2-DEG density of  $7 \times 10^{11}\text{ cm}^{-2}$  (DB633:  $150\text{\AA}$  well,  $x=0.22$ ,  $y=0.15$  and  $150\text{\AA}$  spacer layer). Photoluminescence is not generally used for characterizing standard HEMTs as there is no confinement of holes in the valence band for efficient recombination. However, we have found photoluminescence is a useful non-destructive technique for measuring 2-DEG sheet carrier density,  $n_s$  and sub-band occupancy in the asymmetric well formed at pseudomorphic HEMT interface as is shown below.

The 2 K, luminescence spectrum of a pseudomorphic HEMT is dominated by the electron to heavy-hole transition,  $E_{1h}$ . In figure 5.42 the  $E_{1h}$  transition for DB622 ( $150\text{\AA}$  well,  $x=0.22$ ,  $y=0.15$  and a  $40\text{\AA}$  spacer layer) is seen at  $1.4279\text{ eV}$  (figure 5.41) with emission to the Fermi edge at  $1.4673\text{ eV}$ . The luminescence lineshape is strongly effected by many body processes as in the case of

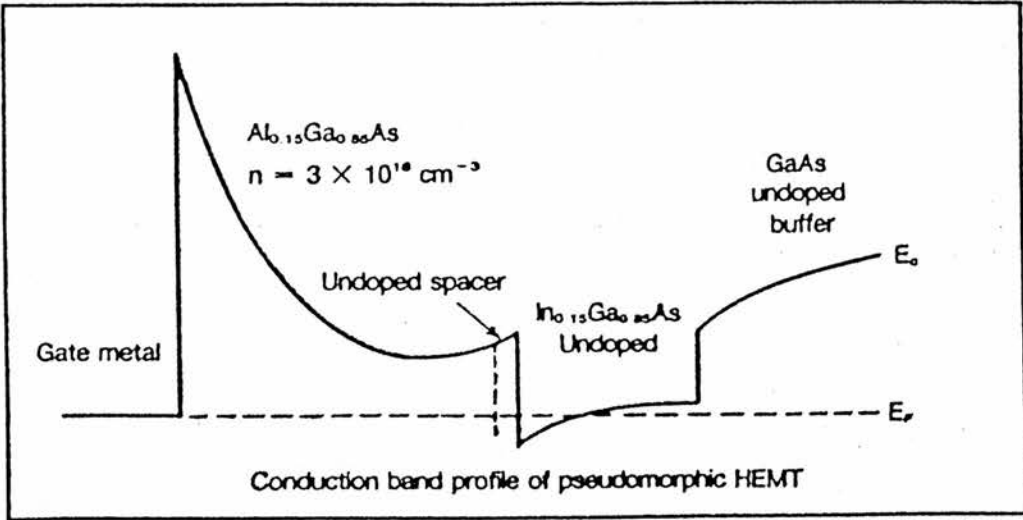


**Figure 5.41** The conduction band profile of the pseudomorphic HEMT clearly shows the quantum well at the  $\text{In}_y\text{Ga}_{1-y}\text{As}$  layer (Swanson 1987).

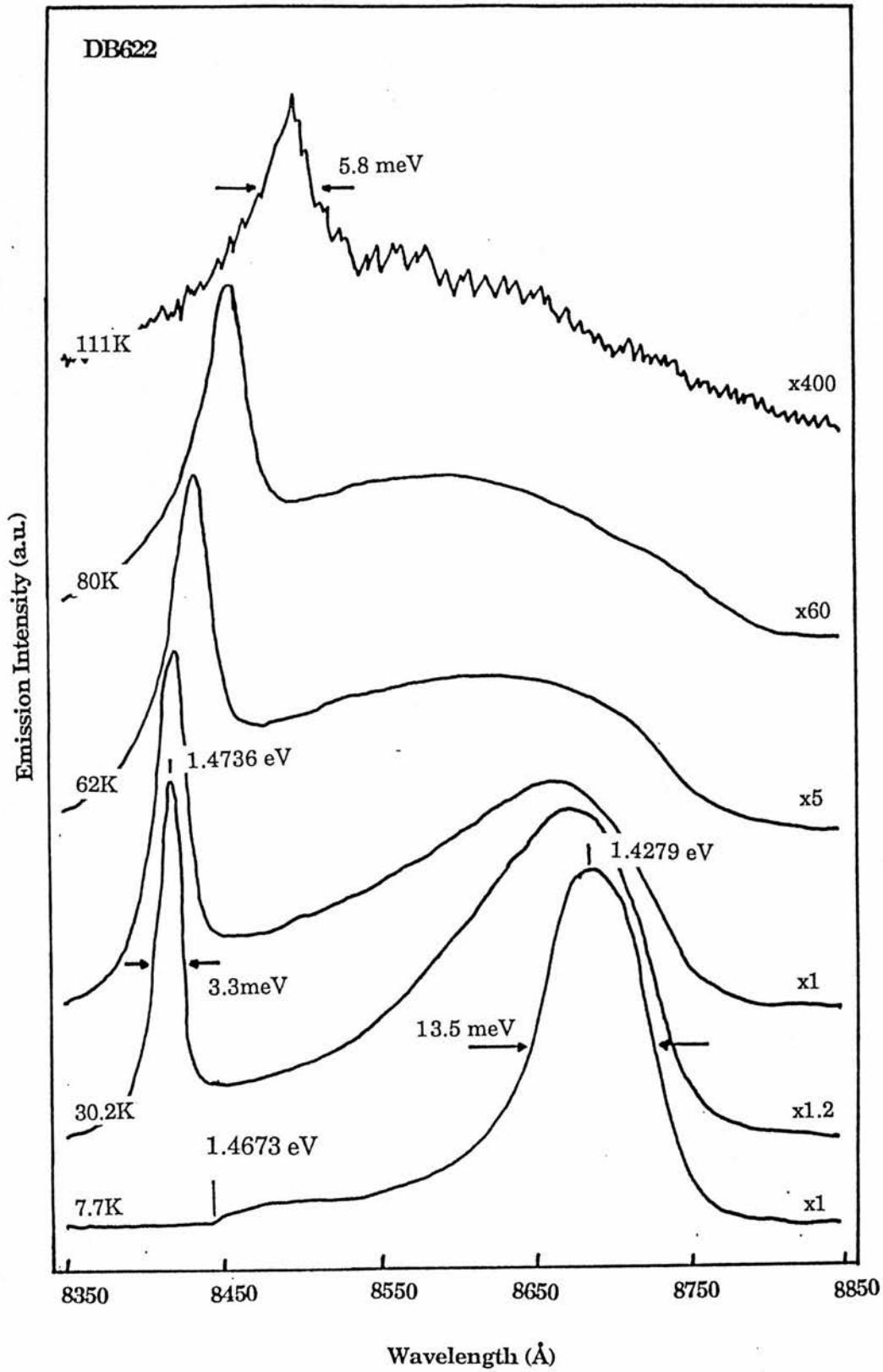


**Figure 5.42** The 8 K spectrum (DB622) from a pseudomorphic HEMT is dominated by a  $E_{1h}$  transition at 1.4279 eV and shows emission to the Fermi edge at 1.4673 eV. On raising the substrate temperature a higher sub-band,  $E_{2h}$ , at 1.4736 eV becomes occupied.

Ga<sub>0.47</sub>In<sub>0.53</sub>As-InP wells and reflects a simple thermal population of carriers (Sooryakumar et al 1987). As sample temperature is increased a higher energy sub-band, E<sub>2h</sub>, at 1.4736 eV appears to be thermally populated. But the rapid increase in intensity of this transition can only be explained if carriers are thermally excited into the well raising the Fermi edge above the n=2 sub-band. The linewidth of the E<sub>1h</sub> transition was found to increase with the 2-DEG density, with FWHM as narrow as 1.4 meV for undoped wells increasing to 13.5 meV for n<sub>s</sub>=1.08x10<sup>12</sup> cm<sup>-2</sup>. Colvard et al (1989) showed the energy difference the E<sub>1h</sub> transition and the Fermi edge gives a more reliable measure of the sheet carrier density.

The results given here are preliminary, growth conditions and samples structures were not yet optimised, but further work is in progress at GEC.

### 5.7 Summary

In this chapter the optical properties of type I, III-V semiconductor quantum well structures were considered. It was shown that the shallow impurity binding energy in a well, depends on its position in the well. Two peaks in the density of states were observed in the acceptor emission and were associated with the well centre and well edge. High quality, atomically flat, interfaces can be produced by growth interruption resulting in a reduction of luminescence linewidth and the observation of discrete structure in the emission due to island formation at the interface. Details of the major scattering mechanisms effecting linewidths were given and interface roughness was shown to have a dominant effect on the linewidth when interface island size was approximately that of the sensing exciton.

Our GaAs-Al<sub>x</sub>Ga<sub>1-x</sub>As samples exhibited very narrow linewidths with two or three peaks in the excitonic region of the emission. On the other hand, the energetic separation of these transitions was such that they could be related to

either impurities or to interface islands. A detailed study of the emission varying temperature, excitation power density and the doping level in the well showed the transitions could be assigned to, in decreasing energy,  $E_{1h}$ ,  $(D^*, X_{1h})$  and  $(A^*, X_{1h})$ . We found during a study of carrier capture by the well that direct excitation of the lower energy gap layer was required to observe true linewidth variation with temperature.

A substantial study of growing very thin GaAs wells structures on [100] GaAs substrates misorientated towards [110] by  $2^\circ$ ,  $4^\circ$  and  $6^\circ$  was completed. There was no evidence in this study that the vicinal planes were broken up into extended step widths or clustered step heights after over-growth. All well samples grown without growth interruption, regardless of Al content or substrate orientation, showed an equivalent 0.2 monolayer fluctuation in the luminescence linewidth (figure 5.43). This corresponded to the pseudo-rough inverted interface which was limited by the Al diffusion length of 40 Å and hence disordered on a fine scale. It is likely that an increase in the growth temperature would improve the interface quality, however other factors such as the group III desorption rate would then become important. When growth interruption was used linewidths were found to increase contrary to work previously reported. It was suggested that this was due to incomplete island formation at the inverted interface with island size now approximately the same as the excitonic diameter. No functional dependence of the linewidth was found for substrate orientation for either the uninterrupted or interrupted growth quantum well samples. Although it appears that in some instances using a  $4^\circ$  misorientated substrate can result in improved luminescence characteristics reflecting better growth conditions.

Emission from  $Ga_{0.47}In_{0.53}As$ -InP well structures is similar to that of  $GaAs-Al_xGa_{1-x}As$  in that the  $E_{1h}$  transition dominates, but at low temperatures,  $< 10$  K, the exciton is bound to potential fluctuation in the well probably due to

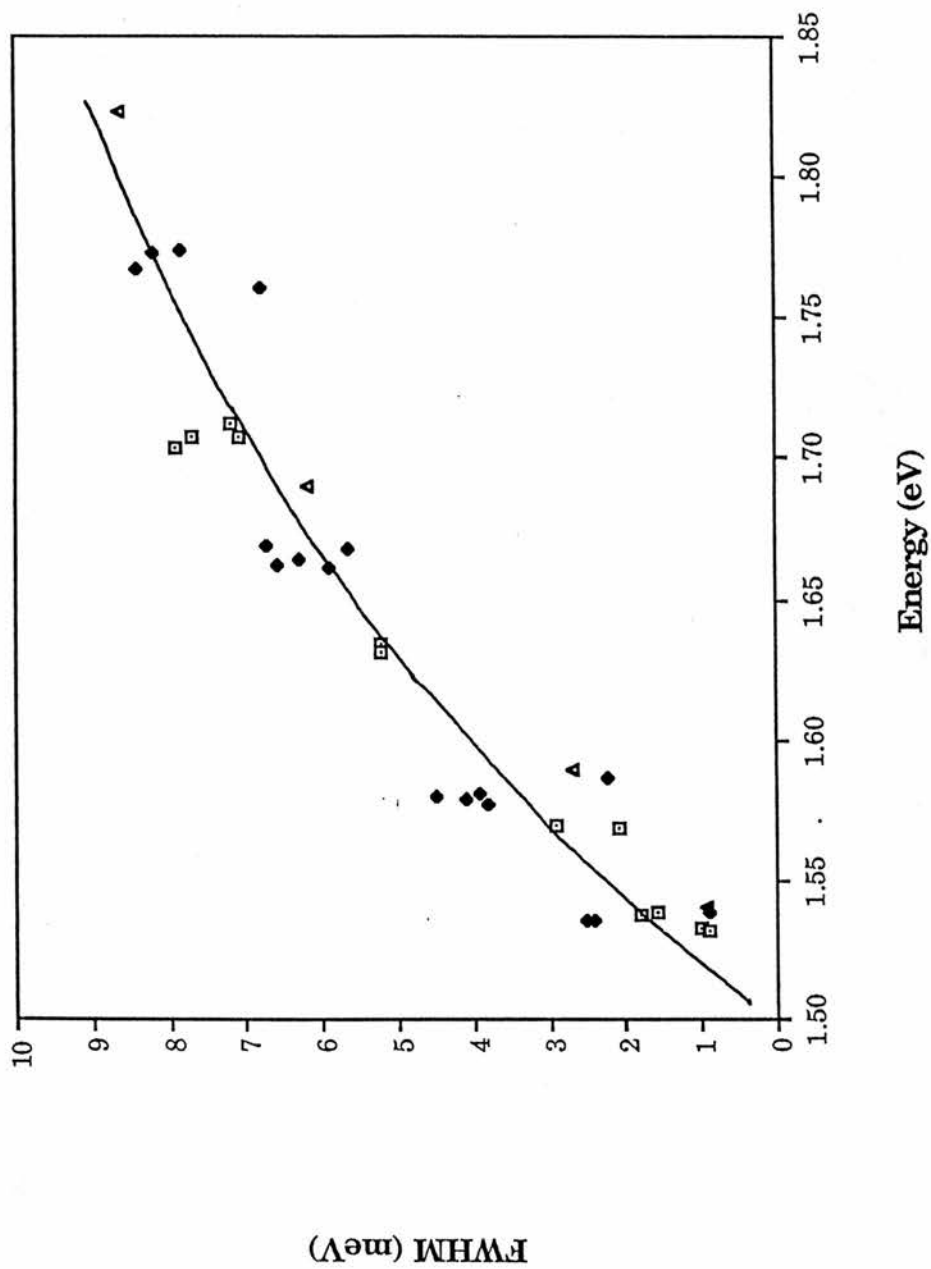


**Figure 5.43** The emission of all the wells grown in this work, without growth interruption, show a  $\sim 0.2$  ML fluctuation in linewidth regardless of well width, substrate orientation and Al content in the barrier.

## V Luminescence from Quantum Well Structures

compositional fluctuations in the  $\text{Ga}_{0.47}\text{In}_{0.53}\text{As}$ . It appears that compositional variations in either the  $\text{Ga}_{0.47}\text{In}_{0.53}\text{As}$ , or  $\text{Al}_x\text{Ga}_{1-x}\text{As}$  barrier in GaAs wells, suppress the observation of interface islands. The InP LO phonon was observed for the 10 Å well showing that there was strong coupling into the barrier.

## VI PL of $\text{Al}_{0.48}\text{In}_{0.52}\text{As}$ UNDER HYDROSTATIC PRESSURE

	<u>Page</u>
6.1 Introduction	141
6.2 Calculation of Deformation Potential	142
6.2.1 Review	144
6.3 $\text{Al}_{0.48}\text{In}_{0.52}\text{As}$ under Hydrostatic Pressure	148
6.3.1 Experimental Considerations	149
6.3.2 Luminescence $\text{Al}_{0.48}\text{In}_{0.52}\text{As}$ under Hydrostatic Pressure	150
6.3.3 Deformation Potential of $\text{Al}_{0.48}\text{In}_{0.52}\text{As}$	152
6.3.4 Effective Mass dependence on Pressure in $\text{Al}_{0.48}\text{In}_{0.52}\text{As}$	155
6.4 Summary	156

## 6.1 Introduction

The application of pressure and the use of diamond anvil cell (DAC) techniques has become popular in many different disciplines and across a broad range of the physical sciences (for reviews see Jayaraman 1983, 1984 and 1986). Here we are limited to the application of pressure to semiconductors and more specifically to the effect upon optical properties. In general, hydrostatic pressure applied to a semiconductor up to a level below a structural phase transition acts as a perturbation on the electronic properties of the crystal without destroying its symmetry. However, the fundamental parameter is not pressure but lattice dilation corresponding to a variation of lattice constant, for example, a  $\sim 3\%$  change with an applied pressure of  $\sim 50$  kbar.

W Paul and his co-workers at Harvard established from optical absorption measurements and electrical transport properties that the principal conduction band minima behave similarly in group IV and III-V semiconductors. In fact pressure measurements were instrumental in solving some of the early questions about the assignment of band structure minima (Paul 1961). Typically when a semiconductor is pressurised (figure 6.1) the  $\Gamma$ -level moves upward in energy relative to the valence band at  $\sim 10 \text{ meV kbar}^{-1}$ , the L-level moves upwards at  $\sim 4 \text{ meV kbar}^{-1}$  and the X-level downwards at  $\sim 1 \text{ meV kbar}^{-1}$ . The first measurements were taken at pressures limited by the available equipment to  $\sim 10$  kbar and as a consequence the observed pressure dependence of the band-edge appeared linear. It was not until the advent of the DAC, enabling higher pressures to be reached, and with more refined spectroscopic techniques becoming available that a sub-linear pressure dependence for the band edge was seen. From the near band-edge luminescence shift to higher energies as the pressure is increased an initial pressure coefficient for the band-gap can be derived. As the pressure is further increased the luminescence quenches

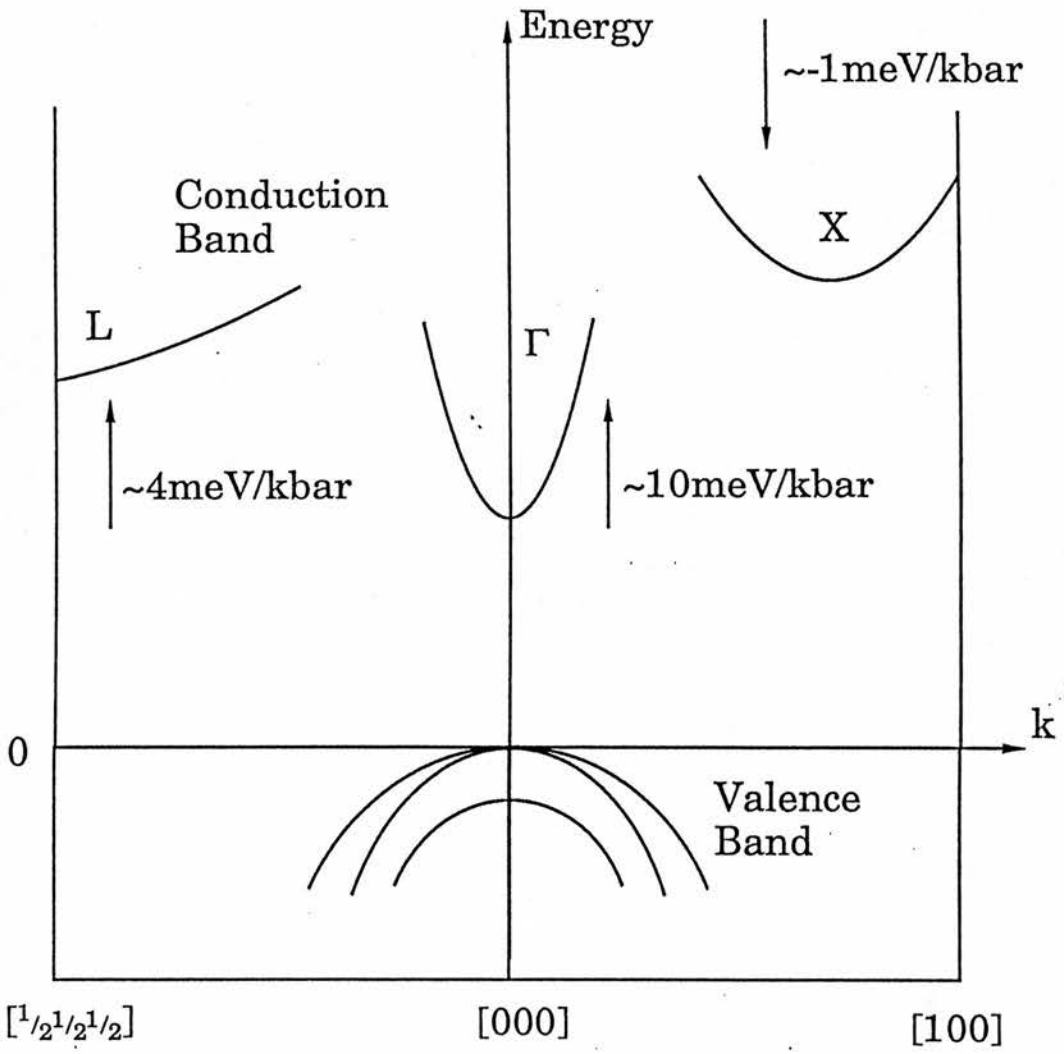


**Figure 6.1** Schematic diagram of the variation of electron energy with wavevector  $k$  for a typical group IV or III-V compound direct-gap semiconductor.

around the  $\Gamma$ -X cross-over as the material becomes dominated by an indirect level which can be tracked to lower energies in the case of the X-point (figure 6.1). This allows the characteristics of the X minima related levels, such as impurity binding energy, to be examined experimentally.

After a review of the most recent work in this area we will present the first high pressure optical data obtained for  $\text{Al}_{0.48}\text{In}_{0.52}\text{As}$ . From this data, an initial pressure coefficient for the  $\text{Al}_{0.48}\text{In}_{0.52}\text{As}$  is obtained, a deformation potential for the band-edge is calculated and the pressure dependence of the effective mass using k.p theory is derived.

## 6.2 Calculation of Deformation Potential

The variation of energy gap with hydrostatic pressure is described by the deformation potential defined as  $dE_g/d(\ln V) = -(c_{11} + 2c_{12})/3E_g/dP$  for zinc blende type crystals where  $c_{11}$  and  $c_{12}$  are elastic constants. The derivation of the deformation potential is important in electron-phonon calculations and for some theoretical estimates of the band-offset (see for example Cardona and Christensen 1987). A summary of some of the pressure dependent parameters for III-V binaries and related compounds relevant to this work is given in table 6.1. The most recent references are quoted and previous work is referenced within. Table 6.1 includes values for bulk modulus, both derived experimentally and calculated, required for the estimation of deformation potential. Details of the various parameters will be discussed as necessary throughout this chapter. In this section we will show how a deformation potential can be derived from high pressure optical data and review the relevant work related to this.

Normally the luminescence or absorption spectra provides a relative measure of the position of the band-gap,  $E_g$ . It is found, in most instances, as the pressure is increased the band-edge varies sub-linearly with pressure and can be fitted to a quadratic equation of the form

	$\alpha$ (meV/kbar <sup>-1</sup> )	$\beta$ (meV/kbar <sup>-2</sup> )	$\Xi_d$ (eV)	$B_0$ (kbar)	$B_0'$
InP <sup>a,b</sup>	8.4	-	-6.1	711	4.67
	7.5	10x10 <sup>-2</sup>	-	-	-
GaAs <sup>c</sup>	10.3	14x10 <sup>-3</sup>	-8.5	747	4.46
GaInAs <sup>d,e</sup>	12.44	66x10 <sup>-2</sup>	-7.79	650	4.67
	10.95	-	-7.9	650	4.00
AlInAs <sup>f</sup>	10.1	47x10 <sup>-3</sup>	-6.51	676	4.59

a) Muller et al (1980), b) Menoni et al (1986), c) Goni et al (1987), d) People et al (1988), e) Lambkin and Dunstan (1988) and f) this work.

**Table 6.1** Summary of pressure-dependent parameters for semiconductors of interest here:  $\alpha$  is the linear pressure coefficient,  $\beta$  is quadratic fit parameter,  $\Xi_d$  is the deformation potential,  $B_0$  the bulk modulus and  $B_0'$  is the derivative with respect to pressure.

$$E_g = E_g(0) + \alpha P + \beta P^2 \quad (6.1)$$

where  $\alpha$  is in  $\text{meV}\text{kbar}^{-1}$ , the initial pressure coefficient and  $\beta$  is in  $\text{meV}\text{kbar}^{-2}$ . The sublinear pressure dependence of  $E_g$  is accounted for by the non-linearity of the equation of state. Since, in the application of pressure, the fundamental parameter is the reduction in crystal volume, a transformation between the two variables is required. Murnaghan's empirical equation of state can be used (1944), given by:

$$-\left(\frac{\Delta a}{a_0}\right)_T = 1 - \left[ 1 + \left(\frac{B_0'}{B_0}\right)P \right]^{-1/(3B_0')} \quad (6.2)$$

where  $B_0$  is the isothermal bulk modulus and  $B_0'$  is the derivative with respect to pressure. The main source of error within equation 6.2 is hidden in the values of  $B_0$  and  $B_0'$ . These have been found experimentally for some binaries but are normally interpolated from the binary endpoints when required for an alloy. A plot of  $E_g$  against pressure, assuming that a linear relationship exists with the lattice constant, gives a gradient corresponding to the deformation potential:

$$E_g = E_g(0) + 3\Xi_d\left(\frac{\Delta a}{a_0}\right) \quad (6.3)$$

where  $\Xi_d$  is the deformation potential. However, this analysis only applies for bulk samples grown as single crystals. A thin, lattice matched, epitaxial layer such as  $\text{Al}_{0.48}\text{In}_{0.52}\text{As}$  grown onto a substrate of different bulk modulus produces further complications considered below.

It was only recently that the problem of studying thin epitaxial layers under hydrostatic pressure was first considered (People et al 1988). Here we will consider the particular problem of  $\text{Al}_{0.48}\text{In}_{0.52}\text{As}$  grown lattice matched onto a InP substrate. Since the elastic constant of the epitaxial layer and the substrate are different, under hydrostatic pressure the  $\text{Al}_{0.48}\text{In}_{0.52}\text{As}$  will not remain cubic but will undergo a tetragonal distortion, similar to that due to lattice

mismatch during growth. It is assumed that since the InP substrate is thicker than the epitaxial layer,  $40\mu\text{m}$  compared to  $\sim 2\mu\text{m}$ , it will retain its cubic symmetry under pressure and will determine the inplane parameter of the epitaxial layer,  $e_{xx}(\text{AlInAs})=e_{yy}(\text{AlInAs})=e_{xx}(\text{InP})$ , therefore:

$$\left(\frac{\Delta V}{V_0}\right)^{\text{AlInAs}} = e_{xx}(\text{InP})+e_{yy}(\text{InP})+e_{zz}(\text{InP}) + [e_{zz}(\text{AlInAs})-e_{zz}(\text{InP})] \quad (6.4)$$

$$\left(\frac{\Delta V}{V_0}\right)^{\text{AlInAs}} = \left(\frac{\Delta V}{V_0}\right)^{\text{InP}} + e_t^{\text{AlInAs}} \quad (6.5)$$

where the tetragonal distortion  $e_t^{\text{AlInAs}}=[e_{zz}(\text{AlInAs})-e_{xx}(\text{AlInAs})]$ . Assuming no mismatch at room temperature and atmospheric pressure then  $e_t(0)=0$ . For cubic InP,  $\frac{\Delta V}{V_0} = 3\left(\frac{\Delta a}{a_0}\right)$  and the term  $\left(\frac{\Delta V}{V_0}\right)^{\text{InP}}$  has already been obtained elsewhere (see for example Muller et al 1980). The tetragonal distortion can be related to the in-plane strain  $e$  by  $e_t=[(1-\nu)/(1+\nu)]e$  where  $\nu=0.3$  is the Poisson ratio. Essentially the in-plane strain is the fractional change in lattice parameter under pressure compared to what it would have been if it remained constant under pressure,

$$e(\text{AlInAs}) = \left[ \left(\frac{\Delta a}{a_0}\right)^{\text{InP}} - \left(\frac{\Delta a}{a_0}\right)^{\text{AlInAs}} \right] \quad (6.6)$$

where  $\left(\frac{\Delta a}{a_0}\right)$  is obtained using equation 6.2 using the material dependent  $B_0$  and  $B_0'$ . People et al (1988) estimated the non-hydrostatic stress component using  $P_u^{\text{Alloy}}=(c_{11}-c_{12})e_t^{\text{Alloy}}$  to gave a non uniaxial stress at  $P=35$  kbar of  $-1.35$  kbar in GaInAs corresponding to maximum splitting of the valence band of  $4.16$  meV. They concluded it is justifiable to use the measured change in band-gap energy for calculating deformation potentials as long as the actual change in epitaxial layer volume is used.

### 6.2.1 Review

High pressure measurements taken by various groups on GaAs (see, for example, Olego et al 1980, Wolford et al 1985) showed that the pressure dependence of the band-edge was linear at low temperatures and sub-linear at

room temperature. Recent work by Goini et al (1987) showed that room temperature absorption data up to 170 kbar could be fitted to the quadratic equation 6.1 with  $\alpha=10.3 \text{ meV/kbar}^{-1}$  and  $\beta=-14 \times 10^{-3} \text{ meV/kbar}^2$ . Since the bowing was slight, the band-gap dependence appears linear upto the  $\Gamma$ -X cross-over at  $42 \pm 2$  kbar. They found on transforming their data to pressure dependence of lattice constant with  $B_0=747$  kbar and  $B_0'=4.46$  that the deformation potential for GaAs was  $\Xi_d=-8.5$  eV. Using PL and PLE other groups have considered the spectroscopic details of the near band-edge transitions as pressure was increased particularly at the onset of the  $\Gamma$ -X cross-over. Wolford et al (1985) found all bound states remained shallow and followed the band-edge with pressure. The  $(e,A^*)$  transition due to Si which occurred at  $\sim 29$  meV below the excitonic emission at 1 bar, appeared  $\sim 31$ - $32$  meV below the excitonic emission at 40 kbar. This was explained by slight change of the acceptor binding energy within the effective mass approximation due to changes in the effective mass of the acceptor and dielectric constant. The excitonic binding energy did not change with pressure until above 40 kbar, above this it increased as a consequence of mixing with the X-level. Other groups, using highly doped GaAs samples, have found evidence for donor deepening with increasing pressure (Kobayashi et al 1983) and unintentional N-doping of Si-doped, MBE grown, GaAs (Leroux et al 1986).

Correlating absorption and PL data, Muller et al (1980) found that for InP the initial pressure coefficient of the band-edge  $\alpha$  was  $8.4 \pm 0.2 \text{ meV/kbar}^{-1}$  at 300 K. The linear variation of the band-gap with lattice constant gave a deformation potential of  $-(6.1 \pm 0.2)$  eV. This value compared well with their pseudopotential calculation that showed  $\Xi_d=-6.0$  eV. They noted, by comparing the values of  $\Xi_d$  previously obtained for GaAs ( $-9.77$  eV) and Ge ( $-12.6$  eV) with that for InP that  $\Xi_d$  decreases rapidly with increasing ionicity. They also questioned whether the linearity of the equation of state was settled because of the crude assumptions made for the value of  $B_0'$ . This is discussed in section 6.3.1. More detailed

spectroscopy of InP under pressure was completed by Woford et al (1984); they showed similar results to those reported in GaAs. Low temperature, 20 K, PL measurements taken by Menoni et al (1986) found the initial pressure coefficient to be  $7.5 \text{ meV/kbar}^{-1}$ . The  $\Gamma$ -X cross-over was observed as a quenching of the luminescence but a large run to run variation in luminescence intensity was found and no X-level was observed. Recent results point to InP under going a structural phase transition at 106.5 kbar before the  $\Gamma$ -X cross-over was reached at an estimated 120-130 kbar (Tozer et al 1988).

With the advent of improved material quality the optical properties of alloys under pressure are being studied again. Lifshitz et al (1979) studied the band-edge dependence of  $\text{Al}_x\text{Ga}_{1-x}\text{As}$ , at different compositions, for pressures up to 10 kbar using absorption measurements at 300 K. The pressure coefficient  $\alpha$  increased linearly with pressure from 11.4 to  $12.2 \text{ meV/kbar}^{-1}$  with  $x=0.0$  to 0.25; above this composition  $\alpha$  dropped to  $10.2 \text{ meV/kbar}^{-1}$  at  $x=0.35$  and remained essentially constant thereafter. This change in  $\alpha$  occurred well away from the compositional  $\Gamma$ -X cross-over at  $x \sim 0.45$ . They noted the sharp change in  $\alpha$  happened around the percolation concentration of Al. Since ionicity changed with Al concentration and Al does not have d-core electrons it could effect  $\alpha$ . Chandrasekar et al (1986) showed the band structure changes with pressure in  $\text{Al}_x\text{Ga}_{1-x}\text{As}$  were similar to those to associated with compositional variations, with the  $\Gamma$ -X cross-over occurring at approximately the same energy. They observed deep L-X like levels which, when compared to the compositional dependence shown by Dingle et al (1979), agreed within  $\pm 5 \text{ meV}$ . This work was extended by Roach et al (1988) who found that shallow levels followed the conduction band but deep levels were highly sub-linear; increasing slightly with energy above 9 kbar, flattening and then decreasing in energy above 40 kbar. For a composition of  $x=0.3$  the initial pressure coefficient was  $\alpha=9.9 \pm 0.1 \text{ meV/kbar}^{-1}$  and the  $\Gamma$ -X cross-over occurred after 14 kbar. Using the temperature evolution to

## VI PL of $\text{Al}_{0.48}\text{In}_{0.52}\text{As}$ under hydrostatic pressure

estimate an activation energy  $E_a$  and excitation power density measurements they showed the deep levels could be associated with those observed compositionally by Henning et al (1984) and others.

Lately the tendency in high pressure spectroscopy has been to use epitaxial layers grown lattice matched to a substrate of a different material, particularly in superlattice structures. Using a sample of  $\text{Ga}_{0.49}\text{In}_{0.51}\text{P}$ , grown lattice matched to GaAs, Patel et al (1988) found that the room temperature  $\alpha=9.6$  meV/kbar<sup>-1</sup>. But this contradicts the low temperature, 6 K, work completed by Tozer et al (1988) who found for  $\text{Ga}_x\text{In}_{1-x}\text{P}$  ( $x=0.15, 0.25, 0.52$ ) the dominant linear term  $\alpha$  was 7 meV/kbar<sup>-1</sup> in each case. Results have been obtained for  $\text{Ga}_{0.47}\text{In}_{0.53}\text{As}$ , grown lattice matched to InP, independently by two groups, using slightly different methods, People et al (1988) and Lambkin and Dunstan (1988). People et al used the stimulated emission of  $\text{Ga}_{0.47}\text{In}_{0.53}\text{As}$  to observe band-to-band transitions within an electron hole plasma at room temperature. A narrow emission of FWHM  $\sim 7$  meV was taken as an estimate of the band-gap with a possible error  $\sim 8$  meV due to band-gap renormalisation. Spectra were obtained for pressures up to 36 kbar with the band-edge showing the expected non-linearity. Fitting to equation 6.1 gave  $\alpha=12.44$  meV/kbar<sup>-1</sup> and  $\beta=-68 \times 10^{-2}$  meV/kbar<sup>-2</sup>. They calculated the deformation potential using the fractional change in volume for the  $\text{Ga}_{0.47}\text{In}_{0.53}\text{As}$  epilayer compared to the InP substrate (see above) to find  $\Xi_d=-7.79 \pm 0.4$  eV. They found a value for  $B_0$  for  $\text{Ga}_{0.47}\text{In}_{0.53}\text{As}$  by extrapolation from its binaries and assumed that  $B_0'$  to be 4.67, the same as that for InP. Lambkin and Dunstan used PL to study the band-gap dependence of  $\text{Ga}_{0.47}\text{In}_{0.53}\text{As}$  under pressure at room temperature and 80 K. Within experimental error the initial pressure coefficient for the emission at both temperatures was the same,  $\alpha=-10.95 \pm 0.1$  meV/kbar<sup>-1</sup>. Since the  $\text{Ga}_{0.47}\text{In}_{0.53}\text{As}$  epitaxial layer was constrained by the InP in two-dimensions and free in the

## VI PL of $\text{Al}_{0.48}\text{In}_{0.52}\text{As}$ under hydrostatic pressure

third, neglecting biaxial strain, they calculated an average value for the bulk modulus:

$$B_{\text{epi}} = \frac{2}{3} B_{\text{InP}} + \frac{1}{3} B_{\text{GaInAs}} \quad (6.7)$$

with the value for  $B_0$  again extrapolated from the binaries. They also suggested that preliminary results showed that the epitaxial layer may take the same value for  $B_0$  as that for the substrate. So using the bulk modulus for InP and the extrapolated value for  $\text{Ga}_{0.47}\text{In}_{0.53}\text{As}$  they found  $\Xi_d$  to be  $-8.25 \pm 0.1$  eV and  $7.9 \pm 0.1$  eV, respectively. These values for  $\Xi_d$  compared well to the theoretical estimates, obtained by linear extrapolation, in models by Cardona and Christensen (1987) and Camphausen et al (1979) of -6.9 eV and -7.6 eV, respectively.

The use of DACs within semiconductor physics has not only been limited to that of optical measurements. Most noticeable is the study of structural phase transition using X-rays when the normal zinc-blende lattice changes under pressure, in most III-V compounds, to a rocksalt structure (Froyen and Cohen 1983). For this work it is important to estimate the bulk modulus  $B_0$  and its derivative with respect to pressure  $B_0'$  required for the calculation of an optical deformation potential. Menoni and Spain (1987) completed measurements on InP up to 190 kbar finding  $B_0 = 760 \pm 40$  kbar,  $B_0' = 40$  kbar and showing a phase transition to occur at 108 kbar, the values obtained for  $B_0$  and  $B_0'$  will be discussed in section 6.3.1.

### 6.3 $\text{Al}_{0.48}\text{In}_{0.62}\text{As}$ under Hydrostatic pressure

The main motivation of this work was to further the assessment of  $\text{Al}_{0.48}\text{In}_{0.52}\text{As}$  started in Chapter 4 and to provide information about some pressure related parameters including the deformation potential (Ferguson et al 1989). A general description of the principle and application of DACs to

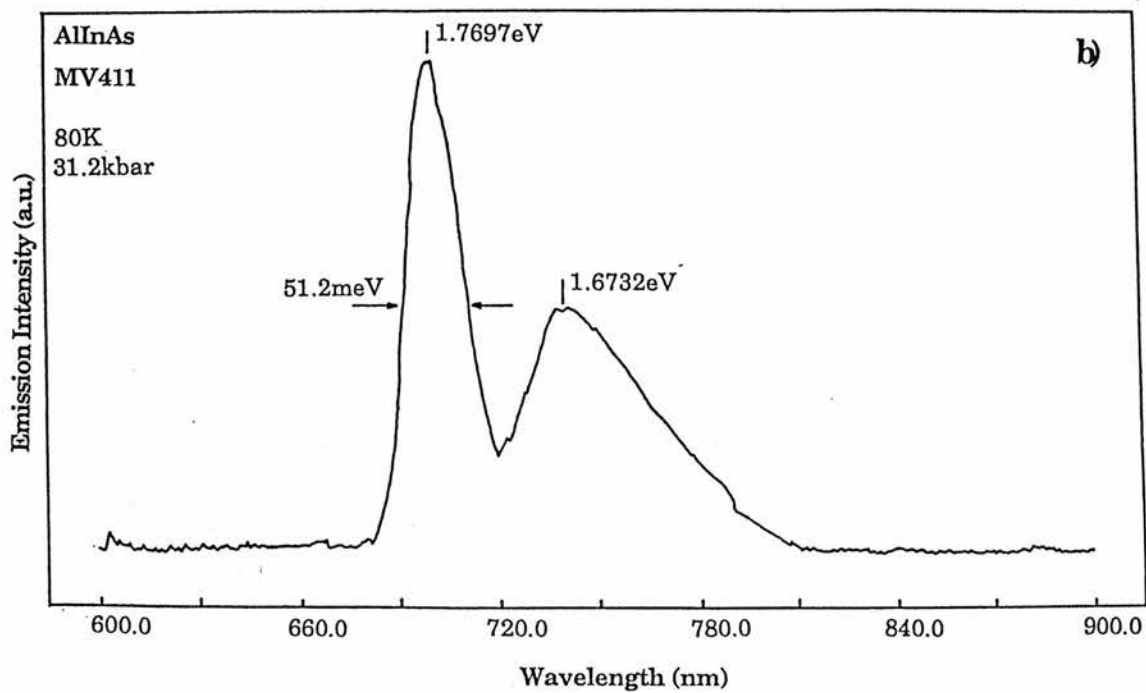
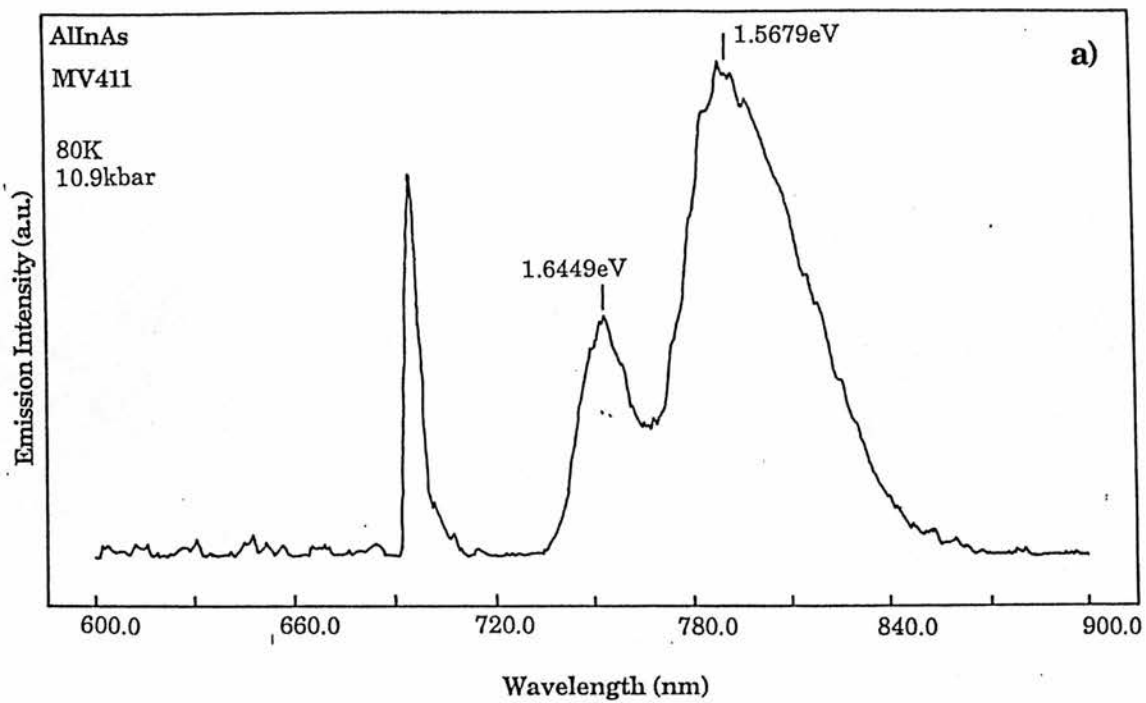
semiconductors can be found in section 2.3 and a detailed description of the apparatus can be found in Beales (1989). A review of the luminescence from  $\text{AlInAs}$  and the atmospheric pressure experimental data obtained for the samples used in this work is given in chapter 4. There it was concluded that the 2 K emission is due to ( $D^{\circ}, A^{\circ}$ ) transitions becoming dominated by ( $e, A^{\circ}$ ) at higher temperatures  $>80$  K (figure 4.9). Since no structure was observed in the luminescence the main criteria for this work was to obtain a deformation potential for the band-edge, so, consequently the spectra were taken at  $\sim 80$  K. It was also hoped to observe the  $\Gamma$ -X cross-over at  $\sim 60$  kbar ( $\Gamma$ -X  $\sim 0.6$  eV) and to compare this to the compositional value found by Onton and Lorenz (1970).

### 6.3.1 Experimental Considerations

Sample preparation was crucial in this work. The best method of thinning the sample, to the required thickness of  $\sim 40$   $\mu\text{m}$ , was found to be mechanically polishing by hand (see Appendix B). Another method of chemically thinning, used for semiconductor laser mounting, worked too closely to the machine's limit and produced samples that were bevelled from 30-60  $\mu\text{m}$ , so it was discarded. Once the sample was thinned, it was cleaved, by hand under 60x magnification, into a piece  $\sim 100 \times 100$   $\mu\text{m}^2$ . In many instances, the process of cleaving appeared to result in the loss of the epitaxial layer. This happened occasionally for sample MV411 and always for sample MV409, so the results reported here are for sample MV411. It had been suggested by Iain Spain (private comm) to use vacuum grease to attach the sample and ruby chip to one of the diamonds. This was not done as it was thought it may result in non-hydrostatic stresses within the DAC. The DAC was always pressurized at room temperature before cooling and warmed back to room temperature before the pressure was changed. The cryostat was operated at liquid nitrogen temperatures with a base temperature of 85-90 K, monitored by a copper-constantan thermocouple.

### 6.3.2 Luminescence of $\text{Al}_{0.48}\text{In}_{0.52}\text{As}$ under Pressure

The high pressure spectra in figure 6.2 a,b,c are typical of those obtained for AlInAs and since the spectra show emission similar to the zero pressure spectrum (figure 4.3), the high energy emission at 1.6449, 1.7697 and 1.9745 eV is assigned to the  $\text{Al}_{0.48}\text{In}_{0.52}\text{As}$ . The lower energy, broad band, emission is due to the substrate. Since the spectra were taken at  $\sim 80$  K the AlInAs emission is due to a  $(e, A^*)$  transition, section 4.7. To check this assignment the excitation power density was varied when the sample was pressurized at 23 kbar (figure 6.3), an exponent of  $s \sim 1.8$  from equation 4.15 was found. This corresponds well with the value obtained for the sample at zero pressure for this temperature confirming the  $(e, A^*)$  transition assignment (see figure 4.15). A strong emission intensity was observed for AlInAs even though previously lower radiative efficiencies were evident at this temperature. This was a consequence of the reduced laser spot size,  $\sim 10$   $\mu\text{m}$  diameter, which resulted in an increased power density of  $\sim 1000$  compared to that used previously. No change in the luminescence integrated intensity or radiative efficiency occurs when a sample is under pressure, and the transition is well away from any resonant levels (Muller et al 1980). The slight broadening in the AlInAs linewidth is a consequence of free carrier generation and does not effect the observed energy position of the emission. Since the emission at  $\sim 80$  K is not due to band-to-band transitions but to a  $(e, A^*)$  transition the change in the acceptor effective mass with pressure must be considered. Wolford and Bradley (1985) found the ionization energy of a silicon acceptor in GaAs to change by only  $\sim 2\text{-}3$  meV at 40 kbar, and Nilsson and Samuelson (1988) showed the energetic position of a carbon acceptor in GaAs did not vary relative to the valence band under pressure. We can thus conclude that the  $(e, A^*)$  transition at 80 K can be taken as direct measure of the band-gap for the calculation of the deformation potential.



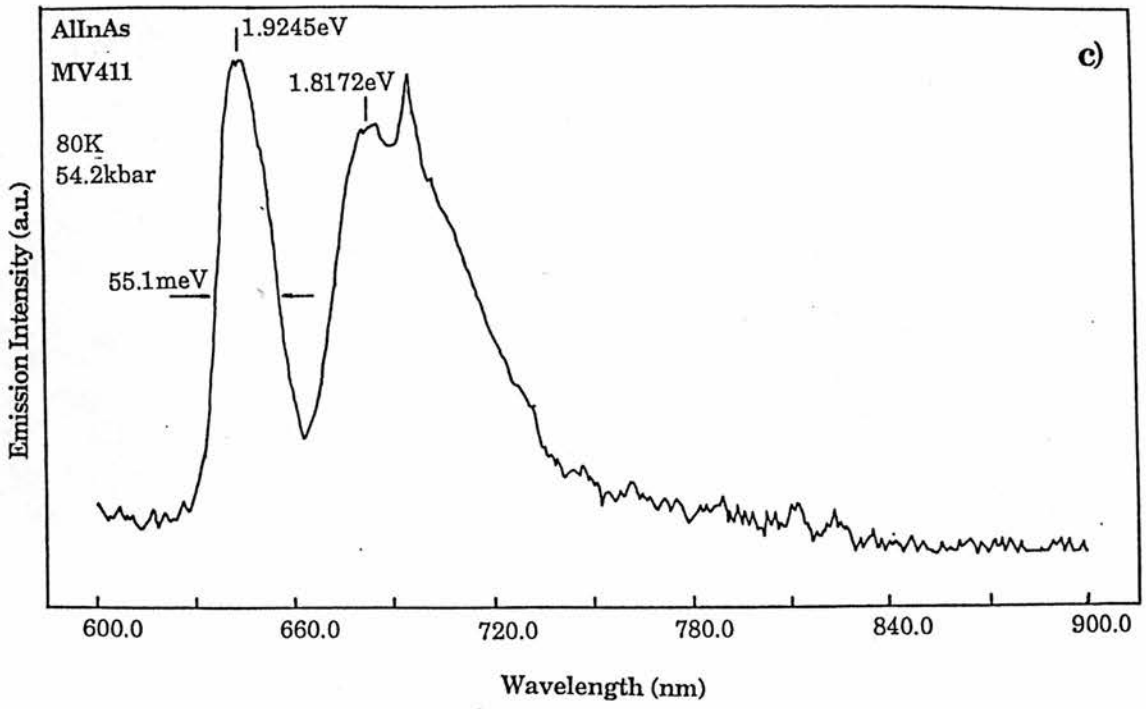


**Figure 6.2** Typical spectra of  $\text{Al}_{0.48}\text{In}_{0.25}\text{As}$  epitaxial layer and S-doped InP substrate at 80K and various pressures a) 10.9, b) 31.2 and c) 54.2 kbar

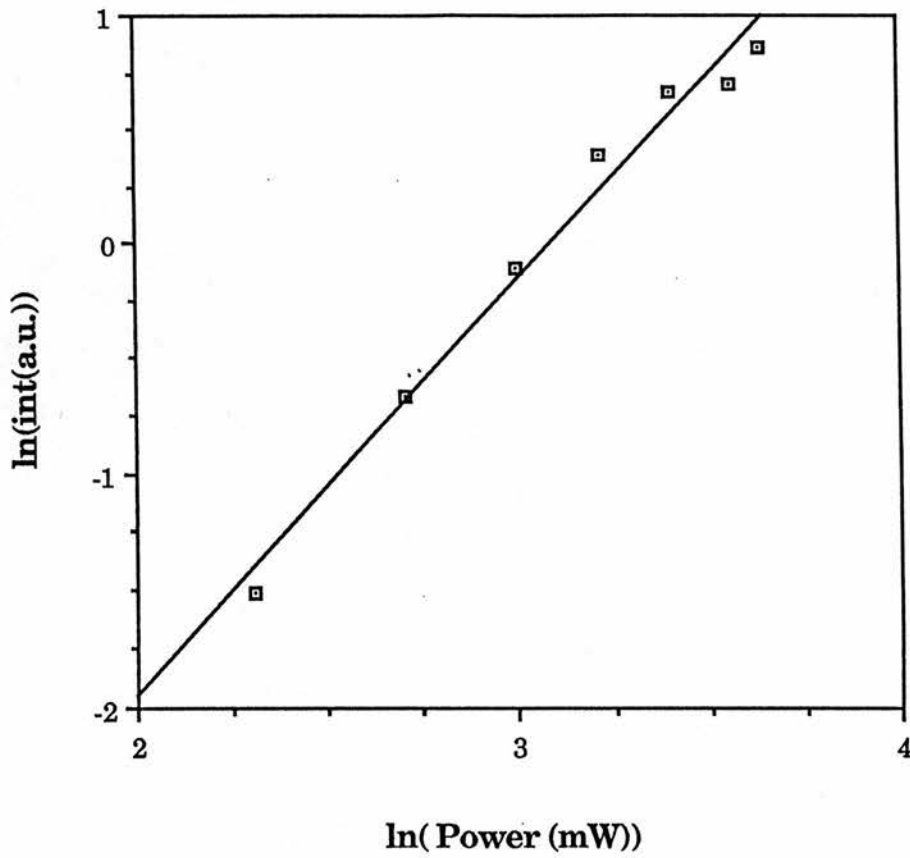


**Figure 6.3** The integrated luminescence intensity dependence upon excitation power density of the AlInAs emission at 23 kbar. The exponent of  $s \sim 1.8$  indicates we are still observing a  $(e,A')$  transition under pressure.

## VI PL of $\text{Al}_{0.48}\text{In}_{0.52}\text{As}$ under hydrostatic pressure

Recently the hydrostaticity of the alcohol mix at low temperatures has been questioned (Lambkin and Dunstan 1988). They found that the band-edge in  $\text{Ga}_{0.47}\text{In}_{0.53}\text{As}$  at 80 K showed a systematic reduction with pressure of around 10% when an alcohol mix was used compared to argon as the pressure transmitting medium. At no time was any non-hydrostatic stress observed in our ruby fluorescence and no shift occurred between the  $R_1$  and  $R_2$  lines. As a further check to test that no non-hydrostatic stresses were generated within our DAC, Beales (1989) completed some work on InP and observed that the linewidth of the InP due to band-to-band transitions,  $12 \pm 2$  meV, did not vary with pressure and corresponded to that expected for this emission at this temperature,  $\sim 14$  meV ( $\sim 1.8$  kT) (figure 6.4). A pressure coefficient of  $\alpha = 7.2 \pm 0.2$  meV/kbar $^{-1}$  (figure 6.5) compares well with that obtained by Menoni et al (1988) at 20 K of 7.5 meV/kbar $^{-1}$  and by Tozer et al (1988) at 5 K of 7 meV/kbar $^{-1}$ . Thus it must be concluded that our DAC measurements are free from non-hydrostatic components. Jayaraman (1986, private comm) pointed out the importance of pressurization at room temperature with a fresh methanol-ethanol mixture of the correct proportions (4:1) otherwise non-hydrostatic pressures, similar to that observed by Lambkin and Dunstan, could be generated. Subsequent cooling of the DAC after pressurization should preserve hydrostaticity although no phase diagram for the alcohol mix exists. It was found experimentally that when the methanol-ethanol mixture was frozen at 80K a waxy media was obtained. Subsequently, if any water vapour was present, or included in the mix, the frozen alcohol became slightly milky and appeared to acquire a crystalline structure. This suggests that the inclusion of water vapour may be the culprit for generating non-hydrostatic stresses. It is difficult to see otherwise how Lambkin and Dunstan could have generated such large uniaxial components,  $\sim 3$ -4 kbar, in their DAC since no bonding exists between the methanol and ethanol, and the atomic weight is similar to that of argon.

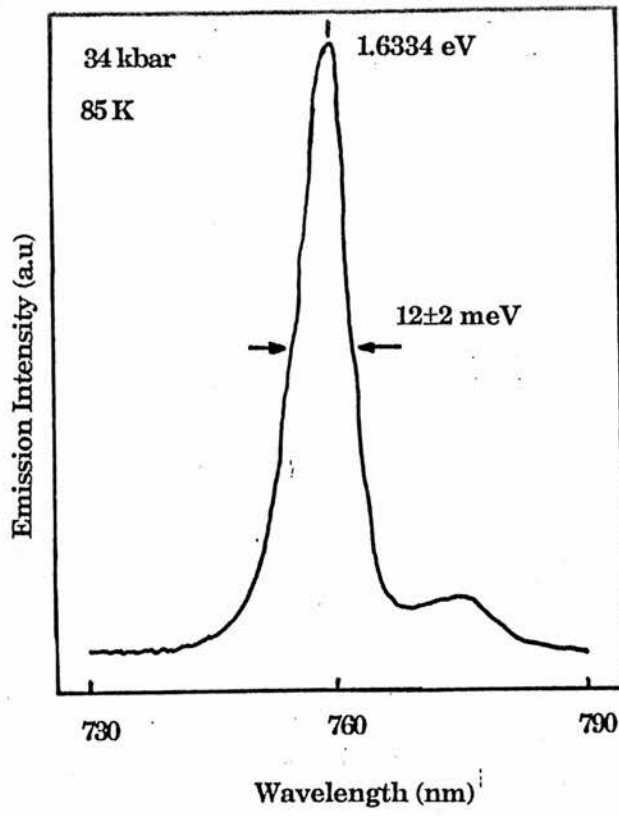


Figure 6.4 A typical undoped InP emission with the linewidth showing no evidence of non-hydrostatic stresses using Ethanol:Methanol mixture (Beales 1989).

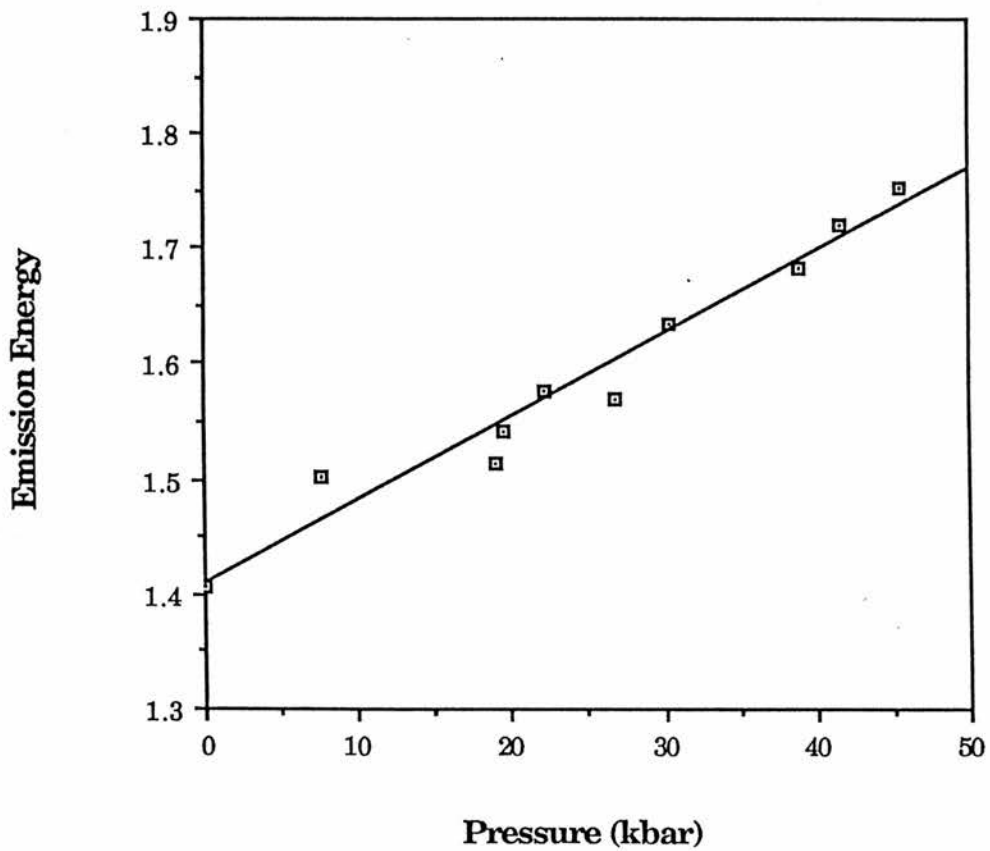
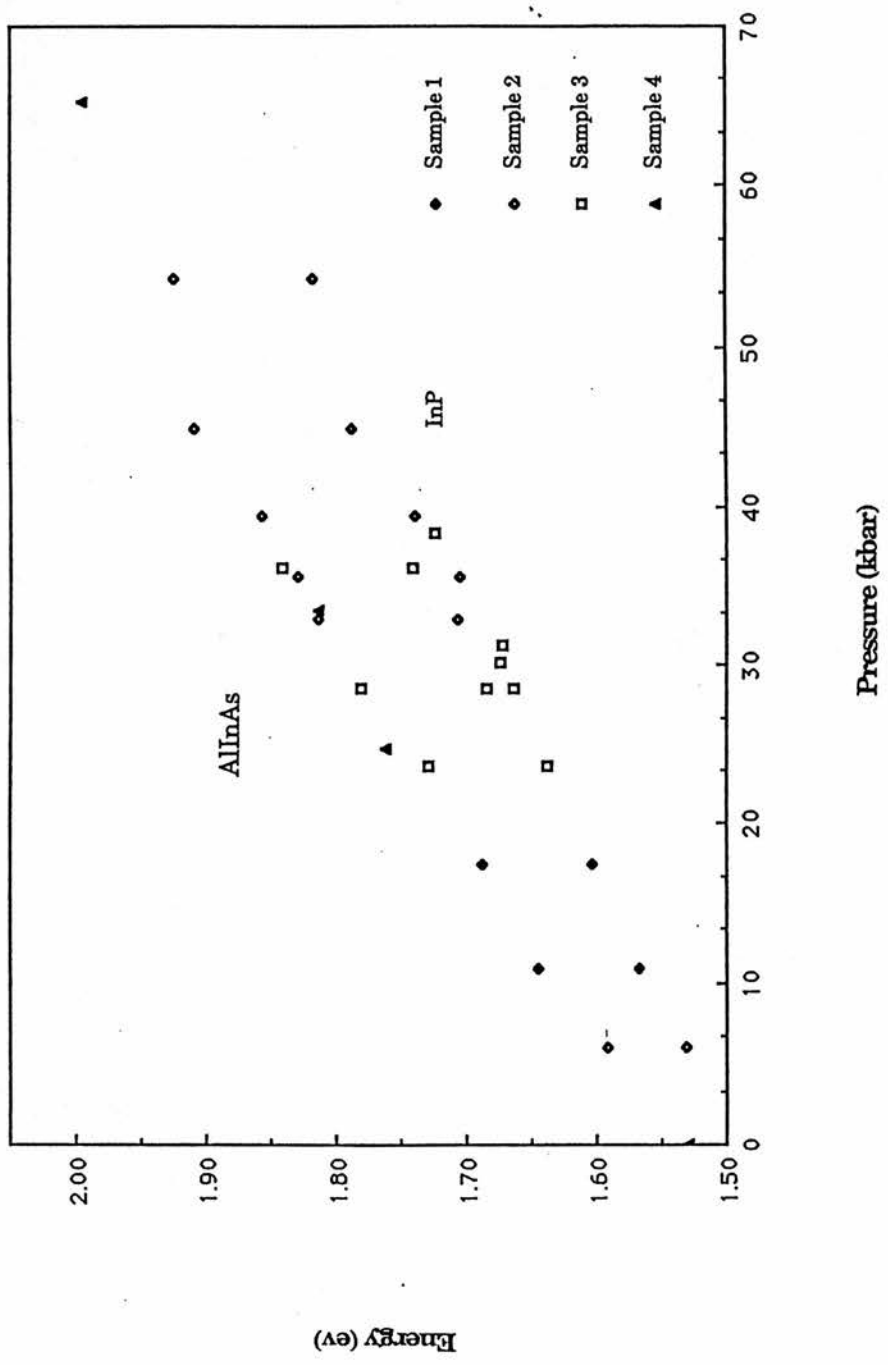


Figure 6.5 Pressure dependence of the undoped InP emission peak at 85 K

A plot of all the peak energy against pressure data for MV411 for both the AlInAs and InP emission is shown in figure 6.6. Four different sample pieces, shown as different points, were used to obtain these results. It is apparent from the spread in the InP peak emission that it could not be used accurately as a secondary pressure calibration. In figure 6.7 a plot of the ratio of AlInAs-InP peak intensity against pressure is shown. The emission intensity varied from sample to sample so this ratio provides a measure of the relative intensity of the AlInAs emission since the InP emission intensity should not change significantly  $\sim 90$  kbar (Muller et al 1980). Due to the scatter in the points (figure 6.8) it is not possible to pin point the  $\Gamma$ -X cross-over, although the luminescence quenches around the energy found compositionally, 2.05 eV at 300 K (Onton and Lorenz 1970), indicating that a structural phase has not occurred. Pressures around and above 60 kbar are difficult to obtain due to experimental difficulty associated with the gaskets. Observing the sample through the Tetravar viewing system (Beales 1989) below the  $\Gamma$ -X cross-over a red spot is seen where the laser spot is incident. Well above the  $\Gamma$ -X cross-over,  $\sim 70$  kbar, no laser spot is observed and the whole crystal glows a deep orange due to emission from the InP substrate. No emission associated with the X-level was observed for the AlInAs either, due to the InP substrate emission masking it or as is more likely, the low signal-noise ratio of the photomultiplier.

### 6.3.3 Calculation of the Deformation Potential of $\text{Al}_{0.48}\text{In}_{0.52}\text{As}$

Since the  $\text{Al}_{0.48}\text{In}_{0.52}\text{As}$  emission energy (figure 6.6) showed the expected bowing with pressure, a least square fit to the data using equation 6.1 gave  $\alpha = 10.1 \pm 0.2 \text{ meV kbar}^{-1}$  and  $\beta = -47 \pm 4 \times 10^{-3} \text{ meV kbar}^{-2}$  (figure 6.8). The empirical equation of state derived by Murnaghan (1944) (equation 6.2) involves a first order expansion of the elastic strain energy, thus the bulk modulus is linear with pressure,  $B(P) = B_0 + PB_0'$ . Higher pressures could result in contributions from non-linear terms in the bulk modulus becoming important, then a universal



**Figure 6.6** Emission peak dependence on pressure for MV411  $\text{Al}_{0.48}\text{In}_{0.52}\text{As}$  epitaxial layer and InP substrate. The different symbols indicate different samples.

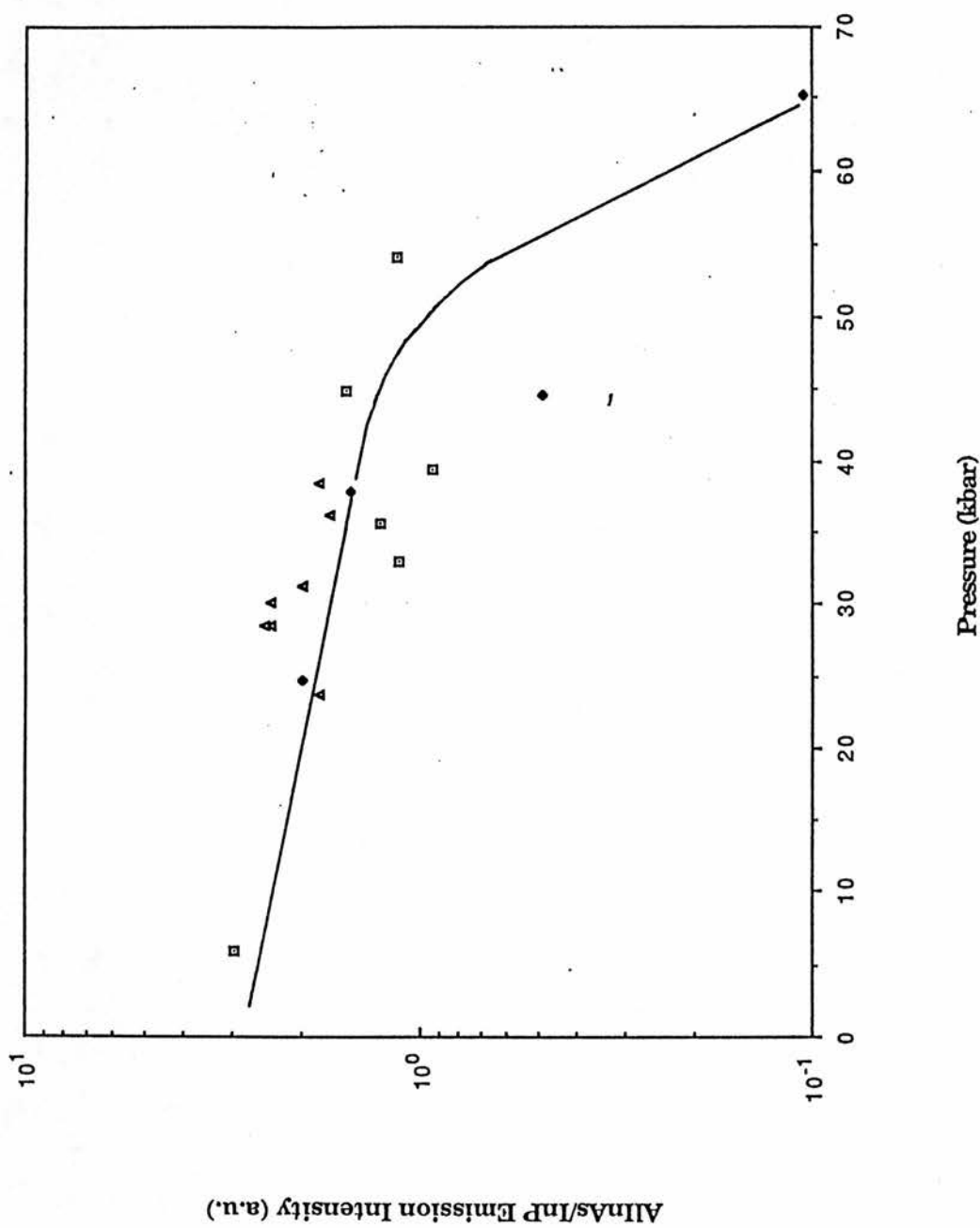


**Figure 6.7** Quenching of the  $\text{Al}_{0.48}\text{In}_{0.52}\text{As}$  emission relative to the InP with pressure in the vicinity of the  $\Gamma$ -X cross-over.

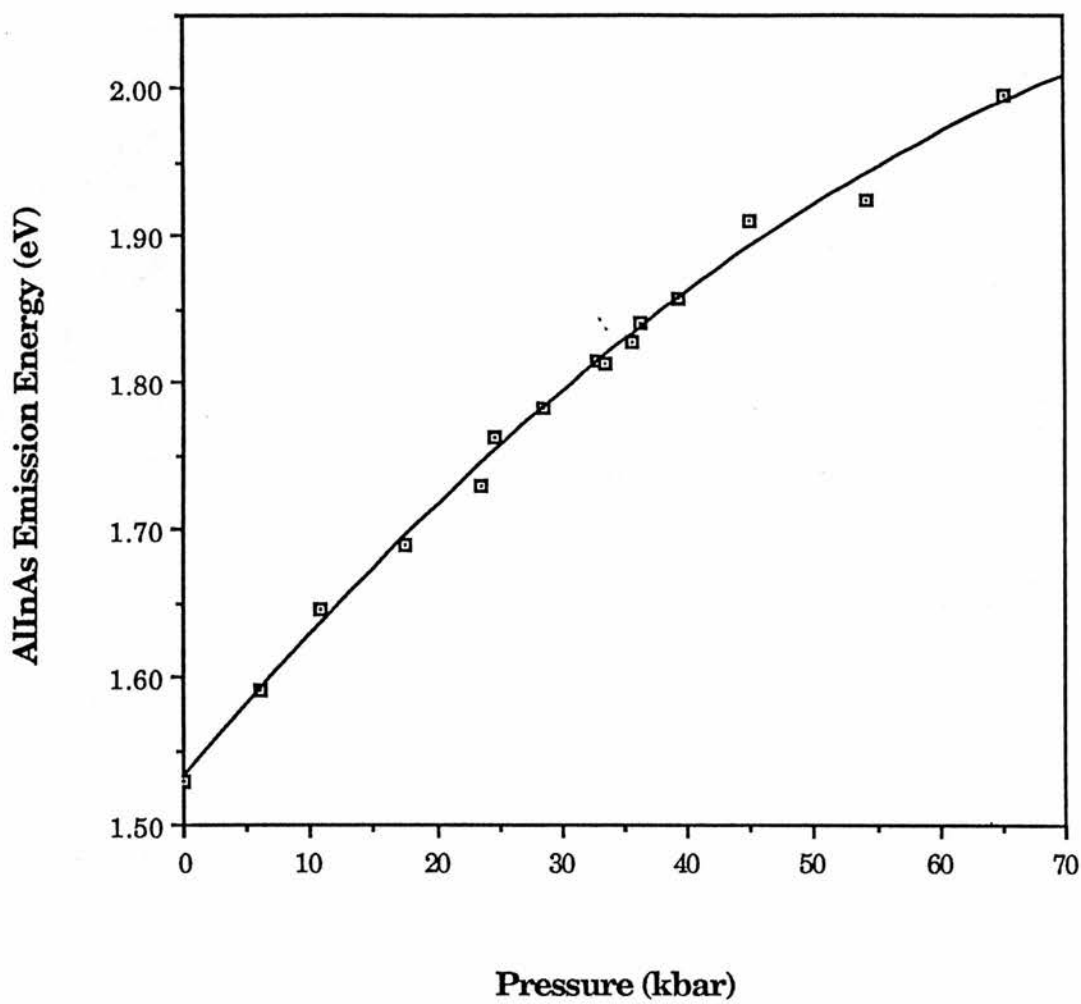


**Figure 6.8** The  $\text{Al}_{0.48}\text{In}_{0.52}\text{As}$  emission energy versus the applied hydrostatic pressure. The solid line represents a quadratic least square fit.

## VI PL of $\text{Al}_{0.48}\text{In}_{0.52}\text{As}$ under hydrostatic pressure

form of the equation of state would be required (Vincet et al 1987). This does not appear to have been the case here, although slight deviations from linearity observed by some authors (Muller et al 1980) may be explained by this limitation of equation 6.2. Care must be taken when estimating the values for  $B_0$  and  $B_0'$  for  $\text{Al}_{0.48}\text{In}_{0.52}\text{As}$  in equation 6.2.

No experimental measurements of  $B_0$  and  $B_0'$  exist for  $\text{Al}_{0.48}\text{In}_{0.52}\text{As}$  in the literature. For cubic crystals the bulk modulus is given by

$$B_0 = \frac{1}{3} (c_{11} + 2c_{12}) \quad (6.8)$$

where  $c_{11}$  and  $c_{12}$  are the elastic moduli. So, the bulk modulus of  $\text{Al}_{0.48}\text{In}_{0.52}\text{As}$  can be interpolated from the values given for the elastic moduli of its binaries. From Madelung (1982) the elastic moduli for InAs and AlAs are given as  $c_{11}=8.329$  and  $c_{12}=4.526$ , and  $c_{11}=12.5$  and  $c_{12}=5.34$ , respectively, in units of  $10^{11}$   $\text{dyncm}^{-2}$ . Accordingly the bulk modulus for  $\text{Al}_{0.48}\text{In}_{0.52}\text{As}$  is 676 kbar which agrees well with that estimated using pseudopotential calculation of 678 kbar (Lam et al 1987). Fortunately, values for  $B_0$  and  $B_0'$  for the InP substrate are better defined, these have been found experimentally from the elastic moduli as  $B_0=711$  kbar and  $B_0'=4.59$  (Nichols et al 1980) or from X-ray data as  $B_0=760\pm 40$  kbar and  $B_0'=4\pm 0.2$  (Menoni et al 1987). The values derived by Menoni et al must be questioned for two reasons; they were obtained from a fit to data for which the values derived by Nichols et al provided just as good a correlation and the value quoted for  $B_0'$  is lower than that expected. Weiner and Riter (1978) have shown  $B_0'$  is approximately constant in zinc-blende structures, 4.46, 4.79 and 4.76 for GaAs, InAs and Ge, respectively; so it seems likely that  $B_0'$  will be 4.59 in InP and that  $\text{Al}_{0.48}\text{In}_{0.52}\text{As}$  can be assumed to take the same value. Measurements of bulk modulus on thin lattice matched GaInAsP epilayers,  $\sim 2 \mu\text{m}$ , on a relatively thick InP substrate,  $\sim 40 \mu\text{m}$  (Prins and Dunstan 1988); suggest that the epilayer may take the same  $B_0$  value as that of the substrate in agreement with Keye's empirical scaling law,  $c_{ij}\sim d^{-4}$ , where  $d$  is the nearest neighbour distance.

## VI PL of $\text{Al}_{0.48}\text{In}_{0.52}\text{As}$ under hydrostatic pressure

So, in calculating the deformation potential we have a) used the extrapolated value of  $B_0$  for  $\text{Al}_{0.48}\text{In}_{0.52}\text{As}$  considering the volume change in the epilayer  $(\Delta V/V_0)^{\text{AlInAs}}$  and b) assumed the AlInAs takes the same values as InP, giving two values for  $B_0$  where it is only necessary to consider the change in lattice constant  $(\Delta a/a_0)$ . It is evident that no structural phase transitions occur as a consequence of structural ordering within the epitaxial layer (section 6.2.2) and the slight change in the bulk modulus, ~1%, due to cooling the crystal is included within the errors.

To calculate the deformation potential from the AlInAs epilayer firstly the in-layer strain due to increasing lattice mismatch with pressure was found using the equation 6.6 enabling the tetragonal distortion to be estimated. The change in epitaxial layer volume  $(\Delta V/V_0)^{\text{AlInAs}}$  can be found using equation 6.5 and plotting this against the energetic position of the AlInAs emission gave the deformation potential as the gradient. Except for the two points at the highest pressures the data plotted in figure 9b gives an excellent fit from which a deformation potential of  $6.51 \pm 0.25$  eV is found. Using  $P_u^{\text{AlInAs}} = (C_{11} + C_{12})_{\text{e}t}^{\text{AlInAs}}$ , the effective uniaxial stress is found to increase from zero to 0.88 kbar at 44.9 kbar reflecting the maximum uncertainty to which the pressure in the alloy is known, this is within the error of the ruby calibration. Assuming that the AlInAs takes the same value for the bulk modulus as InP, discussed above, then the deformation potential is found from figure 10a, using equation 6.3, to be  $6.67 \pm 0.25$  eV. Calculating an average value for  $B^{\text{epi}}$  (equation 6.7) gives the deformation potential as  $6.59 \pm 0.25$  eV (figure 10b) which compares well with that obtained using  $(\Delta V/V_0)^{\text{AlInAs}}$ , the more rigorous method.

How do these values for deformation potential agree with those expected theoretically? Cardona and Christensen (1987) argued that the absolute deformation potential calculated for tetrahedral semiconductors must be screened by the dielectric response of the material particularly when considering

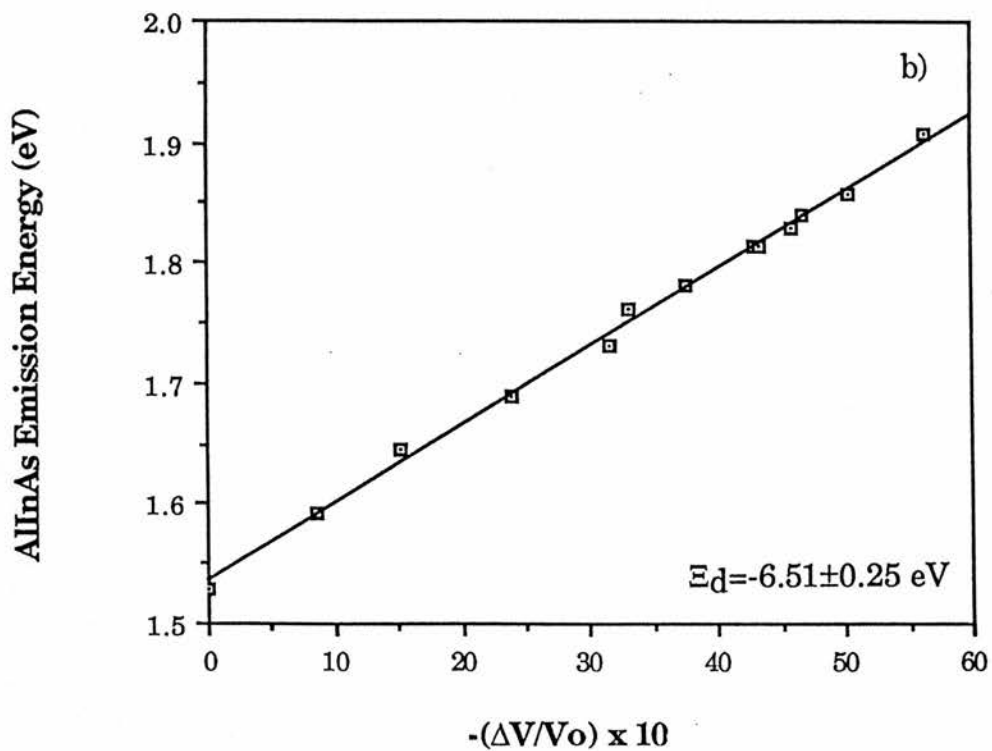
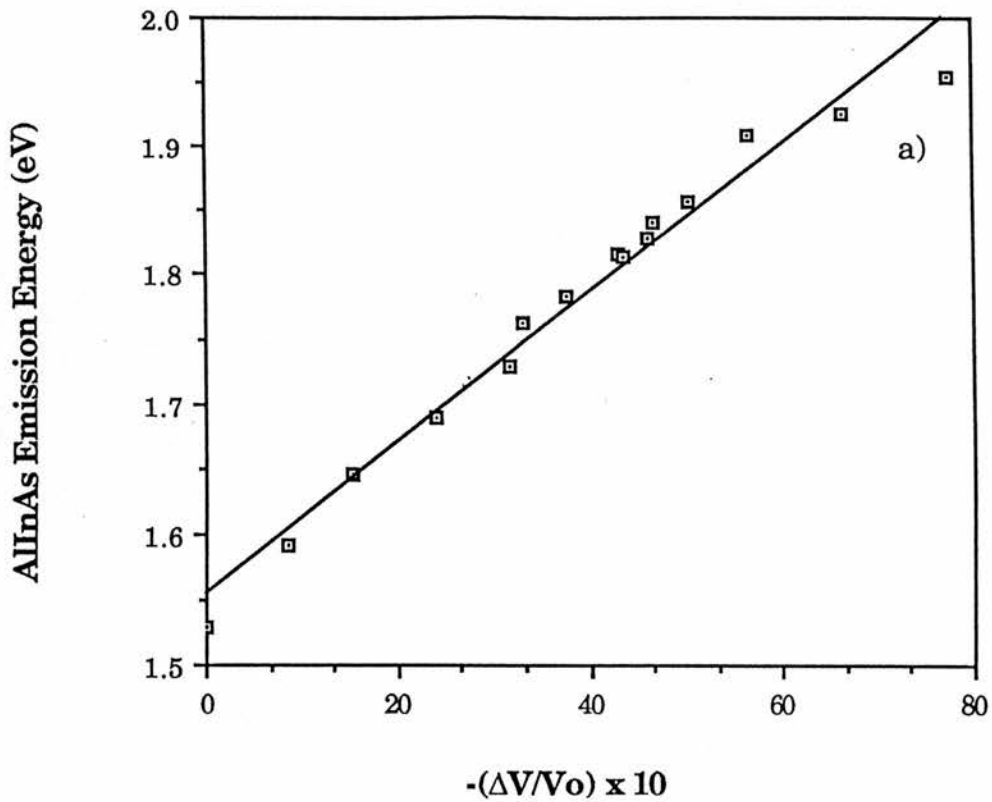


**Figure 6.9**  $\text{Al}_{0.48}\text{In}_{0.52}\text{As}$  emission energy against change in epitaxial layer volume,  $(\Delta V/V_0)^{\text{AllInAs}}$ . The solid line is a least square linear fit that yields the deformation potential a) the two highest pressure points show a loss of ruby calibration so, b) these are omitted to give the best fit.

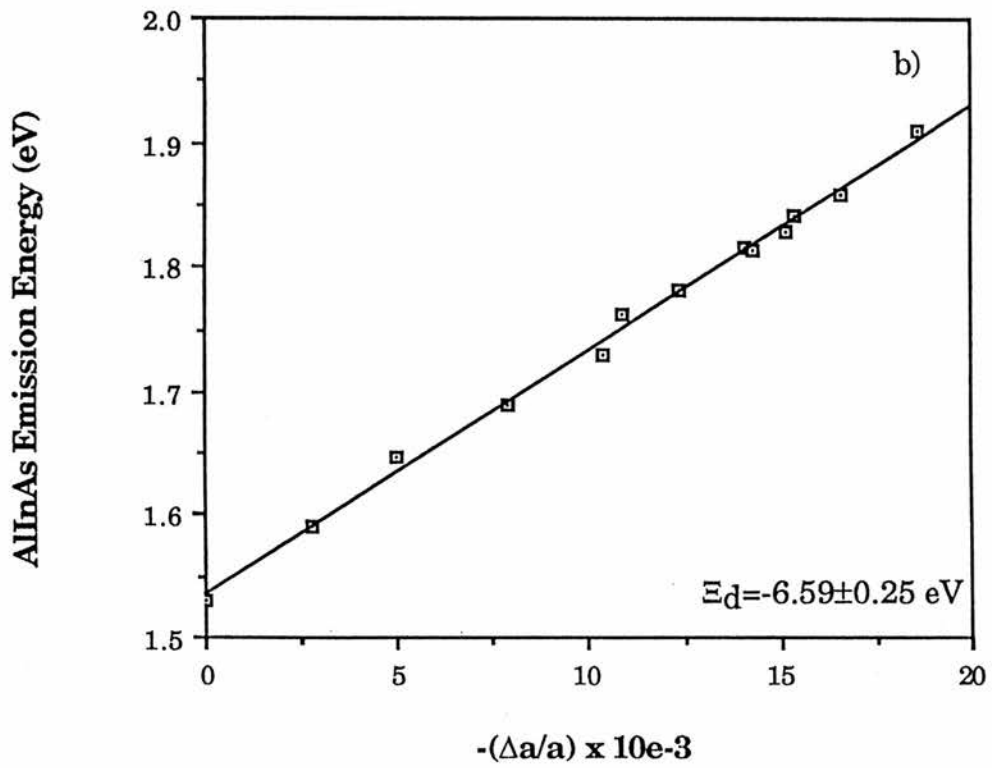
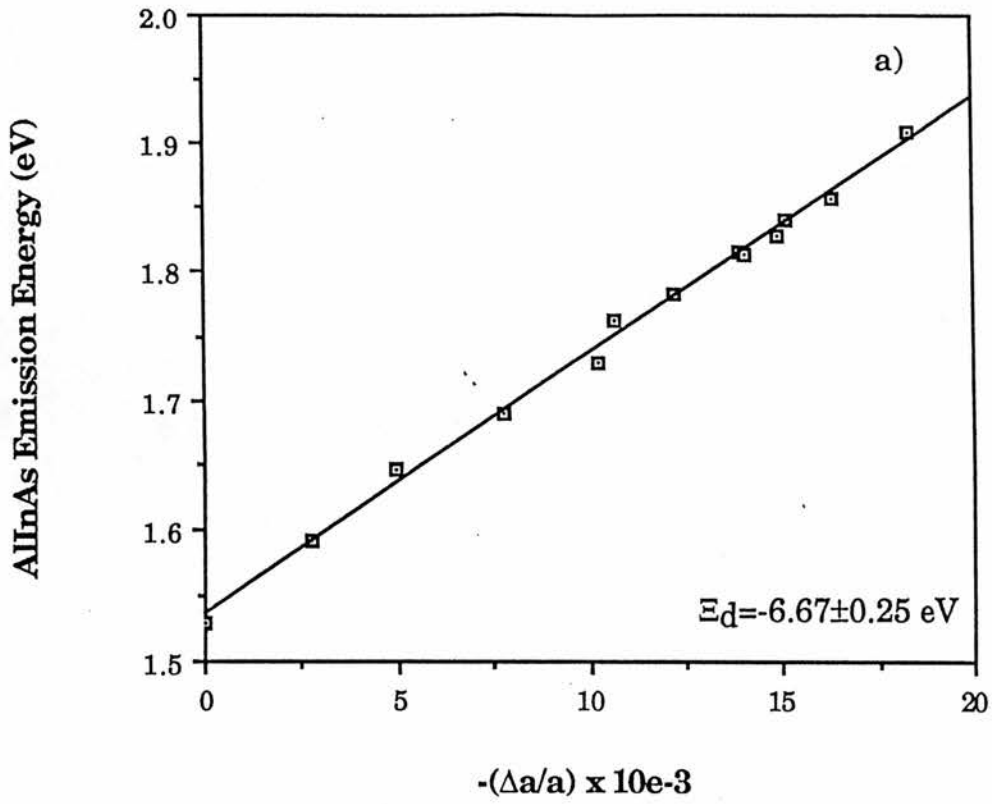


**Figure 6.10** AlInAs emission energy against the change in lattice constant for a) using the InP bulk modulus and b) using the AlInAs bulk modulus.

the electron-phonon interactions. The deformation potential can be defined with respect to a fixed energy relative to the conduction and valence bands. They used the average of the conduction and valence band energies at the Penn gap known as the dielectric midpoint energy DME. The screening ( $\epsilon^{-1}(\omega, q)-1$ ) calculated at the deformation potential of the DME,  $a_D$ , is subtracted from the absolute deformation potentials at other band levels estimated previously. In Cardona and Christensen the screened values for the deformation potentials for the minimum conduction band ( $\Gamma$  or X) and valence band are given, table 6.2. We will assume that an estimate for the deformation potential for  $\text{AlInAs}$  can be made from interpolation of the  $\text{AlAs}$  and  $\text{InAs}$   $\Gamma$ -levels. Hence, the screened deformation potential for  $\text{AlAs}$   $\Gamma$ -point is found by adding the screening deformation potential from table 6.2, 5.3 eV, to the unscreened value in table 6.3, -13.83 eV, to give -8.5 eV. We essentially find a deformation potential for the energy gap when we subtract the screened deformation potentials for the conduction-valence bands and interpolate to give -7.0 eV for  $\text{Al}_{0.48}\text{In}_{0.52}\text{As}$ . This is in reasonable agreement with those values found experimentally.

### 6.3.4 Effective Mass dependence on Pressure in $\text{AlInAs}$

Since the band-gap energy increases with pressure this implies that the effective mass will also increase. Deriving the practical properties of semiconductors from their band structure does not require the detailed knowledge of energy levels but can be approximated by considering extrema points. One such theory is the semi-empirical  $\mathbf{k}\cdot\mathbf{p}$  method which allows band structure to be calculated using experimental band-gap energies and momentum matrix elements,  $E_p$  (Kane 1957). The magnitude of the vector  $\mathbf{k}$  is treated as being small and perturbation theory is used near  $\mathbf{k}=0$  and critical points. This is appropriate for semiconductors because free carriers are concentrated within a small region of  $\mathbf{k}$ -space. The form of the calculation

	$\epsilon$	$\Delta a_D$	$\bar{a}_D$	$\bar{a}_V$	$\bar{a}_V$	$\bar{a}_V$	$\bar{a}_V$	$\bar{a}_C$
C	5.7	13.0	-2.8	-2.4				-4.7
Si	12	6.3	-0.5	-1.6	-0.4	-1.0	+0.8	+0.6
Ge	16	6.5	-0.4	-1.6	+0.65	+0.2	+1.8	-4.5
$\alpha$ -Sn	20	5.9	-0.3	-1.5				
AlP	8	6.1	-0.9	-1.5				+0.8
AlAs	9.1	5.3	-0.6	-1.2	+0.4	-0.2		+0.7
AlSb	10.2	5.7	-0.6	-1.2				+0.7
GaP	9.1	6.6	-0.6	-1.5				+0.8
GaAs	10.9	7.1	-0.7	-1.6	+0.65	-0.1	+0.7	-8.8
GaSb	14.4	6.5	-0.5	-1.4				-9.8
InP	9.6	6.5	-0.7	-0.4				-5.9
InAs	12.3	7.2	-0.6	-0.6				-7.3
InSb	15.7	6.5	-0.5	-0.8				-6.6
ZnSe	5.9	7.9	-1.6	-0.7				-7.4
ZnTe	7.3	7.5	-1.2	-2.0				-7.3
CdTe	7.2	7.2	-1.1	-1.0				-3.7
HgTe	9.3	8.5	-1.1	-2.0				

**Table 6.2** Infrared dielectric constant  $\epsilon$  and various hydrostatic deformation potentials for materials under consideration.  $\bar{a}_V$  and  $\bar{a}_C$  represent the screened deformation potentials of the highest and lowest valence band states,  $\bar{a}_D$  that of the dielectric midgap point.  $\Delta a_D$  represents the effect on screening on the deformation potentials. All deformation potentials are given in eV (Cardona and Christensen 1987).

	(a)							
	Valence bands				Deformation potentials $a$			
	$\Gamma_8$	$X_7$	$L_{4,5}$	$B$	$\Gamma_8$	$X_7$	$L_{4,5}$	$B$
C	3.73	-2.73	0.91	-0.70	-15.42	-8.77	-12.59	-11.02
Si	-0.85	-3.76	-2.02	-2.99	-7.95	-5.06	-6.97	-5.62
Ge	-0.79	-4.03	-2.18	-3.19	-8.09	-4.28	-6.45	-5.15
$\alpha$ -Sn	-1.39	-4.26	-2.59	-3.53	-7.34	-3.60	-5.68	-4.46
AlP	-1.78	-3.95	-2.53	-3.26	-7.67	-5.39	-7.02	-5.98
AlAs	-1.51	-3.84	-2.35	-3.18	-6.46	-4.13	-5.71	-4.73
AlSb	-1.65	-3.96	-2.57	-3.43	-7.35	-4.41	-6.21	-5.02
GaP	-1.59	-4.32	-2.68	-3.51	-8.07	-4.43	-6.57	-5.34
GaAs	-1.07	-3.85	-2.19	-3.08	-8.77	-4.92	-7.15	-5.89
GaSb	-1.46	-4.18	-2.62	-3.56	-7.95	-4.10	-6.21	-4.97
InP	-2.08	-4.39	-2.99	-3.68	-6.91	-3.77	-5.59	-4.63
InAs	-1.94	-4.56	-2.94	-3.72	-7.83	-4.18	-6.29	-5.20
InSb	-1.95	-4.41	-2.94	-3.79	-7.31	-3.67	-5.72	-4.60
ZnSe	-2.80	-5.08	-3.67	-4.33	-8.62	-4.79	-7.09	-6.11
ZnTe	-2.28	-4.64	-3.22	-4.05	-9.49	-4.79	-7.51	-6.13
CdTe	-2.94	-4.94	-3.71	-4.41	-8.16	-4.45	-6.61	-5.60
HgTe	-2.45	-5.04	-3.43	-4.25	-10.45	-4.69	-8.02	-6.79
	(b)							
	Conduction bands				Deformation potentials $a$			
	$\Gamma_6$	$X_6$	$L_6$	$B$	$\Gamma_6$	$X_6$	$L_6$	$B$
C	17.67	8.54	12.14	10.96	-39.71	-17.69	-39.92	-20.41
Si	2.15	-0.25	0.51	1.74	-20.97	-5.73	-11.49	-8.17
Ge	-1.11	-0.23	-0.85	1.66	-17.20	-6.55	-10.99	-8.71
$\alpha$ -Sn	-2.53 <sup>a</sup>	-0.91	-1.81	0.50	-15.28 <sup>a</sup>	-5.84	-9.18	-8.00
AlP	-1.38	-0.32	0.92	1.96	-16.81	-5.31	-11.51	-8.06
AlAs	+0.49	-0.30	-0.54	2.00	-13.83	-4.59	-9.96	-7.15
AlSb	-0.59	-0.73	-0.69	0.95	-15.78	-5.02	-9.91	-7.59
GaP	-0.03	-0.05	-0.11	1.78	-15.90	-5.82	-11.14	-9.11
GaAs	-0.94	+0.20	-0.35	2.04	-15.93	-6.59	-11.49	-10.06
GaSb	-2.01	-0.85	-1.47	0.75	-16.35	-6.51	-9.80	-9.08
InP	-1.58	-0.42	-0.76	1.26	-12.37	-5.23	-9.38	-9.92
InAs	-2.60	-0.85	-1.34	1.08	-14.49	-5.90	-10.18	-10.45
InSb	-2.72	-0.93	-1.82	0.30	-13.12	-6.51	-8.75	-9.39
ZnSe	-1.91	-0.02	-0.53	1.61	-13.26	-6.28	-10.59	-12.85
ZnTe	-1.68	-0.31	-0.44	0.93	-14.74	-6.54	-3.56	-11.21
CdTe	-2.73	-0.68	-1.56	0.18	-10.88	-5.88	-9.06	-11.10
HgTe	-3.66	-0.81	-2.18	-0.33	-12.88	-9.27	-10.24	-12.35

**Table 6.3** Energies (in eV) of (a) the top of the valence band and (b) the bottom of the conduction band calculated with the fully relativistic LMTO method at the  $\Gamma$ , X, L and B (first Baldereschi) points. The corresponding volume deformation potentials are also given.

depends on the number of bands considered, a five band model gives the effective mass  $m^*$  at  $\Gamma_1^c$  as:

$$\frac{m_0}{m^*} - 1 = \frac{E_p}{3} \left[ \frac{2}{E_g} + \frac{1}{E_{g+\Delta_0}} \right] - \frac{E_p}{3} \left[ \frac{2}{E_{0'+\Delta_0}-E_g} + \frac{1}{E_{0'}-E_g} \right] + C \quad (6.9)$$

where  $E_{0'}$  is the energy at  $\Gamma_1^c$  and  $E_0'$  is the energy at the next highest conduction band minima,  $\Delta_0$  is the spin-orbit splitting and  $C$  is a constant involving contributions from higher bands. Since no value for  $E_p'$  for AlAs could be found and although Herman and Wiesbuch (1977) suggested that a five-band model was necessary to calculate  $m^*$  accurately in alloys, we will, like most authors, use a three band model which will suffice for an order of magnitude calculation, so equation 6.9 simplifies to

$$m^* = \left\{ 1 + \frac{E_p}{3} \left[ \frac{2}{E_g} + \frac{1}{E_{g+\Delta_0}} \right] \right\}^{-1} \quad (6.10)$$

Values for  $E_p$  and  $\Delta_0$  were interpolated from the binaries as 20.1 eV and 0.333 eV ( $E_p=21.1$  and 19.1 eV,  $\Delta_0=0.275$  and 0.340 eV for AlAs and InAs, respectively, Madelung 1982, El-Sabbahy 1978) and the energetic position of the AlInAs luminescence gives a measure of  $E_g$ . It was assumed that  $E_p$  will not vary with pressure and since the dominant deformation is of the conduction band compared to the valence band  $\Delta_0$  will be assumed not to change. The zero pressure estimate of  $m^*=0.0748$  using equation 6.10 compares well with that found using equation 4.8,  $m^*=0.0755$ . In figure 6.11 the variation of  $m^*$  with increasing pressure is shown. Since  $E_g$  has a quadratic dependence with pressure (figure 6.8) then  $m^*$  will show the same bowing as the energy-gap.

## 6.4 Summary

The linear pressure coefficient of the  $\Gamma$  minima of  $\text{Al}_{0.48}\text{In}_{0.52}\text{As}$  was found to be  $10.1 \text{ meV/kbar}^{-1}$  which is in agreement with that expected for all group IV and III-V compound semiconductors. An estimate of the deformation potential

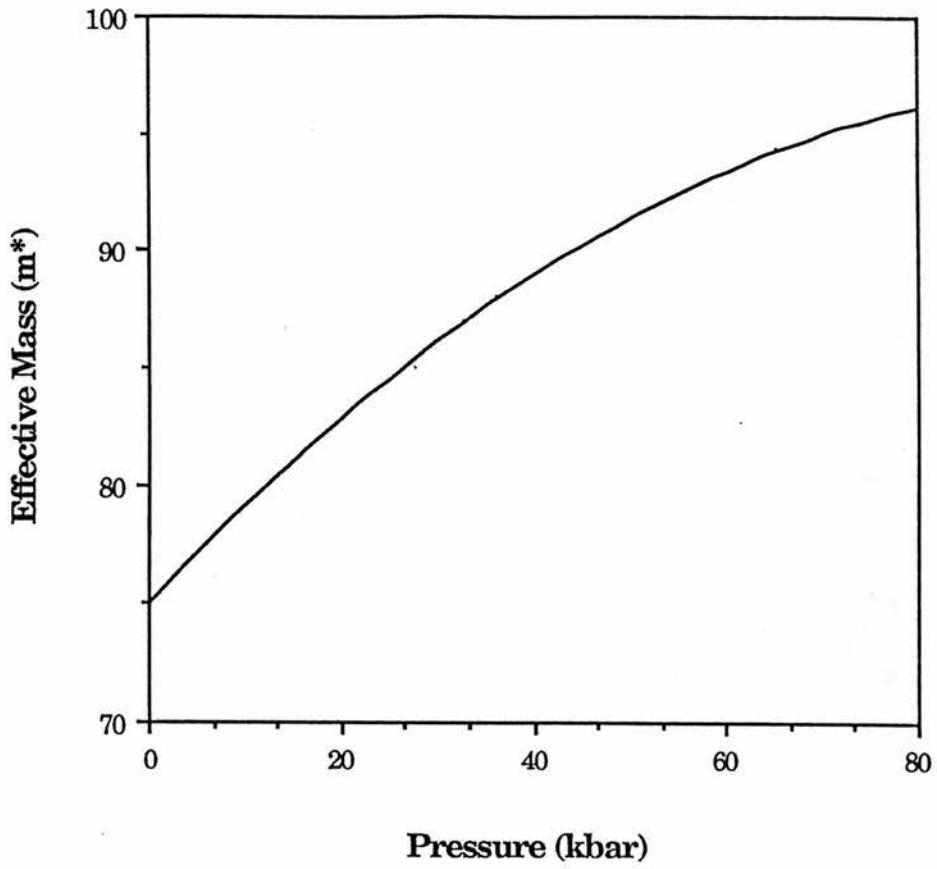


**Figure 6.11** The pressure dependence of the electron effective mass in the  $\Gamma$ -conduction band upon pressure is deduced from **k.p** theory .

## VI PL of $\text{Al}_{0.48}\text{In}_{0.52}\text{As}$ under hydrostatic pressure

was made considering the  $\text{Al}_{0.48}\text{In}_{0.52}\text{As}$  epitaxial layer to have both a different bulk modulus from that of the substrate,  $-6.51 \pm 0.25$  eV, and the same bulk modulus,  $-6.67 \pm 0.25$  eV. In either case the value obtained for the deformation potential agrees well with that from a calculation by Cardona and Christensen (1987) of  $-7.0$  eV. A recent measurement of the bulk modulus of  $\text{Ga}_{0.47}\text{In}_{0.53}\text{As}$  on InP showed the value was not consistent with either, Keye's rule or the interpolated value (Prins and Dunstan 1989). So it is likely the actual value of the deformation potential will be some average of those quoted above.

## VII CONCLUSIONS

	<u>Page</u>
7.1 Conclusions and suggested further work	159

## VII Conclusions

### 7.1 Conclusions and suggested further work

This thesis has considered the optical properties of various III-V semiconductor compounds, alloys and quantum well structures grown by MBE. Perhaps the main contribution of this work has been to provide, to the best of our knowledge, the first detailed optical assessment of the near band-edge luminescence from high quality  $\text{Al}_{0.48}\text{In}_{0.52}\text{As}$  including the use of photoluminescence excitation and the application of hydrostatic pressure.

The emission from  $\text{Al}_{0.48}\text{In}_{0.52}\text{As}$  at 2 K is dominated by a broad luminescence band of FWHM 15-25 meV which had been previously assigned to excitonic recombination. The linewidths observed were too large to be accounted for by a simple model of alloy scattering used successfully in other III-V alloys. An additional broadening mechanism of compositional alloy clustering had been postulated since MBE growth occurs within the InAs-AlAs miscibility gap and thermodynamically this was thought to favour clustering. Experimental results from the samples used in this work show that the low temperature emission is not excitonic, but due to 'deep' ( $D^0, A^0$ ) transition thus providing a viable explanation for the increased linewidth without invoking additional linewidth broadening mechanisms. The possibility of bimodal or structural ordering, already observed in many similar III-V alloys including  $\text{Al}_{0.48}\text{In}_{0.52}\text{As}$  has been discussed. A higher energy peak emerging at 50 K was assigned to a ( $e, A^0$ ) transition by excitation power density measurements and photoluminescence excitation. It would be useful to complete TEM measurement for these samples to see if structural ordering occurs, as at least one sample shows a higher energy peak that could be assigned to this. An attempt to extend the PLE tuning range with a white light source and monochromator failed due to the low quantum efficiency of the samples. This would be better achieved using the dye laser with Pyridine 2 dye to observe the actual band-edge.

## VII Conclusions

The first high hydrostatic pressure optical data was obtained for  $\text{Al}_{0.48}\text{In}_{0.52}\text{As}$  at low temperatures. A linear pressure coefficient of  $10.1 \text{ meV kbar}^{-1}$  was found for the  $\Gamma$  minima which is similar to that previously reported for other III-V compound semiconductors. An estimate of the deformation potential was made assuming the  $\text{Al}_{0.48}\text{In}_{0.52}\text{As}$  had a bulk modulus of 676 kbar (interpolated value) giving  $-6.51 \pm 0.25 \text{ eV}$  and with the same bulk modulus of the substrate 711 kbar (Keye's rule) giving  $-6.67 \pm 0.25 \text{ eV}$ . These values agree well with a theoretical calculation of deformation potential of  $-7.00 \text{ eV}$ . The  $\Gamma$ -X cross-over point needs to be studied in more detail to give additional information about the  $\text{Al}_{0.48}\text{In}_{0.53}\text{As}$  band structure. The development of a low temperature variable pressure system would save the time lost in warming and repressurizing the present clamp cell at room temperature. The cell should be modified to include bevel washers to adjust for slight contractions during temperature cycling. Different and more accurate methods of pressure calibration are required, as is a detailed study of gasket technology. At the time of writing InP and a garnet-based compound are being researched at the SERC-STC High Pressure Facility as alternative sensors and a study of gasket behaviour is close to completion.

Emission spectra were obtained from some other III-V semiconductors GaAs, InP,  $\text{Al}_x\text{Ga}_{1-x}\text{As}$  and  $\text{Ga}_{0.47}\text{In}_{0.53}\text{As}$  to provide the necessary background to the  $\text{Al}_{0.48}\text{In}_{0.52}\text{As}$  and the quantum well luminescence considered in this work. It was concluded that MBE grown material was of a comparable quality to that obtained by any other growth method. The first observation of structure in the free exciton from InP was tentatively assigned to a polariton-exciton. A model of scattering of the polariton from neutral donors was proposed as an explanation of the excitation power density dependence. Surface recombination velocity is expected to have a dominant effect on the observation of the polariton. the use of reactive ion etching techniques to vary the damage to the InP surface

## VII Conclusions

may provide an interesting study of the polariton emission dependence on surface recombination velocity.

The excitonic emission from quantum well heterostructures reflects that obtained from the bulk, modified by the variation of impurity binding energy and increased excitonic recombination as a consequence of larger oscillator strengths. The dominant emission from GaAs-Al<sub>x</sub>Ga<sub>1-x</sub>As and Ga<sub>0.47</sub>In<sub>0.53</sub>As-InP wells was from a free exciton electron to heavy hole transition E<sub>1h</sub>. In Ga<sub>0.47</sub>In<sub>0.53</sub>As-InP the exciton was bound to potential fluctuations due to compositional variation of the Ga<sub>0.47</sub>In<sub>0.53</sub>As. The very narrow linewidths observed for the E<sub>1h</sub> transition in the GaAs-Al<sub>x</sub>Ga<sub>1-x</sub>As wells were comparable with the best reported, although no evidence was found for interface islands with the corresponding discrete structure in the emission due to monolayer fluctuations. Compositional variations in either the well or barrier appear to inhibit the formation of large interface islands. The use of post growth hydrogenation of GaAs and Al<sub>x</sub>Ga<sub>1-x</sub>As has resulted in the a strong enhancement of luminescence efficiencies probably due to the passivation of donors. It would interesting to extend this work to our GaAs-Al<sub>x</sub>Ga<sub>1-x</sub>As well structures, in which strong donor emission is observed, to test many of the passivation hypotheses in the literature.

A detailed study of the growth and luminescence from thin GaAs-Al<sub>x</sub>Ga<sub>1-x</sub>As wells, of thickness 5, 10, 20, and 40 monolayers, on [110] substrates misorientated towards the [110] direction by 2°, 4° and 6°, was undertaken. There was no evidence in the well luminescence that the vicinal planes were broken up into extended step widths or clustered step heights. The linewidths of all the wells grown, without growth interruption, showed a 0.2 monolayer fluctuation regardless of substrate orientation. This was a consequence of the exciton sensing a pseudo-rough inverted interface which was limited by the Al diffusion length of 40 Å. Growth interruption did not result in a decrease of the linewidth

## VII Conclusions

and the observation of interface islands reported by other groups. Instead linewidths increased by a factor of 3-4 attributed to incomplete island formation at the inverted interface at the growth temperatures used. It was concluded that the interface island size was similar to the excitonic diameter thus having a dominant effect on the linewidth. The luminescence from the wells did not show a functional dependence on substrate orientation. This suggests the different vicinal plane widths did not limit either the Al or Ga diffusion length. It would be useful to extend this study using other characterization methods such as triple X-ray rocking curves and phonon Raman scattering to give a more quantitative measure of interface roughness. In addition, the use of misorientated substrates has also been suggested as method of fabricating quantum wires which look promising for optoelectronic devices.

The study of the properties of two dimensional structure has lead quite naturally to the fabrication of one and zero dimensional structures. However, for the near future, strained layer systems such as pseudomorphic HEMTs mentioned briefly in this work will probably gain much technological and commercial importance particularly for device applications.

## References

- Adachi S (1985) *J.Appl.Phys.* **58** R1
- Adams A R, Shantharama L G, Nicholas R J and Sarkar C K (1986)  
*Physica* **139 & 140B** 401
- Adams M D and Sharma S K (1977) *J.Phys.E* **10** 680
- Al-Duduni M (1987) Thesis presented to the University of St Andrews
- Anderoni C C and Pasquarello A (1988) *Europhys. Lett.* **6** 259
- Arthur J R (1968) *J.Appl.Phys.* **39** 4032
- Aspnes D E and Stunda A A (1983) *Phys.Rev.***B27** 985
- Bardeen J, Brattain W and Shockley W (1948) *Phys. Rev.* **75** 230, 231, 232
- Bastard G (1981) *Phys. Rev. B* **24** 4714
- Bastard G (1982) *Phys. Rev. B* **12** 7584
- Bastard G (1987) *Nato ASI series. Series B; Physics Vol. 170* 'Physics and Applications of Quantum wells and Superlattices'. Plenum Press, NY. pp 21
- Bastard G and J A Brum (1986) *IEEE J. Quantum Elect.* **22** 1625
- Bastard G, Delalande C, Meynadier, Frijink P M and Voos M (1984) *Phys. Rev. B* **29** 7042
- Bauer G and Ando T (1986) 18<sup>th</sup> ICPS, Stockholm, Sweden. pp 537
- Bauer R, Bimberg D, Christen J, Oertel D, Mars D, Miller J N, Fukunaga T and Nakashima H (1986) 18<sup>th</sup> ICPS, Stockholm, Sweden pp 525
- Beales T P (1989) to be published in *High Pressure and High Temperatures*
- Ben Amor S, Goutiers B, Dmowski L, Portal J C, Praseuth J C and Quillec M (1989)  
*Proc 19<sup>th</sup> ICSP, Poland. Ed. Zawadski W. Polish Academy of Science.*
- Bimberg D, Bauer R, Oertel D, Mars D and Miller J N (1986) *J. de Physique Coll* **5** C5-93
- Bimberg D, Christen J, Fukunaga T, Nakashima H, Mars D and Miller J N (1987)  
*J. Vac. Sci. Technol B* **5** 1191
- Bimberg D, Mars D, Miller J N, Bauer R and Oertel D (1986) *J. Vac. Sci. Technol B* **4** 1014

## References

- Bimberg D, Schairer W and Sondergeld M (1970) *J. Lum.* **3** 175
- Blakemore J S (1982) *J. Appl. Phys.* **53** R123
- Boguslaskuski and Baldereschi (1989) Proc 19<sup>th</sup> ICSP, Poland. Ed. Zawadski W.  
Polish Academy of Science.
- Brickwedde F G, Van Dick H, Durieux M, Clement J R and Logan J K (1960)  
*J. Res. Natn. Bur. Stand.* **64 A**, 1
- Camphausen D L, Connell G A and Paul W (1971) *Phys. Rev. Lett.* **26** 184
- Cardona M and Christensen N E (1987) *Phys Rev B* **35** 6182
- Casey H C and Buehler E (1977) *Appl. Phys. Lett.* **30** 247
- Casey H C and Panish M B (1978), 'Heterostructure Lasers: Part A Fundamental Principles'. Academic Press, New York, London.
- Cavendett B (1978) in 'Luminescence Spectroscopy' Ed. Lumb M D.  
Pub. Academic Press, NY
- Chandrasekhar M, Venkateswaran U, Chandrasekhar H R, Chambers F A, Vojak B A  
and Meese J M (1986) presented at 18<sup>th</sup> ICSP Stockholm, Sweden.  
Ed. O Engstrom. Pub. World Scientific.
- Charreaux C, Guillot G and Nouailhat A (1986) *J. Appl. Phys.* **60** 768
- Charreaux C, Guillot G, Nouailhat A, Heut D and Lambert M (1985) *Physica* **129B** 413
- Chaudhuri S and Bajaj K K (1984) *Solid State Comm.* **52** 967
- Cheng T S (1988) Private communication
- Cho A Y (1970) *J. Appl. Phys.* **41** 2780
- Chomette A, Deveaud B, Baudet M, Auvary P and Regreny A (1986) *J. Appl. Phys.* **59** 3835
- Christen J, Bimberg D, Steckenbun A and Weimann W (1984) *Appl. Phys. Lett.* **44** 84
- Christen J, Krahl M and Bimberg D (1989) *Superlat. Mircost.* in press
- Cingolani R, Chen Y and Ploog K (1988) *Phys. Rev. B* **38** 13478
- Claxton P (1989) private communication

## References

- Claxton P A, Roberts J S, David J P, Sotomayor-Torres C M, Nash K J, Skolnick M S and Tapster P R (1986) *J. Crystal Growth* **81** 288
- Colvard C, Nouri N, Lee H and Ackley D (1989) *Phys. Rev. B* **39** 8033
- Contour J P, Neu G and Leroux M (1983) *J. Vac. Sci. Technol B* **1** 811
- Cryogenic Calibration Ltd, Pitchcott, nr Aylesbury, Bucks
- Davey S T, Scott E G, Wakefield and Davies G J (1988) *Semicond. Sci. Technol.* **3** 365
- Davies G J, Kerr T, Tuppen G G, Wakefield B and Andrews (1984) *J. Vac. Sci. Technol. B* **2** 219
- Dawson P, Moore K J, Duggan G, Ralph H I and Foxon C T (1986) *Phys. Rev. B* **34** 6007
- Dean P J (1973) *Prog. Solid State Chem.* **8** 1
- Dean P J (1982) *Prog. Cryst. Grow. Charact.* **5** 89
- Dean P J and Skolnick M S (1983) *J. Appl. Phys.* **54** 346
- Dean P J and Skolnick M S (1983) *J. Appl. Phys.* **54** 346
- Dean P J, Robbins D J and Bishop S G (1979) *Solid State Comm.* **32** 379
- Delalande C (1986) in 'Heterojunctions and Semiconductor superlattices'  
Pub. Springer-Verlag, NY.
- Delalande C and Voos C (1984) *Surface Science* **142**
- Deveaud B, Damen T C, Shah J and Tu C W (1987) **51** 828
- Deveaud B, Regreny A, Emery J-Y and Chommette A (1986) *J. Appl. Phys.* **59** 1633
- Di Forte-Poisson M A, Brylinski C and Duchemin J P (1985) *Appl. Phys. Lett.* **46** 476
- Dingle R (1985) *Festkoperpobleme* **15** 21
- Dingle R, Logan R A and Arthur J R (1977) in 'GaAs and related compounds'.  
Pub, Inst of Phys. London. pp 216
- Drummond T J, Masselink W T and Morkoc H (1986) *Proc IEEE* **74** 773
- Duggan G, Raplh H and Moore K (1985) *Phys. Rev. B* **32** 8395

## References

- Duncan K R, Eaves L, Ramdone A, Roys W B, Skolnick M S and Dean P J (1984)  
J. Phys. C: Solid State Phys. **17** 1123
- Eagles D M (1960), J.Phys. Chem.Solids **16** 76
- Eaves L and Halliday D P (1984) J. Phys. C: Solid State Phys. **17** L705
- El-Sabbahy A, Adams A R and Young M L (1978) Solid State Elect. **21** 83
- Elenberg U and Altarelli M (1987) Superlat. Microst. **3** 199
- Elliot R J and Gibson A F (1982) 'Solid State Physics'. Pub. Macmillan Press Ltd, London
- Elman B S, Koteles E S, Zeman S A and Chi Y J (1987) J. Vac. Sci. Technol. B **15** 757
- Esaki L (1986) IEEE J. Quantum Elect. **22** 1611
- Esaki L and Tsu R (1970) IBM J. Res. Develop. **14** 61
- Evangelisti F, Fischbach J U and Frova (1982) Phys. Rev. B **9** 1516
- Ferguson I T, Beales T P, Cheng T S, Sotomayor-Torres C M and Scott E G (1989)  
Semicond. Sci. Technol. **4** 243
- Fischer B and Stolz H J (1982) Appl. Phys. Lett. **40** 56
- Forman R A, Piermarini G J, Barnett J D and Block S (1972) Science **176** 284
- Fouquet J and Burnham R (1986) IEEE Quant. Elect. **22** 1799
- Froyen S and Cohen M (1983) Phys. Rev. B **28** 3258
- Gal M, Kuo C P, Lee B, Ranganathan R, Taylor P C and Stringfellow G B (1986)  
Phys. Rev B **34** 1356
- Glemboch D J and Piller H (1985) in 'Handbook of Optical Constants of Solids'.  
Ed. Palik E D, Pub. Academic Press. pp503
- Goetz K H, Bimberg D, Jurgensen H, Selders J, Solomonov A V, Glinskii G F and  
Razeghi M (1984) J. Appl. Phys. **54** 4543
- Goldstein L, Horikoshi Y, Tarucha S and Okamoto J (1983) Jap. J. Appl. Phys. **22** (1983)
- Gomyo A, Susuki T, Kobayashi K, Kawata S, Hino I and Yuasa T (1987)  
Appl. Phys. Lett. **50** 673

## References

- Goni A R, Strossner K, Syassen K and Cardona M (1987) *Phys. Rev B* **36** 1581
- Greene R and Bajaj K K (1983) *Solid State Comm.* **45** 825
- Greene R and Bajaj K K (1983) *Solid State Comm.* **45** 831
- Greene R, Bajaj K and Phelps D (1984) *Phys. Rev.* **29** 1807
- Hatton P D (1988) *Priv. Comm.*
- Hayakama T, Kondo M, Morita T, Takahashi K, Suyama T, Yamamoto S and Hijikata T (1987) *Appl. Phys. Lett* **51** 1705
- Haynes J R (1960) *Phys.Rev.Lett.* **4** 361
- Heiblum M, Mendez EE and Osterling L (1983) *J. Appl. Phys.* **54** 6982
- Heim U and Hiesinger P (1979) *Phys. Status Solidi b* **66** 461
- Henning J and Ansems J (1987) *Semicond. Sci. Technol.* **2** 1
- Henning J, Ansems J and Roksnoer P (1988) *Semicond. Sci. Technol.* **3** 361
- Herman C and Wiesbuch C (1977) *Phys. Rev. B* **15** 823
- Hoenk M E, Chen H Z, Yariv A, Morkoc H and Vahula K J (1989) *Appl. Phys. Lett.* **54** 1347
- Holmes S (1988) Phd thesis presented at Imperial College, London.
- Hong W -P, Bhattacharya P K and Singh (1987) *Appl. Phys. Lett.* **50** (1987)
- Hopfield J J (1964) *Physics of semiconductors. Proc. 7<sup>th</sup> Int. Conf. Dunod, Paris.*  
*Pub. Academic Press, NY. p725*
- Hopfield J J (1966) *J. Phys. Soc. (sup)* **21** 77
- Hull R, Carey K W, Fouquet J E, Reid G A, Roser S J, Bimberg D and Oertel D (1986)  
*Inst. Phys. Conf. Ser. No83. pp209*
- Ilegem (1985) in 'Technology and Physics of MBE'. Ed. Parker E H C,  
*Pub. Plenum Press.*
- Inspec (1986), The Institute of Electrical Engineers, EMIS Data review Series No 2
- Ito I (1985) *Phys. Stat. Sol. (b)* **129** 559

## References

- Ito I (1986) Phys. Stat. Sol. (b) **135** 493
- Jaing D S, Jung H and Ploog K (1988) J. Appl. Phys **64** 1371
- Jayaraman A ( April 1984) Scientific America pp 42
- Jayaraman A (1983) Rev. Mod. Phys. **55** 65
- Jayaraman A (1986) Rev .Sci. Instrum. **57** 65
- Jayaraman A (1988) Private communication
- Juang F -Y, Hong W -P, Berger P R, Bhattachrya P K, Das Y and Singh J (1987)  
J. Cryst. Grow. **81** 373
- Juang F-Y, Nashimoto Y and Battacharya P K (1985) J. Appl. Phys. **58** 1896
- Kamiya T, Wagner E J (1977) J.Appl.Phys. **48** 1928
- Kana'ah (1988) Private communication
- Kane E (1986) Phys. Rev. B **33** 4428
- Kane E O (1957) J. Phys. Chem. Solid **1** 249
- Kawaguchi Y and Asahi H (1987) Appl. Phys. Lett **50** 1243
- Kawamura Y, Asahi H and Nagai H (1983) J. Appl. Phys. **54** 841
- Kelly M J and Nicholas R J (1985) Rep. Prog. Phys **48** 1699
- Kerr T (1984) PHD Thesis, Glasgow University. Dept. of Elect. Eng.
- Kirby P (1989) private communication.
- Knox R S (1963), Solid State Physics, supplement 5: Theory of excitons.  
Academic Press, London.
- Kobayahi M, Yokoyama T and Narita S (1983) Jap. J. Appl. Phys. **22** L612
- Kohrbrock R, Mannx S, Bimberg D, Larkins C S and Harris J S (1989)  
Appl. Phys. Lett **54** 623
- Kubota E, Ohmari Y and Sugii K (1984) J. Appl. Phys. **55** 3779

## References

- Kunzel H and Ploog K (1980) *Appl. Phys. Lett* **37** 416
- Lam P, Cohen M and Martinez G (1987) *Phys Rev B* **35** 9190
- Lambert B, Caulet J, Regrency A, Baudet M, Deveau D and Chomette A (1987)  
*Semicond. Sci. Technol.* **2** 491
- Lambkin J D and Dunstan D J (1988) *Solid. State. Comm.* **67** 827
- Lane P and Greene R C (1986) *Phys. Rev. B* **33** 5871
- Langer J M and Heinrich H presented at 18<sup>th</sup> ICSP Stockholm, Sweden.  
Ed. O Engstrom. Pub. World Scientific.
- Larsen D M (1973) *Phys. Rev. B* **8** 535
- Lee J, Koteles E and Vassell M O (1986) *Phys. Rev. B* **33** 5512
- Lee J, Koteles E S, Vassell M O and Salerno J P (1985) *J.Lum.* **34** 63
- Leroux M, Neu G and Verie C *Solid State Comm.* **58** 289
- Leroux M, Neu G and Verie U (1986) *Solid State Comm.* **58** 289
- Lester S D, Kim T S and Streetman B G (1988a) *J. Appl. Phys.* **63** 853
- Lester S D, Kim T S and Streetman B G (1988b) *Appl. Phys. Lett.* **52** 474
- Levine J (1965) *Phys. Rev.* **140** A586
- Levy-Leblond J-M (1969) *Phys.Rev.* **178** 1526
- Lewis B F, Grunthner F J, Madhukar A, Lee T L and Fernandez R. (1985)  
*J. Vac. Technol. B* **3** 1317
- Liete R C (1978) *Solid State Elect.* **21** 177
- Lifshitz I M (1965) *Adv Physics* **13** (1965) 483
- Lifshitz N, Jayaraman A, Logan R A and Maines R G (1979) *Phys. Rev. B* **20** 2398
- Liu S M, Das M B, Peng C K, Klem J, Henderson T, Kupp W and Morkoc H (1987) *J. Cryst. Grow.* **81** 359
- Lorenz M R and Onton A (1970)

## References

- Lorenz M R, Morgan T N, Pettit G D (1968) Proc. 9<sup>th</sup> Int. Conf. Semiconductors. Moscow.Pub. Nauka, Leningrad. pp 465
- Lucas C A, Hatton P D, Bates S, Ryan T W, Miles S and Tanner B K (1988) J. Appl. Phys. **63** 1936
- Lumb M D (1978) 'Luminescence Spectroscopy' pub. Academic Press, NY.
- Madelung O, Schulz M and Weiss H (1982), Landolt-Bornstein, Vol 17a, Semiconductor Physics of Group IV and III-V compounds. Springer-Verlag Berlin, London.
- Mailhot C, Chang Y-C and McGill T C (1982) Phys. Rev. B **26** 4499
- Mao H K, Bell P M, Shaner J W and Steinberg (1978) J. Appl. Phys. **49** 3276
- Marsh J H, Roberts J S and Claxton P A (1985) Appl. Phys. Lett. **46** 1161
- Martain T, Stanley C R, Iliadis A, Whitehouse and Sykes D E (1985) Appl. Phys. Lett **46**
- Marzin J Y, Benchimol J L and Sermage B (1983) Solid State Comm. **45** 79
- Masselink W T, Chang Y-C, Morkoc H, Reynolds D D, Litton C W, Bajaj K K and Yu P W (1986) Solid State Elect. **29** 205
- Matayas EE (1979) Sov. Phys. Semicond. **13** 1194
- Menoni C S and Spain I L (1987) Phys. Rev B **35** 7520
- Menoni C S, Hochheimer H D and Spain I L (1986) Phys. Rev. B **33** 5896
- Meyadier M, Delalande C, Bastard B, and Voos M (1985) Phys. Rev. B **31** 5839
- Miller R C and Kleinman D A (1985) J. Lum. **30** 520
- Miller R C, Kleinman D A, Tsang W T and Gossard A C (1981) Phys. Rev. B **24** 1134
- Miller R C, Tu C W, Sputz S K and Kopf R F (1986) Appl. Phys. Lett **49** 1245
- Miller R, Gossard A, Kleinman D and Munteanu M (1984) Phys. Rev. B **29** 3740
- Mowbray D J, Haynes W, Bland J A, Skolnick M S and Bass S J (1987) Semicond. Sci. Technol. **2** 822
- Muller H, Trommer R and Cardona M (1980) Phys. Rev B **21** 4879

## References

- Murnaghan F D (1944) Proc. Nat. Acad. Sci. USA **30** 244
- Nakajima K, Tanahashi T and Akita K (1982) Appl. Phys. Lett. **41** 194
- Nakashima S and Yamaguchi Y (1979) J. Appl. Phys **50** 4958
- Nakayama H, and Fujita M (1985) Inst. Phys. Conf. Ser. No79. pp289
- Naok R A and Holzapfel W B (1979) in 'High pressure Science and Technology',  
Plenum press, New York, Vol 1 p748
- Nash K J, Skolnick M S, Rorison J M, Bass S J and Pitt A D (1988) Superlatt. Microst. **4** 553
- Neave J H, Joyce B A and Dobson P J (1983) Appl.Phys.**A31** 1
- Neave J H, Joyce B A and Dobson P J (1984) Appl.Phys.**A33** 184
- Neave J H, Joyce B A, Dobson P J and Zhang J (1985) Appl.Phys.Lett. **47** 100
- Neuberger N (1971), Handbook of Electronic Materials, Vol 2, III-V Semiconducting  
Compounds.IFI/Plenum Press, New York, London.
- Nichols D N, Rimai D S and Sladek R J (1980) Solid State Comm. **36** 667
- Nilsson S and Samuelson L (1988) Solid State Comm. **67** 19
- Oelgart G, Schwade R, Heider M and Jacobs B (1987) Semicond. Sci. Technol. **2** 468
- Okamoto H (1987) Jap. J. Appl. Phys. **26** 315
- Olego D, Cardona M and Muller (1980) Phys. Rev. B **22** 894
- Olego D, Chang T Y, Silberg E P, Caridi E A and Pinczuk (1982) Appl. Phys. Lett. **41** 476
- Onho H, Wood C E C, Rathbun D L, Morgan D V, Wicks G W and Eastman L F (1981)  
J. Appl. Phys. **52** 4033
- Parker E H C (1983) 'Technology and Physics of MBE'. Pub, Plenum Press  
pp 56-57, 114-115
- Patel D, Chen J, Spain I L, Quigley J H, Hafich M J and Robinson G Y (1988)  
Phys. Rev. B **38** 13206
- Patel D, Crumbaker T, Sites J and Spain I L (1986) Rev. Sci. Instrum. **57** 2795

## References

- Patel D, Sites J R and Spain I L (1987) *Appl. Phys. Lett.* **50** 1829
- Paul W (1961) *J. Appl. Phys.* **S32** 2082
- Pauling L (1935) *'Introduction to Quantum Mechanics'*. Pub. M Graw-Hill, NY.
- Pearah P J, Masselink W T, Klem J, Henderson T, Morkoc H, Litton C W and Reynolds D C (1985) *Phys. Rev. B* **32** 3857
- Pearsall T P (1982) *'GaInAsP Alloy Semiconductors'*. pub, John Wiley & Sons, NY
- Penna A F S, Shah J, DiGiovanni A E and Dentai A G (1984) *Solid State Comm.* **51** 217
- People R, Jayaraman A, Wecht K W, Sivco D L and Cho A Y (1988) *Appl. Phys. Lett.* **52** 2124
- Petrou A, Waytena G, Liu X, Ralston J and Wicks G (1987) *Superlat. Microst.* **3** 133
- Pickering C, Tapster P R, Dean P J and Ashen D J (1982) *Int. Phys. Conf. Ser.* **23** 469
- Piermarini G J, Block S and Barnett J D (1973) *J. Appl. Phys.* **44** 5377
- Piermarini G J, Block S, Barnett J D and Forman R A (1975) *J. Appl. Phys.* **46** 2774
- Praseuth J P, Goldstein L, Henoc P and Primot J (1987) *J. Appl. Phys.* **61** 215
- Prins and Dunstan D (1988) *Phil Mag Lett* **58** 37
- Prins and Dunstan D (1989) *Semicond. Sci. Technol.* **4** 239
- Promreke G S, Park Y S and Hengehold R L (1981) *J. Appl. Phys* **52** 969
- Queisser H J (1981) *J. Lum.* **24/25** 3
- Reynolds D C et al (1984) *Solid State Comm* **52** 685
- Reynolds D C, Bajaj K K, Litton C W, Yu P W, Masselink W T, Fischer R and Morkoc H (1984) *Phys. Rev. B* **29** 7038
- Reynolds D C, Bajaj K K, Litton C W, Yu P W, Singh J, Masselink W T, Fischer R and Morkoc H (1985) *Appl. Phys. Lett.* **46** 51
- Rikken G L, Wyder P, Chamberlain J M, Grimes R T and Halliday D P (1988) *Semicond. Sci. Technol* **3** 302

## References

- Roach W P, Chandrasekhar M, Chandrasekhar H R, Chambers F A and Meese J M (1989)  
Semicond. Sci. Technol. **4** 290
- Rogers D C, Singleton J, Nicholas R J, Foxon C T and Woodbridge K (1986)  
Phys. Rev. B **34** 4002
- Rose-Innes A.C (1964) in 'Low Temperature Laboratory Techniques', Applied Physics,  
English Universities
- Saker M K, Skolnick M S, Claxton P A, Roberts J S and Kane M J (1988)  
Semicond. Sci. Technol. **3** 691
- Sauer R, Harris T D and Tsang W T (1987) J. Appl. Phys. **62** 3374
- Schubert E F and Tsang W T (1986) Phys. Rev. B **34** 2991
- Schubert E F, Gobel E O, Horikoshi Y, Ploog K and Qieisser H J (1984) Phys. Rev. B **30** 813
- Schubert E F, Ploog K (1985) J.Phys.C **18** 4549
- Schulteis L and Tu C W (1985) Phys Rev B **32** 6978
- Scott E G, Andrews D A and Davies G J (1987) J. Cryst. Grow. **81** 296
- Scott E G, Davey S T and Davies G J (1987) Elect. Lett. **23** 761
- Sell D (1972) Phys. Rev. B **6** 3750
- Shah J (1978), Sol.Stat.Elect. **21** 43
- Shahid M A and Makajan (1988) Phys. Rev. B **38** 1344
- Shanabrook B V (1986) Surface Sci. **170** 459
- Shanabrook B V and Comas J (1984) Surface Sci. **142** 504
- Shaw R W and Nicol M (1981) Rev. Sci. Instrum. **52** 1103
- Shum K, C, Ho P P and Alfano (1988) Phys. Rev. B **37** 1404
- Shum K, Zhang C, Ho P P and Alfano R (1988) Phys.Rev.B **37** 1408
- Silvera I F and Wijngaarden R J (1985) Rev. Sci. Instrum. **56** 121
- Singh J and Bajaj K K (1984) Appl Phys Lett **44** 1075

## References

- Singh J and Bajaj K K (1985) *J. Appl. Phys.* **57** 5433
- Singh J and Bajaj K K (1986b) *Appl. Phys. Lett.* **48** 1077
- Singh J, Bajaj K K and Chaudhuri S (1984) *Appl. Phys. Lett.* **44** 805
- Singh J, Dudley S, Davies B and Bajaj K (1986) *J. Appl. Phys.* **60** 3167
- Skolnick M S and Dean P J (1982) *J. Phys. C: Solid State Phys.* **15** 5863
- Skolnick M S, Harris J D, Tu C W, Brennan T M and Sturge M D (1985) *Appl. Phys. Lett.* **46** 427
- Skolnick M S, Nash K J, Saker M K, Bass S J, Claxton P A and Roberts J S (1987a) *Appl. Phys. Lett* **50** 1885
- Skolnick M S, Nash K J, Tapster P R, Mowbray D J, Bass S J and Pitt A D (1987b) *Phys. Rev B* **35** 5925
- Skolnick M S, Tapster P R, Bass S J, Apsley N, Pitt A D, Chew N G, Cullis A G, Aldred S P and Warwick C A (1986b) *Appl. Phys. Lett* **48** 1455
- Skolnick M S, Tapster P R, Bass S J, Pitt A D, Apsley N and Aldred S P (1986a) *Semicond. Sci. Technol.* **1** 29
- Skromme B J, Stillman G E, Oberstar J D and Chan S S (1984) *Appl. Phys. Lett.* **44** 319
- Smith (1985) 'Semiconductor Physics' Pub. Cambridge University Press, Cambridge.
- Sooryakumar R, Pinczuk A, Gossard A C, Chemla D S and Shum L J (1987) *Phys. Rev. Lett.* **58** 1150
- Spain I (1979) in 'High pressure Science and Technology'. Pub. Plenum press, New York
- Spain I (1987) Private communication
- Stanley C R, Farrow R F C and Sullivan P W (1985) in 'Technology and Physics of MBE'. Ed. Parker E H C, Pub. Plenum Press. pp275
- Steinerr T, Thewalt M L W, Koteles E S and Salerno J P (1986) *Phys. Rev.* **B34** 1006
- Swaminathan V, Stall R A, Macrander A T and Wunder R J (1985) *J. Vac. Sci. Technol. B* **3** 1631

## References

- Swaminathan V, Zilko J L, Tsang W T and Wagner W (1982) *J. Appl. Phys.* **53** 5163
- Swanson A W (1987) in the March edition of 'Microwaves and RF' pp 139
- Taguchi A and Yamada S (1987) *J. Appl. Phys.* **61** 2412
- Tanaka M and Sakaki H (1987) *J. Cryst. Grow.* **81** 153
- Tanaka M and Sakaki H and Yoshino J (1986) *Jap. J. Appl. Phys.* **25** L155
- Tanaka M, Ichinose H, Furuta T, Ishida Y and Sakaki H. *J. de Physique Coll* **5** C5-101
- Thomas D G, Hopfield J J and Augustyniak W M (1965) *Phys.Rev.* **140** A202
- Thurmond C D J. *Electrochem. Soc.* (1975) **122** 1133
- Tozer S W, Wolford D J, Bradley and Bouf D (1988) presented at 19<sup>th</sup> ICPS Warsaw, Poland.
- Tranikov V Vand Krivolopchuk V V (1983) *Sov. Phys. JETP* **58** 1210
- Tsang W and Miller R (1985) *Appl. Phys. Lett.* **48** 1288
- Tsang W T and Schubert E F (1986) *Appl. Phys. Lett* **49** 220
- Tsang W T, Miller R C, Capasso F and Bonner W A (1982) *Appl. Phys. Lett* **41** 467
- Tu C W, Miller R C, Wilson B A, Petroff P M, Harris T D, Kopf R F, Sputz S K and Lamont M G (1987) *J. Cryst. Grow.* **81** 159
- Turco F, Massies J and Contour J P (1987) *Revue Phys. Appl.* **22** 827
- Tusi R K, Curless J A, Kramer G D and Peffley M O (1985) *J. Appl. Phys.* **58** 2570
- Ulbrich R G (1978) *Solid State Electronics* **21** 51
- Van Valkenburg A (1965) Conf Int Sur-les-Hautes Precisions, Soane-et-Loire, France
- Van Vechten J A and Bergstresser T K (1970) *Phys. Rev. B* **1** 3351
- Varshni Y P (1967) *Physica* **34** 149
- Venghaus, Skolnick and Dean (1984) *J.Phys. C* **17** 6229

## References

- Voisin P (1986) in 'Heterojunctions and Semiconductor superlattices'  
Pub. Springer-Verlag, NY. pp 73
- Voisin P, Bastard G, and Voos M (1984) Phys Rev B **29** 935
- Wada K, Kozen A, Hasumi Y and Temmyo J (1989) Appl. Phys. Lett **54** 436
- Wakefield B, Halliwell M A, Kerr T, Andrews D A, Davies G J and Wood D R (1984)  
Appl. Phys. Lett. **44** 341
- Walukiewicz W, Lagowski J, Jastrzebski, Rava P, Lichensteiger M, Gatos C H and  
Gatos H C (1980) J. Appl. Phys. **51** 2659
- Wang W I, Mendez E E, Kuan T S and Esaki L (1985) Appl. Phys. Lett **47** 826
- Watt M, Sotomayor-Torres C M, Hatton P D, Vass H, Claxton P A and Roberts J S (1987)  
J. de Physique Colloq **48** C5-483
- Wavefield B, Eaves L, Prior K A, Nelson A W and Davies G J (1984) J. Phys D:  
Appl.Phys. **17** L133
- Weiner E R and Riter J R (1978) J. Phys. Chem. Solids **39** 1139
- Weinstein B (1986) Rev. Sci. Instrum. **57** 910
- Weisbuch C (1987) Nato ASI series. Series B; Physics Vol. **170** 'Physics and Applications  
of Quantum wells and Superlattices'. Plenum Press, NY. pp 261
- Weisbuch C and Ulbrich R G (1979) J. Lum. **18/19** 27
- Weisbuch C, Dingle R, Gossard A C and Wiegmann (1981) Solid State Comm. **38** 709
- Weisbuch C, Miller R, Dingle R, Gossard C and Wiegman (1981)  
Solid State Comm. **37** 319
- Welch D F, Wicks G W, Eastman L F, Parayanthal P and Pollak F H (1985)  
Appl. Phys. Lett. **46** 169
- Westland D J, Fox A  $\mu$ , Maciel A C, Ryan J F, Scott M D, Davies J I and Riffat J R (1987)  
Appl. Phys. Lett. **50** 839
- White A M, Dean P J, Fairhurst K M, Bradsley W, Williams E W and Day B (1972)  
Solid State Comm. **11** 1099

## References

- White A M, Dean P J and Day B (1974) *J.Phys. C: Solid State Phys.* **7** 1400
- Wicks G W, Wang W I, Wood C E C, Eastmann L F and Rathbun J. *Appl. Phys.* **52** 5792
- Wiesbuch C (1978) *Solid State Elect.* **21** 179
- William E W and Bebb H B (1972) in 'Semiconductors and Semimetals', Vol 8.  
Ed Willardson R K and Beer A C. Academic Press, London, NY. pp182...
- Williams E W (1968) *Phys. Rev.* **168** 922
- Williams E W and Bebb H B (1967) *J.Phys.Chem.Solids* **30** 1289
- Wolford D J and Bradley J A *Solid State Comm.* **53** 1069
- Wolford D J, Mariette H and Bradley J A (1984) *Inst. Phys. Conf. Ser. No. 74* pp 275
- Wolford D, Kuech T and Bradley J (1986) *J. Vac. Sci. Tech.*
- Wood C E C (1983) in 'The Technology and Physics of Molecular Beam Epitaxy',  
Ed. Parker E H C. Plenum, New York, p 61
- Wright M G, Kana'ah A, Cavendett B C, Johnson G R and Davey S T (1989) submitted to  
*Semicond. Sci. Technol.*
- Yu P W and Kuphal E (1984) *Solid State Comm* **49** 907
- Yu P W, Reynolds D C, Bajaj K K, Litton C W, Klem J, Huang D and Morkoc H (1987)  
*Solid State Comm.* **62** 41
- Zhu L D, Chan K T and Ballantyne J M (1985) *Appl. Phys. Lett.* **47** 47

## **APPENDICES**

- A: Compensation ratio from optical spectra
- B: Pressurization of a diamond anvil cell
- C: Programs used in this work

## Appendix A

### Compensation ratio from optical spectra

The theory derived by Kamiya and Wagner allows the estimation of stationary donor and acceptor concentrations and hence compensation ratio (section 3.2.2). It describes the overall lineshape as the sum of the  $(e, A^{\circ})$  and  $(D^{\circ}, A^{\circ})$  envelopes, calculated separately, but taking account of competing transitions on the  $(D^{\circ}, A^{\circ})$  spectra. The  $(D^{\circ}, A^{\circ})$  intensity is then given by

$$I_{DA}(E)dE = P(R) \frac{dR}{dE} W_{DA}(R) P^{\circ}_D(R) P^{\circ}_A(R) N_A dE \quad (A.1)$$

where  $P(R)$  is the Poisson distribution,  $P^{\circ}_D(R)$  is the probability of a donor being neutral ( $= (N_D - N_A) / N_D$  if  $n \ll (N_D - N_A)$ ) and  $P^{\circ}_A(R)$  is the probability of an acceptor being neutral given by  $P^{\circ}_A(R) = W_{hA} / W + W_{DA}(R)$  where  $W_{hA}$  is the hole capture rate and  $W$  includes  $W_{hA}$  with other competing processes such as the non-radiative transitions and the  $(e, A^{\circ})$ .  $W_{DA}$  the transition probability between a neutral donor and a neutral acceptor at distance  $R$  (see equation 3.4) and is given by

$$W_{da}(R) = \frac{4e^2 n' E}{(4\pi\epsilon_0) m_e^2 h^2 c^3} |M_{cv}|^2 I^2(R) \quad (A.2)$$

Here  $n'$  is the refractive index,  $|M_{cv}|$  is the interband momentum matrix element and  $I(R)$  is the overlap integral between donor and acceptor wavefunctions. The intensity of the  $(e, A^{\circ})$  band is given by

$$I_{eA}(E)dE = c(E - E_g + E_a)^{0.5} \exp\left(-\frac{E - E_g + E_a - E_f}{kT}\right) N^{\circ}_A dE \quad (A.3)$$

where

$$c = \frac{4e^2 n' E}{(4\pi\epsilon_0) m_e^2 h^2 c^3} \frac{32\sqrt{2} a_A^3 m^{*1.5}}{\pi h^3} |M_{cv}|^2$$

$a_A$  is the effective Bohr radius of the acceptor,  $E_f$  is the Fermi energy and  $N^{\circ}_A$  is the stationary neutral acceptor concentration given by

## Appendix A

$$N^{\circ}_A = \int P(R) \frac{N_A W_{hA} dR}{W + W_{DA}(R)} \quad (\text{A.4})$$

Fits are made to the (e,A<sup>•</sup>) and (D<sup>•</sup>,A<sup>•</sup>) emission lineshape at various temperatures at which these peaks are still well resolved (see figure 3.9 for an example of a suitable spectra). This analysis also gives information about the distribution of electrons between the conduction band and the donors.

## Appendix B

### INSTRUCTIONS FOR USE OF THE 'DIACOLD' D-01

#### 1. INTRODUCTION

In this cell type a high pressure is applied to a sample by forcing two diamond anvils together along a common axis, by means of six M5 cap-head bolts working in left hand - right hand pairs. One diamond is mounted on a plate of hardened tool steel set into the base of a cylinder. The opposing diamond is mounted on a piston, also of hardened tool steel, which fits tightly into the cylinder. The complete assembly is termed the 'central insert'.

Ancillary equipment. A standard metallurgical microscope with magnification up to x40 and a long working distance is essential for setting up and maintaining the cell. A fiber optic lamp provides a particularly convenient source of direct illumination. Several needles, each preferably mounted on a small handle, are necessary for loading.

#### 2. ABOUT ALIGNMENT.

The 'Diacold' was correctly aligned before shipping. Nevertheless it is most important to check it before use. Further, in all high pressure devices distortion occurs in operation; the 'Diacold' is no exception. To ensure long anvil lifetimes it is essential to make frequent checks of alignment. It is good practice to make visual checks on the sample-gasket during and after any significant increase in applied pressure, and following standing at pressure for a long period.

NEVER apply pressure to the diamond anvils unless there is a sample or gasket between them.

#### Alignment checks.

(i) Dismantle the cell: remove the top plate (three l.h. and three r.h. bolts). Extract the piston using a ring magnet (in the case of non-magnetic cells use the extraction bolt provided). Remove the packing from between the anvils.

Using a microscope, examine the diamond anvil on the piston. Remove any dirt or grease by gently drawing across the anvil a lens tissue on which a drop of ethanol has been allowed to spread. Examine and clean the lower anvil similarly but DO NOT remove the lower anvil plate from its cylinder.

The anvils are mounted using Araldite epoxy resin. This resin disintegrates in dichloromethane ( $\text{CH}_2\text{Cl}_2$ ). Care should be taken if loading this or similar liquids into gaskets to keep any overflow to a minimum.

## Appendix B

(ii) Holding the cylinder approximately horizontal, very gently insert the piston. DO NOT FORCE IT IN. This operation is best done with the piston-cylinder assembly horizontal to avoid any possibility of dropping the top anvil onto the lower one. Before insertion, the fiducial mark on the piston should be aligned with the scale position indicated in Figure 1. This is the position in which the two anvil faces come into coincidence. NEVER rotate the anvil faces relative to each other when they are in contact.

Note especially that the alignment of Figure 1 applies only to the condition in which the cell was shipped. If an anvil is remounted or replaced, the new position after alignment must be used.

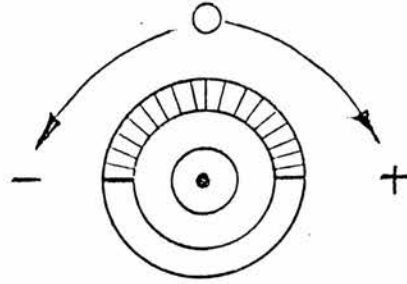


Figure 1

(iii) Having brought the anvils very gently into contact, place the cell under the microscope and focus on the interface between the anvils. The field of view will probably be clear. There may be one or more coloured fringes visible. Very gently increase the load using finger pressure on the piston, watching the behaviour of the fringes, if any. They will probably travel off in one direction, leaving a clear field. The 'Diacold' was set up before shipping such that the alignment is correct when under pressure. If the alignment is not correct, the procedure below must be carried out as the anvil faces are no longer parallel to each other.

### 3. FULL ALIGNMENT OF THE 'DIACOLD' D-01

The following procedure should be used if it is necessary to align the cell for any reason, such as after replacing an anvil.

(i) Fix the lower anvil plate to the cylinder using the posidrive screws, but leave them barely tightened. Insert the piston but do not bring the anvils into contact. Viewing the assembly under the microscope, rotate the piston until the anvils are as nearly coincident as possible. Both top and bottom illumination is helpful for this operation. Bring them into exact coincidence using the four lateral set screws (1.5 mm Allan key). Tighten these and the posidrive screws. Note the position of the piston relative to the cylinder, as in Figure 1. Now bring the two anvils very gently into contact. Mount the insert on the microscope stage and illuminate from below.

## Appendix B

(ii) Fringes will be visible, at least on one side of the field. Figure 2 shows a typical situation. Remove the piston and slightly loosen the three positive screws. Then tighten, by say  $20^\circ$ , whichever of the screws is appropriate to drive the pattern in the direction of fewer fringes. Thus, in the situation of

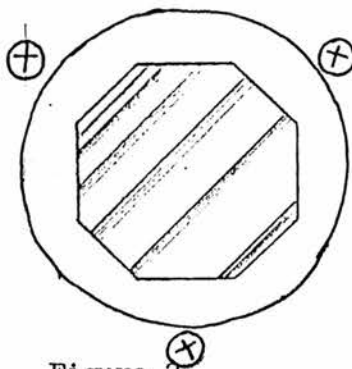


Figure 2

Figure 2, tighten screws 1 and 3. Continue the procedure until only two or three fringes cover the face. Very small adjustments should then allow the fringes to be altogether eliminated. This may be a time-consuming process. With practice it can be done in 20 to 30 minutes. Make sure that all three screws are well tightened at the end of the alignment procedure.

### 4. GASKETS

If a solid sample is compressed directly between the anvils there will be a pressure gradient from maximum at the centre to zero at the edges.

Liquid and solid samples may be examined using a gasket between the anvils. For infrared work thicknesses of 0.075 mm are generally used. For Raman spectroscopy 0.20 mm is more common. The gasket hole diameter is usually about half that of the anvil culet, or a little less. The most commonly used gasket materials are inconel and stainless steel.

It is convenient to mount gaskets on the lower anvil plate using two small pieces of plasticene. Once the gasket is loaded with the sample, ruby for pressure calibration, etc, insert the piston and check that the sample is still within the hole. Attach the top plate, ensuring that it is level, and finger-tighten the bolts. Apply pressure by tightening diametrically-opposed pairs of l.h.-r.h. bolts simultaneously with two Allan keys. Observe the behaviour of the gasket and sample as pressure is applied. Pressure should be released gradually, reversing the above procedure.

---

# Appendix C

```

Program Deconvolution
Implicit real*8(a-h,o-z), integer(i-n)
Character*8 outfile
real*8 a1,e1,e2,fwhm,op,hl
real*8 nline(1000)
real*8 energy(1000),intensity(1000),intensity2(1000),total(1000)
integer peak

c
write(6,*) 'How many transitions'
read(6,*) n
write(6,5)
5 format(17,'Output Filename')
6 read(5,7) Outfile
7 format(a80)
write(6,*) 'Input energy range in eV'
read*,e1,e2
m=(e2-e1)*20000
open(unit=1,file=outfile,status='new')
write(6,*) m
write(6,*) 'Input fwhm and energy (eV) and height'
read*,fwhm,op,hl
fwhm=fwhm/2.36
e=e1
do 10, i=1,m
intensity(i)=hl*((fwhm**2/4)/((e-op)**2+(fwhm**2/4)))
intensity2(i)=hl*exp(-0.5*(e-op)**2/(fwhm**2))
q=abs(e-op)
intensity2(i)=hl*(e-op)**0.6*exp(-(e-op)/(15*1.7236e-4))
energy(i)=e
total(i)=intensity(i)
write(1,*) energy(i),intensity(i)
e=(energy(i)+0.0005)
10 continue
if (n.eq.1) then
close (unit=3)
stop
endif
do 25 peak=2,n
write(6,16) peak
15 format(17,'Output Filename for Transition #1')
6 read(6,7) Outfile
open(unit=4,file=outfile,status='new')
open(unit=2,file='testcon',status='new')
write(6,*) m
write(6,*) 'Input fwhm and energy (eV) and height'
read*,fwhm,op,hl
fwhm=fwhm/2.36
e=e1
do 20, j=1,m
intensity2(i)=hl*((fwhm**2/4)/((e-op)**2+(fwhm**2/4)))
intensity2(i)=hl*exp(-0.5*(e-op)**2/(fwhm**2))
e=e
write(4,*) energy(i),intensity2(i)
total(i)=total(i)+intensity2(i)
write(2,*) energy(i),total(i)
e=(e+0.0005)
20 continue
close (unit=4)
close (unit=3)
close (unit=2)
25 continue
stop
end

```

```

Program Fitting
Implicit real*8(a-h,o-z),integer(i-n)
parameter (i=100,ix=100,npts=500)
integer iw(iw)
real*8 y(100),t(100),x(5),w(iw),xn(5),xw(5)
real*8 xdata(100),ydata(100),xmin,xmaxin
character infile*128,file_type*128,f2*128,outfile*128,type*1
character coeffn*128,inchar*79
logical no_file,file_exist
common/valuen/y,t,xn,xw

c
General curve fitting program; function required in set up in
f1n0(w,n,x) with number of coefficients given below.
c
data_read=0
data_cmc=0
n=3 ! the number of unknown coeffs
c
1 write(6,*) ' '
write(6,*) '0. Quit'
write(6,*) '1. Read file data'
write(6,*) '2. Calculate coefficients'
write(6,*) '3. Re-calculate using output coeffs'
write(6,*) '4. Output file of interpolated curve for YPO'
write(6,*) '5. not available'
write(6,*) '6. not available'
write(6,*) '7. not available'
write(6,*) '8. Output coeff values and sumsq to file'
call getint('Select option',iopt)
if (iopt.lt.0.or.iopt.gt.8) goto 1
write(6,*) ' '
c
if (iopt.eq.0) then
stop
endif
c
if (iopt.eq.1) then
call getfile('File with data for fit (0 to abort) ?',
&'*.dat',no_file,' ',' ',.DAT',infile)
if (infile.ne.'0') then
if (no_file) then
write(6,*) 'Requested file to read from does not exist'
else
open(unit=1,file=infile,status='old',form='formatted')
read(1,*) m
do i=1,m
read(1,*) xdata(i),ydata(i)
enddo
close(unit=1,status='keep')
data_read=1
xmin=xdata(1)
xmax=xdata(m)
do i=2,m
xmin=min(xmin,xdata(i))
xmax=max(xmax,xdata(i))
enddo
endif
endif
endif

```

```

if (iopt.eq.2.or.iopt.eq.3) then
if (data_read.eq.0) then
write(6,*) 'No data. Use option 1 first'
else
do i=1,m
t(i)=dbl(xdata(i))
y(i)=dbl(ydata(i))
enddo
if (iopt.eq.3.and.data_cmc.eq.0) iopt=2
endif
endif
c
if (iopt.eq.2) then
do i=1,n
call getdouble('Please enter initial guess for coeff',
&'//char(i+68)',xn(i))
x(i)=1.0d0
enddo
else
do i=1,n
xn(i)=w(i)
x(i)=1.0d0
enddo
endif
call
call E0EDEF(m,n,x,fsumsq,iw,iw,w,w,w,w,ifail)
call print_ifail(ifail)
c
write(6,*) ' '
if (ifail.ne.1) then
write(6,*) 'sum squares = ',fsumsq
do i=1,n
xw(i)=x(i)*xn(i)
enddo
write(6,*) 'At the point '//char(i+68)///' ',xw(i)
data_cmc=1
endif
endif
endif
c
write(6,*) 'Do calculation first. Use option 2'
else
call getfile('Output file for interpolated curve (0 to abort) ?',
&'*.dat',no_file,' ',' ',.DAT',outfile)
if (outfile.ne.'0') then
write(6,*) 'Range of input data: x = ',xmin,' to ',xmaxin
call getdouble('Start x value for output ?',w1)
call getdouble('End x value for output ?',w2)
wstep=(w2-w1)/(npts-1)
open(unit=1,file=outfile,status='new',form='formatted')
write(1,*) npts
do j=1,npts
xout=w1+dbl(j-1)*wstep
yout=f1n0(xout,n,xw)
write(1,*) xout,yout
enddo
write(1,*) 'x value'
write(1,*) 'y value'
write(1,*) 'Fitted curve for ('//infile(1:len(infile))//')'
write(1,*) 'nch'
write(1,*) 'nwb'
close(unit=1,status='nove')
endif
endif
endif
c
if (iopt.eq.5.or.iopt.eq.6.or.iopt.eq.7) then
write(6,*) 'options 5 to 7 have not been programmed'
endif
c
if (iopt.eq.8) then
if (data_cmc.eq.0) then
write(6,*) 'Do calc first. Use option 2'
else
coeffn=infile(1:len(infile))//'.CF'
call textint(coeffn,file_exist)
if (file_exist) then
open(unit=1,file=coeffn,status='old',form='formatted')
endif
23 format(i,x,a)
open(unit=2,file=coeffn,status='new',form='formatted')
if (file_exist) then
39 read(1,23,err=38) inchar
write(2,*) inchar(1:len(inchar))
goto 39
endif
38 continue
if (file_exist) close(unit=1,status='delete')
write(2,*) 'Sum of squares = ',fsumsq
do i=1,n
write(2,*) 'At the point '//char(i+68)///' ',xw(i)
enddo
write(2,*) ' '
close(unit=2,status='nove')
endif
endif
c
goto 1
end
c
Set up required function
c
function f1n0(w,n,x)
implicit real*8(a-h,o-z),integer(i-n)
real*8 x(n)
f1n0=x(3)*exp(-0.5*(w-x(2))**2/(x(1))**2)
f1n0=x(3)*((x(1)**2/4)/((w-x(2))**2+(x(1)**2/4)))
return
end
c
subroutine lcfunc(m,n,xo,fvcc)
implicit real*8(a-h,o-z),integer(i-n)
real*8 fvcc(m),xo(n)
real*8 y(100),t(100),xn(5),xw(5)
common/valuen/y,t,xn,xw
do i=1,n
xw(i)=xo(i)*xn(i)
enddo
do i=1,m
fvcc(i)=f1n0(t(i),u,xw)-y(i)
enddo
return
end

```

# Appendix C

```

10 ***** Well Width of Quantum wells *****
20 !SI UNITS IN CALC
30 Updated on 6 August 1987
40 GINIT
50 QUIT( EBD1"E" )
60 RAD
70 BI=0
80 BO=0
90 BO=0
100 FID=0
110 OPTION BASE 0
120 DIM Diff(100),Diffa(1000),Fo(1000),F1(1000),F2(1000),F3(1000)
130 DIM Crosspoint(1000),Crosspoints(1000)
140 DIM Runc(1000),Runcv(1000),Width(1000)
150 H=1.05457E-34 !Planck constant
160 H=9.10956E-31 !Mass
170 G=2.43406E-19 !GaAs Gap /J
180 Countw=1
190 IN$="The sample number",title
200 IN$="Hole Fraction of Al",X
210 IN$="Initial Well Width approximation (Å)",A
220 IF A=0 THEN
230 B=1.41E-2
240 BI=1
250 GO TO 360
260 END IF
270 IF A=100 THEN
280 B=1.0E-2
290 BI=1
300 GO TO 360
310 END IF
320 IF A=200 THEN
330 B=7.5E-3
340 BI=1
350 END IF
360 P=INI(A/2,B)
370 A=2.03A
371 IF BI=0 THEN B=(2.6776E-3+5.05132E-1A)+(2.487505E-3A^2)+(-6.019062E-6
40 5)A+.E-5
380 A=A+1.E-10
400 A=A+1.E-10
410 N=1000
420 IN$="The experimental peak energy (eV)",We
430 We2=-We
440 We=-We-1.51924We
450 We=-We
460 IN$="Enter the tolerance for the energy match (meV)",We
470 We=We+1.E-3
480 B=1
490 DISP "Do you want a hardcopy ""
500 ON KEY 5 LABEL " YES " GO TO 560
510 ON KEY 9 LABEL " NO " GO TO 590
520 ON KEY 4 LABEL " " GO TO 520
530 ON KEY 7 LABEL " " GO TO 530
540 ON KEY 8 LABEL " " GO TO 540
550 GO TO 560
560 PRINTER IS 701
570 FID=0
580 GO TO 610
590 PRINTER IS 1
600 Pd=1
610 IN$="The sample is ",title
620 DISP USING "E,X,Z,DDD"!"The hole fraction of Al is ",X
630 IN$="The initial well width approximation was",A/1.E-10,"Å"
640 IN$="The number of points is",N
650 IN$="The energy is ",We2,"eV"
660 IN$="The experimental energy is ",We2,"eV"
670 IN$="The tolerance between experimental and theoretic
680 is ",We/1.E-3,"meV"
690 IN$="The change in well width is 2.03A (1 mono-layer)"
700 PRINT
710 DISP "Choose one..."
720 ON KEY 5 LABEL "All the values" GO TO 780
730 ON KEY 9 LABEL "Results only" GO TO 790
740 ON KEY 6 LABEL " " GO TO 740
750 ON KEY 7 LABEL " " GO TO 750
760 ON KEY 8 LABEL " " GO TO 760
770 GO TO 770
780 GO TO 810
790 GO TO 1980
1980 *****
1990 *****
2000 *****
2010 *****
2020 *****
2030 *****
2040 *****
2050 *****
2060 *****
2070 *****
2080 *****
2090 *****
2100 *****
2110 *****
2120 *****
2130 *****
2140 *****
2150 *****
2160 *****
2170 *****
2180 *****
2190 *****
2200 *****
2210 *****
2220 *****
2230 *****
2240 *****
2250 *****
2260 *****
2270 *****
2280 *****
2290 *****
2300 *****
2310 *****
2320 *****
2330 *****
2340 *****
2350 *****
2360 *****
2370 *****
2380 *****
2390 *****
2400 *****
2410 *****
2420 *****
2430 *****
2440 *****
2450 *****
2460 *****
2470 *****
2480 *****
2490 *****
2500 *****
2510 *****
2520 *****
2530 *****
2540 *****
2550 *****
2560 *****
2570 *****
2580 *****
2590 *****
2600 *****
2610 *****
2620 *****
2630 *****
2640 *****
2650 *****
2660 *****
2670 *****
2680 *****
2690 *****
2700 *****
2710 *****
2720 *****
2730 *****
2740 *****
2750 *****
2760 *****
2770 *****
2780 *****
2790 *****
2800 *****
2810 *****
2820 *****
2830 *****
2840 *****
2850 *****
2860 *****
2870 *****
2880 *****
2890 *****
2900 *****
2910 *****
2920 *****
2930 *****
2940 *****
2950 *****
2960 *****
2970 *****
2980 *****
2990 *****
3000 *****
3010 *****
3020 *****
3030 *****
3040 *****
3050 *****
3060 *****
3070 *****
3080 *****
3090 *****
3100 *****
3110 *****
3120 *****
3130 *****
3140 *****
3150 *****
3160 *****
3170 *****
3180 *****
3190 *****
3200 *****
3210 *****
3220 *****
3230 *****
3240 *****
3250 *****
3260 *****
3270 *****
3280 *****
3290 *****
3300 *****
3310 *****
3320 *****
3330 *****
3340 *****
3350 *****
3360 *****
3370 *****
3380 *****
3390 *****
3400 *****
3410 *****
3420 *****
3430 *****
3440 *****
3450 *****
3460 *****
3470 *****
3480 *****
3490 *****
3500 *****
3510 *****
3520 *****
3530 *****
3540 *****
3550 *****
3560 *****
3570 *****
3580 *****
3590 *****
3600 *****
3610 *****
3620 *****
3630 *****
3640 *****
3650 *****
3660 *****
3670 *****
3680 *****
3690 *****
3700 *****
3710 *****
3720 *****
3730 *****
3740 *****
3750 *****
3760 *****
3770 *****
3780 *****
3790 *****
3800 *****
3810 *****
3820 *****
3830 *****
3840 *****
3850 *****
3860 *****
3870 *****
3880 *****
3890 *****
3900 *****
3910 *****
3920 *****
3930 *****
3940 *****
3950 *****
3960 *****
3970 *****
3980 *****
3990 *****
4000 *****
4010 *****
4020 *****
4030 *****
4040 *****
4050 *****
4060 *****
4070 *****
4080 *****
4090 *****
4100 *****
4110 *****
4120 *****
4130 *****
4140 *****
4150 *****
4160 *****
4170 *****
4180 *****
4190 *****
4200 *****
4210 *****
4220 *****
4230 *****
4240 *****
4250 *****
4260 *****
4270 *****
4280 *****
4290 *****
4300 *****
4310 *****
4320 *****
4330 *****
4340 *****
4350 *****
4360 *****
4370 *****
4380 *****
4390 *****
4400 *****
4410 *****
4420 *****
4430 *****
4440 *****
4450 *****
4460 *****
4470 *****
4480 *****
4490 *****
4500 *****
4510 *****
4520 *****
4530 *****
4540 *****
4550 *****
4560 *****
4570 *****
4580 *****
4590 *****
4600 *****
4610 *****
4620 *****
4630 *****
4640 *****
4650 *****
4660 *****
4670 *****
4680 *****
4690 *****
4700 *****
4710 *****
4720 *****
4730 *****
4740 *****
4750 *****
4760 *****
4770 *****
4780 *****
4790 *****
4800 *****
4810 *****
4820 *****
4830 *****
4840 *****
4850 *****
4860 *****
4870 *****
4880 *****
4890 *****
4900 *****
4910 *****
4920 *****
4930 *****
4940 *****
4950 *****
4960 *****
4970 *****
4980 *****
4990 *****
5000 *****
5010 *****
5020 *****
5030 *****
5040 *****
5050 *****
5060 *****
5070 *****
5080 *****
5090 *****
5100 *****
5110 *****
5120 *****
5130 *****
5140 *****
5150 *****
5160 *****
5170 *****
5180 *****
5190 *****
5200 *****
5210 *****
5220 *****
5230 *****
5240 *****
5250 *****
5260 *****
5270 *****
5280 *****
5290 *****
5300 *****
5310 *****
5320 *****
5330 *****
5340 *****
5350 *****
5360 *****
5370 *****
5380 *****
5390 *****
5400 *****
5410 *****
5420 *****
5430 *****
5440 *****
5450 *****
5460 *****
5470 *****
5480 *****
5490 *****
5500 *****
5510 *****
5520 *****
5530 *****
5540 *****
5550 *****
5560 *****
5570 *****
5580 *****
5590 *****
5600 *****
5610 *****
5620 *****
5630 *****
5640 *****
5650 *****
5660 *****
5670 *****
5680 *****
5690 *****
5700 *****
5710 *****
5720 *****
5730 *****
5740 *****
5750 *****
5760 *****
5770 *****
5780 *****
5790 *****
5800 *****
5810 *****
5820 *****
5830 *****
5840 *****
5850 *****
5860 *****
5870 *****
5880 *****
5890 *****
5900 *****
5910 *****
5920 *****
5930 *****
5940 *****
5950 *****
5960 *****
5970 *****
5980 *****
5990 *****
6000 *****
6010 *****
6020 *****
6030 *****
6040 *****
6050 *****
6060 *****
6070 *****
6080 *****
6090 *****
6100 *****
6110 *****
6120 *****
6130 *****
6140 *****
6150 *****
6160 *****
6170 *****
6180 *****
6190 *****
6200 *****
6210 *****
6220 *****
6230 *****
6240 *****
6250 *****
6260 *****
6270 *****
6280 *****
6290 *****
6300 *****
6310 *****
6320 *****
6330 *****
6340 *****
6350 *****
6360 *****
6370 *****
6380 *****
6390 *****
6400 *****
6410 *****
6420 *****
6430 *****
6440 *****
6450 *****
6460 *****
6470 *****
6480 *****
6490 *****
6500 *****
6510 *****
6520 *****
6530 *****
6540 *****
6550 *****
6560 *****
6570 *****
6580 *****
6590 *****
6600 *****
6610 *****
6620 *****
6630 *****
6640 *****
6650 *****
6660 *****
6670 *****
6680 *****
6690 *****
6700 *****
6710 *****
6720 *****
6730 *****
6740 *****
6750 *****
6760 *****
6770 *****
6780 *****
6790 *****
6800 *****
6810 *****
6820 *****
6830 *****
6840 *****
6850 *****
6860 *****
6870 *****
6880 *****
6890 *****
6900 *****
6910 *****
6920 *****
6930 *****
6940 *****
6950 *****
6960 *****
6970 *****
6980 *****
6990 *****
7000 *****
7010 *****
7020 *****
7030 *****
7040 *****
7050 *****
7060 *****
7070 *****
7080 *****
7090 *****
7100 *****
7110 *****
7120 *****
7130 *****
7140 *****
7150 *****
7160 *****
7170 *****
7180 *****
7190 *****
7200 *****
7210 *****
7220 *****
7230 *****
7240 *****
7250 *****
7260 *****
7270 *****
7280 *****
7290 *****
7300 *****
7310 *****
7320 *****
7330 *****
7340 *****
7350 *****
7360 *****
7370 *****
7380 *****
7390 *****
7400 *****
7410 *****
7420 *****
7430 *****
7440 *****
7450 *****
7460 *****
7470 *****
7480 *****
7490 *****
7500 *****
7510 *****
7520 *****
7530 *****
7540 *****
7550 *****
7560 *****
7570 *****
7580 *****
7590 *****
7600 *****
7610 *****
7620 *****
7630 *****
7640 *****
7650 *****
7660 *****
7670 *****
7680 *****
7690 *****
7700 *****
7710 *****
7720 *****
7730 *****
7740 *****
7750 *****
7760 *****
7770 *****
7780 *****
7790 *****
7800 *****
7810 *****
7820 *****
7830 *****
7840 *****
7850 *****
7860 *****
7870 *****
7880 *****
7890 *****
7900 *****
7910 *****
7920 *****
7930 *****
7940 *****
7950 *****
7960 *****
7970 *****
7980 *****
7990 *****
8000 *****
8010 *****
8020 *****
8030 *****
8040 *****
8050 *****
8060 *****
8070 *****
8080 *****
8090 *****
8100 *****
8110 *****
8120 *****
8130 *****
8140 *****
8150 *****
8160 *****
8170 *****
8180 *****
8190 *****
8200 *****
8210 *****
8220 *****
8230 *****
8240 *****
8250 *****
8260 *****
8270 *****
8280 *****
8290 *****
8300 *****
8310 *****
8320 *****
8330 *****
8340 *****
8350 *****
8360 *****
8370 *****
8380 *****
8390 *****
8400 *****
8410 *****
8420 *****
8430 *****
8440 *****
8450 *****
8460 *****
8470 *****
8480 *****
8490 *****
8500 *****
8510 *****
8520 *****
8530 *****
8540 *****
8550 *****
8560 *****
8570 *****
8580 *****
8590 *****
8600 *****
8610 *****
8620 *****
8630 *****
8640 *****
8650 *****
8660 *****
8670 *****
8680 *****
8690 *****
8700 *****
8710 *****
8720 *****
8730 *****
8740 *****
8750 *****
8760 *****
8770 *****
8780 *****
8790 *****
8800 *****
8810 *****
8820 *****
8830 *****
8840 *****
8850 *****
8860 *****
8870 *****
8880 *****
8890 *****
8900 *****
8910 *****
8920 *****
8930 *****
8940 *****
8950 *****
8960 *****
8970 *****
8980 *****
8990 *****
9000 *****
9010 *****
9020 *****
9030 *****
9040 *****
9050 *****
9060 *****
9070 *****
9080 *****
9090 *****
9100 *****
9110 *****
9120 *****
9130 *****
9140 *****
9150 *****
9160 *****
9170 *****
9180 *****
9190 *****
9200 *****
9210 *****
9220 *****
9230 *****
9240 *****
9250 *****
9260 *****
9270 *****
9280 *****
9290 *****
9300 *****
9310 *****
9320 *****
9330 *****
9340 *****
9350 *****
9360 *****
9370 *****
9380 *****
9390 *****
9400 *****
9410 *****
9420 *****
9430 *****
9440 *****
9450 *****
9460 *****
9470 *****
9480 *****
9490 *****
9500 *****
9510 *****
9520 *****
9530 *****
9540 *****
9550 *****
9560 *****
9570 *****
9580 *****
9590 *****
9600 *****
9610 *****
9620 *****
9630 *****
9640 *****
9650 *****
9660 *****
9670 *****
9680 *****
9690 *****
9700 *****
9710 *****
9720 *****
9730 *****
9740 *****
9750 *****
9760 *****
9770 *****
9780 *****
9790 *****
9800 *****
9810 *****
9820 *****
9830 *****
9840 *****
9850 *****
9860 *****
9870 *****
9880 *****
9890 *****
9900 *****
9910 *****
9920 *****
9930 *****
9940 *****
9950 *****
9960 *****
9970 *****
9980 *****
9990 *****
1000 *****

```